Synthesis and Characterization of Dye-Containing Covalent Organic Frameworks

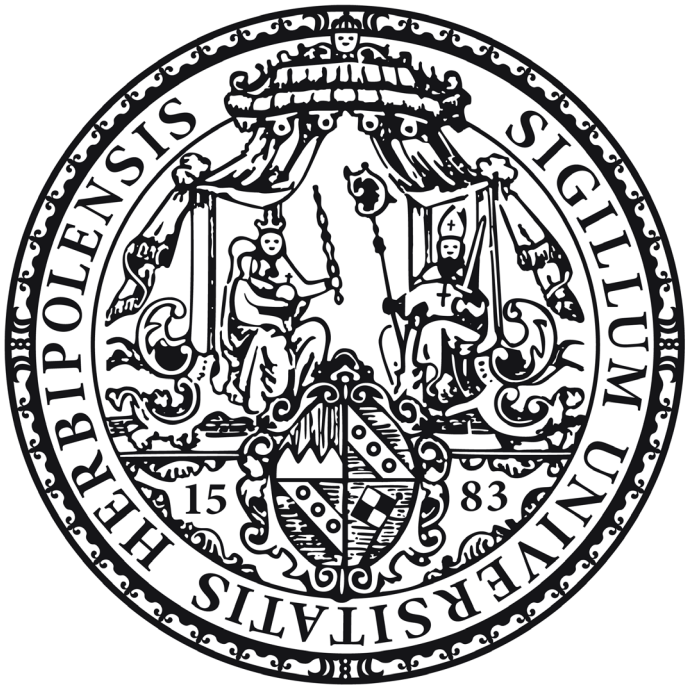

Dissertation zur Erlangung des
naturwissenschaftlichen Doktorgrades der
Julius-Maximilians-Universität Würzburg

vorgelegt von

Roberto Sánchez Naya

aus Madrid, Spanien

Würzburg 2022

Eingereicht bei der Fakultät für Chemie und Pharmazie am:

_____

Gutachter der schriftlichen Arbeit:

1. Gutachter: Priv.-Doz. Dr. Florian Beuerle

2. Gutachter: Prof. Dr. Frank Würthner

Prüfer des öffentlichen Promotionskolloquiums:

1. Prüfer: Priv.-Doz. Dr. Florian Beuerle

2. Prüfer: Prof. Dr. Frank Würthner

3. Prüfer:

Datum des öffentlichen Promotionskolloquiums:

_____

Doktorurkunde ausgehändigt am:

A mi familia

“I've missed more than 9000 shots in my career. I've lost almost 300 games. 26 times, I've been trusted to take the game winning shot and missed. I've failed over and over and over again in my life. And that is why I succeed.”

— Michael Jordan

List of Abbreviations

1D/2D/3D	One/Two/Three Dimensional
ABDA	9,10-Anthracenediyl-bis(methylene)dimalonic acid
ACQ	Aggregation-caused Quenching
Anh.	Anhydrous
ATR	Attenuated Total Reflectance
a.u.	Arbitrary Unit
BDBA	Benzene-1,4-diboronic acid
BET	Brunauer-Emmett-Teller
BODIPY	Boron-dipyrromethene: 4,4-difluoro-4-bora-3a,4a-diaza-s-indacene
BPA	Bisphenol A
BZD	Benzidine
C_e	Concentration at the equilibrium
CEES	2-Chloroethyl ethyl sulfide
CEESO	2-Chloroethyl ethyl sulfoxide
$CEESO_2$	2-Chloroethyl ethyl sulfone
CIE	International Commission on Illumination (French: *Commission Internationale de l'Eclairage*)
COF	Covalent Organic Framework
CON	Covalent Organic Nanosheet
COOH-FeO	Carboxylic acid functionalized Iron Oxide Nanoparticles
CP/MAS	Cross-Polarization Magic-Angle Spinning
CTF	Covalent Triazine Framework
D−A	Donor-Acceptor
DBB	1,2-Dibenzoylbenzene
DCM	Dichloromethane
DEPT	Distortionless Enhancement by Polarization Transfer
DFT	Density Functional Theory
DMF	Dimethylformamide
DMSO	Dimethylsulfoxide
DPBF	1,3-Diphenyl-*iso*-benzofuran
DPP	Diketopyrrolopyrrole
DRS	Diffuse Reflectance Spectroscopy

EDXS	Energy-dispersive X-Ray Spectroscopy
e.g.	For example (Latin: *Exempli gratia*)
ESB	Energy Selective Backscattered
EtHex	2-Ethyl hexyl substituted
ETTA	1,1′,2,2′-tetra-*p*-aminophenylethylene
FeO	Iron Oxide, combination of Fe_2O_3 and Fe_3O_4
FRET	Förster Resonance Energy Transfer
FT-IR	Fourier-transform Infrared Spectroscopy
HHTP	Hexahydroxytriphenylene
HMTA	Hexamethylenetetraamine
HOMO	Highest Occupied Molecular Orbital
HOPG	Highly Oriented Pyrolytic Graphite
HR-STM	High Resolution Scanning Tunneling Microscopy
HWE	Horner–Wadsworth–Emmons
i.e.	Which means (Latin: *Id est*)
IR	Infrared
ITO	Indium Tin Oxide
K_F	Freundlich constant
K_L	Langmuir constant
LED	Light Emitting Diode
LUMO	Lowest Unoccupied Molecular Orbital
MAS	Magic-Angle Spinning
MB	Methylene Blue
MCR	Multicomponent Reaction
MOF	Metal-Organic Framework
NH_2-FeO	Amine functionalized Iron Oxide Nanoparticles
NIR	Near-Infrared
NIS	*n*-Iodo succinimide
NMR	Nuclear Magnetic Resonance
NP	Nanoparticle
***o*-DCB**	*ortho*-dichlorobenzene
OFET	Organic Field-effect Transistor
OLED	Organic Light Emitting Diode
PBI	Perylene bisimide

PET	Photoinduced Electron Transfer
POP	Porous Organic Polymer
ppb	Parts per billion (Equivalent to $\mu g\ kg^{-1}$)
ppm	Parts per million (Equivalent to $mg\ kg^{-1}$)
PTFE	Polytetrafluoroethylene
PXRD	Powder X-Ray Diffraction
q_e	Equilibrium Adsorption Capacity
q_{max}	Maximum Adsorption Capacity
R_L	Separation factor
R_p	Residual of least-squares
ROS	Reactive Oxygen Species
Rpm	Revolutions per minute
RT	Room temperature
R_{wp}	Weighted residual
SCOF	Surface Covalent Organic Framework
SEM	Scanning Electron Microscopy
SFTB	(4,4′,4″,4‴-(9,9′-spirobi[fluorene]-2,2′,7,7′-tetrayl)-tetrabenzaldehyde
STM	Scanning Tunneling Microscopy
TAPP	5,10,15,20-tetrakis(4-aminophenyl)porphyrin
TBAF	Tetrabutylammonium fluoride
TBPP	5,10,15,20-tetra(*p*-boronic acid-phenyl)porphyrin
TEA	Triethylamine
TFA	Trifluoroacetic acid
TFP	1,3,5-Triformylphluoroglucinol
TGA	Thermogravimetric Analysis
THF	Tetrahydrofuran (-d_8: deuterated)
TNP	2,4,6-Trinitrophenol
Tol	Toluene
TPE	Tetraphenylethylene
TTF	Tetrathiafulvalene
UV	Ultraviolet
VIS	Visible
VSM	Vibrating-sample Magnetometry
w/o bck	Without background

WLED	White Light Emission Device
Wt	Weight
ΔG	Gibbs free energy change

Table of Contents

Chapter 1: Introduction and Aim of the Thesis 1

Chapter 2: State of the Art 5

2.1. Definition of COFs 5

2.2. Dynamic Covalent Chemistry and COF formation 5

2.3. Synthetic methodologies 8

2.3.1. Solvothermal synthesis 9

2.3.2. Ionothermal synthesis 10

2.3.3. Microwave assisted synthesis 10

2.3.4. Mechanochemical synthesis 11

2.3.5. On-surface synthesis 11

2.3.6. Sonochemical synthesis 12

2.3.7. Light-promoted synthesis 12

2.4 Linkages 13

2.4.1 Boron-containing bonds 13

2.4.2 Nitrogen-containing bonds 14

2.4.3 Olefinic Bonds 17

2.4.4 Linkages through other heteroatoms bonds 18

2.4.5 Unconventional linkages 19

2.5 Molecular Design and Topology 20

2.5.1 2D COFs 23

2.5.2 3D COFs 26

2.6 Dye-Containing COFs and applications 29

Chapter 3: Modulation of Crystallinity and Optical Properties in Composite Materials Combining Iron Oxide Nanoparticles and Dye-Containing Covalent Organic Frameworks 37

3.1 Introduction 37

3.2 Results and Discussion 38

3.3 Conclusions 46

Chapter 4: A BODIPY-Containing Covalent Organic Framework as a Highly Porous Photosensitizer for Environmental Remediation. 47

4.1 Introduction 47

4.2 Results and discussions 49

4.2.1 Synthesis and characterization of BDP-TFP-COF 49

4.2.2 Adsorption experiments: Removal of model pollutants from water 56

4.2.3 Sensing of Methylene Blue 66

4.2.4 Singlet oxygen generation 69

4.2.5 Photoconversion of a Mustard Gas Simulant 73

4.2 Conclusions 75

Chapter 5: Synthesis and Characterization of a Low-Bandgap Diketopyrrolopyrrole-Pyrene Covalent Organic Framework 77

5.1 Introduction 77

5.2 Results and Discussion 78

5.3 Conclusions 84

Chapter 6: Summary and Conclusions 85

Chapter 7: Zusammenfassung und Fazit 91

Chapter 8: Appendix 97

8.1 Supporting information for Chapter 3: Modulation of Crystallinity and Optical Properties in Composite Materials Combining Iron Oxide Nanoparticles and Dye-Containing Covalent Organic Frameworks 97

8.1.1 Materials and Methods 97

8.1.2 Synthesis and Characterization 98

8.2 Supporting information for Chapter 4: A BODIPY-Containing Covalent Organic Framework as a Highly Porous Photosensitizer for Environmental Remediation 115

8.2.1 Materials and Methods 115

8.2.2 Synthesis and Characterization 116

8.2.3 Adsorption Experiments 123
8.2.4 Sensing of Methylene Blue in water 125
8.2.5 Singlet Oxygen Generation 127
8.2.6 Photoconversion of a Mustard Gas Simulant 128
8.3 Supporting information for Chapter 5: Synthesis and Characterization of a Low-Bandgap Diketopyrrolopyrrole-Pyrene Covalent Organic Framework. 131
8.3.1 Materials and Methods 131
8.3.2 Synthesis and Characterization 132
8.3.3 Singlet Oxygen Generation 136
List of Publications 137
Individual Contributions 139
Acknowledgements 141
References 145

Chapter 1: Introduction and Aim of the Thesis

Porous materials have emerged as a highly versatile platform for a wide variety of applications ranging from gas storage and separation[1-3] to drug delivery,[4-6] environmental remediation[7-9] or catalysis.[10-12] Even though the recent development of artificial porous materials such as metal-organic frameworks (MOFs) or covalent organic frameworks (COFs) have drawn considerable attention in the scientific community, minerals endowed with porosity have been used for millennia. The utilization of porous charcoal was reported in ancient Egyptian papyrus for the treatment of indigestion. In addition, water purification methods employing the same material were described by Indian sources.[13] Another method to make potable water was adopted by the ancient Maya, who employed zeolite minerals as natural adsorbent materials.[14] While charcoal was still used during centuries for filtering and purifying, the establishment of synthetic zeolites as highly absorptive solids for applications in hydrocarbon cracking revolutionized the field of porous materials in the 1940s.[15, 16] While zeolites are a class of inorganic solids composed of aluminosilicate-based frameworks with intrinsic porosity (Figure 1a),[17] purely organic crystalline materials were not a reality at that time. Instead, synthetic one-dimensional polymers represented examples for organic structures with unprecedented complexity.[18] However, achieving a regular order in the macromolecular system remained challenging. The rise of supramolecular chemistry took the advantage of molecular recognition processes by guiding intermolecular forces. This strategy enabled the construction of more intricated architectures arranged and held together by weak non-covalent interactions. This process, termed self-assembly, could achieve the organization of well-defined supramolecular arrangements.[19] Nonetheless, the structural integrity of the formed superstructure is easily compromised due to a limited thermal and chemical robustness of the aggregates. The directed coordination of lone pairs from rigid organic linkers with metal ions or clusters yielded crystalline porous frameworks based on organic-inorganic hybrids, known as MOFs (Figure 1b). The synthesis of the first MOF with permanent porosity and shape persistency after guest removal in 1999 by Yaghi and co-workers entailed a significant step towards constructing arranged structures containing organic building units.[20] With the objective of obtaining covalently linked analogues of MOFs, the Yaghi group developed COFs as crystalline extended framework materials with organic subunits connected by covalent bonds (Figure 1c). In 2005, they reported the first two COFs **COF-1** and **COF-5**.[21]

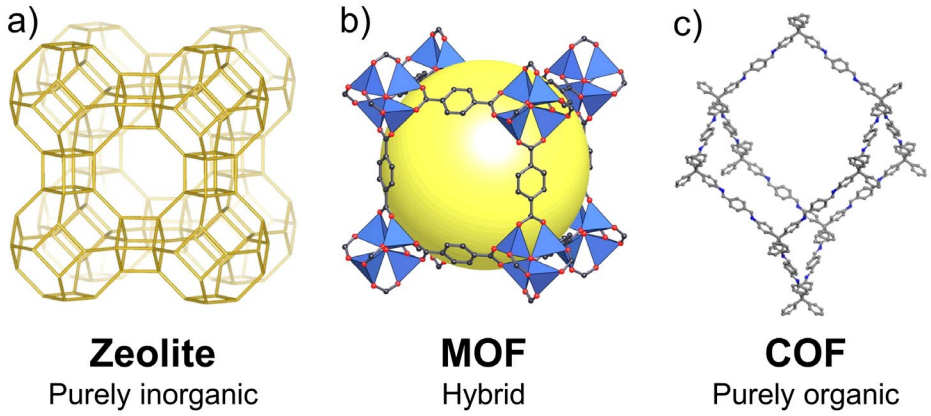

Figure 1. Examples of employed framework-based porous crystalline materials. While the zeolite structure (a) is formed with fused MO_4 tetrahedra (M = Si, Al), MOFs (b) are based on coordination chemistry between metallic clusters and organic building blocks. By contrast, COFs (c) represent a class of purely organic frameworks that present organic building blocks joined by covalent bonds. Adapted with permission from Reference 22 Copyright © 2022, American Chemical Society; Reference 23 Copyright © 2019, Zhengzhou University and Reference 24 (Open Access BY 4.0).

As shown in Scheme 1, both frameworks consist of extended organic structures merely formed by self-condensation of benzene-1,4-diboronic acid (BDBA) for **COF-1** or the co-condensation of BDBA with hexahydroxytriphenylene (HHTP) for **COF-5**. Thus, the formation of boroxine rings or boronate esters, respectively, resulted in layered hexagonal frameworks with long-range order. These unprecedented frameworks showed intrinsic porosity with high surface area, low density, high crystallinity, and excellent thermal stability. The formation of these purely organic polymers implied a significant turning point in the field of organic materials.

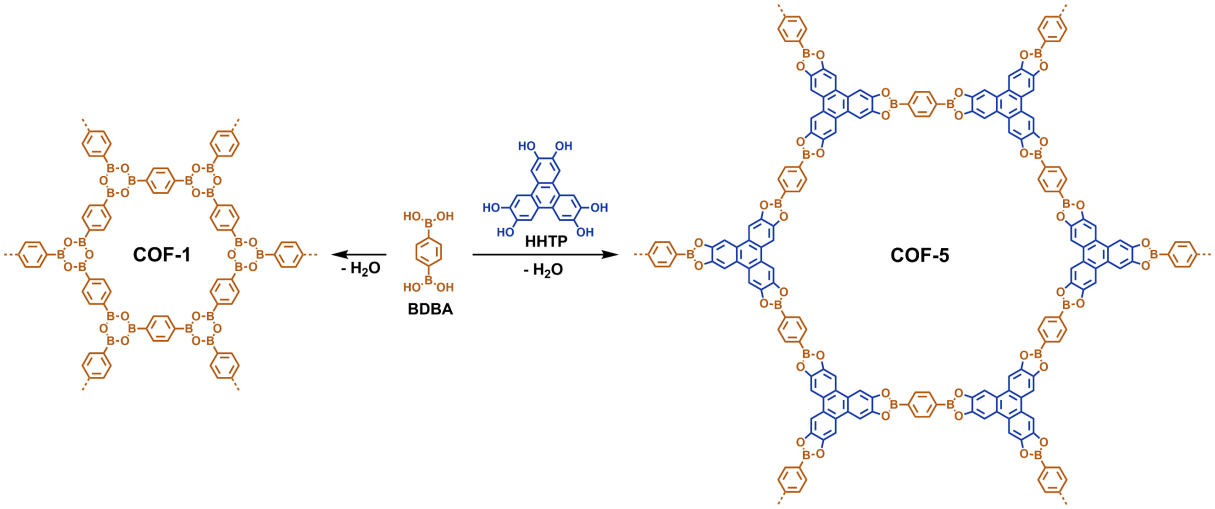

Scheme 1. Synthesis of **COF-1** and **COF-5**.

As a consequence of the facile incorporation of a vast range of functional groups as well as the possibility to control the geometry of the final product, the development of novel COFs ever increased after the publication of this pioneering work.[25, 26] Until now, a wide variety of 2D and 3D topologies, linkages and properties derived directly from the chosen organic components, allowing the tailor-made design of COFs to obtain optimal performances in targeted

applications.[27-29] For instance, the incorporation of chromophores gives access to novel COFs and intriguing physicochemical properties directly arise from the selected dyes. Additional features such as stacking, degree of conjugation or interaction between different monomers triggered by the organic skeleton could also have an impact on the optical properties.[30]

In **Chapter 2**, a general overview on the chemistry of COFs will be given to understand the basics of this immense yet rapidly evolving field. **Chapters 3 to 5** discuss the experimental results of this Thesis in a detailed manner. The overarching goal is the synthesis and characterization of novel COFs that contain dye molecules as integral components of the organic backbone (Figure 2). These chromophore-containing frameworks open new research lines in the field and call for the exploration of applications such as catalysis, sensing, or in optoelectronic devices. In **Chapter 3**, the fabrication of organic-inorganic composites by the growth of **DPP-TAPP-COF** around functionalized iron oxide nanoparticles is reported. By varying the ratio between inorganic nanoparticles and organic COFs, optoelectronic properties of the materials are adjusted. **Chapter 4** reports the synthesis of a novel boron-dipyrromethene-containing (BODIPY) **BDP-TFP-COF**. Synthesis, full characterization and the scope of potential applications with a focus on environmental remediation are discussed in detail. In **Chapter 5**, a novel diketopyrrolopyrrole-containing (DPP) **DPP-Py-COF** based on the combination of DDP and pyrene building blocks is presented. The very low bandgap of these materials and initial investigations on the photosensitizing properties are discussed. Ultimately, the main results of this Thesis are summarized in both English and German in **Chapters 6 and 7**, respectively.

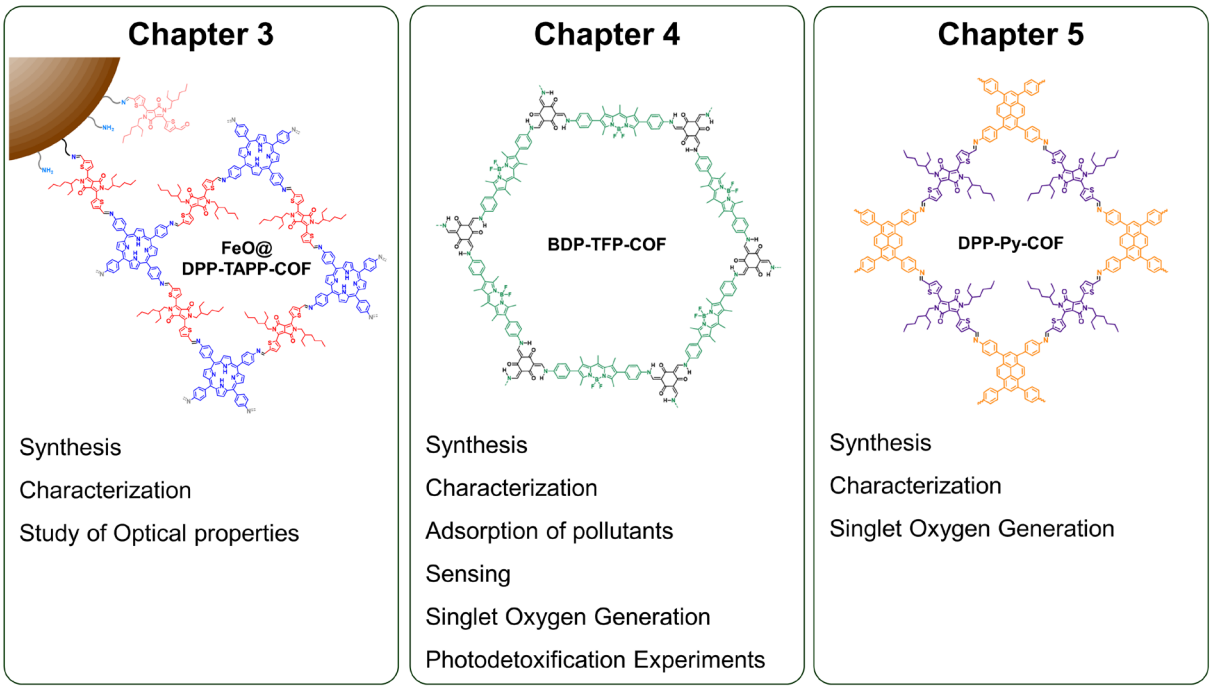

Figure 2. Chemical structures of the COFs targeted in this Thesis.

Chapter 2: State of the Art

2.1. Definition of COFs

As briefly mentioned in Chapter 1, COFs are a class of organic polymers obtained by means of reticular chemistry.[31] They consist of either two-dimensional or three-dimensional polymers composed of covalently bound organic building blocks that are arranged into periodic structures in a geometric manner, thus forming well-defined tessellated motifs.[32] In order to differentiate these structures from other microporous and branched polymers, the fundamental features of COFs typically include intrinsic porosity with usually high specific surface areas and high crystallinity emerging from long-range ordered structures. In contrast to metal organic frameworks, they are exclusively composed of light elements such as H, B, C, N and O, thus providing structures with remarkable low densities e.g. **COF-108** with an extremely low value of 0.17 g cm^{-3}.[33] In addition, the covalent nature of these macromolecules provides excellent thermal and chemical stabilities.[34, 35]

2.2. Dynamic Covalent Chemistry and COF formation

The chemical reaction of an organic building block **A** may follow two different pathways, as observed in Figure 3a: On the one hand, the kinetically controlled reaction in which the covalent bond is formed in a fast and irreversible manner. This implies the spontaneous formation of the kinetic product **C**, which is reached along the transition state with the lower Gibbs Free Energy change ($\Delta G_C^{\ddagger}$). However, the conditions for such reactions must be chosen very carefully since the irreversibility of this transformation prevents further modification of the starting materials. On the other hand, the product formation under thermodynamic control implies an equilibrium process in which reversible covalent bonds are broken and formed until the formation of the thermodynamically more stable product **B**, i.e., the product with the lowest ΔG (ΔG_B, in negative value) is achieved.

This dynamic equilibrium is responsible for the reversibility of the transformation, not only leading to the most stable molecule but also providing the opportunity for “error-checking” processes.[36] The utility of this so-called dynamic covalent chemistry (DCC) has a direct impact on the synthesis of COFs, since such processes allow to fix structural defects and favour the formation of long-ordered domains, i.e., highly crystalline polymers (Figure 3b).[37]

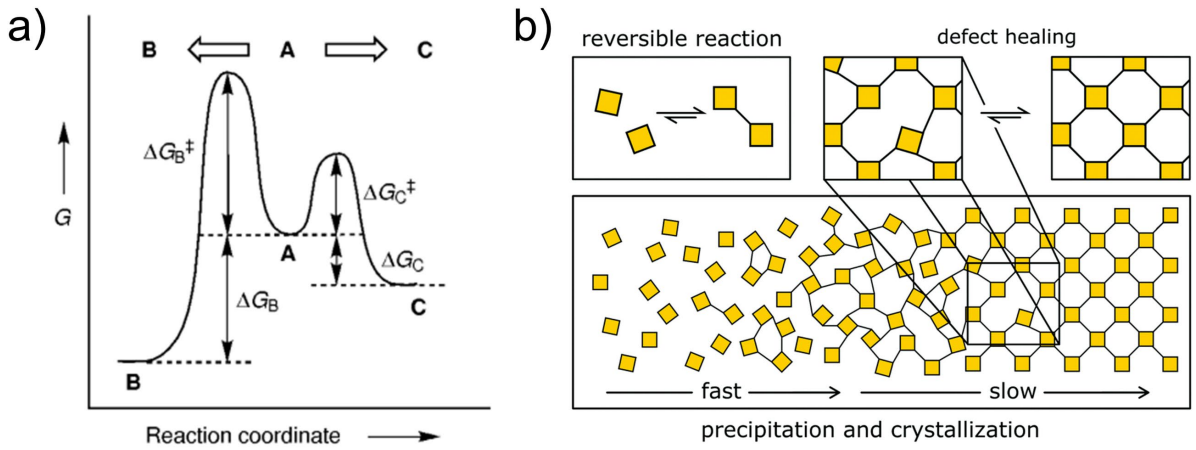

Figure 3. a) Schematic representation of the energy profile indicating the two different reaction pathways. A to C: Kinetic control. A to B: Thermodynamic control. Reproduced with permission from Reference 36. Copyright © 2002 WILEY-VCH Verlag GmbH. b) COF crystallization after a fast initial deposition of the building blocks and further slow reversible bonding and defect healing by DCC. Reproduced with permission from Reference 37 (Open Access CC BY 3.0).

Furthermore, these dynamic equilibria also entail that the formation of the desired product is critically influenced by several external factors including temperature, concentration, pressure or impurities, hence negatively affecting the crystallinity of COFs. This issue, termed as the "crystallization problem"[38] sometimes result in situations in which finding the right conditions for the required microscopic reversibility arises as the major obstacle in COF synthesis. This challenge typically increases with the strength of the covalent bonds formed among building blocks, in contrast to supramolecular structures or MOFs that typically present weaker and hence more reversible interactions (Figure 4).

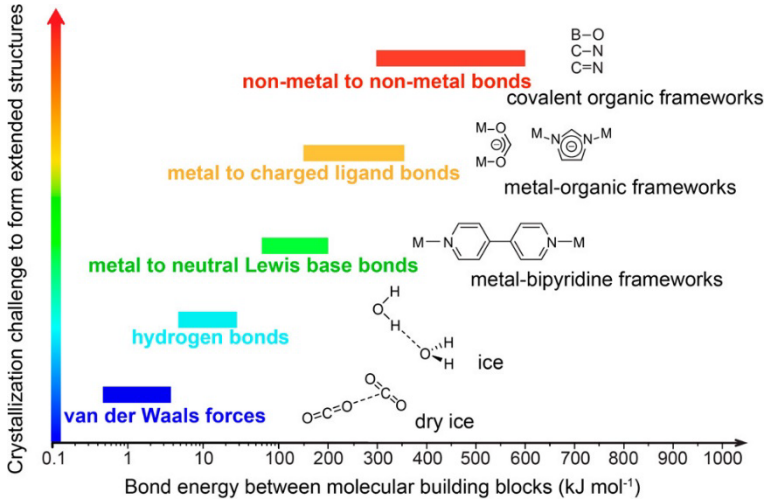

Figure 4. Representation of the increasing difficulty to achieve crystalline structures with the increasing strength of the linkage among building blocks. Reproduced with permission from Reference 38. Copyright © 2016, American Chemical Society.

Due to the slow kinetics of the equilibrium phenomena, the formation of dynamic covalent bonds usually requires catalysis. Moreover, equilibrium reactions are generally classified into

two categories (Figure 5).[36] The first class involves the breaking/making of a reversible bond via condensation reactions that are accompanied with the loss/addition of small molecule side products, e.g., water or methanol. A common example of this class in COF chemistry is the formation of imines by the reaction between an aldehyde and a primary amine with the loss of a molecule of water, typically catalyzed by acetic acid.[39] The second class involves a direct exchange reaction in which the type of bond is preserved in both product and starting material. One exchange reaction applied in COFs is the transimination reaction reported by Dichtel and co-workers to obtain imine-linked 2D COFs in five hours with microwave irradiation.[40]

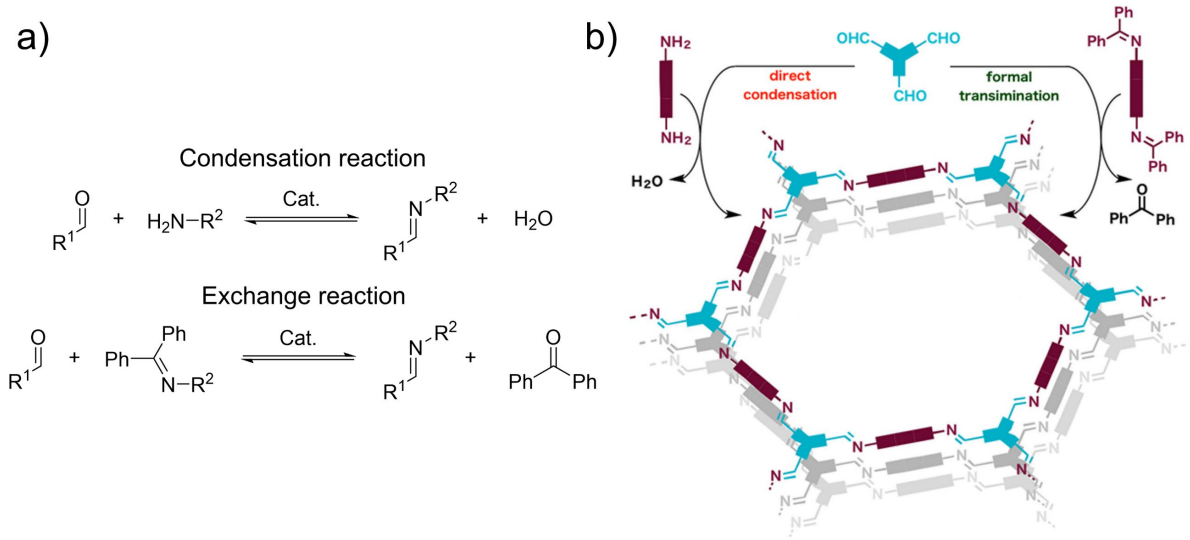

Figure 5. a) Different types of reversible reactions and b) their implementation in the COF synthesis. Adapted with permission from Reference 40. Copyright © 2017, American Chemical Society.

In 2022, the ultimate evidence for the nucleation process that assembles organic building blocks into COFs via dynamic covalent chemistry was published by De Feyter and co-workers.[41] The polymerization steps of **PPy-COF** on a highly oriented pyrolytic graphite (HOPG) substrate could be directly observed and followed over time by using scanning tunnelling microscopy (STM), revealing the emergence of the crystalline regions from the amorphous phase and the dynamic growth of the grain boundaries (Figure 6).

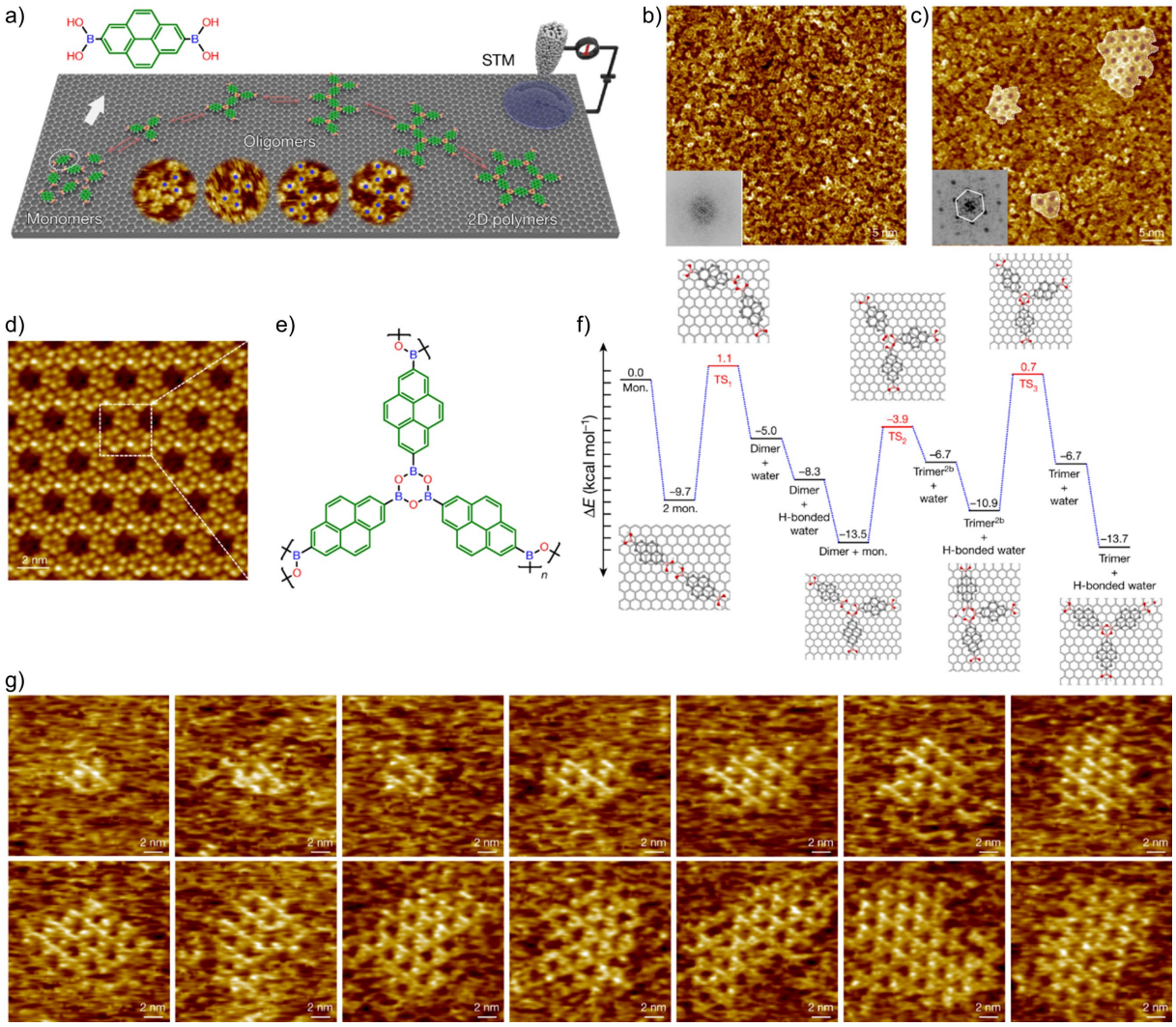

Figure 6. a) Illustration of the COF condensation. b) Amorphous COF phase and c) honeycomb clusters arising. d) HR-STM image of the 2D network and e) chemical structure of the backbone. f) DFT calculations of the energies of dimers, trimers and transition states during the reaction pathway. g) Images of different individual nuclei formed on the HOPG surface. Adapted with permission from Reference 41. Copyright © 2022, The Author(s), under exclusive licence to Springer Nature Limited.

2.3. Synthetic methodologies

The formation of high-quality crystallites has been crucial for the development of the field. For this purpose, it is not only important to select the the adequate building blocks, geometry and functionalities, but also to choose the proper reaction conditions for the correct growth of long-range order structures. In their early years, COFs were predominantly synthesized by solvothermal synthesis. In state-of-the-art protocols however, also modern methods with additional benefits such as simpler conditions, shorter reaction times or eco-friendliness, among others, are applied.[42] In the following, the most exploited synthetic methodologies at the present will be shortly listed and explained.

2.3.1. Solvothermal synthesis

Even though solvothermal synthesis of COFs is certainly the most traditional method, it is still the most used nowadays.[42] The challenge in the crystallization process of COFs comes from two different issues: The reversible reaction requires slow rates and the water, or condensation product, must to some extend remain in the mixture to enable the reversibility of the process. This problem is solved by performing the reaction in Pyrex tubes or flame-sealed ampoules and using solvent mixtures in which the organic building blocks are only partially soluble. Hence, solvothermal conditions involve the co-condensation of complementary organic building blocks in a sealed vessel using a previously degassed solvent, or solvent mixture, with temperatures higher than the boiling point, usually in the presence of a catalyst and allowing the gram scale synthesis of COFs. A typical synthetic procedure starts with the introduction of the reaction components in an ampoule or a capped tube. Then the vessel is flame-sealed or simply closed under inert gas, followed by brief sonication to homogeneously disperse all the reaction components. Then the vessel is stored in a pre-heated oven for the required amount of time. Due to the breaking/formation of strong dynamic covalent bonds, the optimization of the reaction conditions is very crucial for the formation of highly crystalline polymers and the average reaction times of COF formation last for several days (3-7 days in general). Examples that used solvothermal methodology include a wide variety of backbones that encompass long-established COFs as well as recently synthesized polymers. To explain the continuity of this method, we will refer to the Yaghi group and its **COF-1** again.[21] This material, which was the first reported COF ever, was obtained by solvothermal synthesis. The same group recently reported the synthesis of **COF-39** from the condensation of (4,4′,4″,4‴-(9,9′-spirobi[fluorene]-2,2′,7,7′-tetrayl)-tetrabenzaldehyde (SFTB) with benzidine (BZD) (Scheme 2). This highly complex structure is composed of mutually entangled square nets that give shape to a 2D square COF and was synthesized by using the same solvothermal method.[43] These two structures, reported 17 years apart, are representative evidence of the validity of this synthetic strategy.

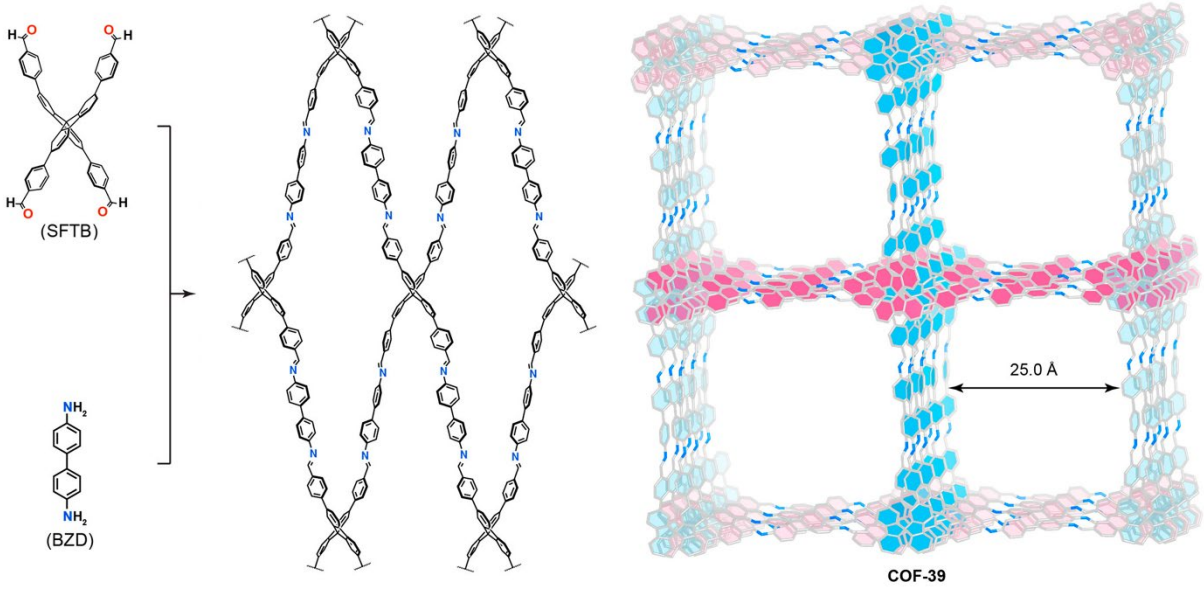

Scheme 2. Synthesis of the entangled structure of **COF-39** from SFTB and BZD building blocks, obtained by solvothermal synthesis by the Yaghi group in 2022. Adapted with permission from Reference 43. Copyright © 2022, American Chemical Society.

2.3.2. Ionothermal synthesis

In analogy to the solvothermal synthesis, this method employs molten metal salts acting as the solvent. However, the requirement of extremely high temperatures up to 300-400 °C to melt the salts involves harsh conditions and might imply the calcination of a large number of COFs. Although the application of this method is less common, the use of molten metal salts at such temperatures catalyses the formation of COFs with less reactive linkages and allows the incorporation of fully insoluble building blocks. For example, the trimerization of dicyanobenzene in molten $ZnCl_2$ salts yields the covalent triazine framework **CTF-1**, reported by the Thomas group in 2008.[44] By following a similar methodology, Lotsch and co-workers synthesized a novel imide-linked and perylene bisimide-containing (PBI) COF without any solvent that resulted in a crystalline precipitate in as few as ten hours. By contrast, the same product cannot be obtained via the solvothermal route.[45]

2.3.3. Microwave assisted synthesis

As used in the synthesis of discrete organic molecules, the implementation of microwave irradiation greatly benefits the growth of COFs. Compared to the heating method applied in solvo/ionothermal synthesis, in which the heat is transferred by convection from the surface, microwave irradiation is more energy efficient. Microwaves can better penetrate the sample and lead to faster and more homogeneous heat transfer, thus resulting in higher yields, shorter reaction times, more narrow pore size distribution and even enhanced physicochemical properties.[46] The application of this synthetic strategy indeed resulted in remarkably reduced

reaction times to obtain crystalline materials, increasing the reaction rates up to 200 times while obtaining comparable or higher surface areas.[47]

2.3.4. Mechanochemical synthesis

In 2013, Banerjee and co-workers demonstrated for the first time the feasibility of obtaining COFs by merely manual grinding in a mortar or alternatively in a ball mill.[48] With this method, three COF powders, **TpPa-1**, **TpPa-2** and **TpBD** were initially obtained by mechanochemical synthesis. The progress of the COF formation could be followed by colour change after 40 minutes of grinding (Figure 7). Unfortunately, this method triggers the exfoliation of the two-dimensional layers causing the hindering of the pores and decreasing the crystallinity and porosity of the framework. In contrast, the mild conditions of this reaction provided considerable benefits such as rapidity, simplicity, eco-friendliness and cost savings. In addition, this strategy also provides an alternative to preparing materials from insoluble building blocks.

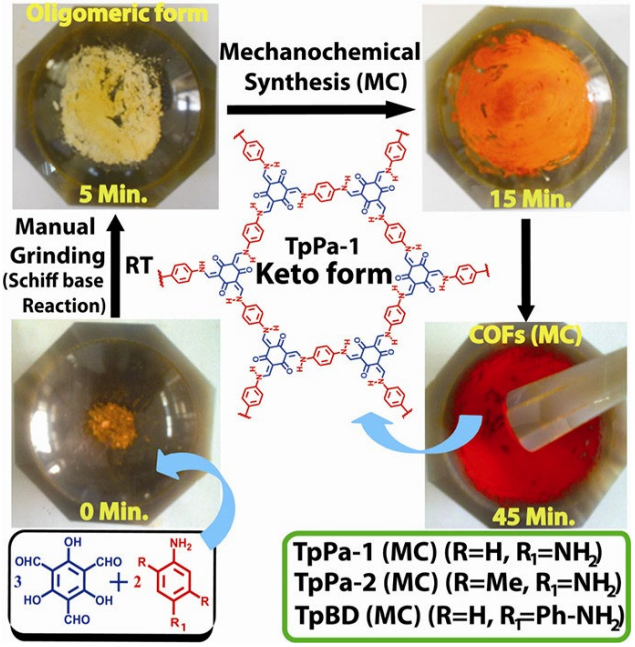

Figure 7. Steps of the mechanochemical synthesis of COFs. Reproduced with permission from Reference 48. Copyright © 2013, American Chemical Society

2.3.5. On-surface synthesis

One way to push the limits of nanoelectronics is the implementation of COF thin films on substrates for further applications in semiconducting devices. The development of surface covalent organic frameworks (SCOFs) offered a synthetic strategy for the efficient growth of COFs on extended surfaces. Porte and co-workers achieved the monolayer formation of the boroxine-linked **sCOF-1** and the boronate ester-linked **sCOF-2** by the sublimation and layer deposition of the corresponding building blocks onto a Ag(111) substrate from a heated

molybdenum crucible between 370 and 460 K under ultrahigh vacuum.[49] STM images after the deposition showed an organized film composed of a network of polygons dominated by perfect hexagons and a small number of faults (Figure 8). Remarkably, the quality of the network was unaffected by changes in the experimental parameters and the frameworks showed no degradation after thermal annealing up to 750 K for five minutes, revealing the high stability of the structures on the surface.

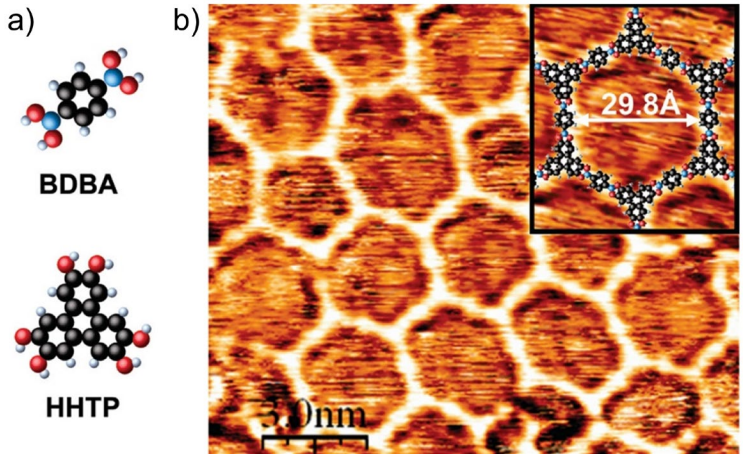

Figure 8. a) Schematic representation of the molecular building blocks of **sCOF-2** and b) STM image of on-surface growth **sCOF-2** after deposition of BDBA and HHTP on a Ag(111) substrate. Adapted with permission from Reference 49. Copyright © 2008, American Chemical Society.

Besides this direct strategy, an indirect approach has been performed by introducing the substrate in the reaction tube and further applying the solvothermal method.[50]

2.3.6. Sonochemical synthesis

The utilization of high-energy ultrasounds provoke the formation and implosion of bubbles in liquids which generate localized hot spots that accelerate reactions. This singular strategy was smartly adopted by Cooper and co-workers in 2022. They reported the synthesis of several 2D and 3D COFs based on Schiff-Base reactions driven by ultrasonication.[51] Remarkably, the method only required water as solvent and acetic acid as catalyst. In addition, the COFs were prepared in less than one hour at room temperature with comparable or higher crystallinities than their equivalents obtained by solvothermal methods, thus making this synthetic method greener, simpler and safer.

2.3.7. Light-promoted synthesis

In 2019, Choi and co-worker induced reversible imine condensations by employing light energy for the synthesis of a highly crystalline and conjugated **hcc-COF**.[52] In a quartz vial, 1,2,4,5-Benzenetetramine and hexaketocyclohexane were dispersed in a methanol/mesitylene mixture in the presence of deionized water and acetic acid. Upon irradiation at a wavelength

range between 200-2500 nm, a black crystalline COF precipitate was obtained within the short time of three hours, evidencing the feasibility of COF synthesis by employing light irradiation.

2.4 Linkages

As mentioned in Chapter 2.2, the incorporation of dynamic covalent bonds is essential for the formation of highly crystalline structures during the reticulation process. For the correct bonding between subunits, they must contain reactive functional groups that allow the reversible bond formation under synthetic conditions that avoid jeopardizing the structural integrity of the organic building blocks. In this section, the dynamic covalent bonds and some further cascade reactions responsible for the adequate connection between organic monomers will be briefly listed. Note that the bonds reported here correspond to the ones that a COF can present after the filtration and purification of the pristine powder, whether from the direct reaction of building blocks or further cascade reactions in one pot methods. Linkages obtained after post-synthetic transformations of previously obtained COFs, while important to the scientific community, might not be fully considered here.

2.4.1 Boron-containing bonds

Reversible boroxine rings and boronate esters were used for the earliest reports on COFs (Scheme 3),[21] thus solving the crystallization problem encountered in the synthesis of large extended 2D organic polymers. During the self-condensation of a boronic acid, the hydroxyl group attacks the Lewis acidic boron of an adjacent molecule. The first B-O bond is formed after the following intramolecular proton transfer and release of one water molecule. A third boronic acid is incorporated after analogous steps, resulting in a six membered cycle known as boroxine. Formation of boronate esters is achieved in a similar condensation reaction after the attack of the hydroxyl groups of a catechol to the boron atom of the boronic acid. Anionic spiroborates can be obtained by the condensation of alcohols with trimethyl borate in the presence of a weak base as catalyst.[53] Besides, hydroxyl groups of silanols can also attack boron centers, and such reactions are not limited to alcohols but also allow the formation of borosilicates.[54] Furthermore, the self-condensation of arylamine-boranes via thermal decomposition led to a six membered borazine ring with the release of hydrogen as by-product and the requirement of milder conditions than other B-N bond containing molecules.[55]

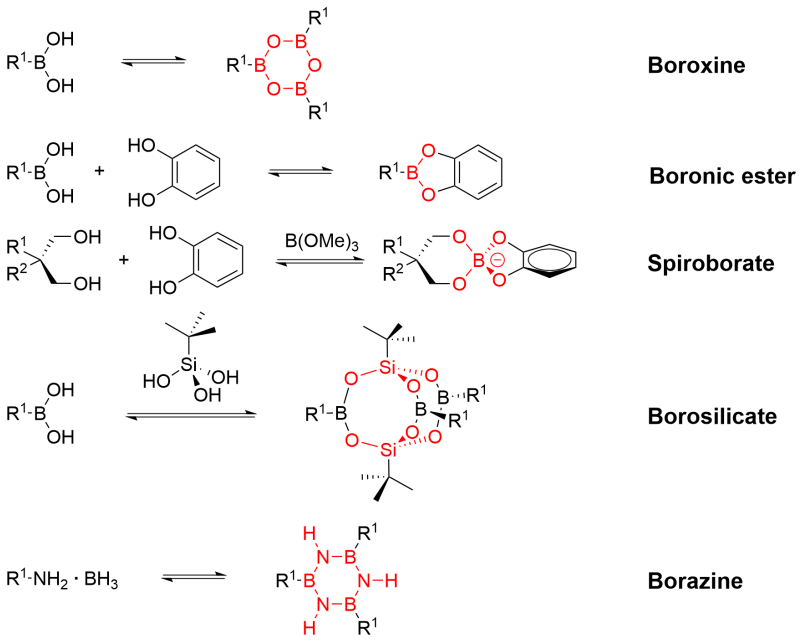

Scheme 3. Boron-containing linkages employed in COF synthesis.

Besides the formation of highly crystalline polymers with high specific surface areas, the implementation of this kind of dynamic covalent bonds enabled the efficient π–π stacking between extended aromatic building blocks in periodic columnar arrangements. This feature promotes one-dimensional conductivity. The main disadvantage of these frameworks is the extreme susceptibility to nucleophilic attack due to the presence of the strong electron-deficient boron atoms. Therefore, COFs with boron-containing linkages tend to decompose in water or in humid environments and their chemical stability is generally compromised.[56]

2.4.2 Nitrogen-containing bonds

The vast majority of nitrogen-containing bonds found among the reported COF structures are based on Schiff-Base reactions (Scheme 5).[57] To achieve reversibility, this reaction usually requires the presence of an acid as a catalyst. A typical Schiff-Base reaction involves the co-condensation of a primary amine moiety with a complementary carbonyl group to form an imine bond and water as represented in Scheme 4:

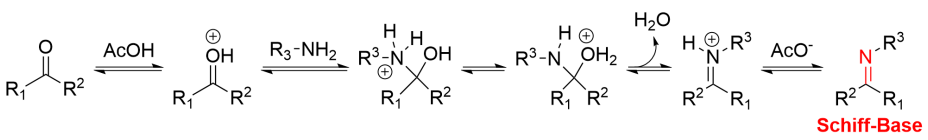

Scheme 4. Mechanism of Schiff-Base formation.

In contrast to boron-containing bonds, imines exhibit enhanced stability towards water, changes in pH and most organic solvents. Therefore, the C=N linkage allows for further post-synthetic reactions such as nucleophilic attacks or coordination of the electron lone pair from the N atom to metal ions.[58] Furthermore, transformations into other interesting linkages via sulfidation,

aza-Diels-Alder, reductions and oxidations, Strecker synthesis or hydrophosphonylation have been reported.[59] As shown in Scheme 5, while the carbonyl-containing groups are limited to aldehydes and ketones, the utilization of amine moieties with different substituents yield a wide scope of imine-based linkages. The first implementation of Schiff-base chemistry in a COF was reported in 2009 by Yaghi and co-workers with the synthesis of **COF-300**, obtained via co-condensation between the tetrahedral tetra-(4-anilyl)-methane and linear terephthaldehyde building blocks. This structure was not only the first imine-linked COF but also the first 3D COF ever, which presented a structure composed of five-fold interpenetrated diamond nets (*dia-c5* topology).[39] One remarkable feature of imine-linked COFs is the highly extended electronic conjugation within these ordered structures due to the combination of aromatic organic building blocks through the imine double bond. Therefore, a variety of imine COFs have been incorporated as semiconducting frameworks into devices.[60, 61] Besides of imines, azine-linked COFs are obtained by using hydrazine instead of primary amines.[62] Another well-established reaction is the condensation of organic hydrazides with aldehydes to yield hydrazone linkages.[63] This linkage presents remarkably enhanced resistance towards hydrolysis compared to imine COFs,[64] thus enabling the utilization of hydrazone-linked COFs in water. For instance, the photocatalytic **TFPT-COF** developed by Lotsch and co-workers can be used for hydrogen generation.[65] The incorporation of a hydroxy group in *ortho* position to an aldehyde will lead to an irreversible keto-enol tautomerization of the initially formed imine into a *β*-ketoenamine. The formation of an intramolecular hydrogen bond furnishes this linkage with exceptional chemical stability. However, due to the irreversibility of the tautomerization step, the structures might not present the optimal crystallinity. Ketoenamine-linked COFs typically incorporate 1,3,5-triformyl phloroglucinol (TFP) and linear ditopic diamines, such as in the **TpPa** COF series reported by Banerjee and co-workers.[66] In these structures, the final irreversible step and the absence of more reactive imine bonds gives facile access to polymers with outstanding robustness, which showed resistance towards highly basic and acidic concentration, as well as boiling water. Squaric acid can also be employed as a linker to form squaraines after the corresponding condensation with amines.[67] The presence of a zwitterionic resonant structure in the squaraine moieties provides COFs with interesting spectroscopic and electronic properties such as enhanced light-harvesting capacities, lower bandgaps and enhanced ionic conductivity. Besides of the keto-enol tautomerization, a condensation reaction might be irreversible when aromaticity is gained in the last step. That is the case after the second consecutive condensation in the formation of phenazine linkages from vicinal diketones with 1,2-diamines. The subsequent formation of a highly stable and aromatic pyrazine moiety

endows COFs with striking stability and extended π-delocalization, both being useful features for optoelectronics.[68]

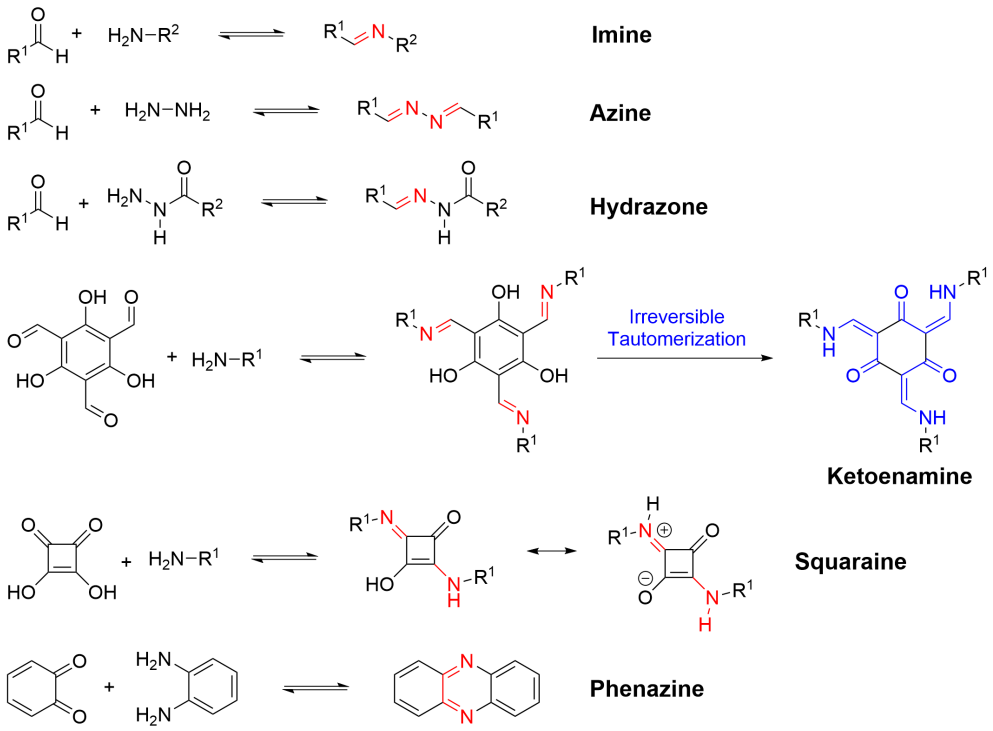

Scheme 5. Nitrogen-containing linkages obtained by Schiff-base reactions employed in COF synthesis. In red, the corresponding imine bond formed after the condensation.

On the other hand, nitrogen-containing linkages that are not obtained via a reversible Schiff-Base formation are also found among the literature (Scheme 6). Contrary to imines, some of these reactions would involve irreversible bond formation at some point, which negatively affects to crystallinity due to the lack of error-checking during COF formation. Among these linkages, imides and amides are well established in COF synthesis and both reactions share some similarities. Formation of these bonds involve reversible condensations of primary amines with carboxylic acid derivatives, such as phthalic anhydrides for imides and acyl halides for the amides. However, due to the poor reactivity of the cyclic imides or amides that are formed during the bonding process, the formation of these polymers is almost irreversible. This challenge was surpassed by the implementation of harsher conditions such as ionothermal synthesis in the case of the imide linkages[45] or the implementation of higher temperatures and pressures to enable reversibility in amide formation reactions that trigger the devitrification of amorphous amide networks into crystalline structures.[69] Besides the imine formation-tautomerization steps in the synthesis of **TpPa** COFs, robust ketoenamine linkages can also be obtained via a reversible Michael addition-elimination reaction of primary amines to *β*-ketoenols.[70] Linkages through carbon nitride aromatic systems can be obtained by forming triazines through the self-condensation of organic nitriles.[44] The high reversibility of the

dimerization of nitroso compounds yielded the synthesis of monocrystalline *trans*-azodioxy linked networks at room temperature.[71] Finally, *N'*-(2,4-dinitrophenyl)pyridine derivatives can be attacked by primary amines to yield viologen-based COFs that present a pyridinium ion bond formed via Zincke reaction.[72] Intriguingly, this cationic COF is an excellent adsorbent for the removal of toxic anions from water.

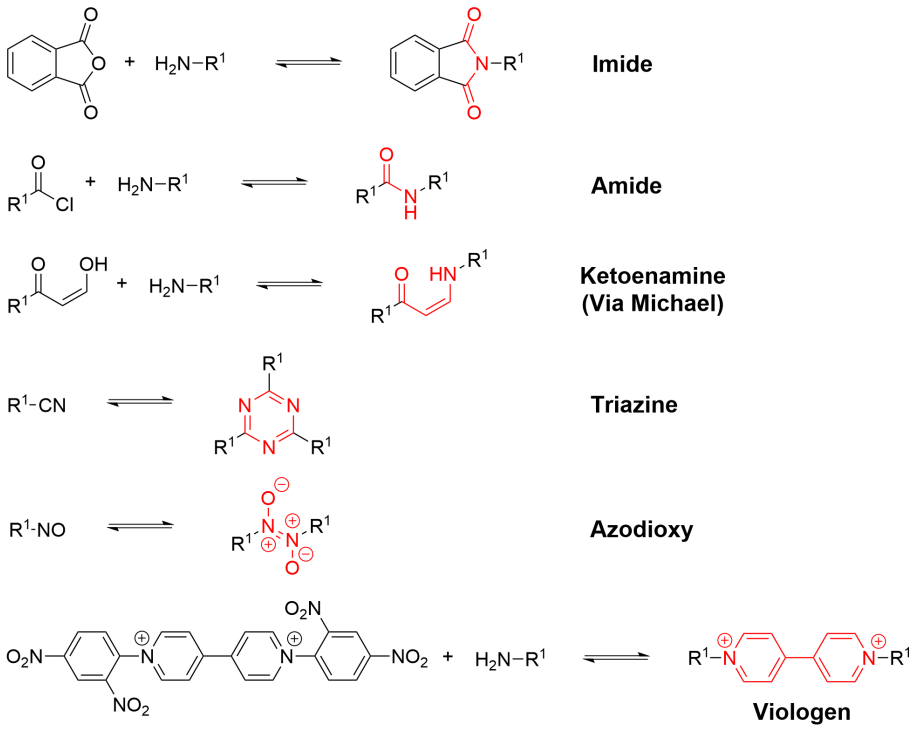

Scheme 6. Nitrogen-containing linkages not obtained with Schiff-base reactions employed in COF synthesis.

2.4.3 Olefinic Bonds

One huge step forward in COF synthesis in recent years was the connection of organic building blocks by strong C=C double bonds that allowed the growth of structures with full π-conjugation and remarkably enhanced chemical stability in comparison to imine COFs, as represented in Scheme 7.[73] Due to the inertness of the double bond, the formation of highly crystalline structures proved to be a major challenge. However, the nearby introduction of strong electron withdrawing groups increases the polarity of the C=C bond, hence enhancing the reversibility of this linkage. Following this strategy, acrylonitrile-bonded COFs were obtained via a reversible Knoevenagel reaction between aldehydes and benzylic nitriles.[74, 75] Unsubstituted vinylene bonds were incorporated by following the same strategy but using methyl substituted cyanopyridine derivatives such as 3,5-dycyano-2,4,6-trimethylpyridine.[76] An alternative reversible reaction for C sp^2 linked COFs synthesis is the aldol-like condensation reaction between aldehydes and 2,4,6-trimethyl-*s*-triazines. Interestingly, this reaction was simultaneously developed by the groups of Yaghi and Thomas, who demonstrated that these

reaction required acid- or base-catalysis depending on the molecular backbone.[77, 78] The most recent methodology developed for the synthesis of olefin-linked crystalline polymers was a Horner–Wadsworth–Emmons (HWE) reaction by employing phosphonates.[79]

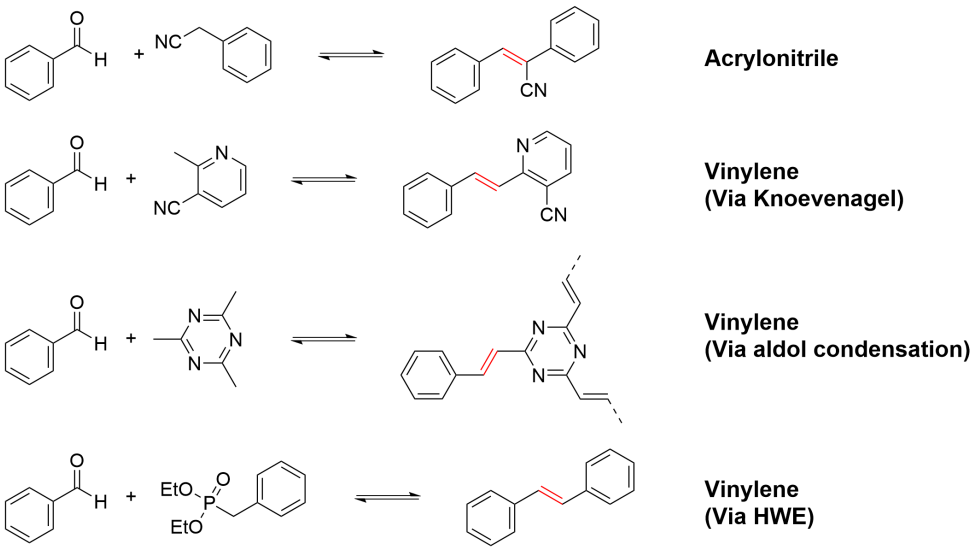

Scheme 7. C sp^2 linkages employed in COF synthesis.

2.4.4 Linkages through other heteroatoms bonds

COF linkages can also be composed of other heteroatoms, such as oxygen, sulphur, silicon or phosphorus (Scheme 8). While the ester linkage is typically not as reversible as other examples, highly crystalline ester-linked COFs were obtained after transesterification reactions.[80] Other types of oxygen- and sulfur-containing bonds were obtained after the formation of 1,4-dioxin[81] or 1,4-dithiin[82] moieties, respectively. In this case, a COF structure is synthesized after a reversible nucleophilic aromatic substitution reaction between the vicinal fluoro atoms of tetrafluorophthalonitrile or 2,3,5,6-tetrafluoro-4-pyridinecarbonitrile and catechol or dithiocatechol moieties. In an analogous manner to the formation of phenazine linkages, the formation of the cyclic heteroaromatic structure is irreversible, thus allowing the framework to withstand extremely harsh conditions. Reversible Si-O bonds allow the synthesis of silicate COFs by condensation of catechol moieties with hexacoordinate silicon species. In contrast to the viologen-based COFs, these polymers consist of a negatively charged backbone which is balanced with external metal cations.[83] Finally, the implementation of phosphazene linkages resulted in the first introduction of phosphorus into COFs.[84] Another phosphorous containing linkage was obtained after the self-condensation of linkers that contain both phosphonic and boronic acids. Multiple formation of B-O-P bonds resulted in cubane-type bonding clusters, thus allowing the formation of COF linkages with higher valences than the typical tris- or tetra-valent forms of organic carbons.[85]

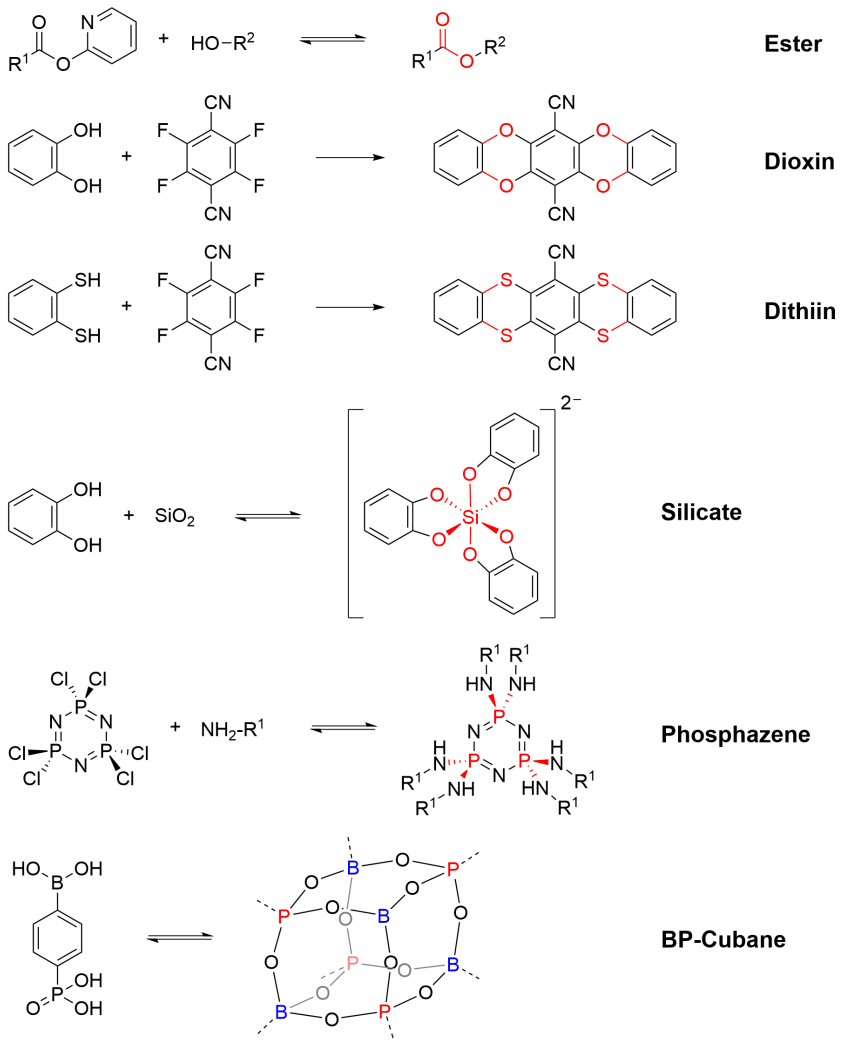

Scheme 8. COF linkages bonded through different heteroatoms.

2.4.5 Unconventional linkages

In some instances, specific molecules or moieties that are present in the reaction media are susceptible to attack the already formed dynamic bonds. These attacks can trigger further bond transformations to obtain more stable products after cascade reactions in one-pot (Scheme 9). Taking advantage of the formed imine bond, Lotsch and co-workers reported the formation of amine-linked COFs after adopting a reductive crystallization strategy by employing formic acid as a simultaneous catalyst and reducing agent.[86] Other example is the formation of aminals after the condensation of secondary amines with aldehydes. This reaction proceeds with good reversibility, as it can be considered as a subsequent attack of a second amine to the initially condensed imine moiety.[87] In a similar way, a variety of strong COF linkages can be obtained after almost, if not fully, irreversible cyclization processes, yielding the formation of oxazole,[88] imidazole[89] or benzofuran[90] moieties. The presence of specific reagents in the reaction media can also lead to further linkage transformations, e.g., the cycloaddition of imine bonds with alkenes to form tetrahydroquinolines.[91] Another interesting approach is the construction of

COFs via multicomponent reactions (MCR), as shown in the synthesis of imidazole-linked COFs from 1,2-diketones, aldehydes and ammonium acetate via a Debus-Radziszewski reaction.[92]

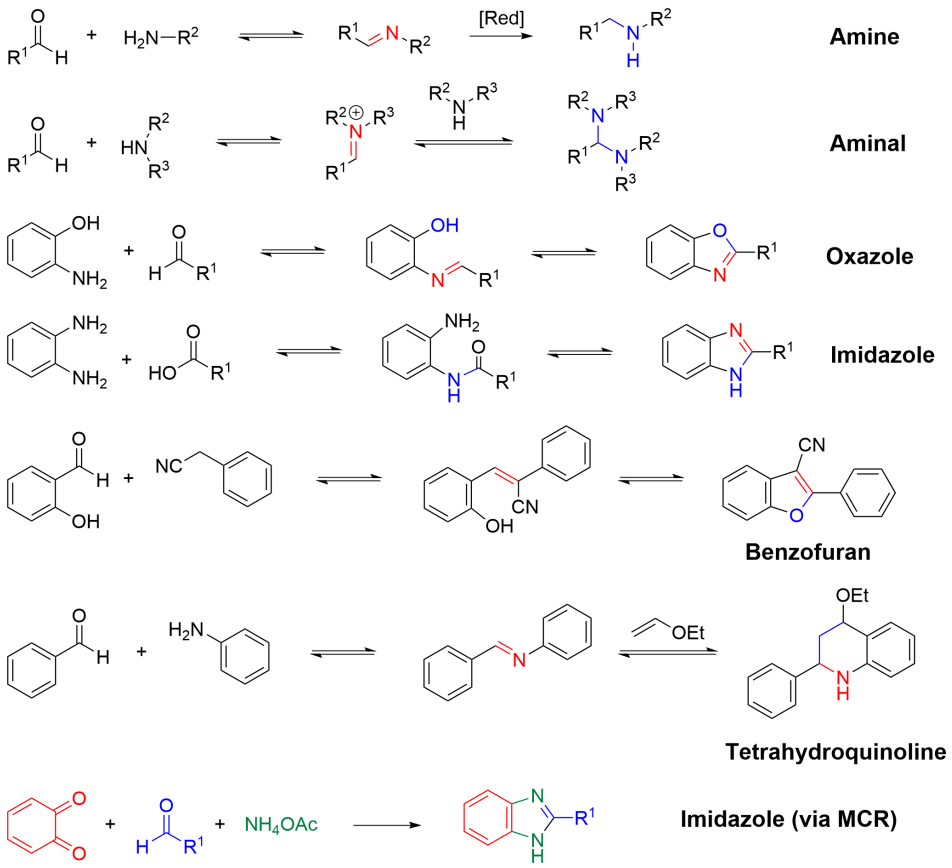

Scheme 9. Unconventional linkages in COFs obtained with further cascade reactions or multicomponent reactions.

2.5 Molecular Design and Topology

The adequate choice of the organic building blocks is a crucial aspect for the optimal construction of crystalline COFs. Every structural feature of the reticulating unit will directly impact in characteristics of the extended structure (Figure 9).

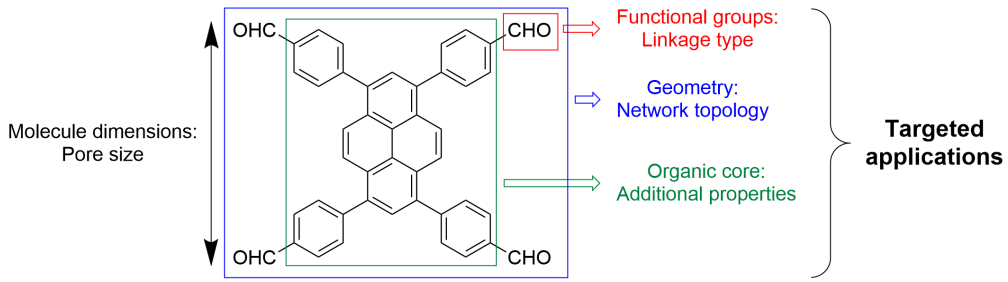

Figure 9. Building block features and their repercussion in the COF properties.

The ideal organic building blocks should possess a highly rigid structure with high symmetry and low degrees of freedom in order to minimize the number of incompatible conformers during the growth of the ordered framework (Figure 10).[37] These requisites will benefit the formation

of crystallites due to the construction of stiff frameworks with long-range order and favourable interactions among intermolecular layers or nets, mainly by π–π stacking due to the presence of aromatic building blocks. Hence, COFs based on linkers with no symmetry, bulky substituents, bent-, highly offset-shaped or flexible structures and/or linkages that possess many conformational isomers may face additional challenges while attempting crystalline solids.[37]

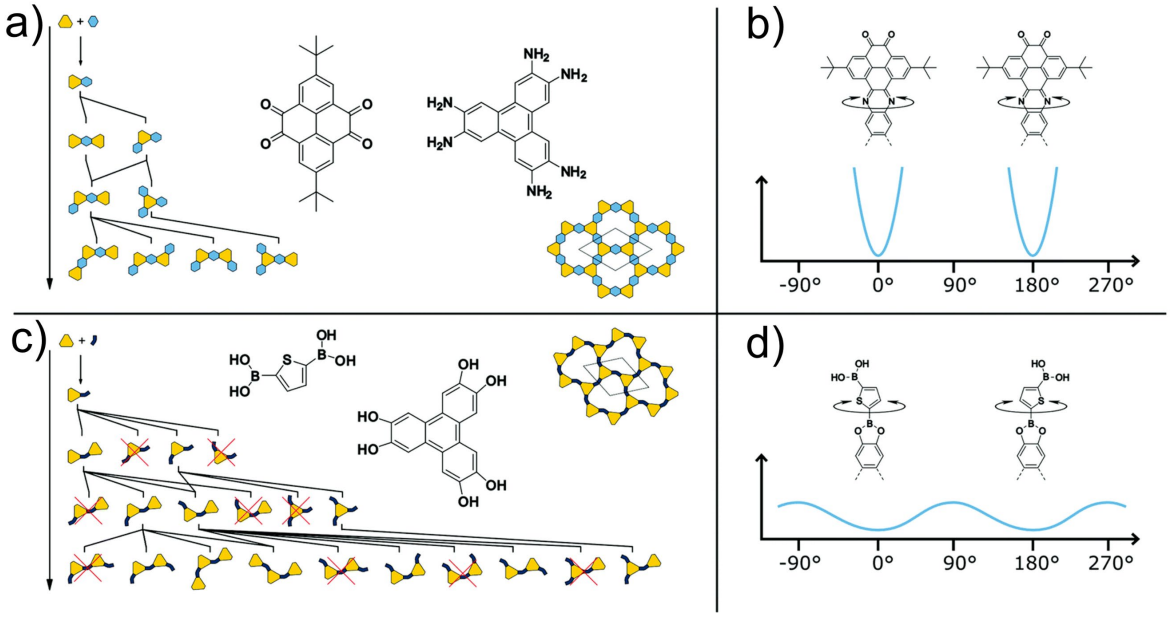

Figure 10. a), c) Impact of the increasing number of orientational conformers during the COF polymerization with the increasing degrees of freedom. b), d) Relative conformation energy with the rotation angle. Adapted with permission from Reference 37 (Open Access CC BY 3.0).

As it was mentioned in Chapter 1.4, the functional groups located at the extension points of the building blocks will guide to specific linkages that should be wisely chosen depending on the desired application. For instance, C sp^2 linkages will have a better impact for the synthesis of semiconducting polymers[75] while imine linkages could be used to chelate metals for sensing[93] or catalysis applications.[58] Variations in the dimensions of the molecules that compose the backbone will affect the pore size, as larger building blocks will result in wider pores.[94] This strategy can be applied for size-selective adsorption or separation applications. On the one hand, **TD-COF-3** with record pore apertures of 10 nm was used for the separation of pepsin (which is ~7 nm in size) from its crudes.[94] On the other hand, **TAPB-PDA-Et COF** as an isoreticular COF with reduced dimensions and a pore size of 3.2 nm was applied as a membrane to reject undesired small solute molecules from water.[95] The shape of the monomers that take part in the polymerization process has an impact on the topology of the resulting COF. A broad variety of 2D and 3D topologies can be designed with the knowledge about the precise geometries and number of extension points for the pre-selected building units.[25] Following a top-down strategy, the topology of target COF structures can be adjusted by choosing the right precursors (Figure 11).

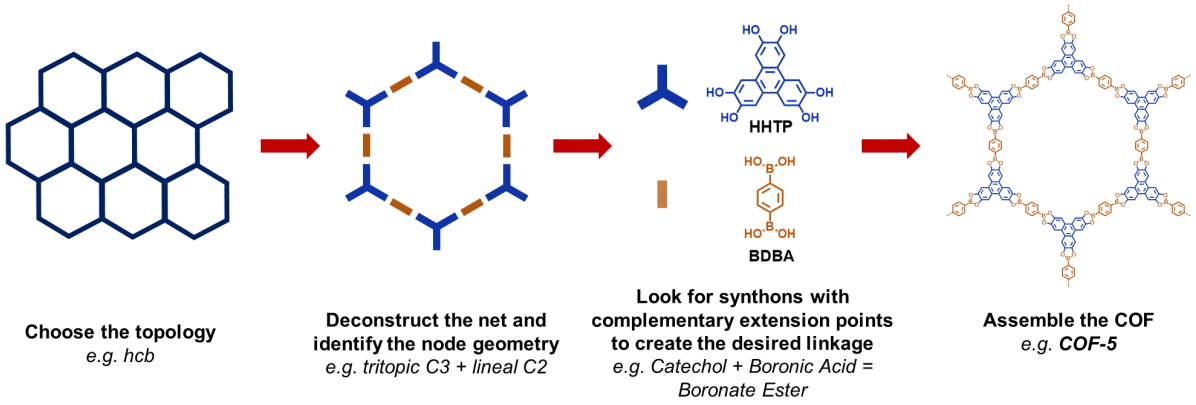

Figure 11. Topological design strategy employed in the synthesis of COFs.[25]

In order to synthesize any COF, the first step is to determine the intended topology. This selection may depend on several factors such as pore size or building block availability. For example, if larger pores were required, the *hcb* topology with hexagonal pores is a good choice. The next step would be to deconstruct the net into suitable components and to identify all possible nodes, edges and to determine the respective geometry of these molecular precursors. For the example shown in Figure 11, the formal disconnection of the polymeric structure in to nodes and edges indicates that this net is constructed by planar tritopic linkers with a C_3 rotation axis and linear edges. Having identified the required geometries, the next step is to determine the molecular synthons that match the geometry requirements to achieve the target topology. In the selected example, the triangular shape of the triphenylene unit is optimal for the incorporation of trigonal nodes, while benzene derivatives functionalized in 1,4-positions might be implemented as linear edges. While the selection of adequate geometries is one crucial factor, the incorporation of complementary functional groups is another key step and the decision may vary depending on target applications or properties. For example, boronate ester linkages may benefit the thermal robustness of COF for gas storage. Hence, the presence of molecules bearing catechol moieties such as HHTP and molecules bearing complementary boronic acids such as BDBA is required. After confirming that the molecular building blocks match in shape and functionality, the final step would be the assembly of the subunits by means of reticular chemistry, implementing the desired synthetic methodology.

Since the first reports on COFs, numerous topologies have been regularly presented in the literature. In order to construct the optimal COF skeleton from selected building blocks, it is beneficial to know the available topologies in advance. Hence, in the next sections a full classification for 2D COFs, and shortly for 3D COFs, will be outlined.

2.5.1 2D COFs

2D COFs mainly consist of polyaromatic organic molecules. The high planarity of the linkers generally triggers an extended interlayer π-stacking, which ultimately favours the precipitation of crystalline domains with eclipsed layers, the so called AA-stacking mode. However, enhanced repulsion between specific organic moieties can be used to pre-design the formation of staggered layer arrangements in which the vertices of the pores for one layer are placed on the pore openings of the adjacent layers.[96, 97] Consequentially, the formation of AB- or ABC-stacks is expected, depending on the number of layers involved in the stacking repetition motif (Figure 12). Zamora and co-workers synthesized **IMDEA-COF-1** in a staggered layer-fashion to minimize the aggregation-caused quenching of the pyrene building blocks and hence triggering emission in the solid state.[98] Very rarely, random stacking might also be observed.[99]

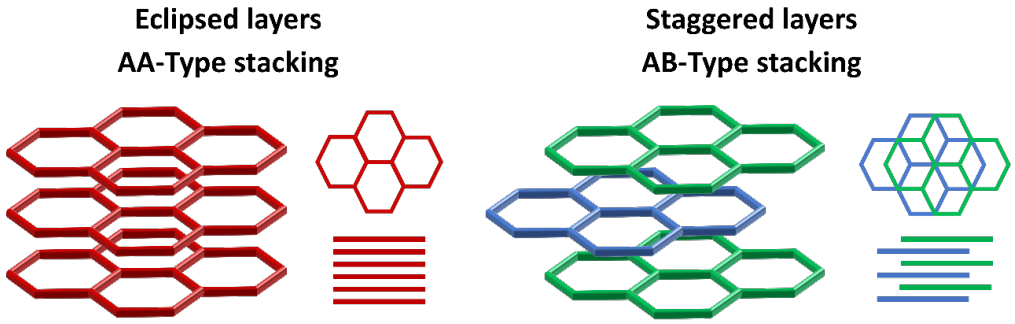

Figure 12. Layer stacking modes of COFs.

In almost all cases, the multitopic monomers possess a higher rotation axis that defines the topology of the network after its connection with another complementary linker. Considering only the spatial disposition of the extension points of the building blocks, ditopic organic molecules with a C_2 rotation axis will constitute a group of linear linkers. Such molecules typically constitute the polygon edges of the COF backbone. The vertex of the polygons is then formed by the complementary precursor with the higher symmetry (Figure 13).

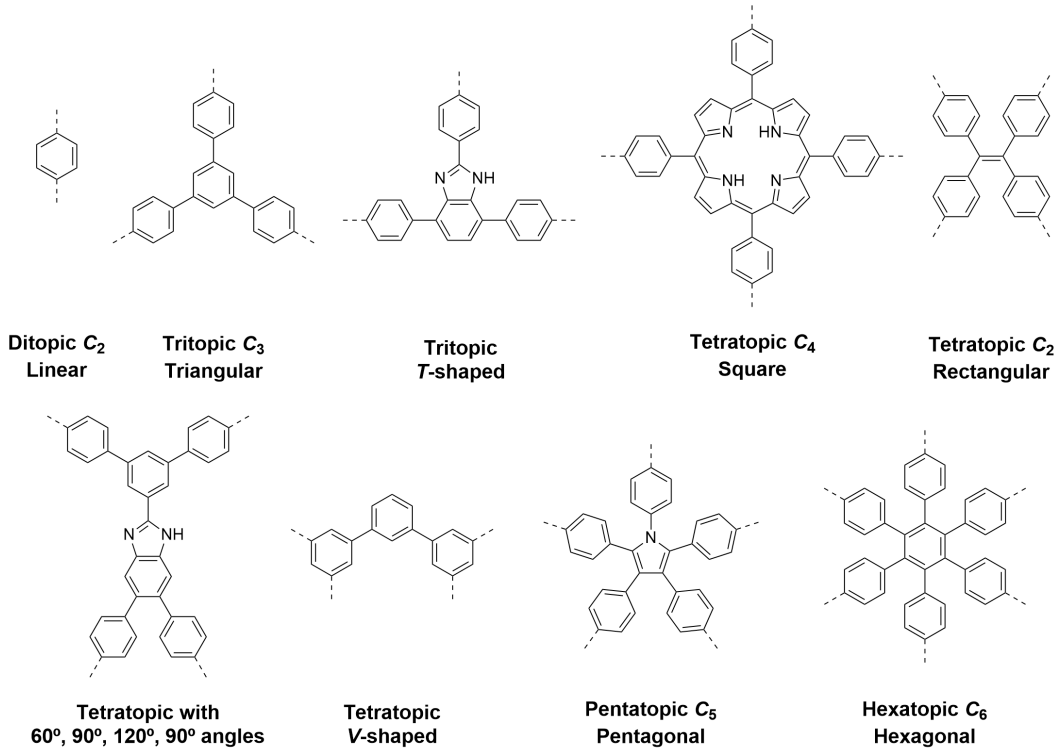

Figure 13. Examples of molecule derivatives with different geometries employed in 2D COFs synthesis. Note that C_n does not indicate the highest symmetry of the molecule but the possession of these symmetry operations.

As shown in Figure 14, the combination of linear edges and nodes with different symmetries leads to a wide variety of 2D topologies. The incorporation of tritopic molecules with a C_3 axis (e.g., 1,3,5-triphenyl benzene derivatives) will generate 120° angles between points of extension, directing the growth of the framework to a honeycomb-like structure that shows big hexagonal pore apertures, so called *hcb* topology.[21] Aside from triangular-shaped molecules, a *brick-wall* topology is constructed from tritopic linkers with T-shapes.[100] Symmetrical tetratopic linkers can be distinguished in two different groups: On the one hand, organic molecules with a C_4 rotation axis, such as porphyrin or phthalocyanine derivatives, represent perfect 90° angles between each extension point, thus generating frameworks with *sql* topology[101] and square-shaped pores, which are usually smaller in size than for the hexagonal *hcb* topology. On the other hand, tetratopic linkers with twofold symmetry such as tetraphenylethene possess an overall rectangular shape in which two different angles of 60° and 120° are present. The incorporation of this shape as knots in a COF backbone will form an arranged dual-pore *kgm* topology that combines triangular micropores and hexagonal mesopores,[102] resembling the six-pointed star-shaped Kagome crest. Remarkably, the formation of homoporous rombic structures can be achieved by introducing specific substituents in the building blocks with the same symmetry as for the previous example.[103] For another unconventional tetratopic molecule with reduced symmetry, specific angles of 60, 90, 120 and 90° between points of extension were obtained. The natural edge extension for such precursors

enabled the growth of more complex COFs with unprecedented *htb* topologies, which contains a triple pore backbone composed by a combination of hexagons, rectangles and triangles.[104] As complexity vary with changes in the molecular shape, other symmetries such as *V*-shaped tetratopic molecule will construct the *fxt* triple pore topology.[105] The only reported example for a COF constructed from building blocks that contain a C_5 axis incorporated a pseudo-fivefold symmetric 1,2,3,4,5-penta(4-formylphenyl)pyrrole to obtain the **PFPP-COF** series with an unprecedented *cem* topology comprised of a combination of rombic and trigonal pores.[106] Finally, the highest symmetry available for an organic vertex would be a C_6 rotation axis due to the maximum functionalization of a benzene system. Supermicroporosity and high π-column densities are the advantages of the *hxl* topology,[107] which allowd the formation of the smallest triangular micropores.

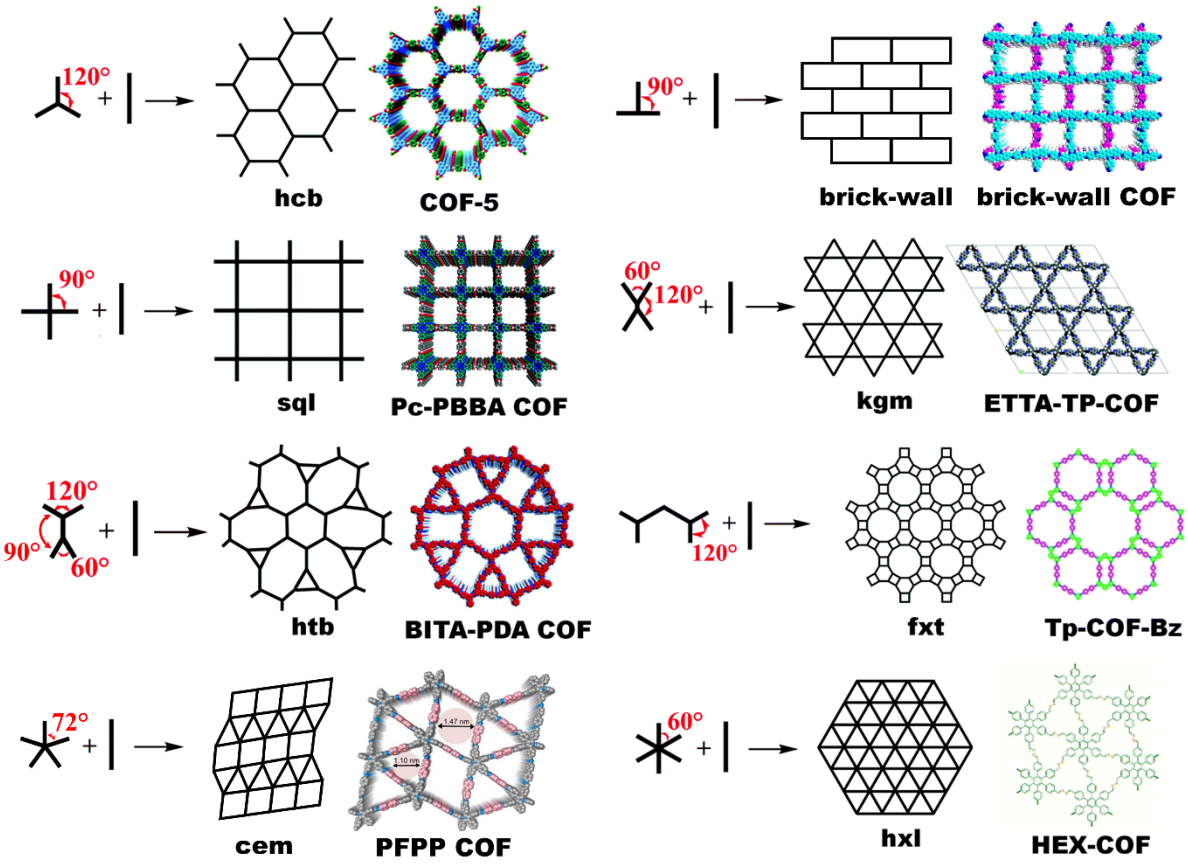

Figure 14. Uninodal 2D net topologies for COFs constructed by combination of linear linkers with higher symmetry linkers. Adapted with permission and updated from Reference 108 (Open Access CC BY 3.0).

The replacement of the C_2 edges with molecules of higher symmetry notoriously increases the structural complexity in COF due to the incorporation of more than one kind of polygon vertex within the backbone (Figure 15). For example, the rombic tessellation found in the homoporous *kgd* topology was constructed by combination of C_3 and C_6 molecules. As another variation, the *tth* topology[109] fuses three rombic pores into a hexagonal one due to the incorporation of an

extra C_2 tetratopic monomer. The combination of T-shaped linkers with C_2 tetratopic monomers will result in a *mtf* topology,[110] similar to a *sql* in which some pores are fused, hence presenting two different sizes of square pores. *bex* and *cpi* Topologies are also rarely observed in COF structures. The *bex* topology is based on a sub-stoichiometric design for a COF that combines C_3 and C_2 tetratopic monomers.[111] For the proper growth of this rare backbone, half of the extension points of the tetratopic linker remain unreacted, generating a crystalline structure with intrinsic structural defects. In addition, the unreacted sites can be beneficial for subsequent skeleton transformations. The *cpi* topology has been found in COFs structures formed by combination of C_2 tetratopic aldehydes and the C_2 piperazine, whose combination yield aminal linkages leading to the resulting topology instead of the expected *kgm* after a single imine formation.[87]

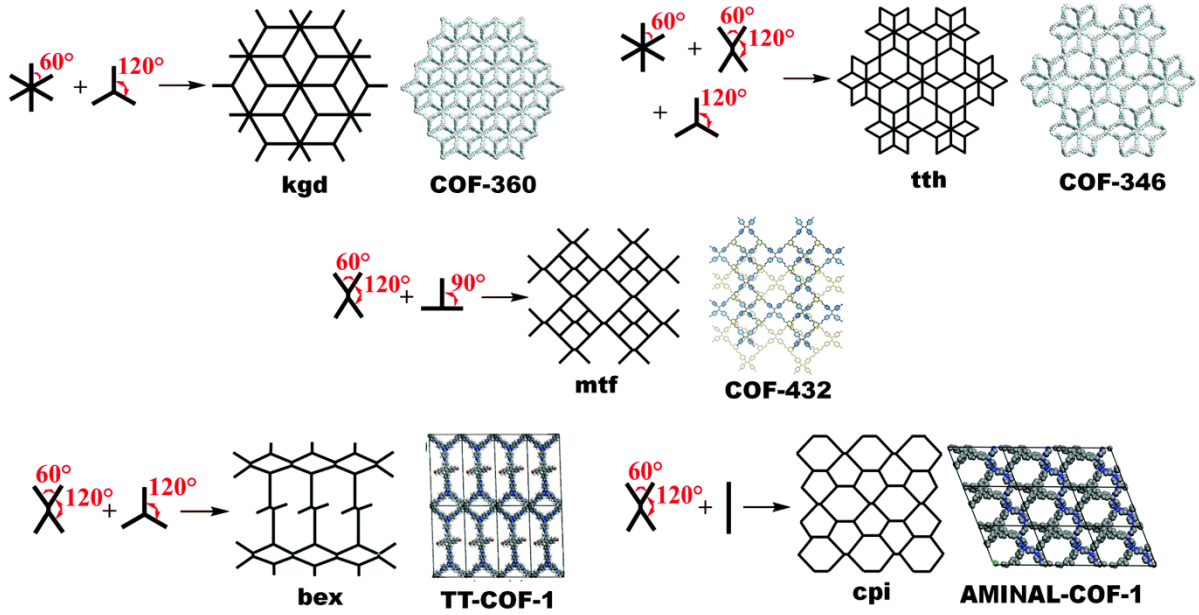

Figure 15. Multinodal 2D net topologies for COFs constructed by combination of higher symmetry linkers, with the exception of *cpi*. Adapted with permission from Reference 108 (Open Access CC BY 3.0).

2.5.2 3D COFs

The growth of non-planar COFs can be induced by including linkers with polyhedral shapes. The added complexity with the increasing dimensionality enabled the formation of a broad number of 3D topologies. Although, the number of available 3D COFs is still much lower than the number of 2D COFs. Since 3D COFs have been subject of recent reviews,[112] and the fact that the COFs synthesized in this Thesis only extends in 2D, a detailed discussion of 3D COFs would be beyond the scope of this Thesis. Therefore, the discussion in this section is limited to the most important *dia*, *bor*, *ctn* and *pts* topologies (Figure 16). All of these nets are based on tetrahedral building blocks, e.g., tetraphenylmethane derivatives. Instead of layer stacking,

interpenetration of individual nets is a common phenomenon frequently occuring in 3D COFs triggered by π–π stacking between components of adjacent nets.[113-115]

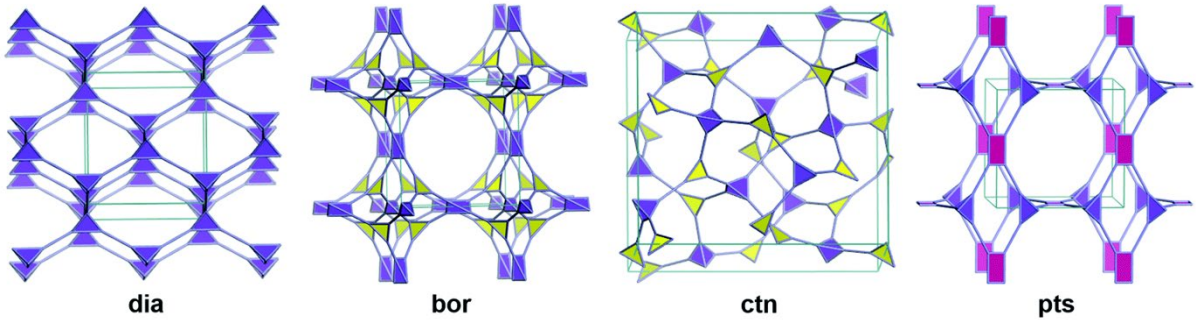

Figure 16. Most common topologies found in 3D COFs. Linker shapes: blue, tetrahedral; yellow, tritopic C_3 and purple, tetratopic (square C_4 or rectangular C_2). Adapted with permission from Reference 112. Copyright © 2020, Royal Society of Chemistry.

Dia nets are obtained by combination of linear C_2 molecules at the edges and tetrahedral molecules at the vertices. The term comes from the resemblance of this network to the diamond structure. **COF-300**, for example, was synthetized by co-condensation of tetra-(4-anilyl)-methane and linear terephthaldehyde and presents a *dia-c5* topology, which means that it is composed of five independent and entangled *dia* frameworks.[39] The degree of net interpenetration could be modified by varying the dimensions of the building blocks (Figure 17).

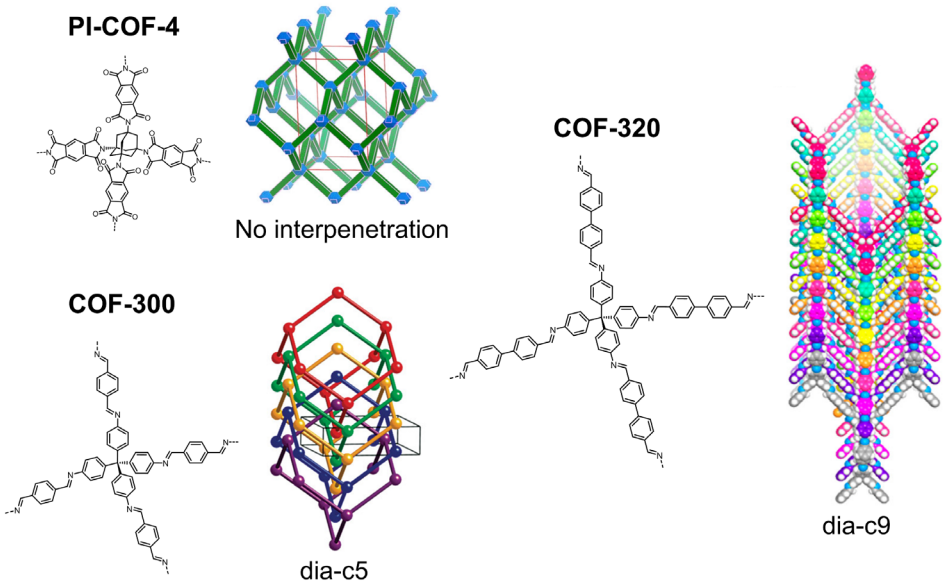

Figure 17. Degrees of interpenetration in *dia* topologies upon variation of building block sizes. Adapted with permission from Reference 117, Copyright © 2015, American Chemical Society; Reference 39, Copyright © 2009, American Chemical Society and Reference 116, Copyright © 2013, American Chemical Society.

While **COF-320** possesses a *dia-c9* topology due to the incorporation of a longer linear ditopic linker, 4,4′-biphenyldialdehyde,[116] the reaction between pyromellitic dianhydride as linear edge and 1,3,5,7-tetraaminoadamantane as tetrahedral node yielded **PI-COF-4** with a

non-interpenetrated single net of *dia* topology due to the reduced net dimensions.[117] The lack of interpenetration resulted in an open pore framework that favoured the entrapment of small drug molecules with high loading and good release profiles.

bor and *ctn* Topologies are obtained by combination of tetrahedral and tritopic C_3 linkers. Both structures have the same connectivity without interpenetration but notably differ in pore size and density, with the *bor* topology being about 15% less dense with larger pores.[33] The formation of these two topologies is equally favoured and any preference cannot be explained in terms of the linker geometries. The first report for these topologies was presented by Yaghi and co-workers, which rationally designed and predicted the three-dimensional disposition of the **COF-102**, **COF-103**, **COF-105** and **COF-108** 3D networks.[33] Among the four synthesized structures, a *ctn* topology was observed for all structures but **COF-108**, which crystallized in *bor* topology. The authors argued that *ctn* was the more stable topology due to the formation of a framework with higher topological density since denser structures are favoured in nature. However, **COF-108** appeared to be one exception that resulted in the crystalline material with the lowest density reported by that time.

Finally, *pts* topology is obtained after the condensation of tetrahedral nodes with square or rectangular tetratopic linkers. Interpenetration is typically observed for *pts* COFs, but to a lesser extent than for *dia* COFs. The first example for a COF with *pts* topology was **3D-Py-COF** reported by Wang and co-workers (Figure 18).[118] This structure consists of a two-fold interpenetrated *pts* net that consists of highly emissive 1,3,6,8-tetraphenylpyrene moieties. Due to the reduced π–π stacking between the aromatic cores, aggregation-caused quenching (ACQ) was avoided and this polymer represented the first fluorescent 3D COF. The unique combination of porosity and emission properties enabled the sensing of picric acid as a model compound for the detection of explosives.

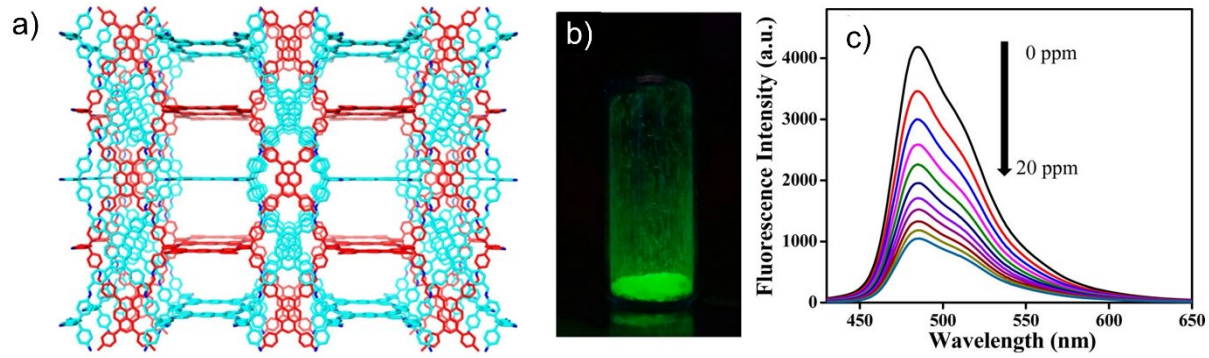

Figure 18. a) *pts* two-fold interpenetrated networks of **3D-Py-COF**. b) COF powders under UV light irradiation. c) Emission quenching upon addition of picric acid. Adapted with permission from Reference 118. Copyright © 2016, American Chemical Society.

2.6 Dye-Containing COFs and applications

As COFs offer a unique platform for the incorporation of organic molecules, the construction of crystalline polymers bearing building blocks with specific physicochemical properties opened the gates for a diverse variety of tailor-made materials with targeted applications.[119, 120] Moreover, the intrinsic COF features such as topology, linkage type or pore size are also a determinant factor. Organic dye molecules typically feature chromophores and auxochromes that trigger efficient visible light absorption with high extinction coefficients.[121] Among the numerous examples of reported dyes, a significant subset matches the requisites needed for efficient COF growth with long-range order, which include highly planar and extended aromatic structures with low degrees of conformational freedom, the presence of symmetry and the possibility of synthetic modification to incorporate the corresponding functional groups that will act as extension points.[37]

General features of dyes that have been incorporated into COFs include an enhanced charge transfer between units of adjacent layers that is favoured by the proper stacking among the planar building blocks.[122] Moreover, the extended conjugation of the aromatic cores typically decreases the HOMO-LUMO gap.[123] In addition, the connection of chromophores in D−A arranged columnar systems could enhance the absorption of low-energy photons.[124, 125] Because of these features, efficient light harvesting over a wide region of the visible and near infrared spectrum is commonly observed in dye-containing COFs with remarkable low bandgaps, thus suggesting the implementation of these highly conductive polymers as organic semiconductors[126] and in optoelectronic materials such as photovoltaic devices,[127] OFETs,[128] OLEDs[129, 130] or photodetectors.[60] Due to their light absorption in the visible range, numerous COF constructed from dyes have also been employed in visible light photocatalysis[131, 132] and ongoing efforts of numerous research groups are focused on implementing dye-COFs for cancer therapeutics.[133] In addition, organic dyes could be suitable emitters via fluorescence or phosphorescence.[134] In this context, any change in photoluminescent properties after guest encapsulation within the pores of dye-containing COF pores might be used for fluorescence sensing.[135, 136]

The sensing process can occur in two different manners. In most of the cases, a sensing effect is achieved via quenching of the intrinsic COF emission after the interaction of the organic backbone with guest molecules.[137, 138] For example, Xian and co-workers reported **PI-COF** as a fluorescent COF based on PBI and 5,10,15,20-tetrakis(4-amino-phenyl)porphyrin (TAPP) units. Upon ultrasound-assisted exfoliation of the bulk COF into covalent organic nanosheets

(CONs), the corresponding **PI-CONs** revealed an enhancement of the fluorescence (PI-COF: ϕ = 4% vs PI-CONs: ϕ = 8%) due to the reduced ACQ. Based on the luminescent properties of **PI-CONs**, the material was employed as a sensor for the nitroaromatic explosive compound 2,4,6-trinitrophenol (TNP). Sensing was achieved via fluorescence quenching of the CONs upon the introduction of increasing concentrations of TNP. This quenching phenomenon was attributed to a possible electron transfer after the formation of a PI-CONs-H^+−TNP^- complex. On the other hand, the fluorescence chemosensing was also achieved in some situations via turn-on emission of dye building blocks in D−A structured COFs by supressing the photoinduced electron transfer process (PET)[139] after a selective deprotonation in adequate linkages such as hydrazones[140] or ketoenamines.[141] In this regard, Jiang and co-workers reported **TFPPy-DETHz-COF** as an hydrazone-linked COF obtained by co-condensation of 1,3,6,8-tetrakis(4-formylphenyl)pyrene and 2,5-diethoxyterephthalo-hydrazide.[140] The dispersion of **TFPPy-DETHz-COF** in THF revealed a weak emission with an absolute quantum yield of 4.5%. Remarkably, a 3.8-fold enhancement in emission with an absolute quantum yield of 17% was observed upon the addition of tetrabutylammonium fluoride (TBAF). The COF showed selectivity towards F^- among other anions including Cl^-, Br^-, I^-, and NO_3^-. The authors stated that the fluorescence enhancement mechanism involved an acid-base reaction in which the N-H bond in the hydrazone moiety is deprotonated upon the incorporation of TBAF, hence provoking the formation of an anionic nitrogen species that impedes the intramolecular PET and improving the emission of the **TFPPy-DETHz-COF**. Based on these results, the authors developed a fluoride switch-on fluorescence sensor with a detection limit of 50.5 ppb.

As shown in Figure 19, a broad selection of tetratopic dye linkers have been used for the construction of COFs. For example, functionalized pyrene and porphyrin moieties as rigid molecules with an extended π-conjugated aromatic core, offer an excellent platform for the growth of COF layers, typically with *sql* topology due to their square shape.[62, 142] Because of these reasons, these molecules comprise two of the most employed dyes in COF chemistry. In addition, COFs constructed with functionalized metallophthalocyanines,[101] also comprise a big number of examples.

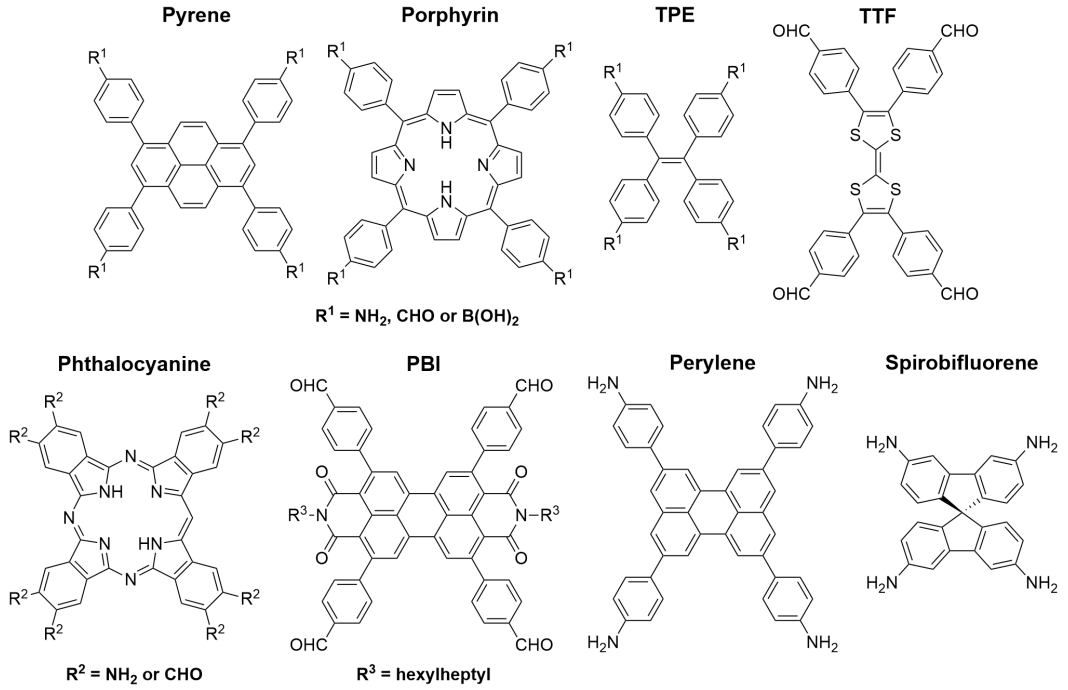

Figure 19. Examples of dye-based tetratopic linkers employed as COFs nodes.

Pyrene units can easily adopt an armchair conformation to facilitate interlayer stacking and, hence, chromophore arrangement and conductivity within the solid phase.[143] Due to the high intrinsic emission, pyrene containing-COFs have been widely exploited for a range of optoelectronic applications. For example, Auras and co-workers developed a humidity sensor with ultrafast response and reversibility based on pyrene-COF thin films.[144] **Py-TT COF** exhibits a red-shifted absorption upon the contact with polar solvents. The authors proved the lack of structural and chemical changes and stated that the solvatochromic behaviour of the material was purely based on electronic factors due to alterations in the electron density after the introduction of guest molecules. Jiang and co-workers reported the synthesis of a set of light-emitting pyrene-based **sp^{2}c-COFs**.[73] These olefin-linked and fully conjugated structures exhibited exceptional stabilities, even retaining the structure after exposure to air for one year, and remarkably high quantum yields up to 22% in dispersion, with the emission maxima wavelengths dependant of the twisting degree of the linkers. Obtaining robust emitting materials may lead the path for the design of novel photoactive semiconductors.

Porphyrin and phtalocyanine-based building blocks have the intriguing opportunity of modifying the π-electron density of the macrocyclic moieties and influence the optoelectronic properties of the COF upon coordination of different metals. In 2011, Jiang and co-workers demonstrated that the coordination of Ni within the phtalocyanine moieties of the panchromatic absorbing **NiPc COF** provoked a blue shift in the B band of the phthalocyanine units, indicating that COFs constituted of metaloporphyrins favoured the formation of H-aggregates that align

the chromophores into the optimal stacking.[101] Afterwards, the same group reported a different set of **MPc-COFs** metalated with Co, Cu or Zn and stated that the kind of metal introduced plays a key role in the optoelectronic properties of the solid due to changes in the charge transfer abilities through the columnar stack, resulting in near infrared (NIR) absorption and high electron conductivity.[145] In 2022, Lan and co-workers prepared a porphyrin-based **Co-TPCOF** via the successful metalation of the porphyrin moieties of **H_2-TCOF** with cobalt (II) acetate for the enhanced sensing of NO_2 by monitoring relative electric current changes.[146] Non-metalated porphyrins are also common among the literature, being especially reported as light harvesting COFs[147-149] and photocatalysts.[131, 150, 151]

Tetraphenylethylene-based (TPE) COFs have been reported as well, especially for enhanced solid-state fluorescence related applications. The interlayer aggregation phenomenon within the COF structure results in the rigidification of the molecular backbone of the TPE units, hence suppressing the nonradiative deactivation triggered by intramolecular motions.[152] This concept was first implemented in COF chemistry by Jiang and co-workers in 2016 via the solvothermal condensation of TPE-cored boronic acids with 1,2,4,5-tetrahydroxybenzene to yield the blue emissive **TPE-Ph COF**.[153] The presence of boronic ester moieties allowed the sensing of ammonia by photoluminescence quenching via Lewis acid-base interactions of the guest molecules with the boron atoms. Later, Wang and co-workers synthesized a seven-fold interpenetrated **3D-TPE-COF** that promoted the stacking among TPE moieties, resulting in a material with yellow solid-state fluorescence.[129] Subsequentially, by merely coating a commercial blue light-emitting diode (LED) with the highly emissive powder, the easy fabrication of a rare-earth free white LED was achieved (Figure 20).

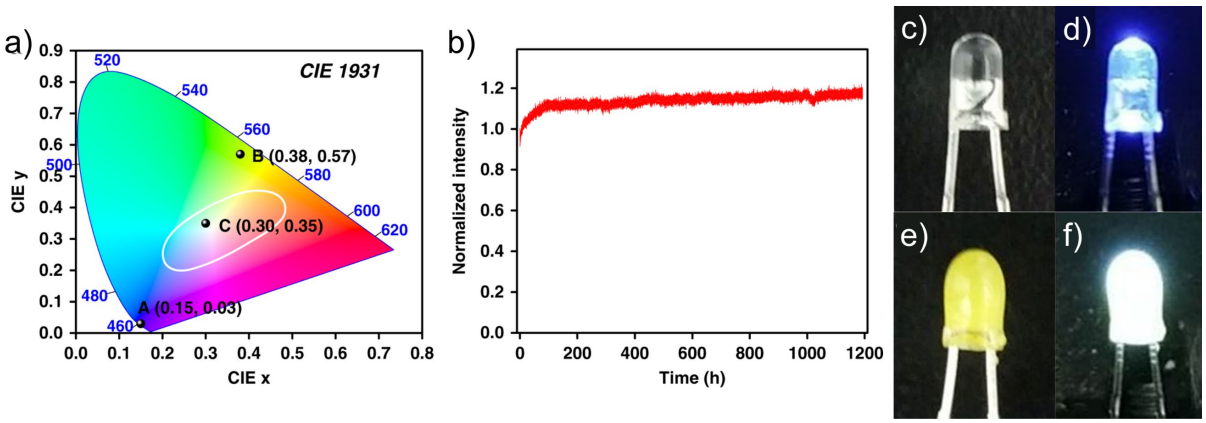

Figure 20. a) Chromaticity diagram indicating the CIE positions of A: Commercial blue LED, B: **3D-TPE-COF** emission and C: Constructed WLED. b) WLED luminiscence intensity vs time. Photographies of the reference commercial blue LED c) turned off and d) turned on. Photographies of the COF-coated WLED e) turned off and f) turned on. Adapted with permission from Reference 129 (Open Access CC BY 4.0).

To a lesser extent, the incorporation of electroactive dye moieties based on tetrathiafulvalene (TTF) has been used to develop COFs with highly tuneable electrical conductivity in two and three dimensions.[154, 155] Up to date, the examples constituted by tetratopic perylene or PBI-containing COFs are singular.[156, 157] Interestingly, the direct condensation of bulky 2,5,8,11-tetra(*p*-formylphenyl)perylene bisimide building blocks did not yield the intended PBI-based COF, as reported by Jiang and co-workers.[157] However, the authors smartly applied a low-temperature approach by trapping perylene molecules between the PBI subunits. Thereby, they obtained the perylene-intercalated PBI-containing COF with a supramolecular columnar assembly of alternating D−A stacks that showed enhanced crystallinity and interlayer charge transfer (Scheme 10).

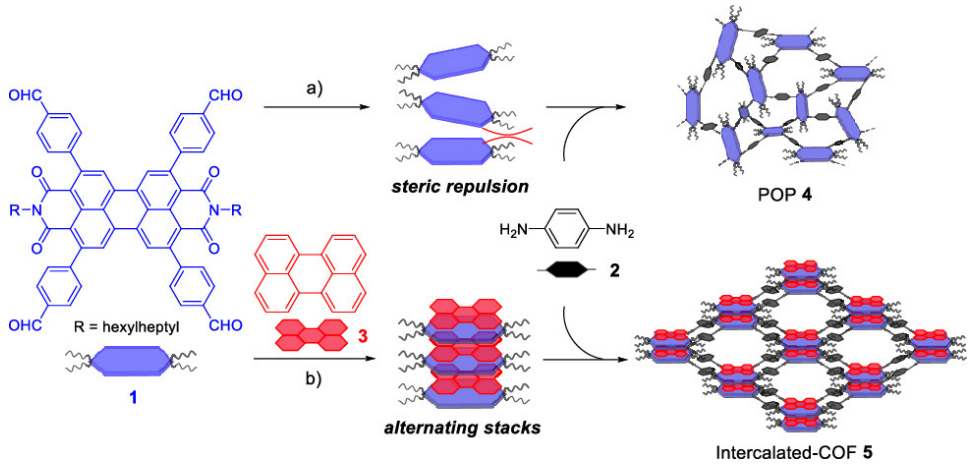

Scheme 10. Synthesic strategy for the bulky PBI-based COF via perylene intercalation. Reproduced with permission from Reference 157. Copyright © 2020, American Chemical Society.

3,3′,6,6′-tetraamine-9,9′-Spirobifluorene can also serve as a tetrahedral node for highly conjugated 3D COFs.[158] In the **SP-3D-COF** series, this building block was introduced as a bulk dopant to enhance the power conversion efficiency of perovskite solar cells by promoting the electron mobility due to the inherent D−A character. In addition, the incorporated COF domains served as seeds to facilitate crystallization of the perovskite films, thus resulting in a stronger light absorption in the range of 740−780 nm.

The functionalization of dye cores with lower symmetry also yielded suitable ditopic building blocks. In recent years, a large variety of dyes (Figure 21) such as DPPs,[147, 159] BODIPYs,[160] squaraines,[161] azobenzenes,[162] fluorenes[163] and derivatives of anthracene,[164, 165] acridine,[166] *iso*-indigo,[167] or flavin[168] have been incorporated within the organic skeleton of COFs. Moreover, square- or rectangular-shaped molecules such as the previously mentioned porphyrins,[169] pyrenes[170] and PBIs[171] can also selectively functionalized to give linear ditopic linkers that can be incorporated at the backbone edges instead of the vertices.

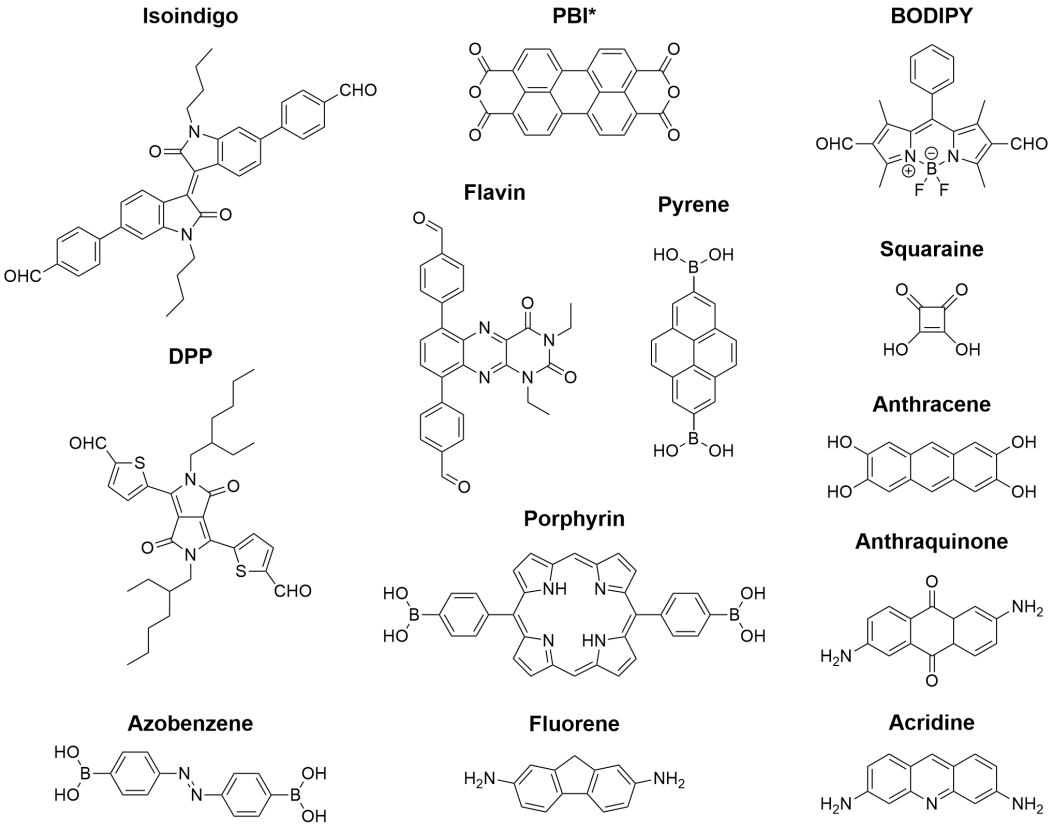

Figure 21. Some selected examples for dye-based ditopic linkers employed as edges in COFs. *Perylenetetracarboxylic dianhydride constitutes the building block for PBI-based COFs.

The combination of such dye-based linkers with the previously mentioned tetratopic chromophores resulted in the formation of panchromatic light absorbers.[67, 147, 167] In 2018, our group synthesized **DPP-TAPP-COF** by condensation of a formylated DPP derivative and TAPP.[147] Due to the extended π-conjugation, this crystalline polymer displayed an absorption maximum at 670 nm and pronounced light absorption over the whole visible spectrum, in contrast to the absorption of the individual monomers at 590 and 430 nm. By combining pyrene and intramolecular D−A-based *iso*-indigo or thieno-*iso*-indigo moieties with enhanced planarity, Bein and co-workers developed conjugated COF materials with light absorption strongly shifted into the NIR regime.[167] From these materials, vertically aligned thin films were grown on the surface of modified transparent ITO electrodes. Taking advantage of the porous surface, the infiltration of soluble fullerene derivatives within the open 1D channels was employed for the fabrication of a heterojunction layer in a COF-based spectrally switchable NIR photodetector.[167]

In some cases, suitable dyes have also been successfully implemented in photocatalytic COFs. For example, the flavin-based **FEAx-COF** reported by Lotsch and co-workers proved to be a sustainable catalyst for the photooxidation of alcohols to aldehydes under aqueous and aerobic conditions.[168] Upon photoexcitation of the COF material, the alcohol substrate is subsequently

oxidized by the heterogeneous photocatalyst. The acridine-containing COF **TPDA** was employed as a photosensitizer by Yan and co-workers in antibacterial photocatalytic therapy for the effective deactivation of *E. coli* and *S. aureus* in contaminated water after inducing the generation of reactive oxygen species upon visible light exposure.[166]

In addition to the direct incorporation of the dye as a building block via condensation reactions, post-functionalization strategies were adopted to link dye molecules with unreacted functional groups of the COF skeleton. For example, Bein and co-workers synthesized the fluorescent **T-COF-OFITC** upon reaction of the hydroxyl-bearing pore walls with fluorescein-*iso*-thiocyanate molecules.[172] Dong and co-workers adopted a different strategy via post-synthetic condensation of unreacted extension points of the COF with BODIPY molecules to yield a set of BODIPY-bearing COFs for photodynamic therapy via singlet oxygen generation.[173]

Chapter 3: Modulation of Crystallinity and Optical Properties in Composite Materials Combining Iron Oxide Nanoparticles and Dye-Containing Covalent Organic Frameworks

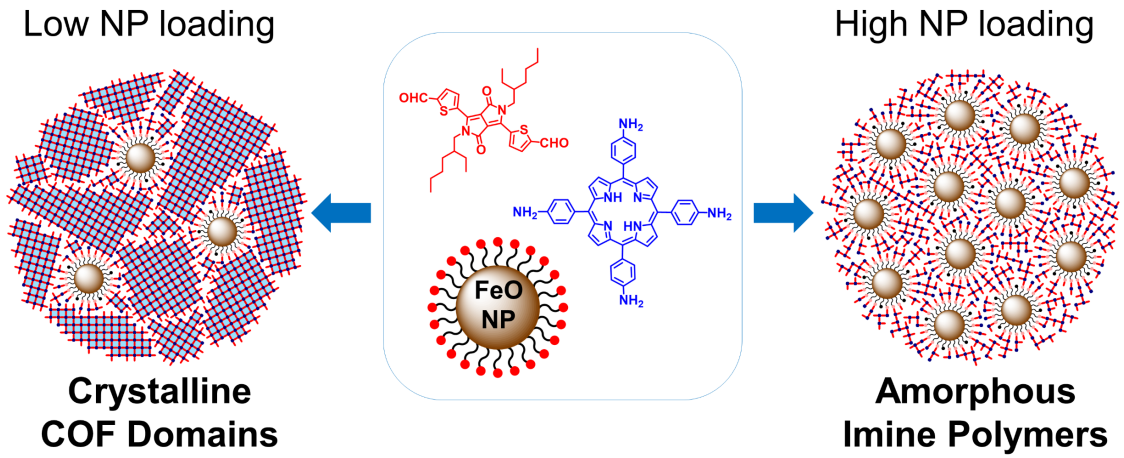

This chapter was published in: Sánchez-Naya, R.; Stepanenko, V.; Mandel, K.; Beuerle, F. *Org. Mater.* **2021**, *3*, 17, DOI: 10.1055/s-0040-1722655.

Abstract: Two series of organic-inorganic composite materials were synthesized through solvothermal imine condensation between DPP dialdehyde derivative **DPP-1** and **TAPP** in the presence of varying amounts of either amino- or carboxy-functionalized superparamagnetic iron oxides nanoparticles (**FeO**). Whereas high **FeO** loading induced cross-linking of the inorganic nanoparticles by amorphous imine polymers, lower **FeO** content resulted in the formation of crystalline COF domains. All hybrid materials were analyzed by magnetization measurements, powder X-ray diffraction, electron microscopy, IR and UV-Vis absorption spectroscopy. Crystallinity, chromophore stacking and visible absorption features are directly correlated to the mass fraction of the components, thus allowing for a fine-tuning of materials properties.

3.1 Introduction

Organic-inorganic hybrid materials[175, 176] can combine highly variable properties of diverse components into multifunctional composites. In nature, the complex hierarchical assembly of

brittle minerals and organic molecules results in biomaterials with exceptional fracture resistance,[177] which also inspired the design of biomimetic materials.[178] Intriguingly, orthogonal functions that are typically hard to achieve in single-phase materials, e.g. luminescence[179] and magnetism, can be successfully merged in artificial hybrid materials. In this regard, we recently succeeded in the combination of magnetic iron oxide nanoparticles and luminescent lanthanoid MOFs into nanocomposites for switching isotropic and anisotropic optical properties,[180] white magnetism,[181] shear stress detection[182] or ratiometric water sensing.[183, 184]

As another class of porous materials, COFs[185-187] have emerged as porous crystalline materials with potential applications in gas storage,[188] heterogeneous catalysis,[189-191] or organic electronics.[192] Aiming for dye-containing COFs,[193] we recently incorporated semiconducting DPP[194-197] moieties into imine-linked **DPP-TAPP-COF**[198] and boronate ester-linked **DPP2-HHTP-COF**[199] that show efficient light harvesting in the visible region[198] or electric conductivity in crystalline pellets.[199] COF-based composite materials have been developed for (photo)catalysis[200-202] and hydrogen evolution[203, 204] in water splitting. Up to date, only a few examples for the combination of COFs and magnetic particles are reported, which have been used as magnetically recoverable adsorbents[205-207] to remove toxins from biological samples,[208-211] for solid-phase extraction[212, 213] or the photothermal conversion of NIR absorption.[214] However, detailed structural investigations are still needed to get a better understanding of organic-inorganic interphases. In particular, systematic studies on the effect of nanoparticle concentration and surface functionalization on the crystallinity and nanoscale morphology of the organic COF domains will help to further optimize the functional properties of these hybrid systems.

3.2 Results and Discussion

Here we report on the synthesis and characterization of hybrid materials that combine superparamagnetic iron oxide nanoparticles and dye-containing COFs. Organic-inorganic composites were obtained by the direct growth of organic COF domains at the surface of amino- or carboxy-functionalized nanoparticles. Crystallinity, magnetic, optical and electronic properties for two series of composites with varying mass fractions between COF and nanoparticle domains were studied by powder X-ray diffraction (PXRD), diffuse reflectance spectroscopy and vibrating sample magnetometer (VSM) measurements. Here, we demonstrate that both crystallinity and absorption features of the COF domains could be controlled by adjusting the ratio between nanoparticle seeds and organic components.

Superparamagnetic nanoparticles were synthesized based on a reported procedure.[215] Surfactant-free particles were obtained by precipitation of a solution of $Fe(III)Cl_3$ and $Fe(II)Cl_2$ in water with aqueous ammonia solution. As shown in prior work, the nanoparticles obtained under these conditions cannot solely be assigned to be either pure magnetite (Fe_3O_4) or maghemite (γ-Fe_2O_3) but rather seem to be a complex mixture of both contributions and are therefore referred to as simply **FeO** in the following. Surface functionalization with either carboxylic acid (**COOH-FeO**) or amino groups (**NH_2-FeO**) was achieved by redispersion of unmodified particles in aqueous citric acid or covalent attachment of 3-aminopropyltriethoxysilane, respectively (see experimental section for further details). Functionalized **FeOs** were separated by collection with an external magnet and centrifugation. Redispersion in ^{t}BuOH yielded stable organic dispersions (4 wt%) for further functionalization. We recently reported the formation of dye-containing 2D **DPP-TAPP-COF** via solvothermal imine formation between **TAPP** and the DPP dialdehyde derivative **DPP-1** at 120 °C in ^{n}BuOH/mesitylene (3:1).[198] Assuming that both, **NH_2-FeO** and **COOH-FeO,** can initially bind aldehyde or amino precursors via imine or amide linkages, respectively, we investigated the growth of crystalline COF domains in the presence of **FeO** particles. COF synthesis was performed under optimized conditions[198] but with varying **FeO** loading to study the effect of seed/monomer ratio on materials properties (Scheme 11). Thereby, we obtained two series of organic-inorganic composites. **NH_2-FeO@DPP-TAPP-COF** and **COOH-FeO@DPP-TAPP-COF** by adding 0.7, 1.4, 6.8, 13, 27 and 42 wt% of **FeO** seeds in relation to a hypothetical quantitative formation of the COF.

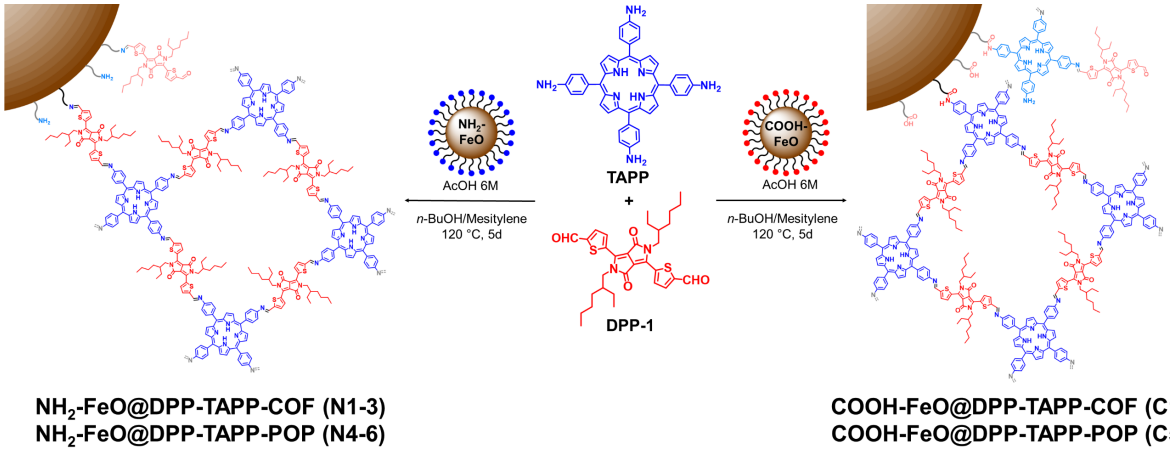

Scheme 11. Synthesis of organic-inorganic composites **FeO@DPP-TAPP-COF** via solvothermal COF synthesis in the presence of **FeO** seeds.

For better readability, we introduce the nomenclature **N*x*** and **C*x*** (*x*=1–6 with increasing nanoparticle content) for the **NH_2-FeO** or **COOH-FeO** based composites, respectively. Solvothermal reaction of **DPP-1**, **TAPP** and **NH_2-FeO** or **COOH-FeO** in ^{n}BuOH/mesitylene

(3:1) for five days resulted in precipitation of magnetizable composite materials (see Figure 22 for photographs of all composites under the effect of an external magnetic field). As expected however, magnetizability significantly decreased for composites **X1–2** with lowest **FeO** content. Notwithstanding, separation from non-magnetic sideproducts and remaining starting materials with a simple magnet made purification by repetitive washing with anhydrous THF much easier for all composites, thus showcasing the potential of magnetically manipulable COF materials.

All materials were characterized by energy-dispersive X-ray (EDX) spectroscopy, scanning electron microscopy (SEM), VSM measures, Fourier-transform infrared (FT-IR) spectroscopy, PXRD and diffuse reflectance spectroscopy to ultimately prove the formation of composites in all systems. In particular, we were interested in identifying and quantifying both inorganic and organic domains besides analysis of morphology, nanoscale structure and optical properties for the integrated chromophores. Presence of **DPP** and **TAPP** moieties in all samples was confirmed by signals for C, O, N, and S in EDX spectra (Figures S1–2). Whereas no Fe could be detected for scarcely loaded **N1** and **C1**, increasing signals at 0.55 (O), 0.7 (Fe) and 6.4 (Fe) KeV indicated the growing proportion of **FeO** in both series of composites **X2–6**.
SEM revealed a granular morphology for all composites (Figures S3–14). The use of an energy-selective backscattered electron (ESB) detector enhanced the chemical contrast and showed the homogeneous and increasingly dense distribution of **FeO** particles throughout the organic matrices for **X3–6** (Figures S15–16). For **X1–2**, no materials contrast was observed due to the very high dilution of the **FeO** nanoparticles in extended COF domains. However, the apparent magnetizability of these samples under the influence of an external magnetic field (see photographs in Figure 22) still indicates the incorporation of tiny amounts of nanoparticles. Magnetization for the composites was measured with a vibrating sample magnetometer (VSM). For pure **NH_2-FeO** and **COOH-FeO**, a saturation magnetization of 50 and 56 emu g^{-1}, respectively, was measured. Figure 22 shows the increment for the magnetization curves within the **X3–6** series of composites, with saturation values of 3.8, 9.1, 19.8, and 33.3 emu g^{-1} for **N3–6** and 5.6, 10.3, 18.1, and 29.4 emu g^{-1} for **C3-6**. For **X1–2**, the magnetic content in the composites was not sufficient for reliable VSM measurements. Based on previous investigations, we can state that the magnetic interaction of nanoparticles, when embedded together in a matrix, might changes significantly, depending on their distance and/or geometrical arrangement to each other. The saturation magnetization however, i.e., the absolute magnetization that can be achieved with the particles or assemblies thereof, is not changed but rather reduced in magnetization per mass by the mass fraction of any non-magnetic material

that is added to the system.[216-219] Under this assumption, we calculated a nanoparticle content of 8, 18, 40, and 67 wt% for **N3**–**6** and 10, 19, 33, and 53 wt% for **C3**–**6** from these values, which are in good agreement with the added amounts of **FeO** particles, thus confirming the quantitative immobilization of the particles in the organic matrix (See Table S3 for more detailed information).

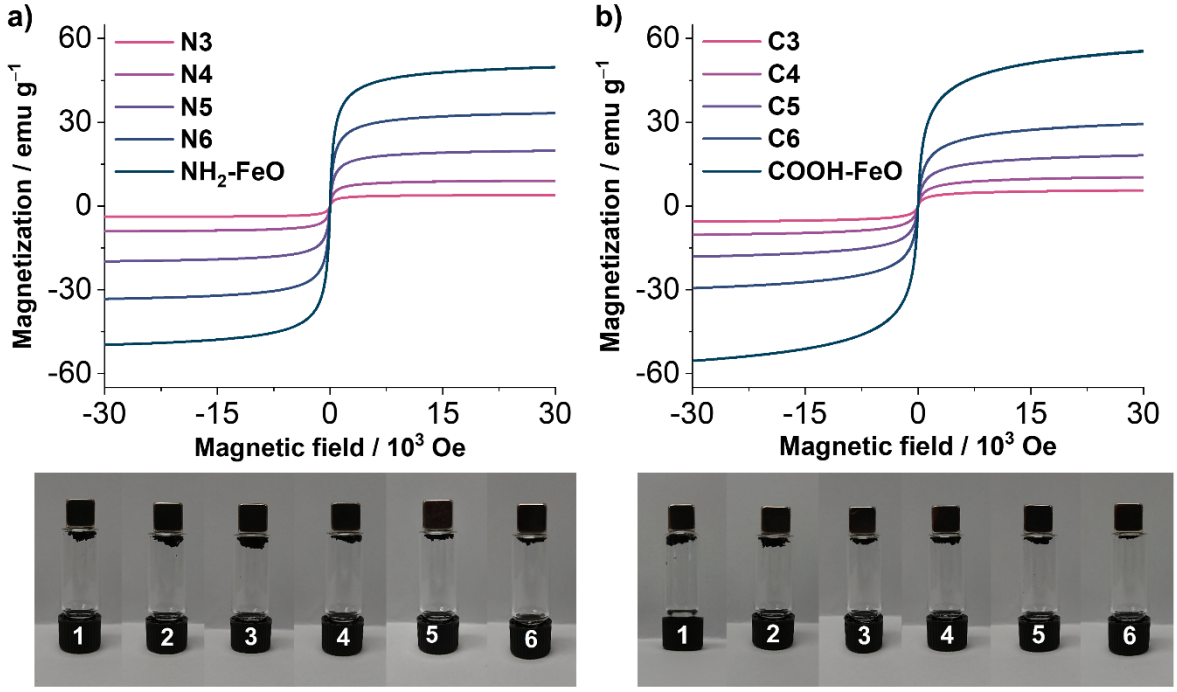

Figure 22. Saturation magnetization measurements for composites **X3–6** and the pure **FeO** particles as reference and photographs of bulk samples of both **N1–6** and **C1–6** under the effect of an external magnetic field.

The nature of the organic cross-links was investigated by FT-IR spectroscopy. In all materials, the characteristic signature for **DPP-TAPP-COF**[198] was observed (Figure S18). In particular, the absence of the aldehyde band for **DPP-1** and the occurrence of a C=N stretching mode at 1580 cm^{-1} confirmed the efficient formation of imine polymers in all composites. With increasing **FeO** content in both **X1–6** series, a rather broad band arises with two characteristic maxima at 580 and 630 cm^{-1} corresponding to the Fe-O stretching vibrations in the inorganic domains.

Whereas FT-IR confirmed the expected functional groups and linkages at the atomic scale, PXRD probes the crystallinity and nanoscale arrangement (Figure 23). For **N1–3** and **C1–4** (Figure 23 and Figures S19-20), PXRD data confirmed the formation of crystalline **DPP-TAPP-COF** domains with Bragg reflections centered at 2θ angles of 2.68°, 3.51, 4.26, 5.49, and 7.17° that correspond to 110, 020, 120, 220, and 040 planes, respectively, of the monoclinic *C2/m* space group of the COF.[198] With increasing **FeO** amount, the crystallinity of the COF domains decreased and only amorphous organic phases are observed for **N4–6** and

C5–6. In contrast, the corresponding reflexes for the inverse cubic spinel structure of Fe_3O_4 arose at 2θ values of 30.48, 35.85, 43.45, 53.89, 57.44, and 63.07° corresponding to the 220, 311, 400, 422, 511 and 440 planes, respectively.[220]

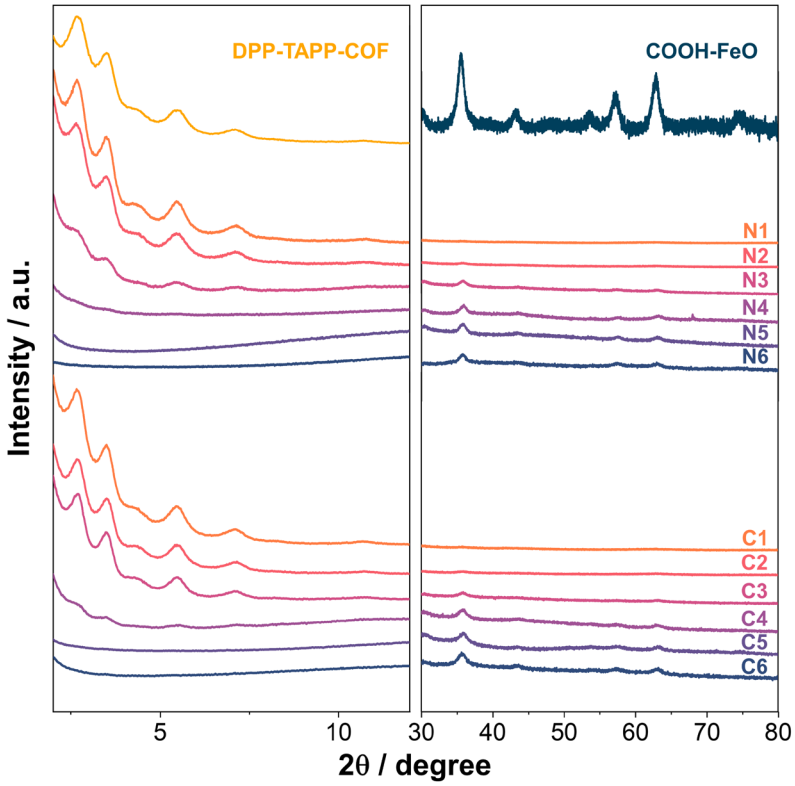

Figure 23. PXRD data for composites **N1–6** and **C1–6** and pure components **DPP-TAPP-COF** and **COOH-FeO** as reference.

Based on these combined analytical data, we propose the following mechanism for composite formation (Figure 24a). Initially, organic precursors or smaller imine oligomers are covalently attached to the functionalized **FeO** surface, either via imine formation between aldehydes of **DPP-1** and NH_2-groups of **NH_2-FeO** or amide formation between NH_2-groups of **TAPP** and COOH-groups of **COOH-FeO** for the **N*x*** and **C*x*** series, respectively. Due to structural constraints at the inorganic-organic interface, these seeds initiate rather amorphous imine polymerization in close proximity of the particle surface. In case of high **FeO** loading, these seeds are quickly cross-linked into composite materials without nanoscale ordering of the linking imine polymer network. With decreasing proportion of **FeO** however, there is enough time and organic feedstock to grow highly ordered COF domains in the periphery of the inorganic seeds, which are ultimately distributed within the crystalline matrix like ‘raisins in a cake’ (Figure 24b).

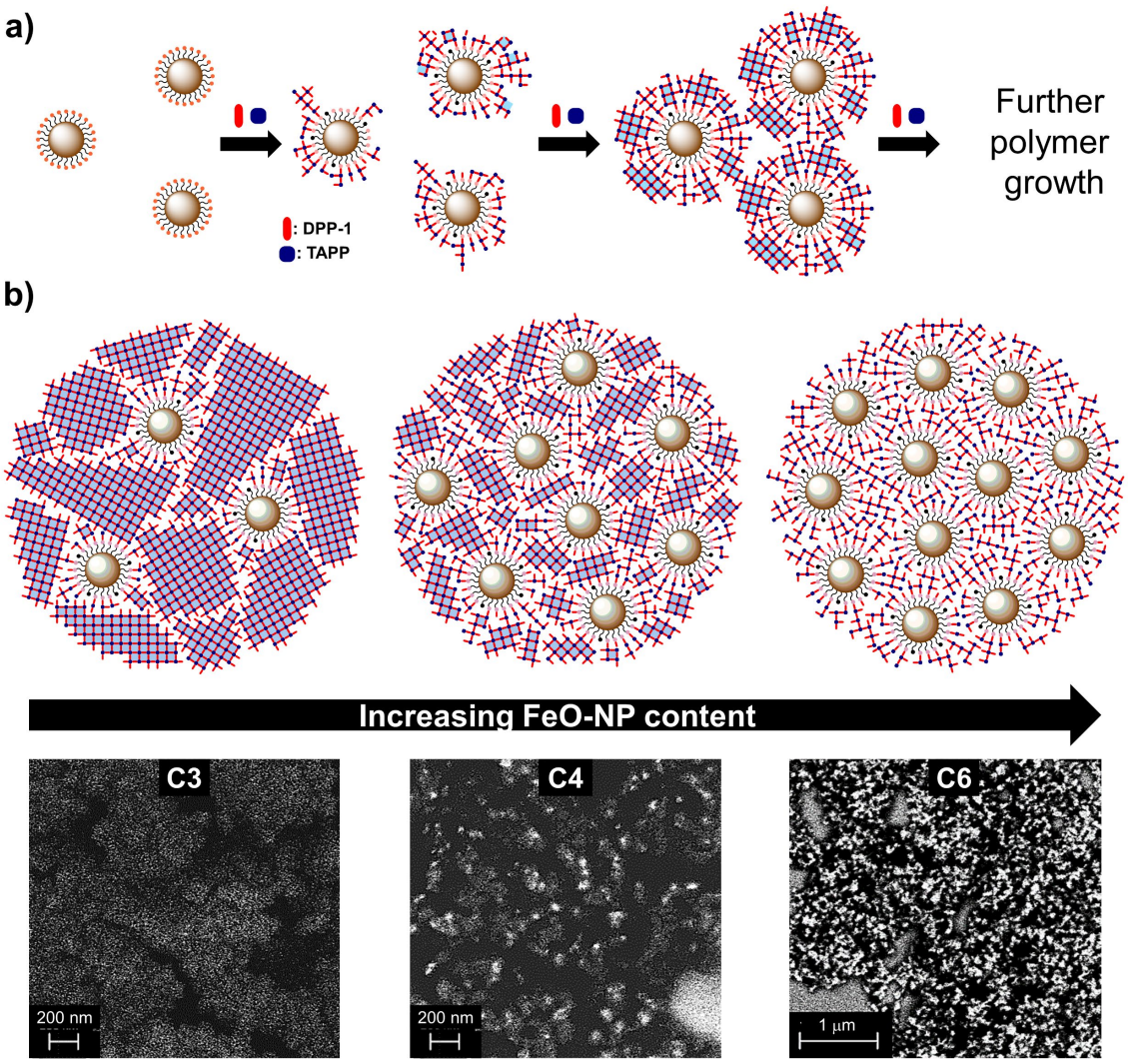

Figure 24. a) Proposed mechanism for composites formation and b) scanning electron microscopy images obtained with a back-scattered electron (BSE) detector indicating different degree of **FeO** loading for selected samples of the **C*x*** series.

Strikingly, the **C*x*** series exhibited a higher crystallinity than the **N*x*** series, as especially evidenced by PXRD for **C3** and **N3** with comparable **FeO** content but significantly different reflex intensities for the COF planes (Figure 23). This ordering effect is most probably explained by the subtle differences in nucleation events at the particle surface. For **NH_2-FeO**, the initial organic shell is most likely formed by linear **DPP** units, which are covalently attached via dynamic imine bonds. For **COOH-FeO** however, FT-IR spectra for the higher loaded composites **C4–6** showed an incremental increase in intensity for the two amide signals at 1673 and 1580 cm^{-1} (Figure S3), thus suggesting that **TAPP** precursors are irreversibly attached via amide bonds to the particle surface. Therefore, we postulate that the primary attachment of the tetragonal porphyrin units to **COOH- FeO** might facilitate the formation of crystalline domains due to pronounced π-stacking of the porphyrins and the immediate possibility to extend the frameworks into three rather than just one direction (See Scheme 11 for a model of the initial

organic shell). However, a catalytic effect of the acidic surface and the higher chemical stability of the amide linkages might also contribute to the higher crystallinity for the **C*x*** series. Under the assumption that the added **FeO** particles quantitatively remain in the composites, we also obtained a slightly higher average yield of 68 compared to 57% for **C*x*** and **N*x***, respectively (53% for pure **DPP-TAPP-COF**,[198] see SI for further details). From these yields, we calculated **FeO** contents of 1, 3, 12, 21, 42, and 56 wt% for **N1–6** and 1, 2, 9, 17, 33, and 59 wt% for **C1–6**, which are in good agreement with the values obtained from the VSM measurements. As demonstrated, the selection of composition can control the structure of the hybrid system and these structural properties ultimately do influence the optical properties of these hybrid materials.

As we have previously shown for the pure **DPP-TAPP-COF**,[198] implementation of both DPP and porphyrin chromophores into a conjugated 2D imine polymer results in a significant shift of the maximum absorption peak due to planarization and pronounced stacking within the crystalline framework. Figure 25a shows UV-Vis absorption spectra for solid samples of **DPP-1**, **TAPP** and **DPP-TAPP-COF** derived from diffuse reflectance measurements via the Kubelka-Munk function. For **TAPP**, the Soret band and three Q bands are observed at 430 and 525, 580, 675 nm, respectively.[221] For **DPP-1**, one broad band around 600 nm is attributed to the DPP charge transfer transition.[222] For a grinded 1:2 mixture of **TAPP** and **DPP-1**, which complies with the composition of the COF, no peak shifts but rather a change in the relative ratio between the Soret and Q-bands is observed, which is typically attributed to π−π-stacking of the porphyrin units in the solid state.[223, 224] For **DPP-TAPP-COF** however, the absorption maximum is shifted towards 693 nm and an almost complete attenuation of the porphyrin Soret band, which we previously attributed to both very good *intra*layer conjugation and *inter*layer aggregation within the 2D COF. The optical signature of DPP-TAPP copolymers should therefore serve as a sensitive probe for the nanoscale arrangement of the chromophores.

For the composite materials **N1–2** and **C1–3**, nearly identical absorption spectra compared to the pure COF were observed (Figure 25a,b and Figure S22). The formation of extended and undisturbed **DPP-TAPP-COF** domains in these materials is further corroborated by the presence of distinct COF reflexes in PXRD data for these materials (Figure 23 and Figures S19-20). Starting with **N3** and **C4**, any further increase in **FeO** content is accompanied with the rise of two bands at around 610 and 445 nm and a hypsochromic shift of the low-energy maximum (Figure 25a,b and Figure S23). Here, the optical features are in much better accordance with the non-reacted 2:1 **DPP-1**/**TAPP** mixture, thus indicating the amorphous

cross-linking of the particles as also seen in the PXRD data. Furthermore, the apparent trend in the relative intensity ratio between the Soret and Q bands illustrates the influence of varying **FeO** content on the π–π stacking and nanoscale arrangement of the **TAPP** moieties.

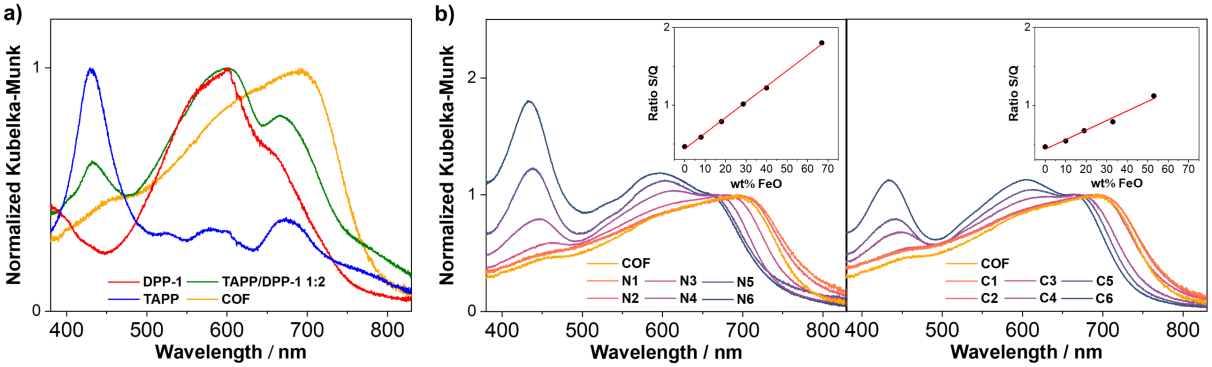

Figure 25. UV-Vis absorption spectra derived from diffuse reflectance measurements with the Kubelka-Munk function for a) solid samples of reference compounds **DPP-TAPP-COF**, **TAPP**, **DPP-1** and a grinded mixture of **TAPP**/**DPP-1** with 1:2 molar ratio (normalized to the global absorption maximum) and b) **N1–6** and **C1–6** composites series (normalized to the local absorption maximum with highest wave length, insets show the linear dependence of Soret/Q band intensity ratio and mass fraction of **FeO** particles).

To quantify this effect, we normalized all spectra to the Q band with highest wavelength and plotted the relative ratio of the Soret band against the wt% of the **FeO** particles. Intriguingly, we obtained a linear relationship for both **N2–6** and **C3–6**, thus indicating that the degree of π-stacking in the rather amorphous organic phases directly correlates to the nanoparticle content. Therefore, these linear regressions could be used to estimate the mass fraction and saturation magnetization of **FeO** domains directly from absorption data without the need for VSM measurements. Furthermore, the significantly flatter slope for **C*x*** in comparison to **N*x*** again demonstrates the superior nucleation capability of **COOH-FeO**, as more ordered COF domains are formed in higher yields for identical nanoparticle loading.

Using a Tauc plot, we also estimated the bandgaps for all composites from the absorption data for both series (Figures S25-26). For the crystalline materials **X1−3**, one transition with bandgaps between 1.6–1.7 eV was observed, which is in very good agreement with the value of 1.65 eV for the pure **DPP-TAPP-COF**. Interestingly, in the higher loaded composites **X4–6**, a second transition arises with higher bandgaps in the range of 2.3–2.5 eV, which further increases with higher **FeO** loading. We attribute this observation to the simultaneous occurrence of two different organic phases, namely highly crystalline COF domains and ill-defined agglomerates of the chromophores for the amorphous imine polymers. Due to both more pronounced intramolecular π–π stacking and better conjugation within the imine polymers, the crystalline COF phases possess a significantly lower bandgap in comparison to the amorphous domains, thus highlighting the beneficial effect of a highly ordered chromophore

arrangement in COF-based organic semiconductors. However, in both series, composites **X1–2** with the lowest nanoparticle loading have an even smaller bandgap as pure **DPP-TAPP-COF** (1.60 and 1.62 versus 1.64 eV). At this point, it is hard to tell if this effect is significant or just an artefact from the manual determination of the bandgaps from the Tauc plots. However, it could well be that doping of the COF matrices with superparamagnetic **FeO** nanoparticles has an intrinsic influence on the photophysical properties of the semiconducting organic domains. An in-depth analysis of these effects will be the subject of future studies.

3.3 Conclusions

In conclusion, two series of composite materials **NH_2-FeO@DPP-TAPP-COF/POP** and **COOH-FeO@DPP-TAPP-COF/POP** were synthesized in solvothermal COF reactions of DPP and porphyrin monomers at the functionalized interface of **FeO** nanoparticles. SEM images and magnetization measurements revealed that the varying amounts of inorganic nanoparticles are homogeneously distributed within the polymeric organic matrix. Even for very low **FeO** loading, magnetizable samples were obtained, which simplifies purification and facilitates further manipulation by external magnetic fields. PXRD and UV-Vis absorption measurements revealed a gradual transition from crystalline **DPP-TAPP-COF** domains towards amorphous imine polymers with increasing **FeO** content. Thereby, crystallinity, nanoscale stacking, optical features and bandgaps of the semiconducting organic domains was precisely controlled by adjusting the mass fraction of the two components. Based upon this proof-of-concept study, we are now aiming for functional composites with that combine magnetic and/or catalytically active inorganic nanoparticles with semiconducting organic polymers in a highly tunable manner.

Chapter 4: A BODIPY-Containing Covalent Organic Framework as a Highly Porous Photosensitizer for Environmental Remediation.

4.1 Introduction

BODIPYs are well-known dye molecules that have been extensively studied and implemented in light-absorbing systems.[225] The BODIPY core structure consists of a 4,4-difluoro-4-bora-3a,4a-diaza-*s*-indacene heteroaromatic scaffold (Scheme 12), but the parent BODIPY has not been reported in the literature so far due to synthetic limitations. However, alkyl-substituted derivatives typically possess narrow absorption and emission bands in the range of 500 to 550 nm, which are typically accompanied by high extinction coefficients and quantum yields up to 81%.[225] BODIPYs are robust enough to undergo a broad range of chemical transformations and core modifications allow the modulation of the photophysical properties in a precise manner. For instance, the absorption and emission maxima can be red-shifted to expand the optical features from the visible to the NIR region, the quantum yield can be increased or intersystem crossing can be enhanced to develop efficient triplet state photosensitizers.[225, 226] Applications of BODIPYs encompass numerous examples in various fields including bioimaging,[227-230] sensing and detection,[231-233] optoelectronics,[234-236] photocatalysis[237-240] and photodynamic therapy.[229, 230, 241]

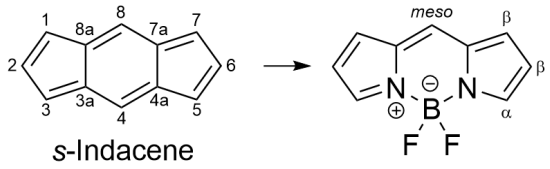

Scheme 12. Structure of the BODIPY core.

The robustness and synthetic versatility of these dyes, in combination with their unique photophysical properties, motivated the development of more complex BODIPY-containing structures. Among the reported architectures are a variety of macrocycles,[242] cages[243] and polymers, including linear polymers, porous branched polymers and MOFs.[237, 244, 245] On the other hand, BODIPY COFs have been realized only recently, with the first crystalline examples emerged during the realization of this work. In 2019, the Dong Group developed a BODIPY-decorated COF for potential applications in photodynamic therapy.[246] This crystalline polymer was obtained by post-synthetic modification via bonding defect functionalization

(Scheme 13). Other examples from the same group using a similar strategy were reported afterwards.[173, 247]

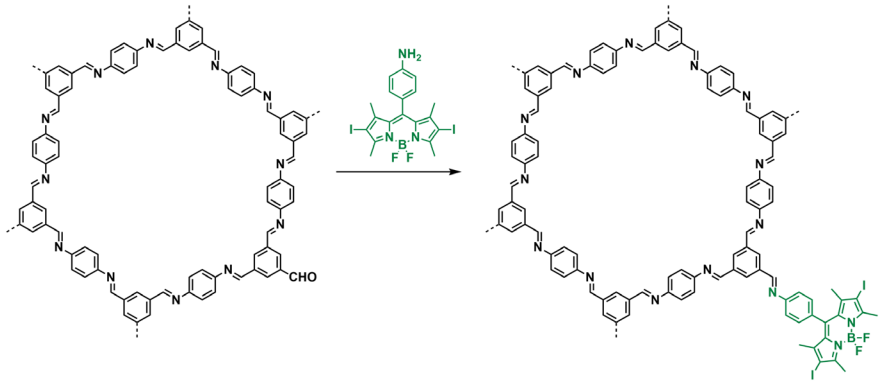

Scheme 13. Dong's approach for the synthesis of BODIPY-decorated COFs via bonding defect functionalization.

However, polymers with increased crystallinity and porosity might be better obtained by direct incorporation of the dye units without the need for post-synthetic modification. This should also lead to higher reproducibility and a more ordered arrangement of the building blocks. Only in 2021 and 2022, the first two examples were reported by Qiu and co-workers. [160, 248] These two D−A COFs were constructed from TAPP and meso-substituted BODIPY derivatives and were tested in the colorimetric detection of uranium or antibacterial applications (Scheme 14). However, the implementation of bulky *meso* substituents at the BODIPY units led to a staggered alignment of the COF sheets, which significantly reduced the porosity of the material.

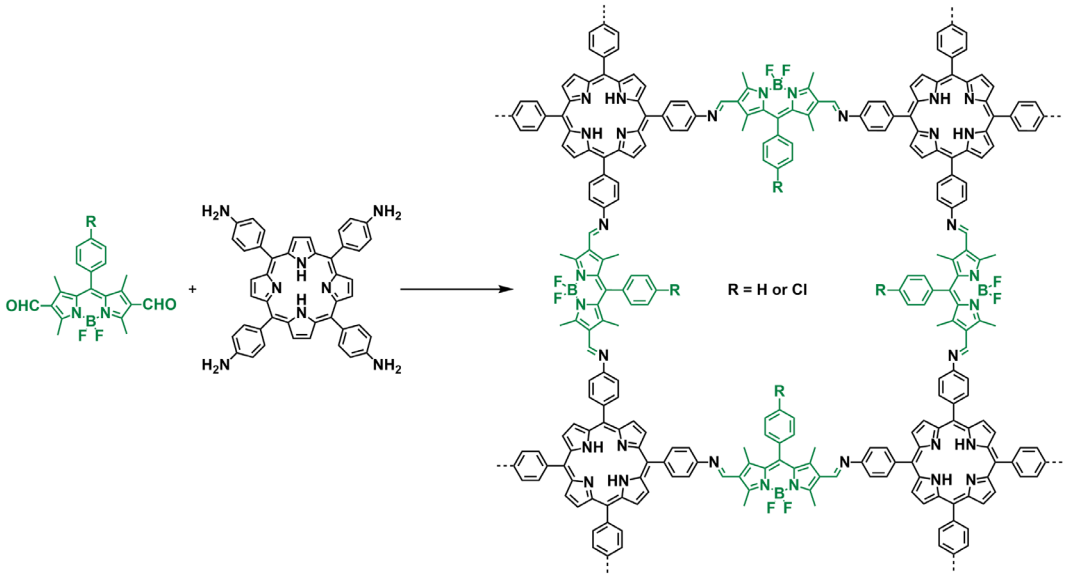

Scheme 14. Qiu's BODIPY-based COFs.

In order to enhance π-stacking and thus promoting an eclipsed layer arrangement, we designed a novel **BDP-TFP-COF** by incorporating small Me groups as *meso* substituents in a diamino BODIPY precursor (Scheme 15). Thereby, we aimed for high crystallinity and large pore channels, hence enabling a larger uptake of guest molecules within the pores for, e.g., enhanced

adsorption capacity or improved catalytic performance. In addition, the incorporation of TFP subunits increases the robustness of the covalent backbone due to the implementation of *β*-ketoenamine linkages. This enhancement of the stability may be beneficial for the use of the COF as a material without losing its structural integrity and properties over time.

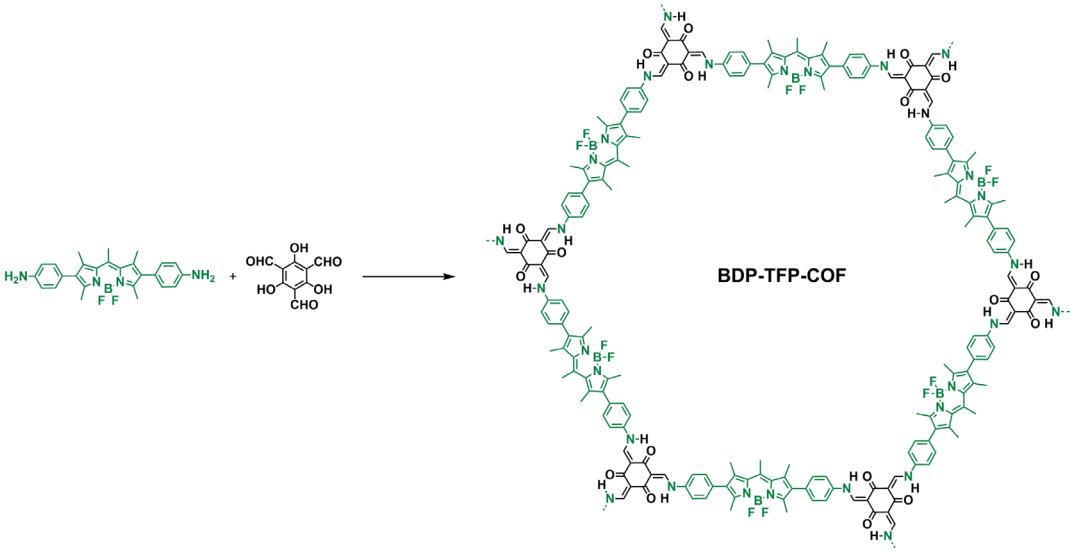

Scheme 15. Molecular design of the target BODIPY-containing **BDP-TFP-COF**.

4.2 Results and discussions

4.2.1 Synthesis and characterization of BDP-TFP-COF

As structure-defining building blocks, we chose the linear ditopic diamino-BODIPY derivative **BDP(NH₂)₂**[243] and the well-established tritopic COF node **TFP**.[249] **BDP(NH₂)₂** was synthesized via a Suzuki C-C cross-coupling reaction of the literature-known diiodo derivative **BDP(I)₂** with commercial 4-aminophenylboronic acid pinacol ester. **BDP(NH₂)₂** was obtained in higher yield and on larger scale than in the reported procedure (Scheme 16).[243] (See Chapter 8.2 for the complete synthetic route and more experimental details).

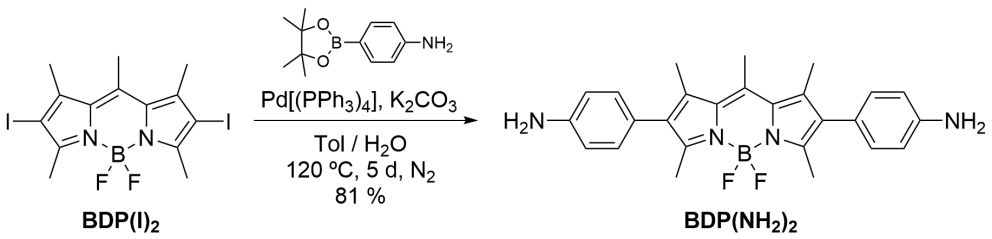

Scheme 16. Synthesis of **BDP(NH₂)₂**.

BDP-TFP-COF was synthesized by the acetic acid-catalysed co-condensation of the two precursors under solvothermal conditions. In a sealed pressure tube under argon atmosphere, both components were reacted in a 1/1 v:v mixture of *ortho*-dichlorobenzene and mesitylene at 120 °C for three days. The obtained precipitate was collected via filtration or centrifugation and

the remaining building blocks and small oligomers were washed out by Soxhlet extraction with anhydrous THF for 16 hours. The solid material was further purified by solvent exchange in acetone and pentane and dried under high vacuum for four hours to unclog the pores. Pure **BDP-TFP-COF** was obtained as a dark red powder in 86% yield.

The reversible condensation between the amino groups of **BDP(NH$_2$)$_2$** and the aldehyde groups of **TFP** yields the corresponding imine bonds by means of dynamic covalent chemistry,[36] which subsequently undergoes a fast and irreversible imino-enol-keto-enamine tautomerization to achieve the *β*-ketoenamine linked **BDP-TFP-COF** (Scheme 17).[66, 250-252] From a topological point of view, the combination of the linear linkers with complementary trigonal planar knots establishes a 2D COF with *hcb* topology and well-defined hexagonal pores.

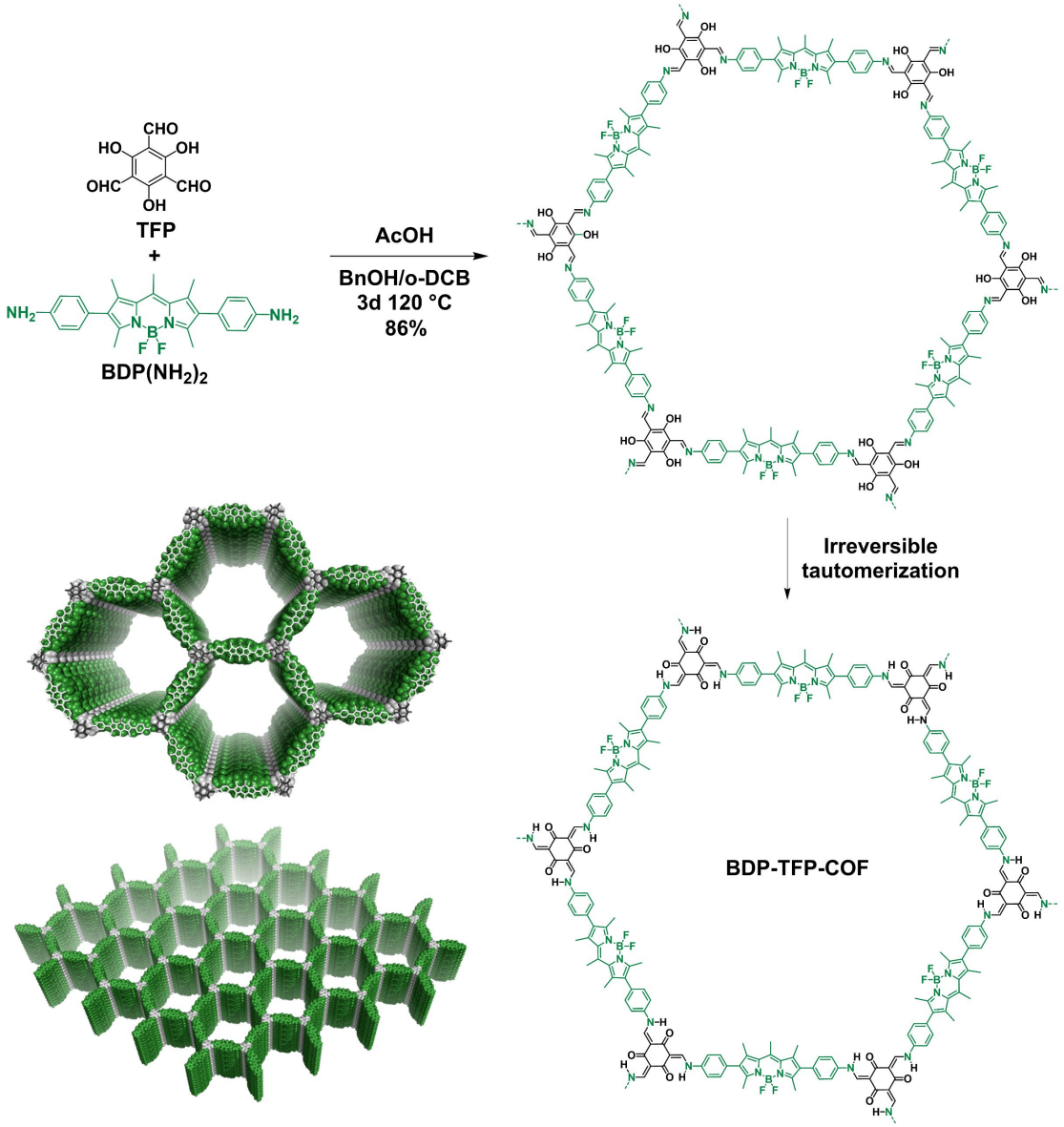

Scheme 17. Synthesis of hexagonal **BDP-TFP-COF** via imine condensation followed by tautomerization process and structural models of the 2D layered structure.

The isolated solid material was initially characterized by FT-IR spectroscopy to confirm the completion of the reaction and the formation of the *β*-ketoenamine linkages. The attenuation of the band at 1636 cm^{-1}, which corresponds to the C=O stretching mode of the aldehydes in **TFP**, indicates proper polymer formation (Figure S31). Solid-state NMR measurements were used to fully characterize the chemical structure. The comparison of a ^{13}C CP/MAS NMR spectrum of **BDP-TFP-COF** with ^{13}C NMR data of the corresponding building block **BDP(NH$_2$)$_2$** in solution evidenced the successful incorporation of the BODIPY unit into the **BDP-TFP-COF** scaffold (Figure 26a). All signals were assigned with the aid of a DEPT 135 spectrum of **BDP(NH$_2$)$_2$** in solution, which was used to differentiate any primary and tertiary from quaternary carbon atoms (Figure S29). The emergence of a new signal at 185 ppm for **BDP-TFP-COF**, which is attributed to the keto groups formed after the tautomerization of the enol-imine moieties, again confirms the formation of the polymer. Furthermore, two distinct regions are observed in the spectrum: The signals in the range of 160−100 ppm can be assigned to sp^2 carbon atoms in both BODIPY and TFP moieties, while the region centered at 17 ppm is attributed to the sp^3 CH_3 groups of the pentamethyl-substituted BODIPY core. The presence of the BODIPY subunits is also confirmed by a strong signal at −145 ppm for the BF_2 units of the BODIPY moieties in both ^{19}F MAS NMR for **BDP-TFP-COF** and ^{19}F solution NMR for monomeric **BDP(NH$_2$)$_2$** (Figure 26b). For the molecular precursor, the splitting of the signal into a quartet with $J = 33$ Hz confirms the coupling between F and B in the BF_2 units (Figure S30).[253]

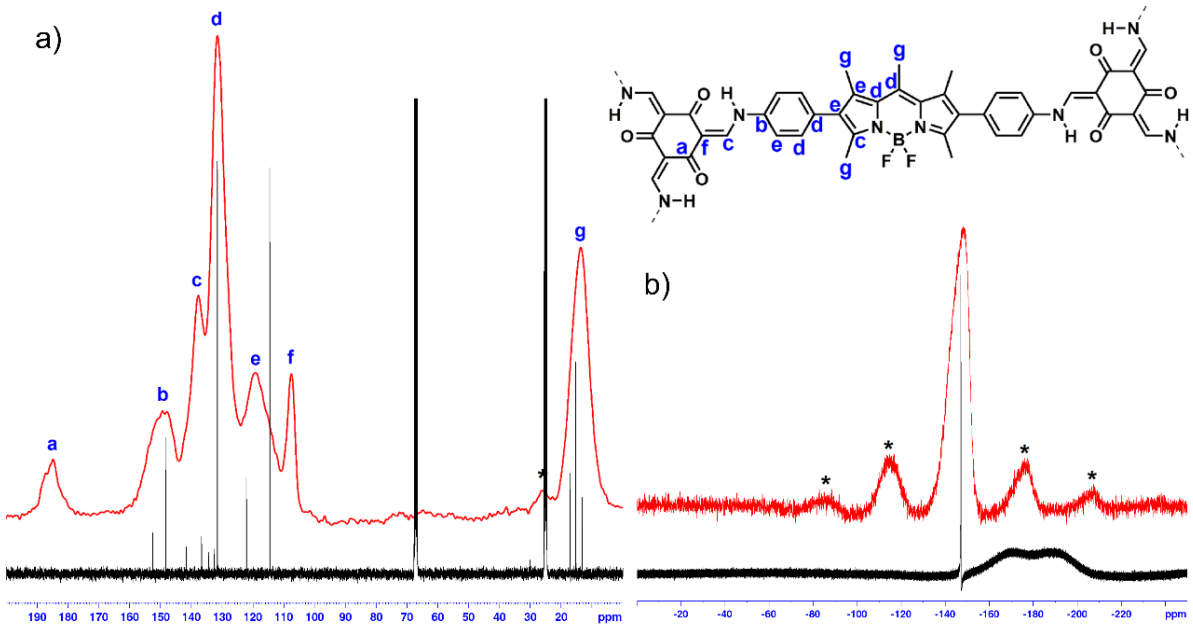

Figure 26. a) ^{13}C CP/MAS NMR and b) ^{19}F MAS NMR of **BDP-TFP-COF** in the solid state (red) and **BDP(NH$_2$)$_2$** in THF-d_8 (black). The peaks assigned with an asterisk correspond to spinning sidebands.

The crystallinity and structure of **BDP-TFP-COF** was analyzed by PXRD (Figure 27). The occurrence of one sharp and intense reflection at a 2θ angle of 2.40° and additional weaker reflections at 4.21°, 4.89°, 6.45° and 8.46° confirmed the formation of a highly crystalline framework. These reflections were indexed to the 100, 110, 200, 120 and 220 planes, respectively. The chemical stability was tested by immersing the solid for 24 hours in a wide variety of solvents. **BDP-TFP-COF** retained the crystallinity after exposure to several polar and non-polar solvents, as well as water and 1M HCl and 1M NaOH, confirming the very high chemical stability and the resistance against hydrolysis for this porous material (Figure 27b).

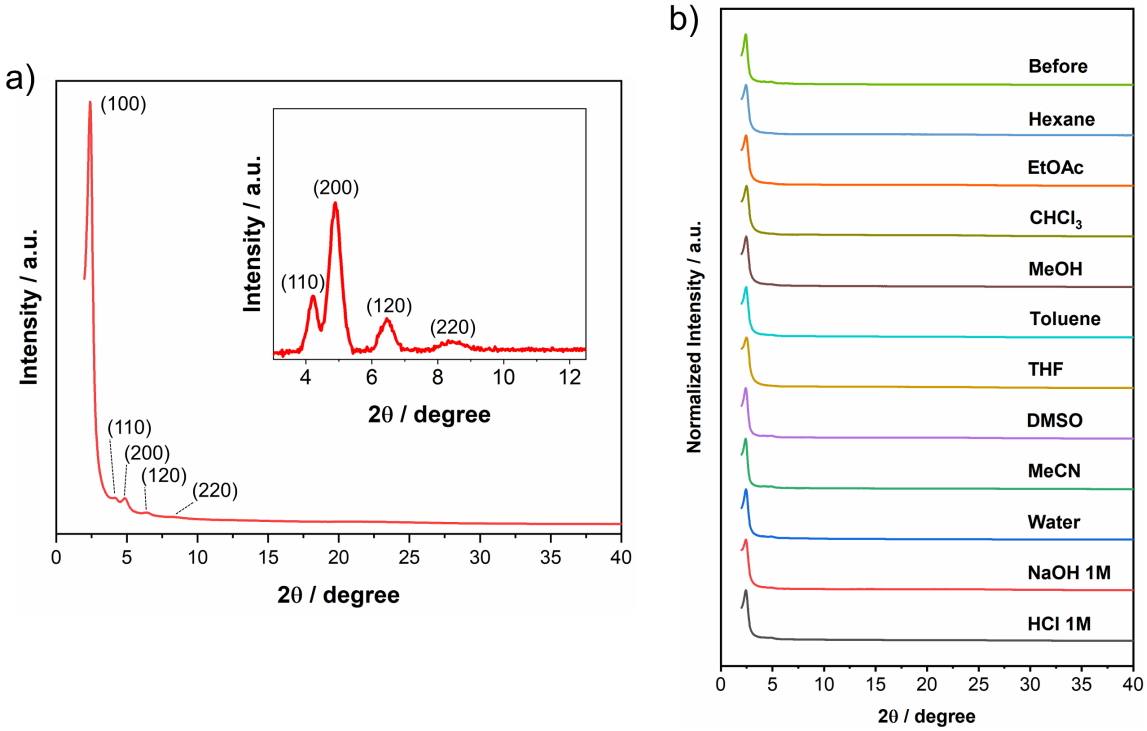

Figure 27. a) Experimental PXRD pattern and hkl indices for **BDP-TFP-COF**. b) PXRD pattern for solid samples of **BDP-TFP-COF** before and after being immersed in varying solvents for 24 hours.

To create an initial structural model, a monolayered unit cell with imposed *P*1 space group was geometry-optimized with the Forcite module of the Materials Studio software. It is reported for face-to-face arranged BODIPY supramolecular polymers that the aggregation is triggered by π–π interactions between the extended aromatic surfaces and that the antiparallel stacking minimizes the repulsion between boron difluoride groups.[254, 255] For a realistic model of the **BDP-TFP-COF** layer arrangement, a similar stacking motif for the 2D layers was assumed. To achieve the antiparallel stacks of the BODIPY subunits, the size of the unit call along the c axis was doubled and a second layer with a flipped arrangement of the BODIPYs was added. Final refinement of the **BDP-TFP-COF** structure and the lattice parameters was performed with the Reflex module of the Materials Studio program and the refined structure is shown in Figure 28.

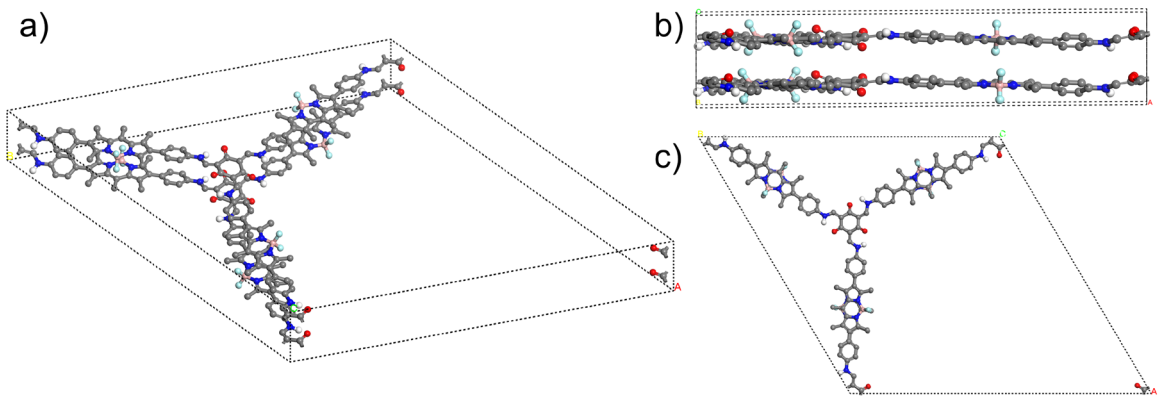

Figure 28. a) Unit cell for the refined structure of **BDP-TFP-COF** and views along the b) a and c) c axis. Hydrogen atoms are omitted for clarity.

After Pawley refinement of the experimental diffraction pattern, lattice parameters of $a = 44.06 \pm 0.19$ Å, $b = 44.53 \pm 0.14$ Å and $c = 7.79 \pm 0.036$ Å (for a thickness of two layers) with angles of $\alpha = 89.65 \pm 0.45°$, $\beta = 89.65 \pm 0.49°$ and $\gamma = 120.62 \pm 0.37°$ and refinement parameters of $R_{wp} = 4.30\%$ and $R_p = 7.53\%$ were obtained (Figure S34). These parameters fit very well to a hexagonal lattice system typically found for COFs with *hcb* topology. A simulated diffraction patter for this eclipsed (AA-type) stacking model is in excellent agreement with the experimental PXRD data, thus confirming the proposed hexagonal pore structure for **BDP-TFP-COF**. In contrast, simulation of a slipped AB-type stacking model does not match the intensity distribution and peak position at larger angles as shown in Figure 29.

From this model, an interlayer distance of 3.9 Å is obtained for the π–π stacking between adjacent COF sheets. Highly symmetrical hexagonal 2D COFs typically crystallize in the *P*6 space group with the first intense reflection attributed to the 100 plane. However, due to the antiparallel stacking of the BODIPY units, the C_2 rotational symmetry at the center of the linkers is lost and a triclinic *P*1 space group without imposed symmetry constraints was used to model this structure.

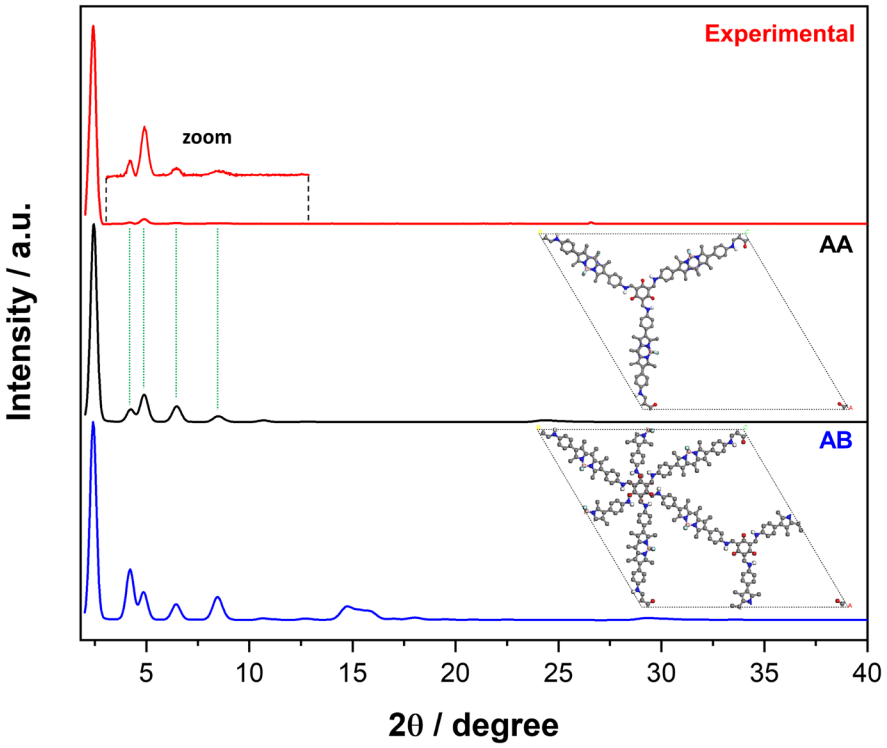

Figure 29. Experimental (red, background removed) and simulated PXRD patterns with AA (black) and AB (blue) stacking for **BDP-TFP-COF**.

Samples for SEM were prepared by coating the surface of a Si/SiO_2 substrate with a **BDP-TFP-COF** dispersion in isopropanol (≈ 0.5 mg mL^{-1}) via drop-casting. The SEM images showed interconnected microcrystalline domains, which further assembled into sponge-like agglomerates with a size of several µm (Figure 30a-c). EDX spectroscopy revealed an atomic composition of C, O, F, N and B, thus confirming the presence of the BODIPY moieties (Figure 30d). TGA of the COF powder demonstrated a high thermal stability up to 400 °C after an initial mass loss of 8 wt%, which is attributed to the release of solvent molecules trapped into the pores (Figure 31a). Nitrogen physisorption measurements revealed a type IV isotherm characteristic for mesoporous materials[256] with a calculated BET surface area of 1042 m^2 g^{-1} (Figure 31b). Analysis of diffuse reflectance measurements for **BDP-TFP-COF** powder samples with the Kubelka-Munk function displayed a broad absorption in the whole visible region with a wavelength maximum at 575 nm (Figure 31c). From the Tauc plot, a direct optical bandgap of 1.82 eV was estimated (Figure 31d).

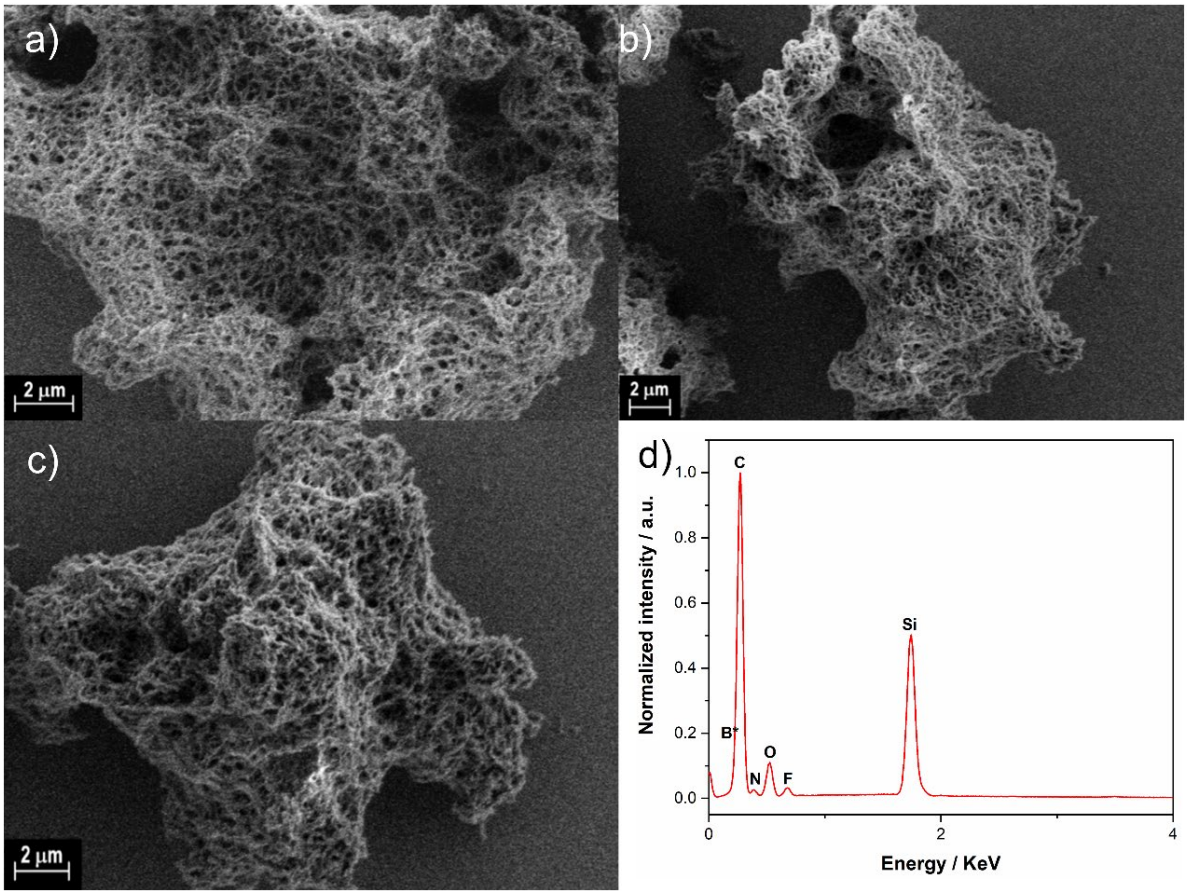

Figure 30. a), b), c) SEM images and d) EDX spectrum of **BDP-TFP-COF**. The pronounced Si peak can be assigned to the SiO_x substrate. * The presence of B was detected by the device, but it is eclipsed by the C signal.

BDP-TFP-COF is still among the first reported examples for COFs with BODIPY units directly incorporated into the structural backbone. During the course of this project, a small number of BODIPY-containing[160, 248] or decorated[173, 246, 247] COFs have been reported. In contrast to these examples, the obtained S_{BET} = 1042 $m^2 g^{-1}$ for **BDP-TFP-COF** is remarkably higher that the other BODIPY-containing COFs (S_{BET} = 71.3,[248] 217.2[160] and 805[246] $m^2 g^{-1}$) due to the favorable combination of the *hcb* topology with an eclipsed stacking mode. Based on the combined analytical data, **BDP-TFP-COF** was established as a highly stable and porous framework with very interesting optical properties originated from the highly ordered BODIPY units. In the following, we elaborate on several applications for this material to explore the potential of **BDP-TFP-COF** as a highly versatile and functional porous material.

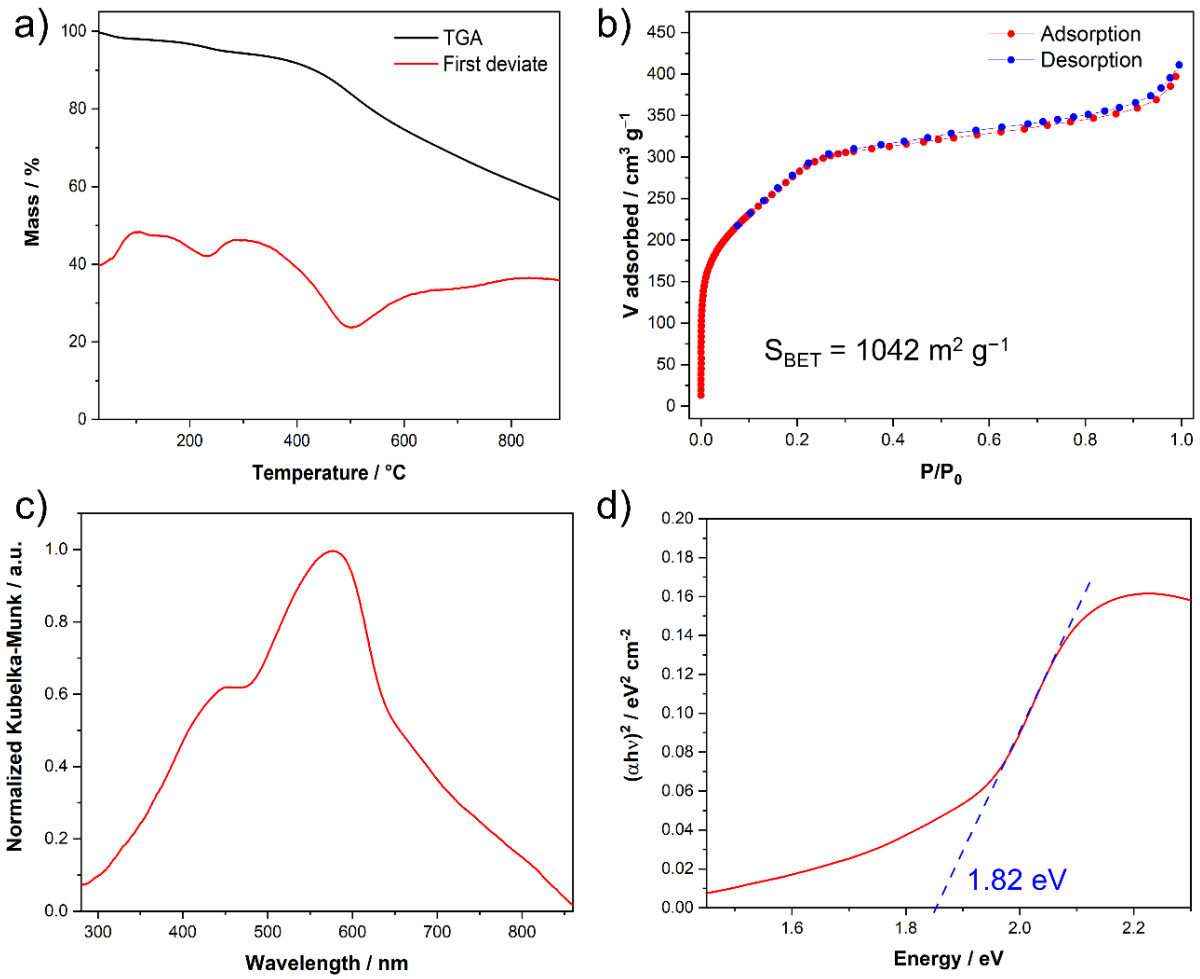

Figure 31. Characterization of **BDP-TFP-COF**: a) TGA (black) and first derivative (red); b) nitrogen physisorption isotherm (adsorption branch: red, desorption branch: blue); c) UV-Vis absorption spectra derived with the Kubelka–Munk function from diffuse reflectance measurements for the solid sample and d) Tauc plot with the intersection of the slope (blue) with the ordinate axis indicating a direct optical bandgap of 1.82 eV.

4.2.2 Adsorption experiments: Removal of model pollutants from water

Inspired by the high porosity and chemical stability of **BDP-TFP-COF**, adsorption experiments in aqueous media were performed. As model compounds for water remediation applications, we selected the common micropollutant bisphenol A (BPA) and the extensively used water-soluble dye methylene blue (MB) (Figure 32) for adsorption and removal studies.

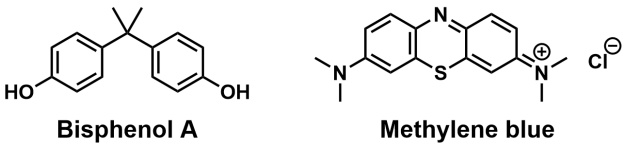

Figure 32. Chemical structures of BPA and MB.

4.2.2.1 Adsorption of Bisphenol A from water

BPA is extensively used as a building block for a broad variety of industrial polymers such as polycarbonates, polyesters or epoxy resins, leading to excellent thermal and mechanical

properties. Otherwise, BPA is used as a materials additive. Therefore, BPA is one of the most manufactured chemicals worldwide, with a global production above 6 million tons in 2017. It is found in everyday objects such as bottles, smartphones, coatings, or toys. However, BPA is confirmed to be an endocrine disrupting and estrogenic chemical, being responsible of adverse health effects and highly toxic for aquatic organisms. Dumped BPA-based plastics can undergo hydrolysis, thus provoking the release of BPA into soils and waters and representing a serious threat for the environment. Hence, finding new solutions for the removal of this pollutant is a common goal among many members of the scientific community.[257]

The BPA uptake by **BDP-TFP-COF** as adsorbent was investigated at 298 K. Due to the low solubility of BPA in pure water, a stock solution with an initial concentration (C_0) of 100 ppm BPA in water was prepared for the experiments. From that, a series of **BDP-TFP-COF** dispersions in the BPA stock solution was prepared with concentrations of 0.05, 0.1, 0.25, 0.5, 0.75, and 1.0 g L^{-1}. All dispersions were stirred at 250 rpm in the absence of light for three hours to provide enough time to reach equilibrium. Afterwards, 1 mL of the remaining BPA solution was taken via syringe filter and diluted in a total volume of 3 mL of Millipore water. To calculate the respective adsorption capacities at equilibrium, the local absorption maximum of BPA at 277 nm was monitored (Figure 33). The concentration at equilibrium C_e, i.e. the concentration of the remaining BPA in the solution, was calculated for each solution by interpolating the obtained absorbance with a freshly prepared calibration curve (Figure S36) considering the dilution factor (C_e (real) = 3·C_e (measured)).

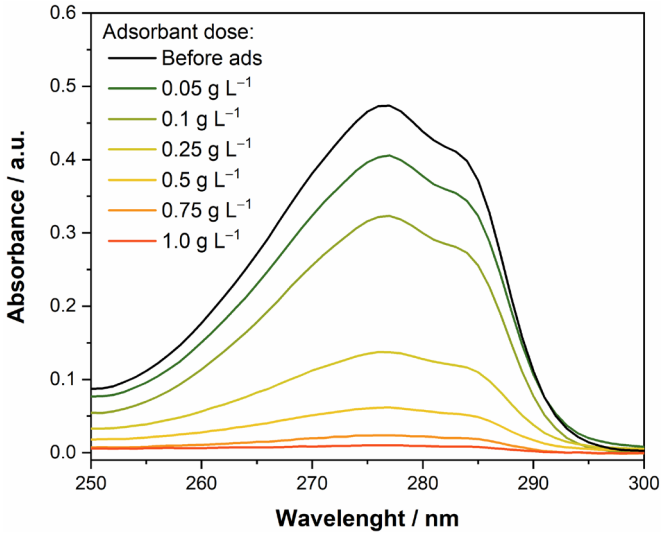

Figure 33. Representative examples for the absorption spectra of a blank BPA solution (black, 100 ppm in water) and after addition of varying amounts of **BDP-TFP-COF**.

From C_e, the adsorption capacity at the equilibrium (q_e) is calculated using the following equation:

$$q_e\,[mg\ g^{-1}] = \frac{C_0 - C_e}{M} V \quad (1)$$

Where C_0 [mg L^{-1}] is the initial concentration of adsorbate, C_e [mg L^{-1}] is the concentration at equilibrium, M [g] is the mass of adsorbant and V [L] the volume of the solution (Note that $\frac{V}{M} = \frac{1}{Adsorbant\ dose}$).

All experiments were repeated three times (Table S4) and the q_e values are summarized in Table 1 as the mean value with the standard deviation. To standardize the data in a graphical representation, Figure 34a displays the adsorption capacity of BPA into **BDP-TFP-COF** against the concentration of BPA at the equilibrium (i.e. the BPA concentration remaining in solution). In Figure 34b, both the adsorption capacity at equilibrium and the percentage of removal for a fixed C_0 of 100 ppm BPA, are plotted against the COF dosage. However, these values will vary upon changes of C_0 and they do not represent a standard display of the data.

These data revealed a very high BPA uptake at low **BDP-TFP-COF** dosage, i.e., high C_e, and the removal of 97% BPA from the aqueous stock solution at a dosage of 1.0 g L^{-1} of adsorbent, indicating the high potential of **BDP-TFP-COF** for BPA removal from contaminated water.

Table 1. Average value and standard deviation (each measurement was repeated three times) of the concentrations at equilibrium and adsorption capacities per **BDP-TFP-COF** dosage in the adsorption experiments of BPA from water at 298 K.

Adsorbant dose $[g\ L^{-1}]$	C_e $[mg\ L^{-1}]$	q_e $[mg\ g^{-1}]$
0.05	81.65 ± 0.35	366.96 ± 7.01
0.1	65.30 ± 0.43	347.04 ± 4.26
0.25	32.23 ± 2.82	271.06 ± 11.30
0.5	11.53 ± 1.92	176.94 ± 3.85
0.75	6.40 ± 1.20	124.80 ± 1.60
1.0	2.93 ± 0.72	97.07 ± 0.72

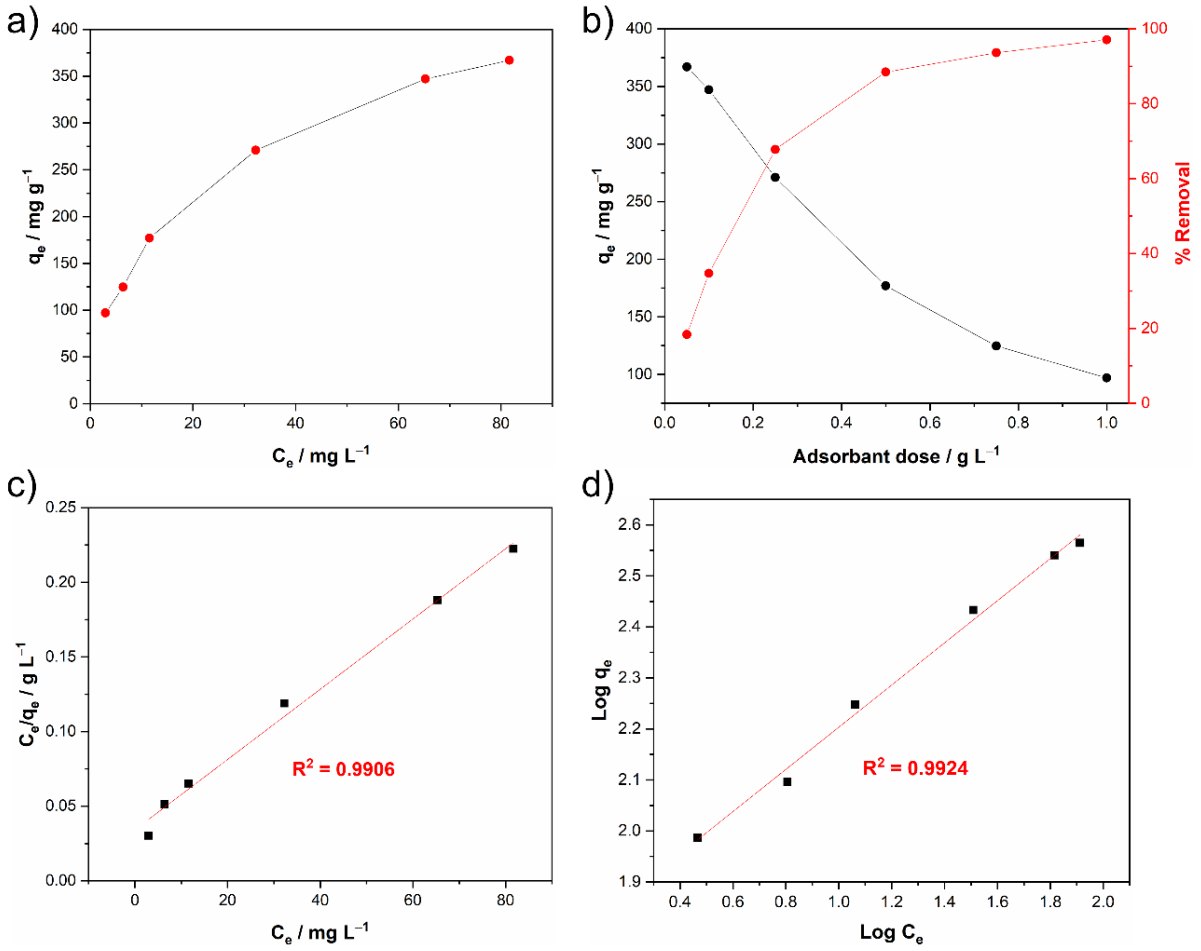

Figure 34. a) Adsorption isotherm, b) plot of adsorption capacity (black) and percentage of removal (red) against the COF concentration and linear plot representation of c) Langmuir and d) Freundlich isotherms for the adsorption of BPA (C_0 = 100 ppm, T = 298 K) from water into **BDP-TFP-COF**.

Two different adsorption models[258] are widely discussed for fitting the experimental data and extracting parameters that describe the adsorption process in a simplified manner. The first one is the Langmuir model. This model proposes that the adsorption energies are equivalent for all the adsorption sites and independent from the surface coverage. Therefore, the adsorption occurs homogeneously in a monolayer. It well explains the behaviour of a binary adsorption system and the equation typically fits for systems with moderately low coverage of adsorbate. The Langmuir isotherm equation (2) is expressed as:

$$q_e = \frac{q^o K_L C_e}{1 + K_L \cdot C_e} \tag{2}$$

This can be linearized with the following transformation:

$$\frac{C_e}{q_e} = \frac{1}{q_{max}} C_e + \frac{1}{q_{max} K_L} \tag{3}$$

Where q_{max} [mg g^{-1}] is the theoretical maximum adsorption capacity and K_L [L mg^{-1}] is the Langmuir constant, which provides information about the strength of the interaction or affinity between the adsorbate and the surface in relation to the free energy of adsorption. From K_L, one can calculate the separation factor R_L which indicates if the adsorption is favourable, unfavourable, or irreversible.

$$R_L = \frac{1}{1 + C_o \cdot K_L} \tag{4}$$

If $R_L = 0$, the adsorption process is irreversible, if $0 < R_L < 1$, the adsorption process is favourable and if $R_L > 1$ the adsorption process is unfavourable.[259, 260] The Gibbs free energy change of the adsorption process can be calculated using the Langmuir constant as follows:

$$\Delta G^o = -RT\ lnK_L \tag{5}$$

In which R is the universal gas constant 8.314 J K^{-1} mol^{-1}, T is the absolute temperature in Kelvin and K_L is the Langmuir constant in L mol^{-1}.

The second model is the Freundlich model. This is an empirical model under the assumption that the adsorption is a heterogeneous process and that the adsorption energy changes with the surface coverage as a consequence of lateral interactions between adjacent molecules. Hence, this model considers further multilayer adsorption and is suitable for both monolayer and multilayer adsorption processes.

The Freundlich isotherm equation (6) is expressed as

$$q_e = K_F C_e^{1/n} \tag{6}$$

with the following linear expression:

$$Log\ q_e = logK_F + \frac{1}{n} Log\ C_e \tag{7}$$

Where K_F [(mg g^{-1})(L mg^{-1})$^{1/n}$] is the Freundlich constant, related to the adsorption capacity, and the value of n is indicative of the intensity and favourability of the adsorption process. Any adsorption process is considered favourable according to the Freundlich model if n is between 1 and 10.[261]

The linearized data of the Langmuir isotherm is represented in Figure 34c. The linear regression of the obtained values allowed the calculation of the Langmuir parameters, which are collected in Table 2. These parameters indicate a favourable adsorption process with a theoretical

maximum adsorption capacity of 425.53 mg g^{-1} of BPA into the **BDP-TFP-COF** pores. This uptake is among the highest reported for COFs so far (Table 3) and reveals a remarkable performance in the removal of BPA from water. In addition, the high correlation with the Langmuir model indicates that the adsorption process may occur as a monolayer.[262] From the Langmuir constant, a free energy of $\Delta G° = -23.93$ KJ mol^{-1} was calculated, which indicates the spontaneity of the adsorption process.[263] The linearized representation for Freundlich isotherm is shown in Figure 34d and the Langmuir parameters are collected in Table 2.

Table 2. Fit parameters of the Langmuir and Freundlich isotherms for the absorption of BPA from water (C_0 = 100 ppm) onto **BDP-TFP-COF** at 298 K.

Langmuir					
a	***b***	q_{max} (mg g^{-1})	K_L (L mg^{-1})	R^2	R_L
0.0342	0.00235	425.531	0.06871	0.9906	0.1270

Freundlich				
a	***b***	K_F (mg g^{-1})(L mg^{-1}) $^{1/n}$	**n**	R^2
1.78996	0.41339	61.654	2.419	0.9924

Table 3. Maximum adsorption capacities for absorption of BPA in literature-known COFs.

COF	BPA q_{max} (mg g^{-1})	Year	Reference
Fe3O4@TpBD	160.6	2017	264
TFPPy-PDA-COF	288.3	2019	265
TFPPy-PyTTA-COF	144.8	2019	265
Compressible Crystalline COF Aerogel COFs-$C_3H_7NH_2$	205.76	2019	266
Compressible Crystalline COF Aerogel COFs-$C_4H_9NH_2$	699	2019	266
PyTTA-Dva-COF	285	2020	267
Fe_3O_4@COF	140	2020	268
TpPa-1	1424.27	2020	269
COF-1	125	2021	270
COF-2	145	2021	270
“Flower-like COF”	56.8	2021	271
Fe_3O_4@TpND	114.97	2020	272
Fe_3O_4@3D-COF-TpTAM	209.9	2021	273
pristine CTF	191.3	2021	274
STCH-CTF_{10}	295.4	2021	274
BDP-TFP-COF	**425.53**	**2021**	**This work**

Considering the coefficient of determination R^2, both models were well suited to describe the adsorption in this binary system and several parameters derived from both isotherms provide information about the process. The favorable adsorption process is presumably driven by attractive intermolecular forces between adsorbent and adsorbate, e.g. hydrophobic interactions induced by the fluorocarbon surface created by the ordered BODIPY stacks,[275-277] π−π stacking interactions and hydrogen bonding.[269, 278] Calculations with the Adsorption Locator module of the Materials Studio software provided information about the most favourable site for the adsorption of BPA within the **BDP-TFP-COF** pores. Apparently, the angular geometry of the BPA molecule facilitates 2.9−3.6 Å edge to face π−π stacking interactions with the phenyl groups of the BODIPY moieties (Figure 35).

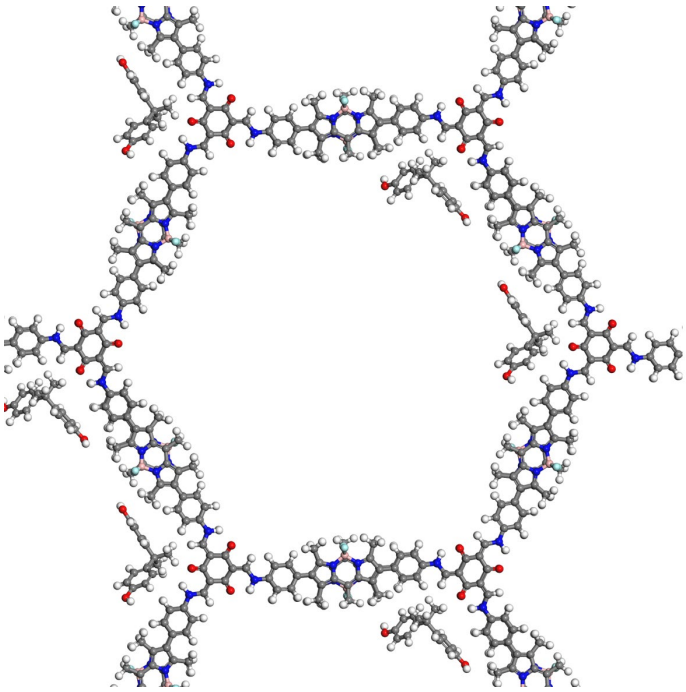

Figure 35. Simulation of the energetically most favorable adsorption sites of BPA onto **BDP-TFP-COF** (For a load of two BPA molecules per unit cell).

4.2.2.2 Adsorption of Methylene blue from water

MB is a cationic dye extensively used in textile and ink industry or clinical applications.[279, 280] The disposal of this pollutant into natural waters leads to severe environmental and health problems as a result of its excellent stability, high toxicity, visible light absorption and decrease of oxygen levels. Despite strong efforts during the last two decades to remediate waters contaminated by MB, the detection and removal of this pollutant is still of concern.[281, 282] The MB uptake by **BDP-TFP-COF** as adsorbent at 298 K was investigated by UV-Vis spectroscopy. Due to the high molar extinction coefficient of MB in water, an initial

concentration of 50 ppm for a stock solution was chosen for all experiments. To different screw cap vials equipped with a magnetic stirrer, **BDP-TFP-COF** dispersions in the MB stock solution were prepared with varying concentrations of 0.1, 0.25, 0.5, 0.75, and 1.0 g L^{-1}. These dispersions were stirred at 250 rpm in absence of light for three hours to provide enough time to reach equilibrium. Afterwards, 300 µL of the supernatant solution were taken via syringe filter and diluted in a total volume of 3 mL of Millipore water. To obtain the different adsorption capacities at equilibrium, the absorption maxima of MB at 664 nm was monitored by UV-Vis spectroscopy (Figure 36), and the concentration at the equilibrium was calculated for each solution by interpolating the obtained absorbance with a freshly prepared calibration curve (Figure S37), considering the dilution factor (C_e (real) = 10·Ce (measured)). All experiments were repeated three times (Table S5) and the mean values with the standard deviation are summarized in Table 4.

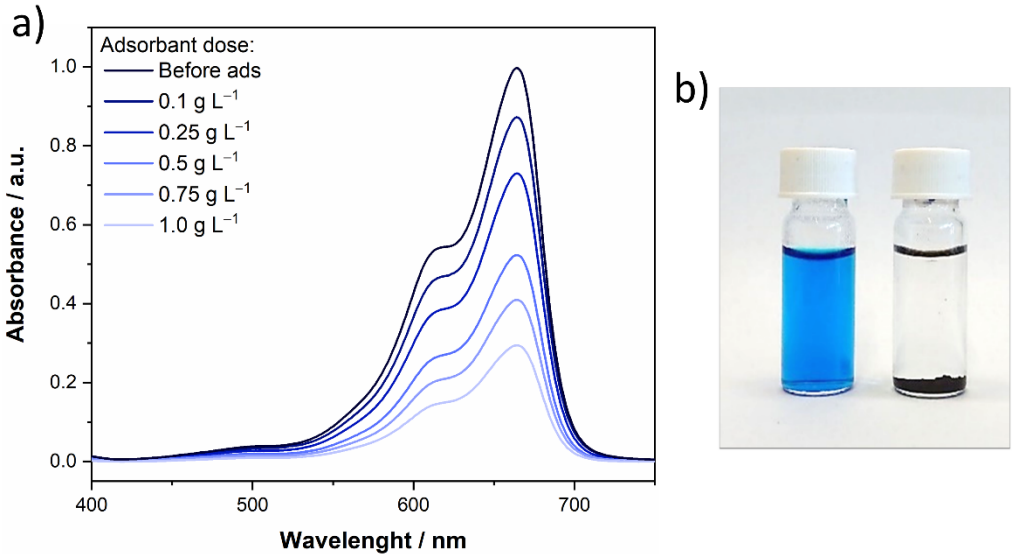

Figure 36. a) Representative examples for the absorption spectra of a blank MB solution (black, 50 ppm in water) and after the addition of varying amounts of **BDP-TFP-COF**; b) visual evidence for dye adsorption after introducing **BDP-TFP-COF** in MB-contaminated water.

Table 4. Average value and standard deviation (each measurement was repeated three times) of the concentrations at equilibrium and adsorption capacities per **BDP-TFP-COF** dosage in the adsorption experiments of MB from water at 298 K.

Adsorbant dose $[g\ L^{-1}]$	C_e $[mg\ L^{-1}]$	q_e $[mg\ g^{-1}]$
0.1	43.33 ± 2.38	66.68 ± 23.85
0.25	35.41 ± 1.25	58.34 ± 4.99
0.5	24.97 ± 2.88	50.07 ± 5.76
0.75	18.20 ± 1.25	42.39 ± 1.66
1.0	12.08 ± 4.51	37.91 ± 4.51

Similar as for the BPA adsorption experiments, Figure 37a displays the adsorption capacity of MB into **BDP-TFP-COF** at equilibrium against the concentration of MB at equilibrium and Figure 37b shows the adsorption capacity at equilibrium and the percentage of removal against the COF dosage for an initial concentration of 50 ppm MB. These results indicate that the adsorption capacity for MB is lower than for BPA, leading to a removal of only 76% at even lower concentrations of the stock solution (50 ppm for MB instead of 100 ppm for BPA).

The linear fits for the Langmuir and Freundlich models are displayed in Figure 37c and d respectively. The parameters for each model are summarised in Table 5 and were calculated in the same manner as introduced in Chapter 4.2.2.1.

Table 5. Fit parameters for the Langmuir and Freundlich isotherms for the absorption of MB from water (C_0 = 50 ppm) onto **BDP-TFP-COF** at 298 K.

		Langmuir			
a	**b**	q_{max} **(mg g^{-1})**	K_L **(L mg^{-1})**	**R^2**	R_L
0.22171	0.01041	96.06	0.0470	0.9580	0.2985
		Freundlich			
a	**b**	K_F **(mg g^{-1})(L mg^{-1})$^{1/n}$**	**n**	**R^2**	
1.08412	0.44394	12.1372	2.253	0.9763	

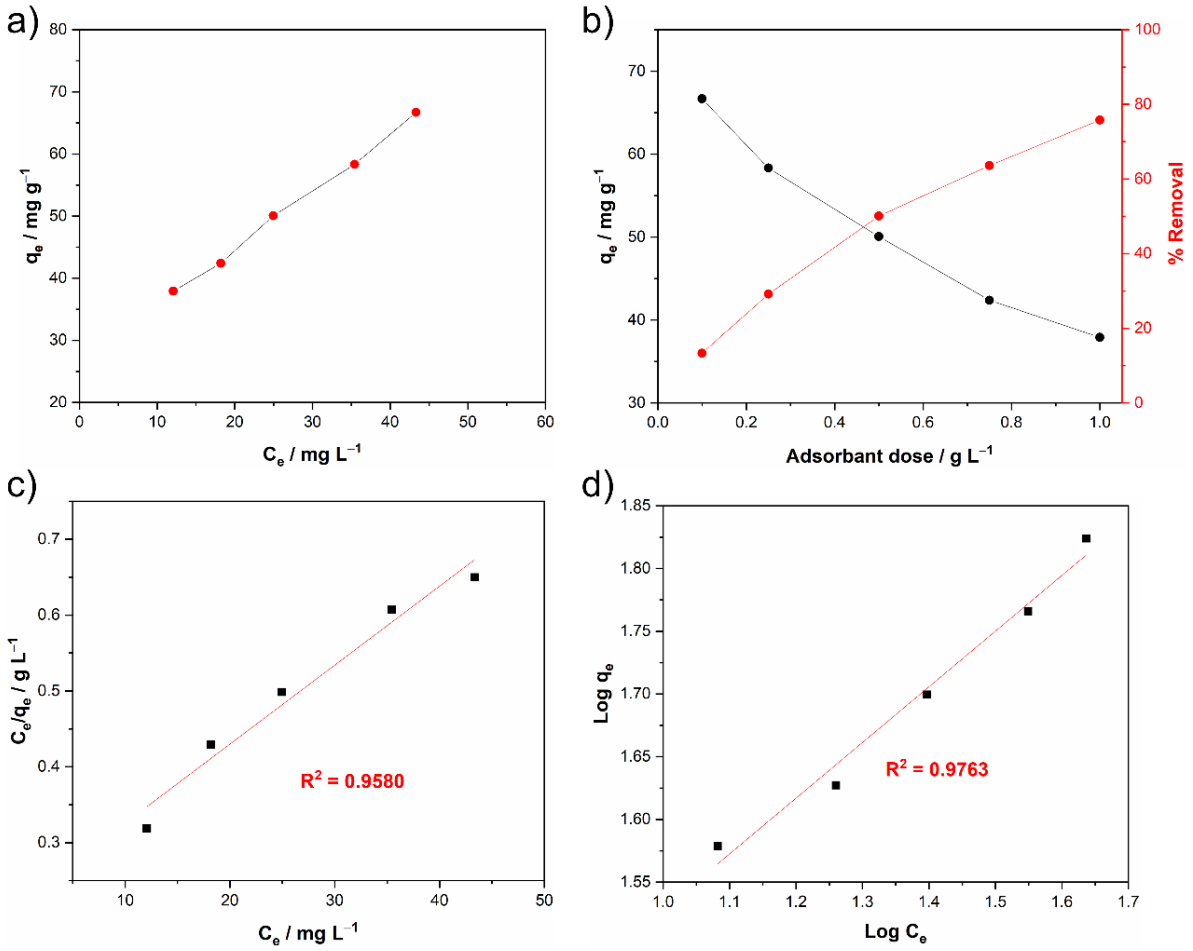

Figure 37. a) Adsorption isotherm, b) plot of adsorption capacity (black) and percentage of removal (red) against the COF concentration and linear plot representation of c) Langmuir and d) Freundlich isotherms for the adsorption of MB from water onto **BDP-TFP-COF** (C_0 (MB) = 50 mg L^{-1}, T = 298 K).

From the Langmuir model, a separation factor R_L of 0.30 indicated a favourable adsorption process with a theoretical maximum adsorption capacity of 96.06 mg g^{-1} of MB into the **BDP-TFP-COF** pores, revealing a decent uptake of this pollutant from water. The calculated $\Delta G° = -23.83$ KJ mol^{-1} indicates a spontaneous process. However, the lower correlation coefficient for the Langmuir model in comparison to the Freundlich model may indicate the likelihood of multilayer adsorption. This assumption might be rationalized by the planarity of MB, which favours further π–π stacking between aromatic cores.

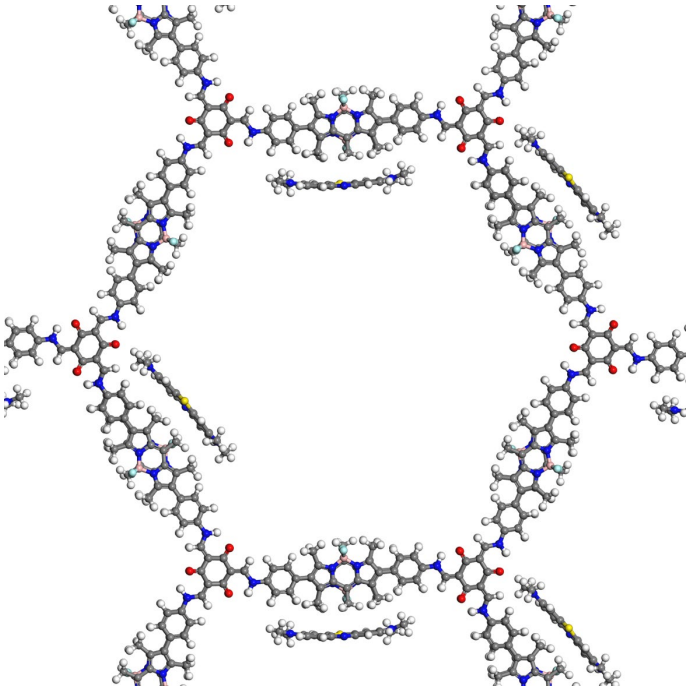

Figure 38. Simulation of most energetically favorable adsorption sites of MB onto **BDP-TFP-COF** (For a load of two MB molecules per unit cell).

For the MB adsorption process, calculations with the Adsorption Locator module of the Materials Studio software reveals that the adsorption is mainly driven by CH–π interactions between **BDP-TFP-COF** and MB, in addition to hydrogen bonds between the amino moieties of the MB and the keto groups of the COF (Figure 38). Presumably, other attractive forces such as electrostatic interactions between the positively charged dye molecule and the fluoride moieties of the BODIPYs might be relevant as well.

4.2.3 Sensing of Methylene Blue

Since many BODIPY derivatives are highly emissive molecules, the incorporation of such chromophores within porous frameworks is an interesting approach to obtain novel optoelectronic materials. On the search for further potential applications for **BDP-TFP-COF**, the fluorescence properties of this solid-state material were evaluated for sensing applications. In continuation with the water remediation investigations in the previous section, fluorescence sensing experiments in water were performed. While bulk samples of **BDP-TFP-COF** showed no emission in the solid state, the preparation of a colloidal dispersion via sonication of pristine COF powder in water (0.1 mg mL^{-1}) generated a weak red emission with a low absolute quantum yield ($\Phi < 1$ %). Aparently, **BDP-TFP-COF** exhibits an aggregation-caused quenching (ACQ) of the emission in the bulk phase as a result of an H-type aggregation provoked by the face-to-face π–π stacking of adjacent BODIPY moieties.[30, 98] Since the sonication of the bulk powder triggers the exfoliation of **BDP-TFP-COF** sheets, the ACQ is

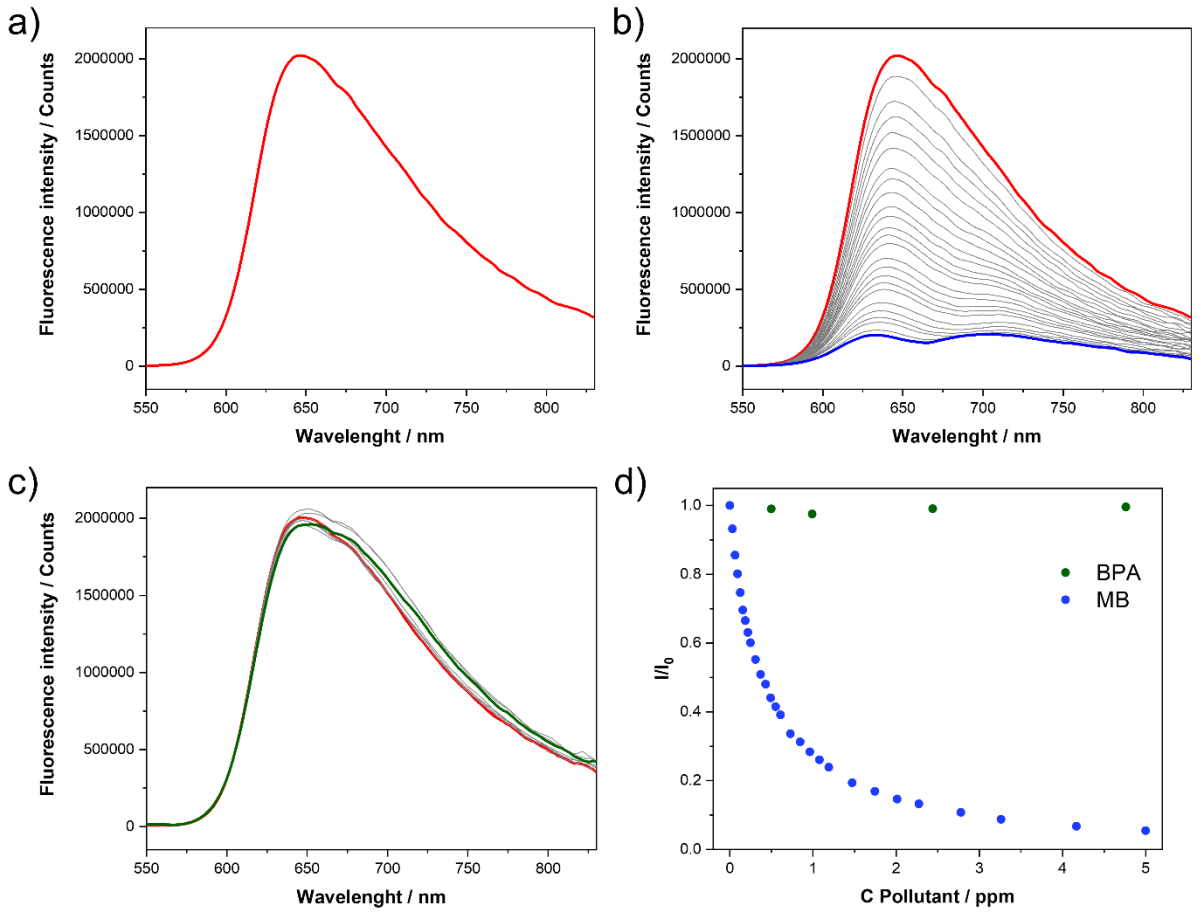

Figure 39. a) Emission spectrum of **BDP-TFP-COF** (0.1 mg mL^{-1} in water, λ_{exc} = 420 nm). b) Fluorescence spectral changes of **BDP-TFP-COF (**0.1 mg mL^{-1} in water, λ_{exc} = 420 nm, red curve) with increasing amounts of MB (25 mg L^{-1} in water, gray and blue curves). c) Fluorescence spectral changes of **BDP-TFP-**COF (0.1 mg mL^{-1} in water, λ_{exc} = 420 nm, red curve) with increasing amounts of BPA (100 mg L^{-1} in water, gray and green curves). d) Plot of the relative fluorescence intensity at the 646 nm maximum versus the concentration of MB and BPA.

reduced and emitting CONs are dispersed in the solution. Upon irradiation of the diluted dispersion with an excitation wavelength of 420 nm, a steady-state emission spectrum (Figure S39a) shows a broad emission band with a maximum located at 646 nm. The rather large width might be explained by the coexistance of agglomerated COF layers with varying thickness.[283] Despite the low absolute quantum yield, these emissive aqueous dispersions of **BDP-TFP-COF** raises hope for potential applications in sensing of selected pollutant molecules in contaminated waters.[284] MB sensing experiments were carried out by monitoring the emission maximum upon adding aliquots of a 25 ppm MB solution in Millipore water to 2 mL of a 0.1 mg mL^{-1} **BDP-TFP-COF** dispersion in Millipore water (Figure S38). Excitation at 420 nm was chosen to avoid an inner filter effect caused by reabsorption at MB (Figure S40a). The cuvette was manually shaken and left undisturbed for one minute before every measurement. This step was repeated two or three times until no fluctuation in emission was noticed and the constant values were retained. Even upon the addition of 1 ppm of analyte, the fluorescence emission was almost completely quenched (Figure 39b,d), while the decrease

exhibited excellent linearity up to 200 ppb (Figure S39). In contrast, no quenching was observed upon the addition of BPA (Figure 39c,d). Unfortunately, the exact quenching mechanism could not be clarified. One possible explanation might be the wide spectral overlap between the emission of the **BDP-TFP-COF** and the absorption of MB, which could facilitate a Förster resonance energy transfer (FRET) (Figure S40b). In fact, the previously shown adsorption of the dye within the COF pores mediated by non-covalent interactions may arrange the energy donor and the energy acceptor at the adequate distance for the FRET process. Simulations with the adsorption tools of the Materials Studio software indicated intermolecular distances in the range of 2.9−3.6 Å between the guest and the the framework, which are stabilized by CH−π interactions between the methyl groups of the BODIPYs and the aromatic core of MB (Figure S41).

On the contrary, the incremental addition of triethylamine provoked an enhancement of the fluorescence, which was triggered by the deprotonation of the enaminone proton via a so-called *pinpoint surgery effect*.[140, 141] The negative charge on the aromatic backbone decreases the PET between the donor and acceptor, thus leading to the emission enhancement shown in Figure 40. This experiment revealed a remarkable dual behaviour of the fluorescence for **BDP-TFP-COF**.

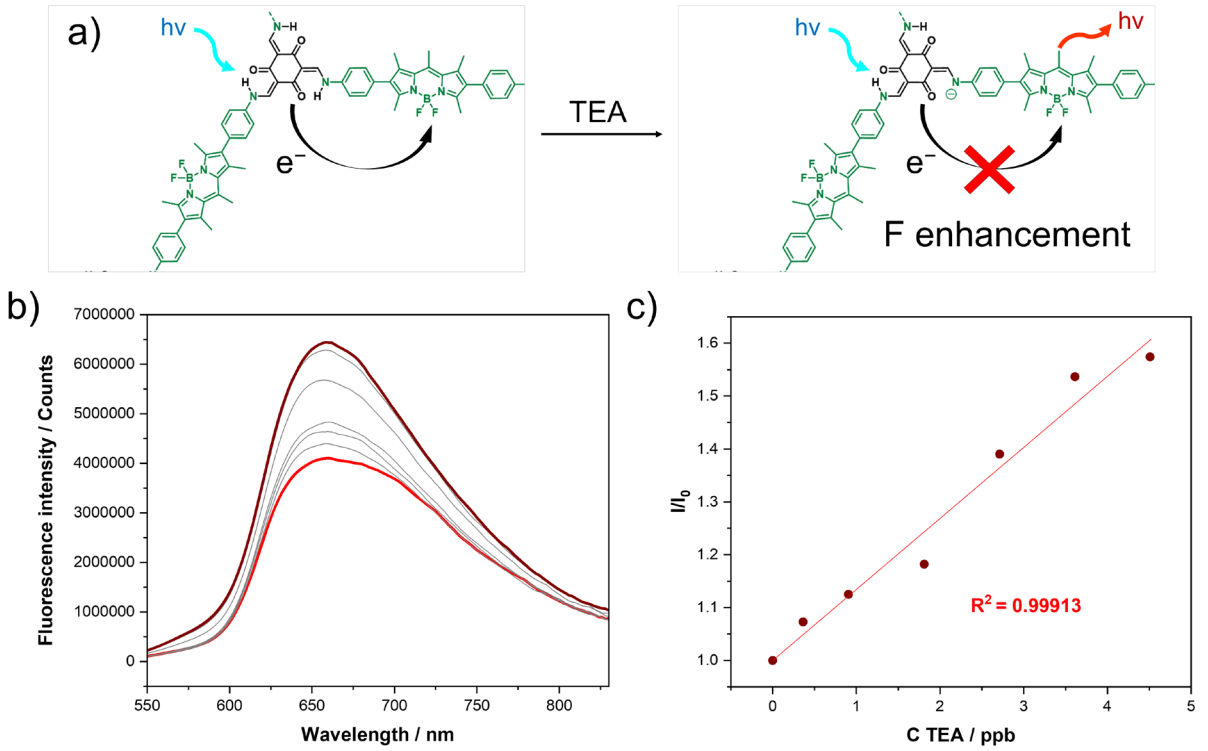

Figure 40. a) Schematic representation of the pinpoint surgery process in the **BDP-TFP-COF**. b) Fluorescence spectral changes of **BDP-TFP-COF** (0.1 mg mL^{-1} in THF, λ_{exc} = 365 nm, red curve) with increasing amounts of TEA (gray and dark red curves). c) Plot of the relative fluorescence intensity at the 660 nm maximum versus the concentration of TEA.

These phenomena may imply great potential in the field of sensing materials and the applications of this polymer as a dual sensor still call to be explored.

4.2.4 Singlet oxygen generation

After excitation and fast relaxation to the first excited singlet state S_1, the radiative decay to the singlet ground ($S_1 \rightarrow S_0$) leads to the fluorescence process discussed in the previous section. However, excited triplet states T_n can also be populated via intersystem crossing from the S_1 ($S_1 \rightarrow T_n$) (Figure 41). This process competes with the radiative deactivation, thus decreasing the fluorescence intensity. The very low absolute quantum yields for **BDP-TFP-COF** may imply an efficient population of T_1, which raised our interest in using this COF as a triplet photosensitizer.[285-287] Such photoactive materials are widely used in important applications such as photocatalysis including organic synthesis,[239, 288-290] hydrogen generation,[200, 291-293] pollutants degradation[294-296] or photodynamic therapy.[297-300] In the presence of dioxygen, an energy transfer can take place from the triplet state of the excited photosensitizer to the triplet ground state of dioxygen, provoking a spin-forbidden electronic transition to the first singlet state that is 95 kJ mol^{-1} above the triplet state (Figure 41).

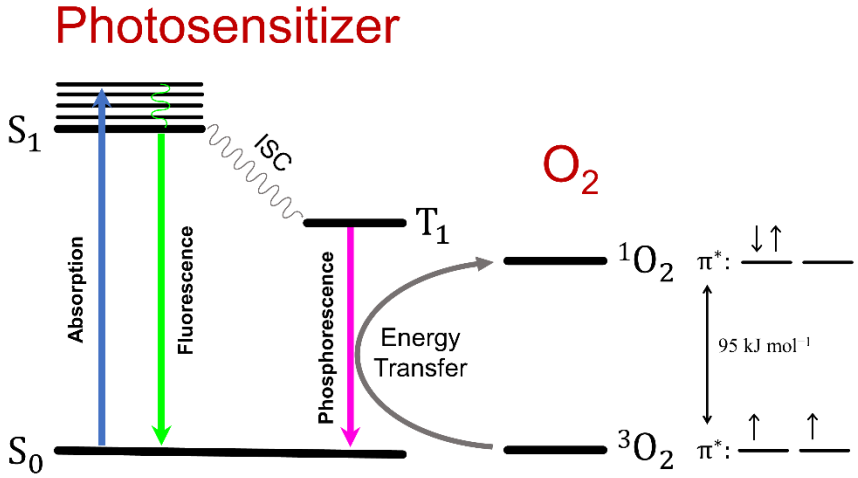

Figure 41. Schematic representation of singlet oxygen generation via excitation of a photosensitizer.

This oxygen species is a highly reactive electrophile with special predilection for unsaturated bonds or neutral nucleophiles such as amines, sulfides, and particularly heterocyclic systems.[301-304] Since molecular oxygen is ubiquitous in the atmosphere, the generation of singlet oxygen upon irradiation of a triplet photosensitizer is inevitable in the absence of an inert environment. Among all applications related to the triplet generation, the vast majority involve the generation of singlet oxygen. Hence, photooxidations derived from the reaction of π-electron rich substrates with singlet oxygen are used in organic synthesis,[238, 305-307] environmental remediation,[308-310] photodynamic therapy[173, 311-313] or disinfection.[314-316] In this

regard, furans are known to be highly prone to the singlet oxygen-mediated photooxidation. Hence, 1,3-diphenyl-*iso*-benzofuran (DPBF) is widely used as a singlet oxygen detection probe. The basis of the detection is the formation of an endoperoxide via a [4+2] cycloaddition with the singlet oxygen followed by an irreversible decomposition into 1,2-dibenzoylbenzene (DBB), which results in a noticeable alteration of the spectroscopical properties due to the loss of the π-system (Figure 42a). These spectral changes allow the easy detection of the ROS species by simple UV-VIS spectroscopy. Fluorescence spectroscopy is another technique that could be used. Nevertheless, UV-VIS absorption experiments are more accessible, and despite the lower sensitivity, they are less susceptible to artifacts.[317, 318]

Singlet oxygen generation experiments for **BDP-TFP-COF** were carried out by monitoring the absorption maximum at 415 nm of a $1 \cdot 10^{-4}$ M DPBF solution in DMF by UV-VIS spectroscopy and plots of the relative decay as a function of time. Upon irradiation with a green LED light (~ 7 W, 528 nm) in the presence of **BDP-TFP-COF**, a continuous decrease of the DPBF signal was observed with increasing irradiation time, thus implying the efficient generation of singlet oxygen (Figure 42c). Figure 42b displays the different absorption decays at varying COF concentration, indicating that singlet oxygen generation increases with the concentration up to a certain limit. Control experiments in the absence of **BDP-TFP-COF** showed negligible changes in absorbance, evidencing that the presence of the COF is necessary for the generation of singlet oxygen (Figure 42e).[319-321] Further control experiments were performed by alternating light and dark cycles, which nicely showed the absence of absorption changes in the dark (Figure 42d). Figure 42f reveals the effect of different irradiation wavelengths, evidencing that the singlet oxygen generation rate also depends on the selected light source. Under green LED light (~ 7 W, 528 nm) the material showed a better performance than under amber (~ 7 W, 590 nm) and red (~ 7 W, 617 nm) LED lights. Since all three LED sources emit at wavelengths close to the absorption maximum of the COF at 575 nm (Figure S44), this trend can be explained by the decreasing energy of the photons with higher wavelengths. Experiments at even shorter wavelengths (blue LED, 400 nm) could not be performed because of a triggered photodegradation of the DPBF upon irradiation.

Singlet oxygen generation with **BDP-TFP-COF** was also studied in pure water. Due to the insolubility of DPBF in aqueous media, the sodium salt of 9,10-anthracenediyl-bis(methylene)dimalonic acid (ABDA) was used as a water-soluble probe. In the presence of singlet oxygen, this anthracene derivative undergoes a similar 2+4 cycloaddition resulting in the photobleaching of the molecule.[317] Singlet oxygen generation experiments using UV-VIS

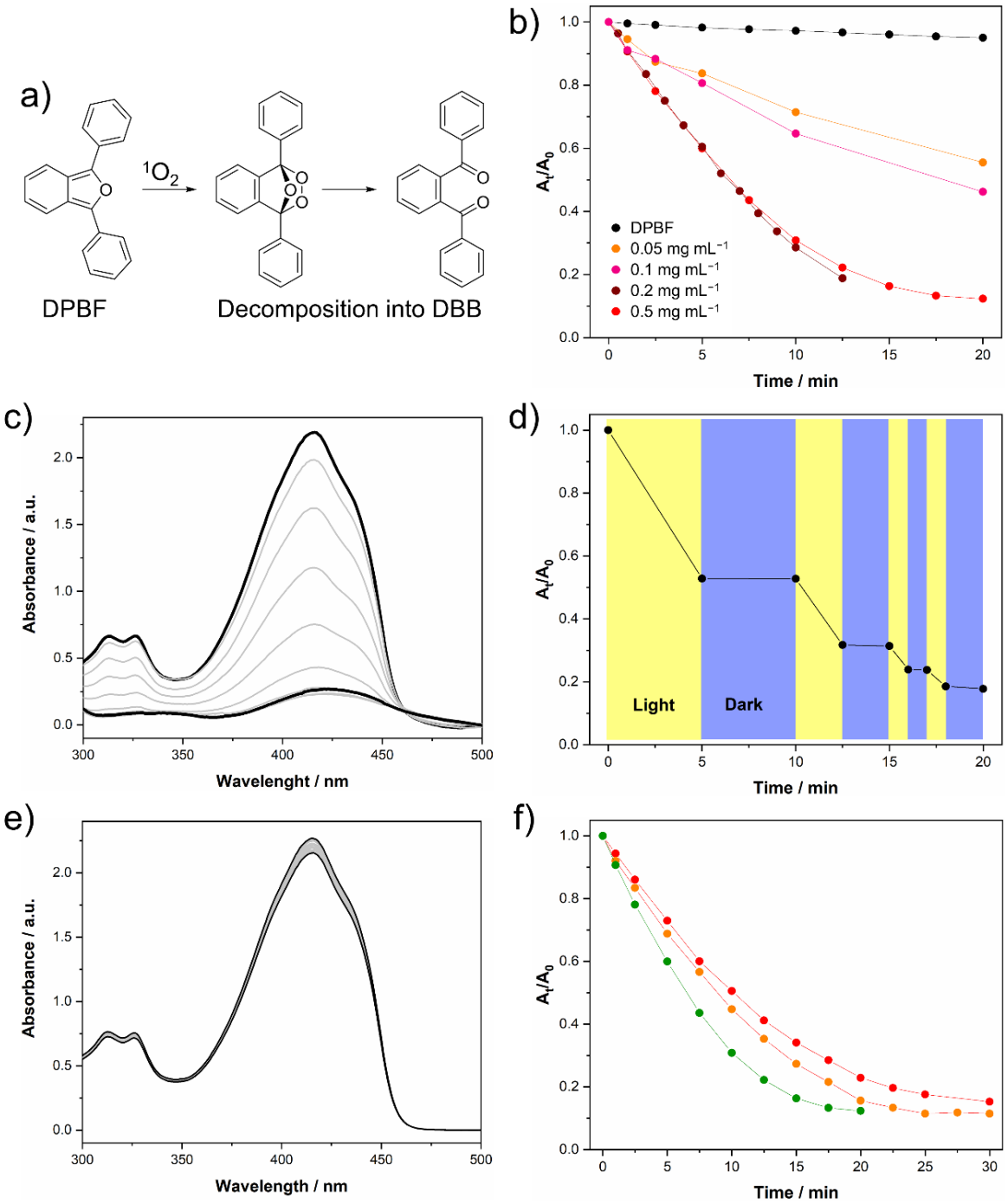

Figure 42. a) DPBF reaction with singlet oxygen and subsequent decomposition. b) Plots of A_t/A_0 at 415 nm of DPBF ($1 \cdot 10^{-4}$ M in DMF) versus irradiation time (green light: λ = 528 nm, intensity ~7 W) in the presence of different concentrations of **BDP-TFP-COF**. c) Absorption spectra of DPBF ($1 \cdot 10^{-4}$ M in DMF) over irradiation time (green light: λ = 528 nm, intensity ~7 W) in the presence of **BDP-TFP-COF** (0.2 mg mL^{-1}). d) Plots of A_t/A_0 at 415 nm of DPBF ($1 \cdot 10^{-4}$ M in DMF) versus irradiation time in the presence of **BDP-TFP-COF** (0.2 mg mL^{-1}) under different wavelengths irradiation (intensity ~7 W, green light: λ = 528 nm, amber light: λ = 590 nm, red light: λ = 617 nm). e) Absorption spectra of DPBF ($1 \cdot 10^{-4}$ M in DMF) over irradiation time (green light: λ = 528 nm, intensity ~7 W). f) Plots of A_t/A_0 at 415 nm of DPBF ($1 \cdot 10^{-4}$ M in DMF) versus irradiation time in the presence of **BDP-TFP-COF** (0.2 mg mL^{-1}) after light (yellow) and dark (blue) cycles (green light: λ = 528 nm, intensity ~7 W).

spectroscopy were carried out by monitoring the absorption maximum at 404 nm of a $1.5 \cdot 10^{-4}$ M ABDA solution in Millipore water under same conditions as for the previously

described DPBF experiments. As shown in Figure 43, the attenuation of the ABDA absorption upon irradiation with green LED light (~ 7 W, 528 nm) in the presence of **BDP-TFP-COF** confirms the formation of singlet oxygen. Again, a control experiment with a pristine ABDA solution under otherwise identical conditions showed no changes in absorbance, indicating the necessity of **BDP-TFP-COF** for the singlet oxygen generation.

In summary, we report a heavy atom-free and metal-free porous photosensitizer that absorbs light in a broad range of the visible spectrum and efficiently generates singlet oxygen whithout common disadvantages such as high toxicity or poor chemical stability.[322]

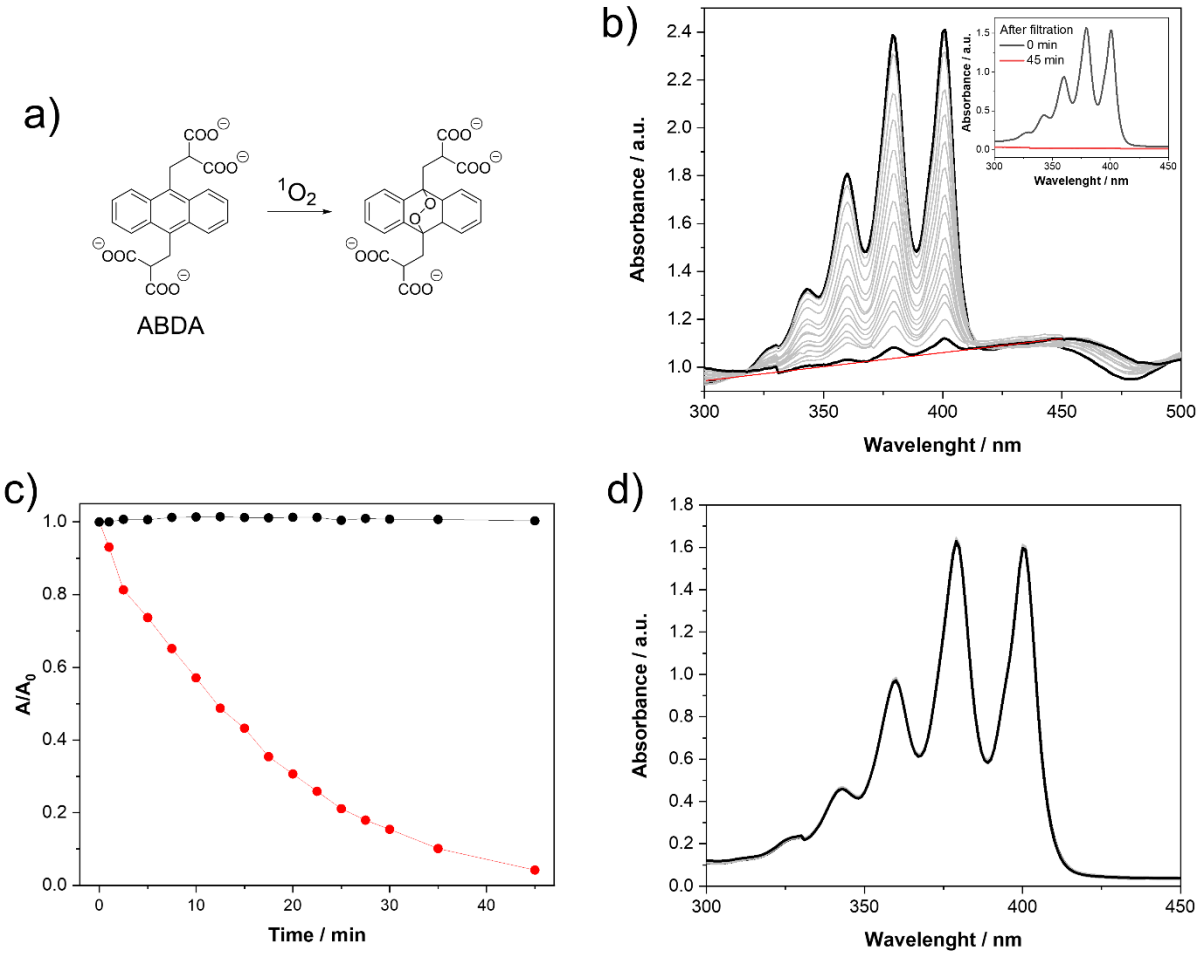

Figure 43. a) ABDA reaction with singlet oxygen. b) Absorption spectra of ABDA ($1.5 \cdot 10^{-4}$ M in H_2O) over irradiation time (green light: λ = 528 nm, intensity ~7 W) in the presence of **BDP-TFP-COF** (0.2 mg mL^{-1}). c) Plots of A_t/A_0 at 404 nm of ABDA ($1.5 \cdot 10^{-4}$ M in H_2O) versus irradiation time (green light: λ = 528 nm, intensity ~7 W) in the absence (Black) and presence (Red) of **BDP-TFP-COF** (0.2 mg mL^{-1}). d) Absorption spectra of ABDA ($1.5 \cdot 10^{-4}$ M in H_2O) over irradiation time (green light: λ = 528 nm, intensity ~7 W).

4.2.5 Photoconversion of a Mustard Gas Simulant

Bis(2-chloroethyl) sulfide (mustard gas or sulfur mustard) is a cytotoxic and blistering agent used in chemical warfare that is responsible of severe skin burns, eye damage and respiratory track injuries.[323] This agent was mass-produced during World War I and quickly became one of the most widely used chemical warfare weapons. Despite of the subsequent prohibition and innumerable efforts of the Chemical Weapon Convention to ban this agent, its use against soldiers and civilians in terrorist atacks is still suspected.[324-326] In addition, the sea-dumping of mustard gas has become a significant risk. Due to its viscosity and hydrophobicity, the mustard gas molecules tend to encapsulate and form lumps in water, possessing a serious hazard to both the ecosystem and marine workers.[327] In general, detoxification of chemical warfare weapons involves hydrolysis, pyrolysis or selective oxidation. However, the first two methods have intrinsic drawbacks, since pyrolisis could lead to incomplete incineration, thus generating a major hazard upon accidental exposure. Furthermore, mustard gas is not miscible enough with water to facilitate hydrolysis.[328] With singlet oxygen as a rather mild oxidant, the sulfide moiety can be selectively oxidized to the enviromentally benign sulfoxide without overoxidation to the sulfone, which is apparently as toxic as the sulfide.[329] Following this strategy, photosensitizing reticular materials such as microporous polymers,[330] porous organic polymers[308] and more abundantly metal organic frameworks[329, 331] have been recently exploited for detoxification.

After confirming singlet oxygen generation with **BDP-TFP-COF** in Chapter 4.2.4, detoxification of mustard gas was investigated for this material. Due to the extreme hazard of mustard gas and its obvious commercial unavailability, these experiments were instead performed using the mustard gas simulant 2-chloroethyl ethyl sulfide (CEES). The photoconversion experiments were carried out in microwave vessels that were capped with a rubber septum connected to an oxygen balloon and equipped with a magnetic stirrer. To a CEES (23.3 mL, 0.2 mmol) solution in MeOD (2 mL), **BDP-TFP-COF** (1 mol%, 3.3 mg) was added. Oxygen was bubbled through the mixture for five minutes. To avoid overheating of the solution during the irradiation time, the tube was inmersed in water (Figure S45). Under stirring, the sample was irradiated with white light at 230 mW cm^{-2} (Figure S46). The emerging oxidation of CEES was monitored by ^{1}H NMR spectroscopy for aliquotes taken from the reaction mixture at specific time intervals via syringe filter and calculation of the intensity ratio from integrals of the same protons in the educt and the product, e.g. H_a and $H_{a'}$. As shown in Figure 44, upon irradiation of CEES with white light in the presence of **BDP-TFP-COF**, proton signals corresponding to the oxidation product CEESO arose while the CEES signals attenuated. After 420 minutes of irradiation, the toxic CEES was almost completely vanished. Apparently, the

phototransformation to the non-toxic CEESO was fully completed and also no signals of the toxic overoxidized product $CEESO_2$ were observed, thus confirming the succesful detoxification. A detailed monitoring of the complete process is depicted in Figure S47. In comparison to other materials, longer conversion times are observed pressumably due to the lower singlet oxygen photogeneration rate in **BDP-TFP-COF**. This could be rationalized by the non-conjugated planar skeleton and the absence of heavy atoms.[308, 332-334] However, more systematic studies may be required in the future to establish a real comparison.

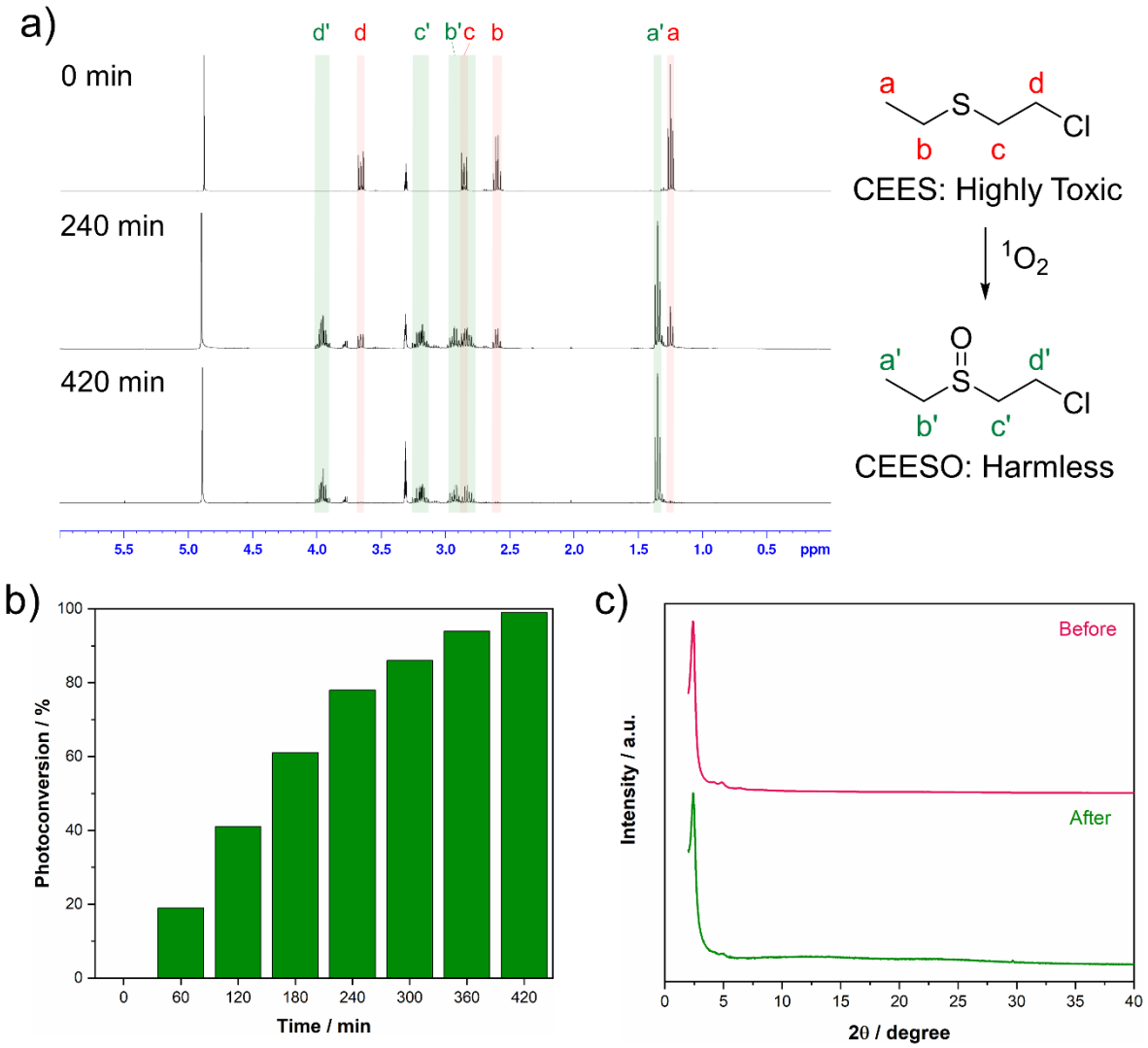

Figure 44. a) NMR spectra of CEES (0.1 M in MeOD) upon irradiation with white light (230 mW cm^{-2}) in the presence of **BDP-TFP-COF** (1% mol) at different reaction times; b) percentage of CEES photoconversion with time, and c) PXRD patterns of **BDP-TFP-COF** before and after the photoconversion in the CEES experiment.

Nevertheless, the photodetoxification process is achieved in the absence of metals or heavy atoms, thus avoiding additional toxicity or poor photo- and chemical stability.[322] Moreover, the use of a more powerful irradiation source might also boost the performance.[330] Remarkably, the highly *β*-ketoenamine linkages provide an enhanced robustness and the PXRD pattern for

the recovered **BDP-TFP-COF** in Figure 44c shows that the polymer retained its crystallinity after the experiments, indicating the stability and potential reusability of this heterogeneous photocatalyst. Future projects will focus on modifications of the BODIPY subunits for the enhancement of the photocatalytic activity.

4.2 Conclusions

In this chapter, we achieved the incorporation of BODIPYs within the backbone of a crystalline 2D COF. This material is among the first examples for a BODIPY-COF that is directly constructed from the dye and not via a post-synthetic incorporation, a process typically reduces both crystallinity and porosity. To the best of our knowledge, the eclipsed AA stacking mode in **BDP-TFP-COF** is unprecedented for BODIPY-COFs but offers larger open channels for a facile introduction and uptake of molecular guests. The characterization of **BDP-TFP-COF** revealed high crystallinity, chemical and thermal robustness, high surface area and pronounced absorption in the visible region. Regarding potential applications, this COF showed very high adsorption capacity for BPA and moderate adsorption of MB from water. Furthermore, trace amounts of MB in water could be detected via fluorescence quenching of colloidal **BDP-TFP-COF** suspensions. On the contrary, fluorescence enhancement was observed after selective deprotonation with triethylamine. This dual behaviour reveals that both quenching and enhancement of the emission can be achieved with **BDP-TFP-COF**, thus widening the scope for sensing applications. Generation of singlet oxygen in both organic solvents and water upon irradiation with visible light was confirmed, revealing the photosensitizing properties of this material. Therefore, **BDP-TFP-COF** was tested as a heterogeneous catalyst for the detoxification of a mustard gas simulant via selective photooxidation under visible light. Highly efficient end exclusive transformation to unharmful products was observed, while the COF remained intact and crystalline after the photoreaction. The unique combination of chemical robustness, high adsorption capacity and photooxidation properties even in the absence of heavy atoms renders **BDP-TFP-COF** as an excellent candidate for environmental remediation. Moreover, the molecularly precise implementation of the versatile BODIPY units could allow the fine-tuning of the skeleton via pre- or post-synthetic modifications. By varying the photophysical properties for tailored applications and enhanced performance, the horizon for the chemistry and applications of BODIPY-COFs is broadened.

Chapter 5: Synthesis and Characterization of a Low-Bandgap Diketopyrrolopyrrole-Pyrene Covalent Organic Framework

5.1 Introduction

DPP dyes are well-studied organic semiconductors with exceptional light harvesting properties due to their robust electron-deficient backbone comprising two fused lactam rings.[335, 336] After introducing thienyl or furyl groups at the 3- and 6-positions of the DPP core, the inherent planarity of these molecules is further enhanced by means of intramolecular hydrogen bonds between the substituents and the aromatic core. This coplanarity facilitates remarkable π–π stacking, thus promoting superior charge carrier mobility. In addition, the functionalization of the core with electron donating groups, such as phenyl or thienyl moieties, allows fine-tuning of the optoelectronic properties and motivates the implementation of DPPs into organic optoelectronic devices, e.g., organic field effect transistors or organic solar cells.[336, 337] After we reported the first example for a DPP-containing framework material in 2017,[198] a few more examples for DPP-COFs have been reported for potential applications in emergent fields such as solar-thermal water production,[338] electrical conductive materials[159] or electrocatalysis.[339]

Dynamic covalent cross-linking of DPP building blocks with other aromatic precursors is expected to give expanded π-systems with enhanced planarity, thus facilitating favorable interlayer interactions, optimized stacking, and higher crystallinity.[340] As an example, pyrene moieties have been incorporated within the backbone of COFs to provide materials with remarkable light absorption and semiconducting properties,[75, 341] which are highly appealing for optoelectronic applications.

The high tunability of the molecular precursors offers a wide range of feasible linkages between the individual subunits.[342] By selecting the adequate chemical linkage for the dynamic bond formation, e.g., C=C or C=N double bonds, infinite and fully conjugated 2D layers are envisioned that assemble chromophores or molecular semiconductors with high planarity and structural precision. In case of a suitable combination of both electron-donor and electron-acceptor building blocks, a highly demanded columnar array of segregated donor and acceptor stacks might be achieved.[343, 344] For such systems, the favorable combination of highly efficient *intra*- and *inter*molecular charge transfer pathways with pronounced light absorption in the visible and near infrared region generates promising materials for optoelectronics or solar

energy conversion.[148, 167, 345] In this chapter, the synthesis and characterization of a novel **DPP-Py-COF** comprising DPP and pyrene chromophores is presented. This semiconducting framework material is a promising candidate for optoelectronic applications with conceivably enhanced performance.

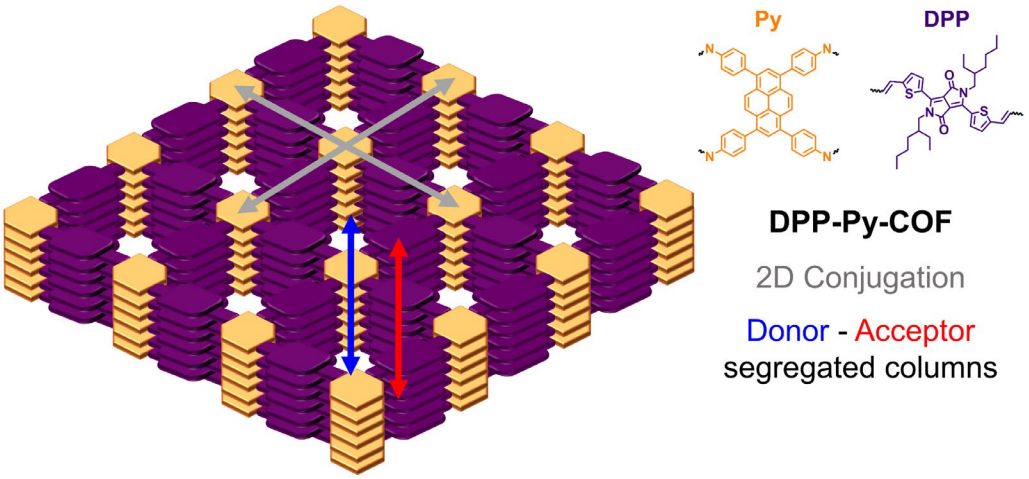

Figure 45. Schematic representation of **DPP-Py-COF** and charge carrier transport paths within the framework.

5.2 Results and Discussion

DPP-Py-COF was synthetized by the co-condensation of the literature-known linker 1,3,6,8-tetrakis(4-aminophenyl)pyrene (**Py(NH$_2$)$_4$**),[156] and diformylated DPP derivative **DPP-1**[198] in 1:2 ratio. In a sealed pressure tube under argon atmosphere, both components were dispersed in a 1:2 v:v mixture of 1,4-dioxane and mesitylene in presence of acetic acid as a catalyst. In a solvothermal reaction, the mixture was heated to 120 °C in an oven for seven days. The obtained precipitate was collected via filtration and unreacted monomers or small oligomers were washed out by Soxhlet extraction with anhydrous THF for 16 hours. The remaining solid was further purified by solvent exchange with acetone and pentane and dried under high vacuum for four hours to unclog the pores. **DPP-Py-COF** was obtained as a black powder in a high yield of 83%.

2D polymerization was achieved by reversible imine formation[39] between the amino and aldehyde groups of **Py(NH$_2$)$_4$** and **DPP-1**, respectively, (Figure 46a). However, it proved to be rather challenging to obtain crystalline phases for this COF. Presumably, the combination of pyrene molecules with DPP units bearing bulky 2-ethylhexyl substituents hampers the crystallization and efficient packing due to the increased steric repulsion between the side chains of adjacent DPP moieties.

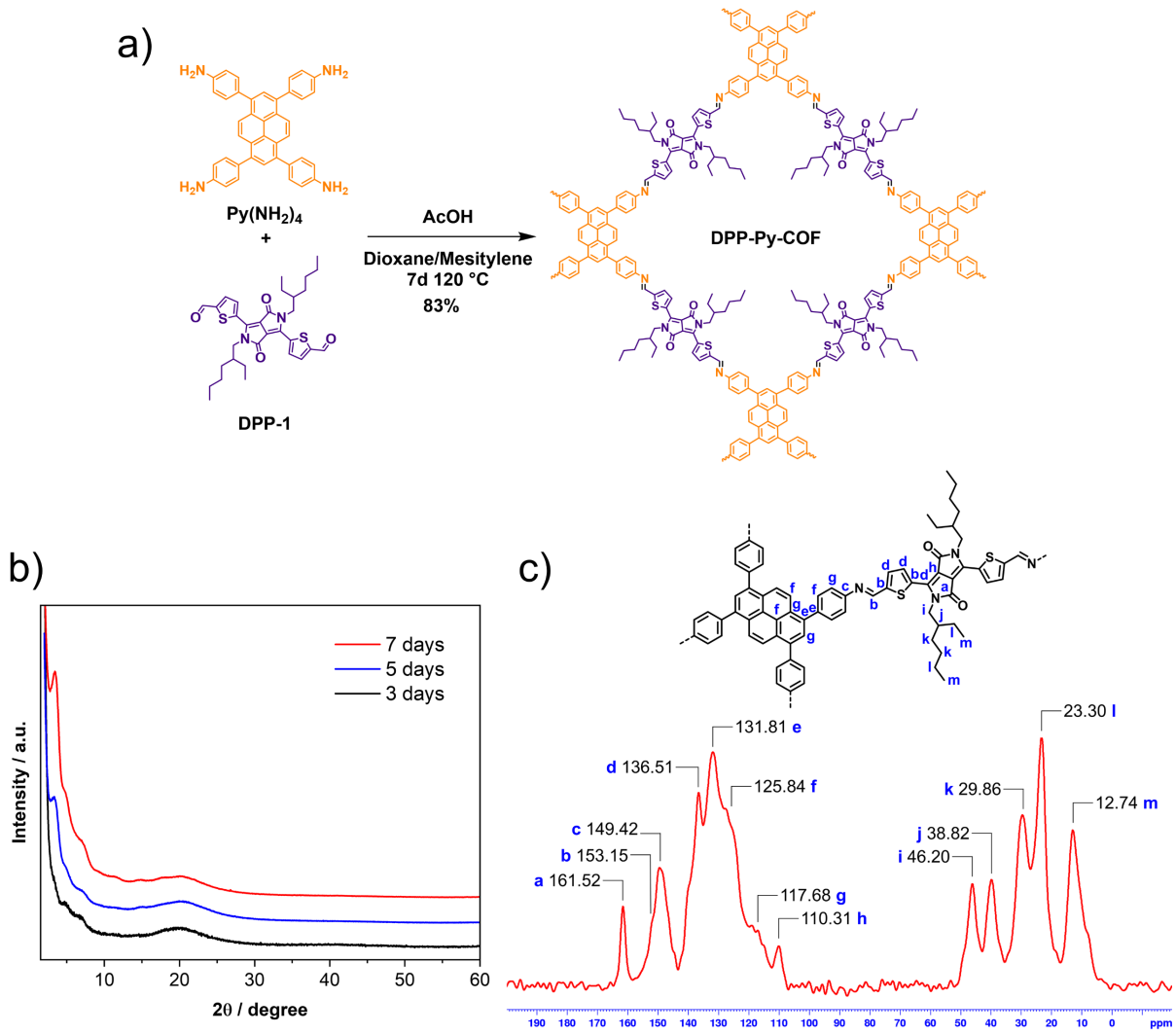

Figure 46. a) Synthesis of **DPP-Py-COF**; b) PXRD patterns of isolated precipitates after different reaction times and c) ^{13}C CP/MAS NMR of crystalline **DPP-Py-COF**.

Based on synthetic protocols for literature-known pyrene-containing COFs,[143, 167] several reaction conditions were screened for 1,4-dioxane/mesitylene solvent mixtures in varying ratios (Table S6). Initially, no reaction or only amorphous products in low yields (~15−20%) were observed for low monomer concentrations. After optimization, 1:2 dioxane/mesitylene mixtures and higher concentrations of building blocks (0.02 mmol mL^{-1} for $Py(NH_2)_4$ and 0.04 mmol mL^{-1} for **DPP-1**) were found beneficial for the crystallization of **DPP-Py-COF**. After a reaction time of three days, a black precipitate was obtained showing only minor crystallinity (Figure 46b). Based on those encouraging results, longer reaction times of up to seven days finally resulted in the isolation of a crystalline COF (Figure 46b). Interestingly, even slight deviations from these conditions, e.g., longer reaction times or higher temperatures, again yielded amorphous polymers or COFs with only minor crystallinity. The isolated solid material was characterized by several analytical techniques. The FT-IR spectrum of **DPP-Py-COF** revealed the disappearance of the C=O band from the aldehyde groups of **DPP-1** centered at

1649 cm^{-1}, as well as the N-H stretching bands of primary amine moieties of **Py(NH$_2$)$_4$** at 3340 and 3212 cm^{-1}. Otherwise, the simultaneous arising of a new band at 1575 cm^{-1} for the C=N stretching mode of the imine bonds in **DPP-Py-COF** indicated facile polymerization (Figure S50). ^{13}C CP/MAS NMR measurements also proved the incorporation of the DPP dyes into the polymer backbone (Figure 46c). The signal at 161.25 ppm can be assigned to the carbon atom of the ketone moiety present in the DPPs, while the carbon atoms from the imine linkage and the thiophene substituents of the DPP correspond to the broad signal centered at 149.2 ppm. The region between 110 and 144 ppm is attributed to the sp^2 carbon atoms of the aromatic cores of the pyrene and DPP subunits in **DPP-Py-COF**. Signals in the aliphatic region between 50 and 10 ppm correspond to the sp^3 carbon atoms of the 2-ethylhexyl side chains of the DPP moieties. The crystallinity and structure of the framework was analyzed by PXRD. Major reflections were found at 2θ angles of 3.5°, 4.9°, 7.1° and 20.3°, which correspond to the 110, 020, 220 and 001 planes, respectively (For a better visualization, the background from the primary beam is removed from the experimental PXRD data in Figure 47a). This diffraction

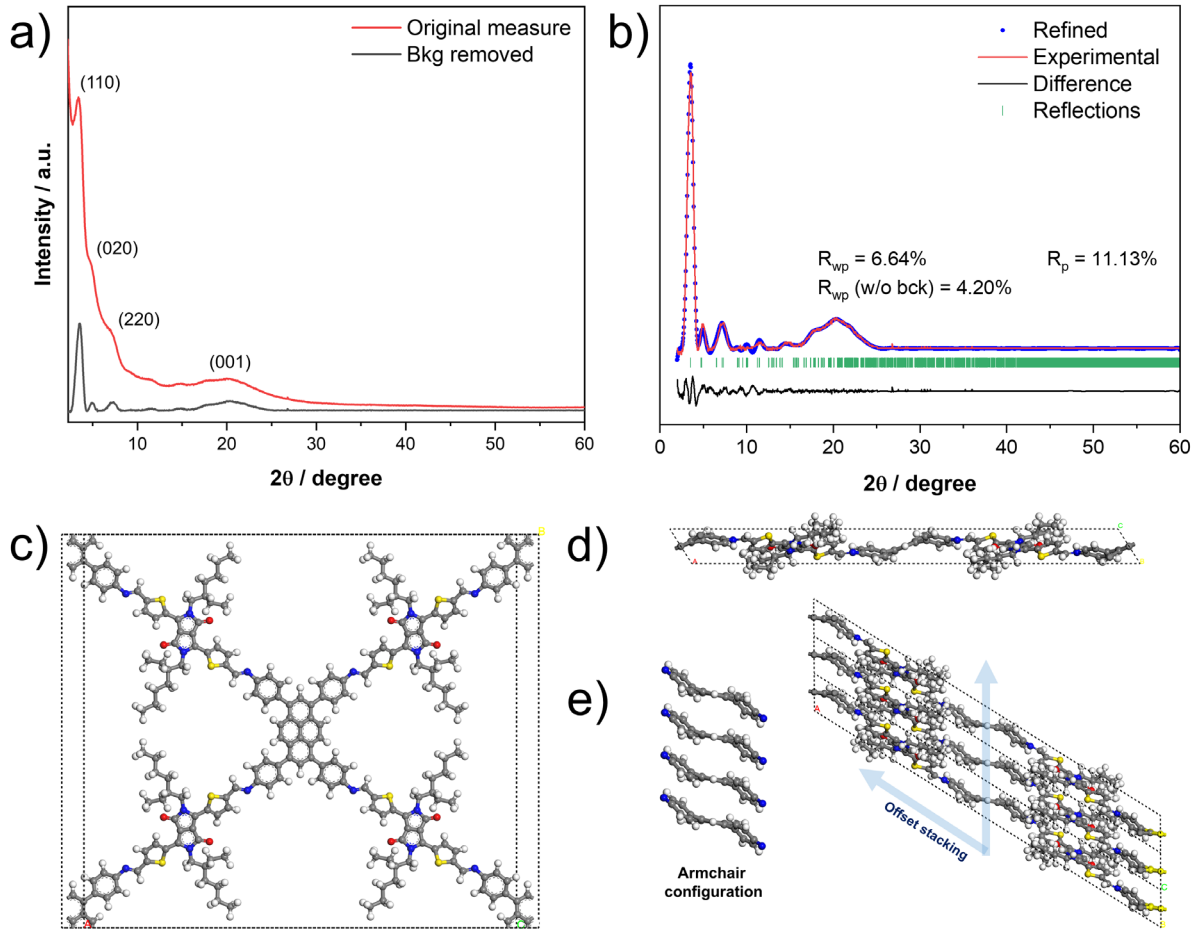

Figure 47. a) Experimental PXRD pattern with hkl indices, b) Pawley refinement and view along the c) a and d) c axis for the refined structure of **DPP-Py-COF**; e) armchair configuration of the pyrene moieties and their offset stacking within the COF structure.

pattern is in good agreement with a simulated model in the monoclinic *C2/m* space group with eclipsed AA-type stacking in *sql* topology (Figure S51). The lattice parameters obtained after Pawley refinement of the experimental diffraction pattern were $a = 48.69 \pm 0.27$ Å, $b = 42.07 \pm 0.20$ Å and $c = 4.45 \pm 0.024$ Å with angles of $\alpha = \beta = 90°$ and $\gamma = 57.67 \pm 0.15$ ° and refinement parameters of $R_{wp} = 4.20\%$ and $R_p = 11.24\%$. The larger distance of 4.4 Å between individual layers might originate from steric repulsion between the bulky side chains of the DPP units. For a proper stacking of the phenyl substituents, the tetraphenyl pyrene subunits adopt an 'armchair' configuration, in which the faces of the phenyl groups are oriented towards the same direction (Figure 47e). This conformation is necessary to achieve an optimal edge-on-face orientation between the phenylene moieties and ensure a coplanar orientation between adjacent pyrenes.[143] Therefore, the pyrene cores exhibit an offset stacking as compared to the layer extension in the c axis (Figure 47e). Additionally, the distances between the phenyl moieties are ~ 3.5 Å, which fits in the typical range of π–π stacking (Figure S52). SEM images of **DPP-Py-COF** revealed a sheet-like morphology with large domains in the size of several μm (Figure 48a-c). Interestingly, for some of the nanosheet domains (see Figure 48b as an example), one side of the sheet shows a well-defined and smooth surface, while the opposite side comprises a group of spherical particles. The coexistence of nanosheets and smaller spherical nanoparticles might suggest the stepwise formation of these laminar structures after aggregation of the nucleated particles into larger and well-defined structures.[346] To confirm the existence of these nucleation mechanism and to have a deeper overview of the laminar domains growth, future investigation would require time dependant SEM experiments. EDX spectroscopy for **DPP-Py-COF** revealed an atomic composition of C, O, N and S, indicating the incorporation of the DPP dye within the COF structure. Nitrogen physisorption measurements after the thermal activation of the material revealed a type III isotherm, typically obtained for non-porous materials,[347] with a very low BET surface of 41 $m^2\ g^{-1}$ (Figure S53). This lack of porosity is caused by the moderate crystallinity of the material in combination with the blockage of the pores by the sterically demanding side chains of the DPP subunits. A similarly low porosity was observed for **DPP-TAPP-COF** ($S_{BET} = 139\ m^2\ g^{-1}$),[198] which also consisted of the **DPP-1** monomer. In contrast, other examples incorporating pyrene and less bulky DPP derivatives showed higher surface areas ($S_{BET} = 1193\ m^2\ g^{-1}$).[198, 339] Absorption spectra for **DPP-Py-COF** were obtained

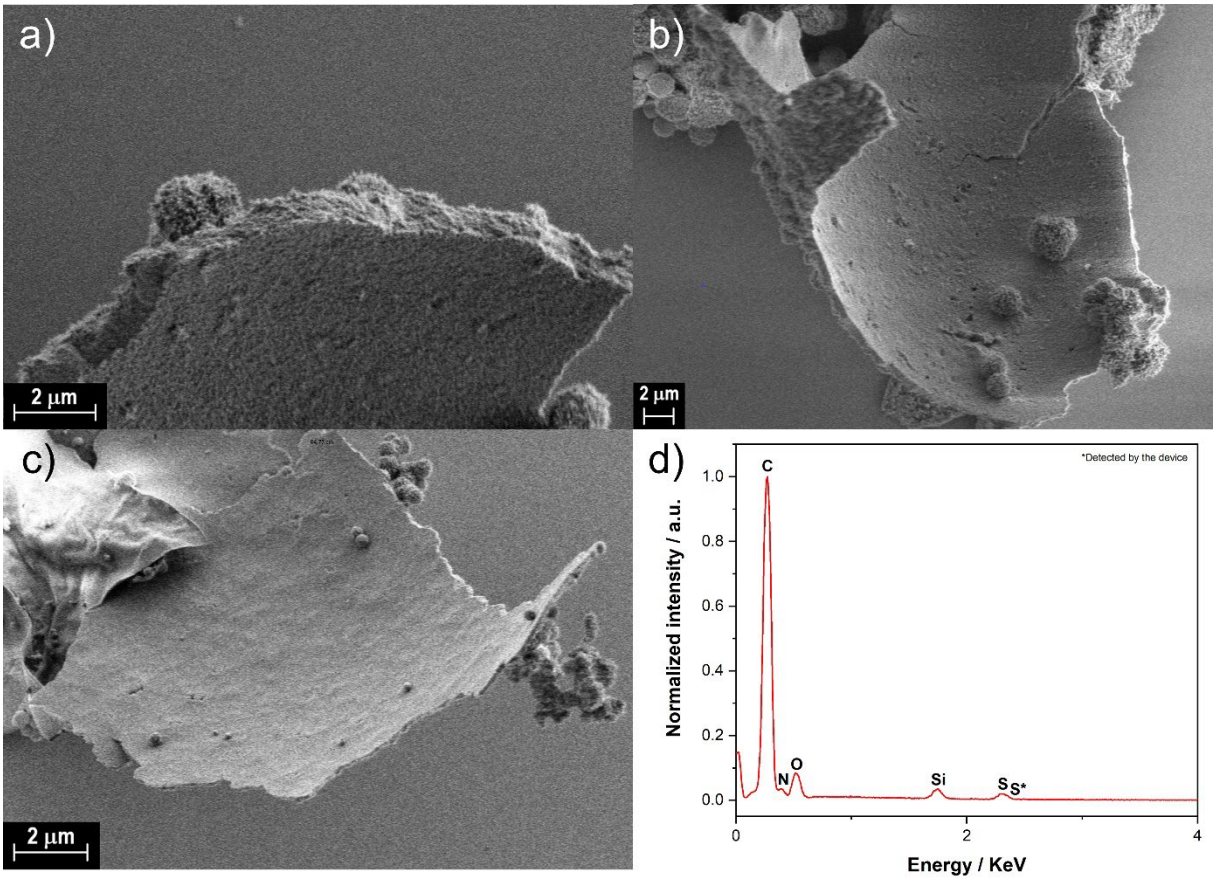

Figure 48. a), b) and c) SEM images and d) EDX spectrum of **DPP-Py-COF**. The pronounced Si peak can be assigned to the SiOx substrate.

after analyzing diffuse reflectance measurements with the Kubelka-Munk function. **DPP-Py-COF** absorption covers the whole visible light range and even extends into the NIR region up to almost 1000 nm (Figure 49a). This panchromatic absorption could be attributed to the formation of extended J-aggregates due to the offset stacking between the planar and fully conjugated donor-acceptor layers,[148] in which the DPP cores act as acceptor units[348, 349] while the thiophene substituents and the amine moieties of the pyrenes serve as the donor part. The absorption spectrum (Figure 49a) showed a maximum at 706 nm and a direct optical bandgap of 1.53 eV was estimated from the Tauc plot (Figure 49b), revealing strong intra- and interlayer charge transfer. This low bandgap is in the same range as state-of-the-art semiconducting polymers[350] with values typically between 0.6–1.5 eV, suggesting potential applications in optoelectronic devices.[123]

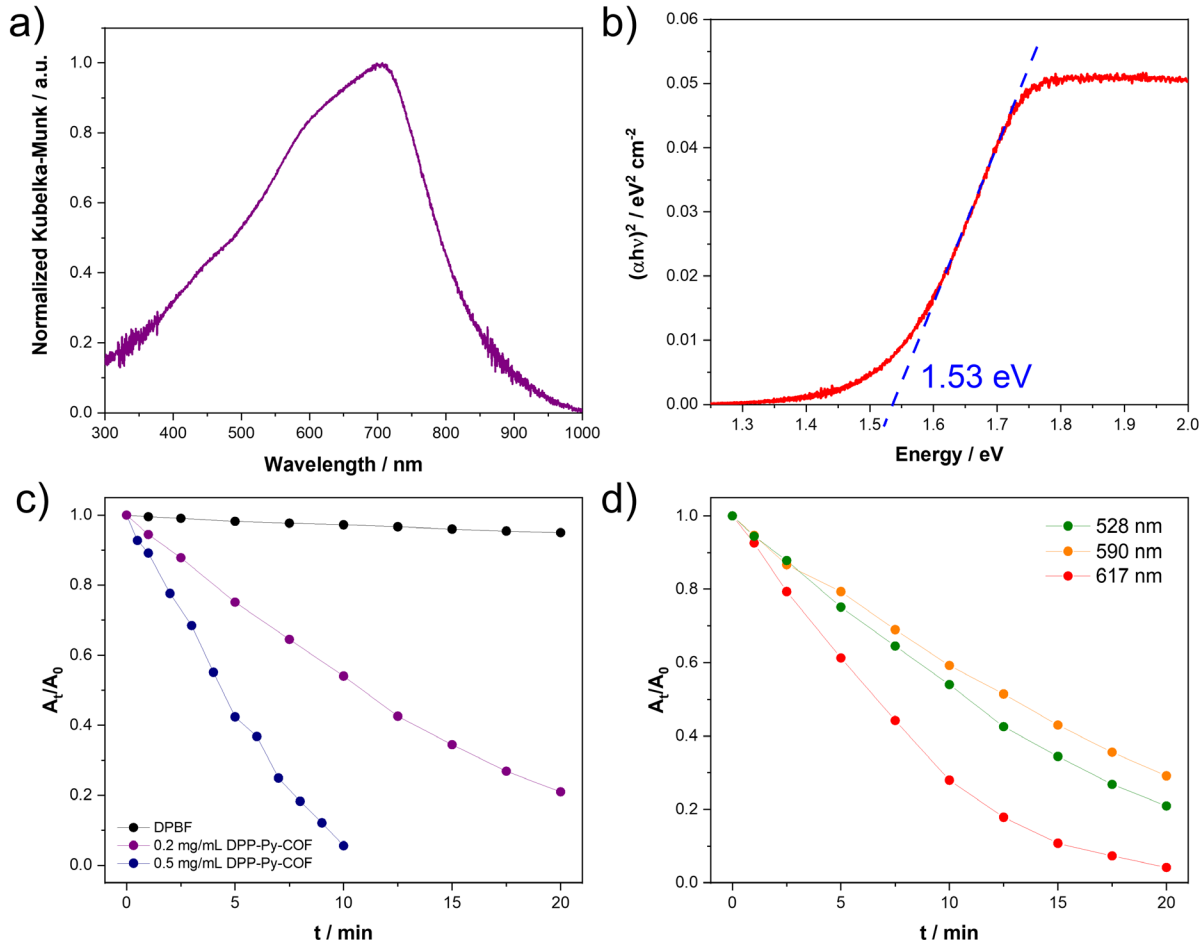

Figure 49. a) UV/Vis absorption spectra derived from diffuse reflectance measurements with the Kubelka–Munk function and b) Tauc plot of **DPP-Py-COF**. The intersection of the slope (blue) with the ordinate axis indicates a direct optical band gap of 1.53 eV; c) plots of A_t/A_0 at 415 nm of DPBF ($1 \cdot 10^{-4}$ M in DMF) versus irradiation time (green light: λ = 528 nm, intensity ~7 W) in the presence of varying amounts of **DPP-Py-COF**; d) plots of A_t/A_0 at 415 nm of DPBF ($1 \cdot 10^{-4}$ M in DMF) versus irradiation time in the presence of **DPP-Py-COF** (0.2 mg mL^{-1}) under irradiation at different wavelengths (intensity ~7 W, green light: λ = 528 nm, amber light: λ = 590 nm, red light: λ = 617 nm).

Remaining challenges for **DPP-Py-COF** encompass further optimization of the crystallinity in order to achieve more ordered and extended arrangements of the chromophores. Moreover, future implementation of this COF in optoelectronic devices will require the preparation of highly ordered COF layers with a few nm thickness (5−10 nm). Hence, future research have to address the exploration of **DPP-Py-COF** exfoliation or thin films growth methods.[351]

To probe the potential of **DPP-Py-COF** as a solid-state photosensitizer, singlet oxygen generation was analyzed by monitoring the absorption maximum of DPBF at 415 nm upon irradiation of a **DPP-Py-COF** suspension with LED light. As shown in Figure 49c, efficient generation of singlet oxygen is observed after irradiation of a DPBF solution ($1 \cdot 10^{-4}$ M in DMF) in presence of varying amounts of **DPP-Py-COF** with green LED light (~7 W, 528 nm). The strong attenuation of the DPBF absorption band revealed the excellent photosensitizing ability of **DPP-Py-COF**, as full decomposition of DPBF was obtained already after ten minutes at

0.5 mg mL^{-1} COF concentration. In a control experiment, the DPBF solution was irradiated in the absence of **DPP-Py-COF** under otherwise identical conditions and only negligible changes of the absorbance were obtained, thus evidencing that **DPP-Py-COF** is indeed essential for the generation of this reactive oxygen species. Figure 49d shows the rates for singlet oxygen generation with LED light sources at different emission wavelengths and a fixed COF concentration of 0.2 mg mL^{-1}. Apparently, the best performance is achieved with red light (~7 W, 617 nm), which is most likely explained by a better match of the LED emission with the absorption maximum of **DPP-Py-COF**. For other LEDs with either green (~7 W, 528 nm) or amber (~7 W, 590 nm) emission, lower rates of singlet oxygen generation were observed (Figure S55). Based on these observations, further research using **DPP-Py-COF** as a photosensitizer under red light or even in the NIR is highly appealing. For instance, the use of low-energy light sources and the skin penetration ability of the NIR radiation envisions novel COF materials for photodynamic therapy.[304]

5.3 Conclusions

The dye-containing **DPP-Py-COF** was synthesized by reversible imine condensations between DPP and pyrene building blocks. Despite the introduction of crystallinity-challenging building blocks, a polymeric structure with decent crystallinity and full π−conjugation was obtained. **DPP-Py-COF** showed a remarkably low optical bandgap and a pronounced light absorption in the whole visible region, which even extends to the NIR. Moreover, the columnar stacking of nanosegregated donor and acceptor arrays may result in efficient photoconductivity, thus suggesting promising applications in optoelectronic devices. In addition, **DPP-Py-COF** proved to be a highly efficient photosensitizer without any heavy atoms or metals. These exciting properties encourage further investigations regarding photocatalytic applications or photodynamic therapy.

Chapter 6: Summary and Conclusions

Research on state-of-the-art porous materials has fuelled the development of COFs as robust, lightweight, highly ordered and versatile organic materials. The utilization of DCC is crucial for the construction of highly crystalline networks capable of self-healing structural defects (**Chapter 2.2**) and several synthetic strategies have been established for a facile formation of well-defined crystallites (**Chapter 2.3**). Furthermore, a detailed understanding of the various reactions utilized for the covalent connection of organic building blocks (**Chapter 2.4**) and the different topologies derived after cross-linking (**Chapter 2.5**) is fundamental for the development of a broad selection of materials for targeted applications. Due to their tuneable and extended structures, COFs offer an excellent platform for the incorporation of functional molecules in a well-arranged and spatially precise manner. In particular, the synthesis of dye-based COFs as semiconducting and light-absorbing materials is exploited for the construction of optoelectronic devices and for selected applications in photocatalysis, photodynamic therapy, sensing, light harvesting, or photoconduction (**Chapter 2.6**).

In this Thesis, the incorporation of chromophores within the rigid skeletons of COFs has been addressed. Based on previous investigations on **DPP-TAPP-COF**, structural modifications at the building blocks were intended to induce and study changes in the aggregation and optical properties of the dye-based crystalline polymers. In the first project, the synthesis of **FeO@DPP-TAPP-COF** composites and detailed investigations on the impact of the nanoparticle amount on the crystallinity and optical properties of the hybrid materials have been realized (**Chapter 3**). In the second project, a BODIPY-containing **BDP-TFP-COF** was synthesized. Full characterization of this dye-based material and further experiments on the scope for potential applications have been performed (**Chapter 4**). In the third project, the TAPP linkers of the previously reported **DPP-TAPP-COF** were substituted by a tetrasubstituted pyrene core to yield the novel donor-acceptor **DPP-Py-COF**. The optical and photosensitizing properties of this material have been studied (**Chapter 5**).

In **Chapter 3**, two series of organic-inorganic composites **NH_2-FeO@DPP-TAPP-COF** (short: Nx) and **COOH-FeO@DPP-TAPP-COF** (short: Cx) have been synthesized via the direct growth of **DPP-TAPP-COF** at the surface of superparamagnetic iron oxide nanoparticles. The hybrid materials have been synthesized by co-condensation of the **TAPP** and **DPP-1** building blocks via solvothermal synthesis in the presence of the amino- or carboxy-functionalized nanoparticles, **NH_2-FeO** for Nx series or **COOH-FeO** for Cx series. The

presence of the nanoparticles was initially confirmed by FT-IR and EDX spectroscopy and the composition was further quantified by VSM measurements. A detailed morphological analysis was performed by electron microscopy techniques, which revealed a homogeneous dispersion of the inorganic nanoparticles within the organic matrix. As the cross-linking between oligomeric COF seeds and inorganic nanoparticles increases with the nanoparticle concentration, a detriment in the COF crystallinity has been observed in the PXRD. Interestingly, the Cx composites gave higher yields and larger crystalline COF domains, which was attributed to the more favourable growth of ordered networks initiated by the stacked **TAPP** moieties directly linked to **COOH-FeO** nanoparticles. Here, the feasibility of the structural control for these hybrid materials was demonstrated. The optical properties of the composites were analyzed by DRS. A transition from one broad panchromatic absorption band into the individual bands of the monomers was observed with increasing **FeO** concentration in both series, revealing the influence of the nanoparticle seeds on the chromophore stacking and the dependent optical properties. Strikingly, for the less crystalline phases, the relative ratio between the Soret and last Q band of the **TAPP** moieties directly correlated with the nanoparticle content. The obtained linear regressions could be used to estimate the mass fraction of **FeO** domains within the organic matrix directly from absorption data.

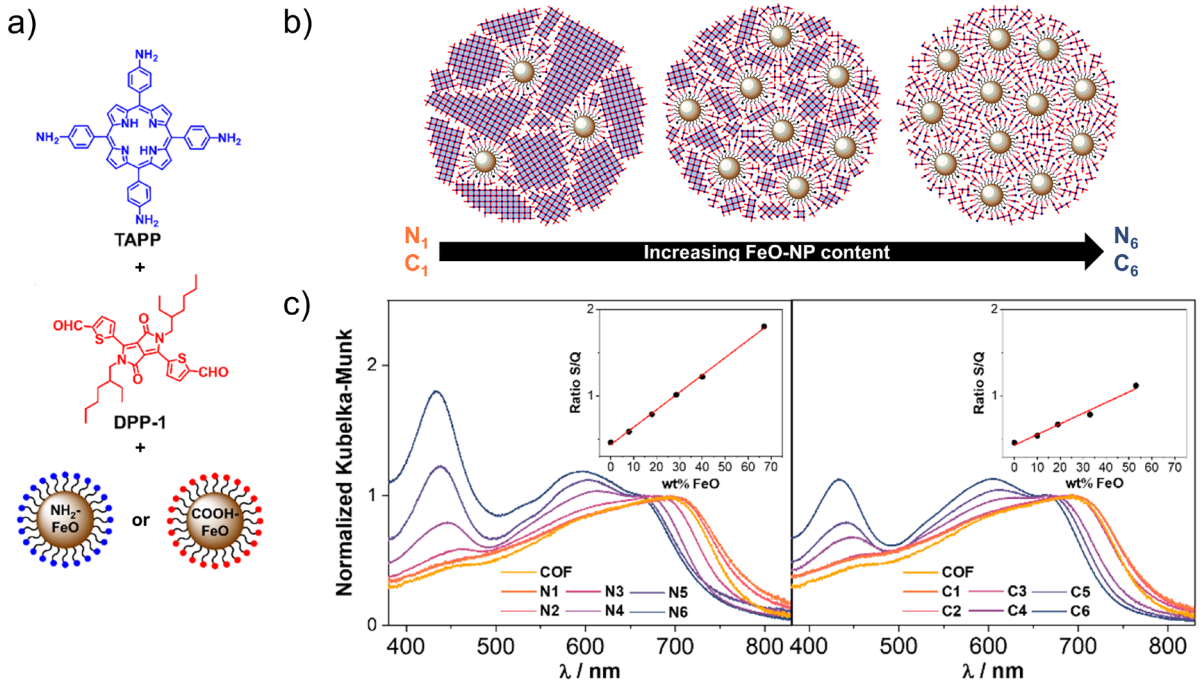

Figure 50. a) Individual components of **FeO@DPP-TAPP-COF** composites. b) Schematic representation of the composites with different concentrations of nanoparticles. c) UV-Vis absorption spectra derived from diffuse reflectance measurements with the Kubelka-Munk function for **N1–6** and **C1–6** composites series (normalized to the local absorption maximum with highest wave length, insets show the linear relationship between the Soret/Q band intensity ratio and the mass fraction of **FeO** particles).

The goal of incorporating BODIPY units into the structural backbone of COFs has been addressed in **Chapter 4**. Motivated by the chemical robustness and enhanced planarity of the BODIPYs and the intriguing optical properties, these dyes were directly implemented into a COF skeleton. The co-condensation of **TFP** and **BDP(NH$_2$)** in presence of acetic acid yielded **BDP-TFP-COF** as a robust *β*-ketoenamine linked 2D COF with *hcb* topology. The presence of BODIPY moieties was unequivocally confirmed by NMR and EDX spectroscopy. PXRD measurements revealed the highly crystalline nature of this COF, as well as the chemical robustness of the organic backbone. The optical properties of the polymer were revealed by DRS, which indicated a panchromatic absorption with a maximum at 575 nm.

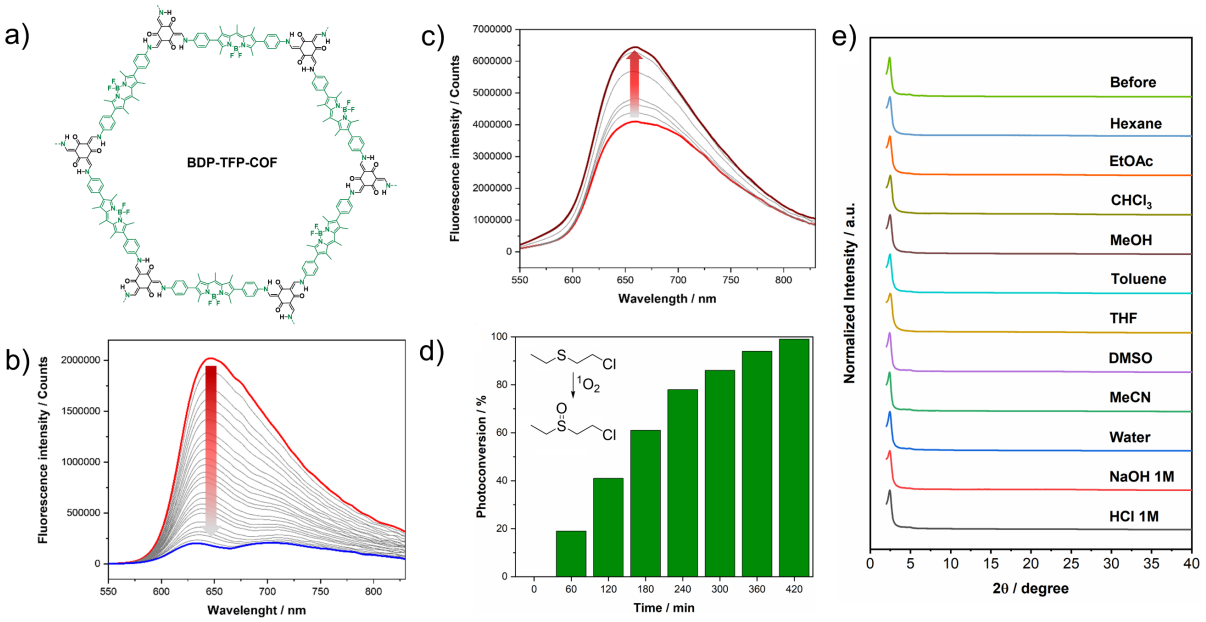

Figure 51. a) Chemical structure of **BDP-TFP-COF**. b) Fluorescence spectral changes of **BDP-TFP-COF** (0.1 mg mL^{-1} in water, λ_{exc} = 420 nm, red curve) with increasing amounts of MB (25 mg L^{-1} in water, gray and blue curves). c) Fluorescence spectral changes of **BDP-TFP-COF** (0.1 mg mL^{-1} in THF, λ_{exc} = 365 nm, red curve) with increasing amounts of TEA (gray and dark red curves). d) Percentage of CEES (0.1 M in MeOD) photoconversion with the time upon irradiation with white light (230 mW cm^{-2}) in presence of **BDP-TFP-COF** (1% mol). e) PXRD pattern of **BDP-TFP-COF** before and after being immersed for 24 h in different solvents.

Adsorption experiments from aqueous solutions were performed with model pollutants BPA and MB, taking advantage of the porous nature and robust structure of the polymer. **BDP-TFP-COF** showed very high uptake of BPA (425.53 mg g^{-1}) and moderate uptake of MB (96.06 mg g^{-1}) from aqueous media. It was assumed that the adsorption was facilitated by the hydrophobic environment in the pores due to the accumulation of F atoms in combination with intermolecular *CH*–π and π–π interactions. Furthermore, the exfoliation of the laminated **BDP-TFP-COF** impeded the ACQ phenomenon present in the bulk phase to yield red-emitting dispersions with a emission maximum centred at 646 nm. This emission was quenched upon introduction of MB aliquotes, which is presumably triggered by an energy transfer from the

BODIPY moieties of the COF host to the MB guests. Remarkably, the addition of TEA to a dispersion of **BDP-TFP-COF** in THF provoked an emission enhancement, which is presumably triggered by an impediment of the PET after the selective deprotonation of the NH groups at the *β*-ketoenamine linkages. This fluorescent double behaviour implies a great potential for **BDP-TFP-COF** as a dual mode fluorescent sensor. In addition, **BDP-TFP-COF** demonstrated photosensitizing properties upon irradiation with visible light, hence generating singlet oxygen. This phenomenon was confirmed by monitoring the photobleaching of DPBF in DMF or ABDA in water by UV-VIS experiments. Motivated by this finding, we applied this ROS generation for the photodetoxification of a mustard gas simulant upon irradiation with visible light. The selective oxidation of the toxic CEES species into unharmful CEESO while avoiding the overoxidation into harmful $CEESO_2$ was demonstrated. As confirmed by PXRD, **BDP-TFP-COF** maintained its structural integrity during this process, hence again demonstrating the robustness of the material and the high potential as a recyclable and metal-free photosensitizer.

Chapter 5 compiles the synthesis and characterization of the novel DPP-containing **DPP-Py-COF**. A solid material with moderate crystallinity was obtained via solvothermal synthesis upon co-condensation of **DPP-1** and **Py(NH₂)₄** building blocks. The dye-based structure was confirmed by FT-IR, NMR and EDX spectroscopy techniques. Structural refinement of the PXRD data using the Materials Studio Software indicated an offset layer stacking, which was already reported for other pyrene-based COFs. Here, the pyrene units adopt an armchair configuration to promote optimal stacking among aromatic cores. This conformation induces a slip between adjacent layers, which is amplified by the incorporation of bulky alkyl substituents at the complementary DPP building blocks. These structural peculiarities jeopardized the porous nature of the material, resulting in a poor S_{BET} value of just 41 $m^2\ g^{-1}$ and a type III nitrogen physisorption isotherm typical for non-porous materials.

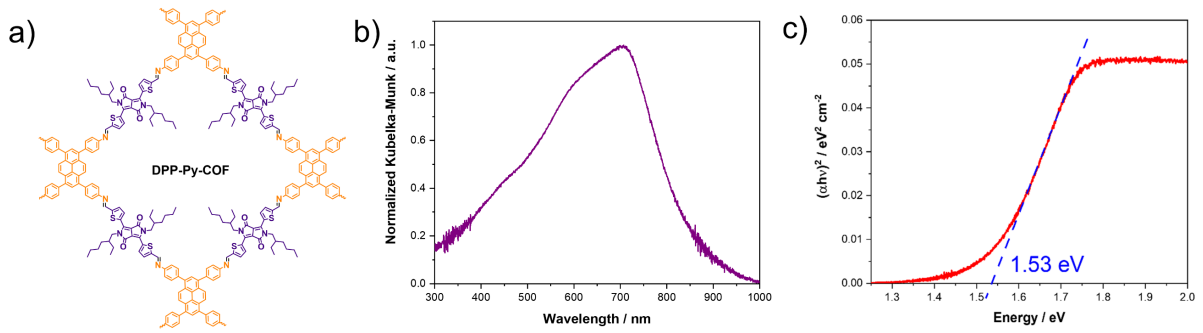

Figure 52. Chemical structure of **DPP-Py-COF**. b) UV-Vis absorption spectra derived from diffuse reflectance measurements with the Kubelka–Munk function for the solid sample and c) Tauc plot.

DRS for **DPP-Py-COF** showed a panchromatic absorption that is efficiently extended into the NIR region up to 1000 nm with a maximum centred at 706 nm. This red-shift was attributed to the extended intralayer conjugation and the efficient dye stacking among D−A layers. A Tauc plot revealed an optical bandgap of 1.53 eV, thus indicating the high potential of this COF as a semiconducting and light harvesting material. In addition, **DPP-Py-COF** showed photosensitizing properties, as confirmed by singlet oxygen generation experiments monitored by UV-VIS measurements.

In conclusion, the construction of COFs containing organic dyes enables the formation of chromophoric polymers with enhanced light harvesting properties at longer wavelengths, reaching the NIR region. In addition, the well-ordered structure comprised of donor and acceptor moieties in segregated columnar stacks is an appealing structural feature that encourages the future implementation of these materials into optoelectronic devices. One key aspect affecting the optical and semiconducting properties is the degree of stacking between the individual chromophores. In this regard, we demonstrated that these properties can be tuned upon structural changes triggered by incorporation of varying amounts of FeO nanoparticles among the COF domains. Furthermore, the aggregation and interaction between the dyes can be tuned by the adequate choice of complementary monomeric subunits, thus resulting in enhanced light harvesting and lower optical bandgaps. By incorporating functional dyes with different physicochemical properties and linkages, novel COFs for specific applications are envisaged. We demonstrated that BODIPY dyes provide new and appealing alternatives for the construction of robust and strongly absorbing COFs with potential applications in environmental remediation, sensing or photocatalysis. Finally, we want to remark the chemical versatility of these dyes for the construction of crystalline polymers with tuneable structures. We envisage that tailor-made variations at the BODIPY subunits, either via pre- or post-synthetic modifications, will offer intriguing strategies for the future development of innovative and high performance functional porous materials.

Chapter 7: Zusammenfassung und Fazit

Die Forschung an modernen porösen Materialien hat die Entwicklung von COFs als robuste, leichtgewichtige, hochgeordnete und vielseitig einsetzbare organische Materialien vorangetrieben. Der Einsatz von DCC ist entscheidend für den Aufbau hochkristalliner Netzwerke, die in der Lage sind, strukturelle Defekte selbst zu heilen (**Kapitel 2.2**). Für die einfache Bildung wohldefinierter Kristallite wurden verschiedene synthetische Strategien entwickelt (**Kapitel 2.3**). Darüber hinaus ist ein detailliertes Verständnis über die verschiedenen Reaktionen, die für die kovalente Verknüpfung organischer Bausteine eingesetzt werden (**Kapitel 2.4**), und der verschiedenen Topologien, die sich nach der Vernetzung ergeben (**Kapitel 2.5**), von grundlegender Bedeutung für die Entwicklung einer breiten Auswahl von Materialien für gezielte Anwendungen. Aufgrund der abstimmbaren und ausgedehnten Strukturen stellen COFs eine vielseitige Plattform für den Einbau funktioneller Moleküle mit hoher räumlicher Präzision zur Verfügung. Insbesondere die Synthese von farbstoffbasierten COFs als halbleitende und lichtabsorbierende Materialien wird für die Konstruktion optoelektronischer Bauelemente und für ausgewählte Anwendungen in der Photokatalyse, der photodynamischen Therapie, der Sensorik, zum Lichtsammeln oder der Photoleitfähigkeit genutzt (**Kapitel 2.6**).

Ziel dieser Doktorarbeit war der Einbau von Chromophoren in das starre Gerüst von COFs. Ausgehend von früheren Untersuchungen an **DPP-TAPP-COF** sollten durch strukturelle Modifikationen an den Bausteinen gezielte Veränderungen in den Aggregations- und optischen Eigenschaften der farbstoffbasierten kristallinen Polymere hervorgerufen und untersucht werden. Im ersten Projekt wurden die Synthese von **FeO@DPP-TAPP-COF**-Kompositen und detaillierte Untersuchungen zum Einfluss des Nanopartikelanteils auf die Kristallinität und die optischen Eigenschaften der Hybridmaterialien durchgeführt (**Kapitel 3**). Im zweiten Projekt wurde ein BODIPY-haltiges **BDP-TFP-COF** synthetisiert. Dieses farbstoffbasierte Material wurde umfassend charakterisiert und weitere Experimente zu möglichen Anwendungen wurden durchgeführt (**Kapitel 4**). Im dritten Projekt wurden die **TAPP**-Bausteine im bereits bekannten **DPP-TAPP-COF** durch eine tetrasubstituierte Pyren-Einheit ersetzt, um ein Donor-Akzeptor-Netzwerk **DPP-Py-COF** zu erhalten. Die optischen und photosensibilisierenden Eigenschaften dieses Materials wurden untersucht (**Kapitel 5**).

In **Kapitel 3** wurden zwei Serien von organisch-anorganischen Kompositen **NH_2-FeO@DPP-TAPP-COF** (kurz: Nx) und **COOH-FeO@DPP-TAPP-COF** (kurz: Cx) durch das direkte Wachstum von **DPP-TAPP-COF** auf der Oberfläche von superparamagnetischen Eisenoxid-Nanopartikeln synthetisiert. Die Hybridmaterialien wurden durch Co-Kondensation der **TAPP**- und **DPP-1**-Bausteine mittels solvothermischer Synthese in Gegenwart von amino- oder carboxyfunktionalisierten Nanopartikeln, **NH_2-FeO** für die **Nx**-Serie oder **COOH-FeO** für die **Cx**-Serie, synthetisiert. Die Inkorporation der Nanopartikel wurde zunächst durch FT-IR- und EDX-Spektroskopie bestätigt und die genaue Zusammensetzung durch VSM-Messungen quantifiziert. Eine detaillierte morphologische Analyse mit Hilfe von elektronenmikroskopischen Techniken zeigte eine homogene Verteilung der anorganischen Nanopartikel in der organischen COF-Matrix. Da die Vernetzung zwischen oligomeren COF-Vorstufen und den anorganischen Nanopartikeln mit der Konzentration der Nanopartikel zunimmt, wurde in Pulverdiffraktogrammen eine geringere Kristallinität der COF-Domänen beobachtet.

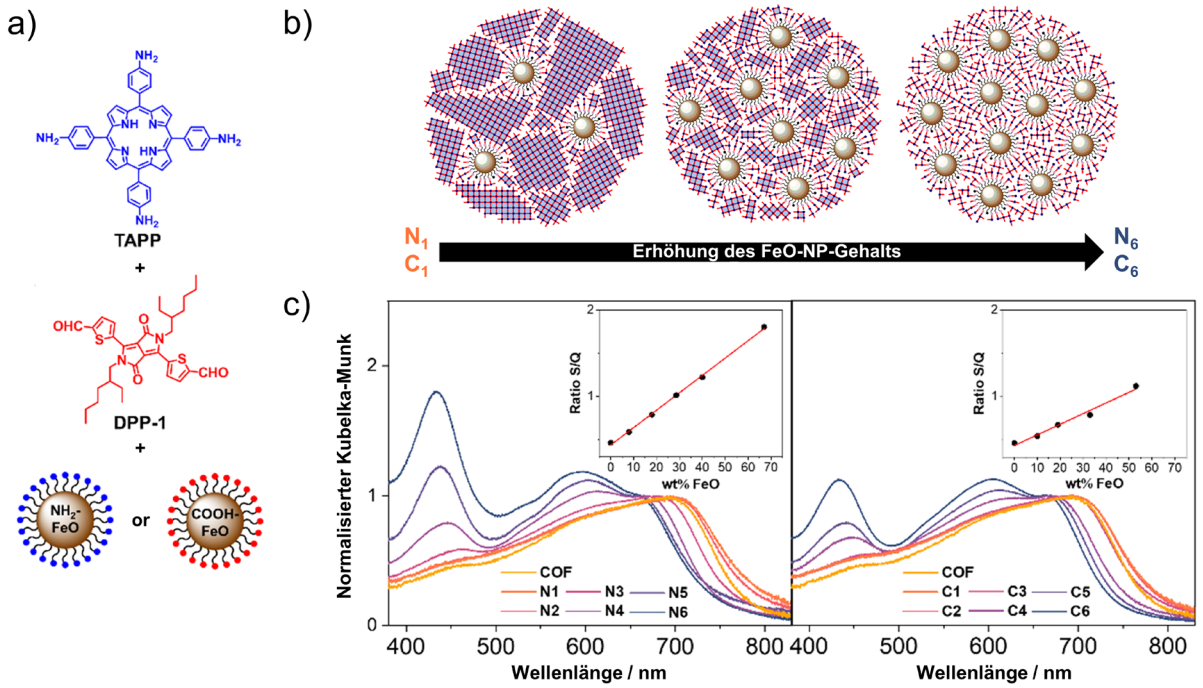

Abbildung 50. Einzelne Komponenten der **FeO@DPP-TAPP-COF**-Komposite. b) Schematische Darstellung der Komposite mit unterschiedlichen Nanopartikel-Anteilen. c) UV-Vis-Absorptionsspektren, die aus diffusen Reflexionsmessungen mit der Kubelka-Munk-Funktion berechnet wurden für die Komposit-Serien **N1-6** und **C1-6** (jeweils normiert auf das lokale Absorptionsmaximum mit der höchsten Wellenlänge, die Einschübe zeigen die lineare Beziehung zwischen dem Intensitätsverhältnis Soret/Q-Banden und dem Massenanteil der FeO-Partikel).

Interessanterweise liefern die Komposite eine höhere Ausbeute und ausgedehntere kristalline COF-Domänen, was auf das geordnetere Wachstum ausgehend von den direkt mit den **COOH-FeO**-Nanopartikeln verbundenen **TAPP**-Einheiten zurückzuführen ist. Damit wurde die Möglichkeit zur strukturellen Kontrolle für diese Hybridmaterialien demonstriert. Die

optischen Eigenschaften der Komposite wurden mittels DRS analysiert. Mit zunehmender **FeO**-Konzentration wurde in beiden Serien ein Übergang von einer breiten panchromatischen Absorptionsbande zu den einzelnen Banden der Monomere beobachtet, was den Einfluss der Nanopartikel-Keime auf die Chromophorstapelung und die davon abhängigen optischen Eigenschaften offenbart. Auffallend ist, dass bei den weniger kristallinen Phasen das relative Verhältnis zwischen der Soret- und der letzten Q-Bande der **TAPP**-Einheiten direkt mit dem Nanopartikel-Anteil korreliert. Über diese linearen Regressionen konnte der Massenanteil der **FeO**-Domänen innerhalb der organischen Matrix direkt aus den Absorptionsdaten abgeschätzt werden.

In **Kapitel 4** wurden BODIPY-Einheiten in das strukturelle Rückgrat von COFs eingebaut. Motiviert durch die chemische Robustheit, die ausgeprägte Planarität sowie die faszinierenden optischen Eigenschaften der BODIPYs wurden diese Farbstoffe direkt in ein COF-Gerüst eingebaut. Die Co-Kondensation von **TFP** und **BDP(NH$_2$)** in Gegenwart von Essigsäure ergab **BDP-TFP-COF** als ein und über β-Ketenamine verknüpftes robustes 2D-COF mit *hcb*-Topologie.

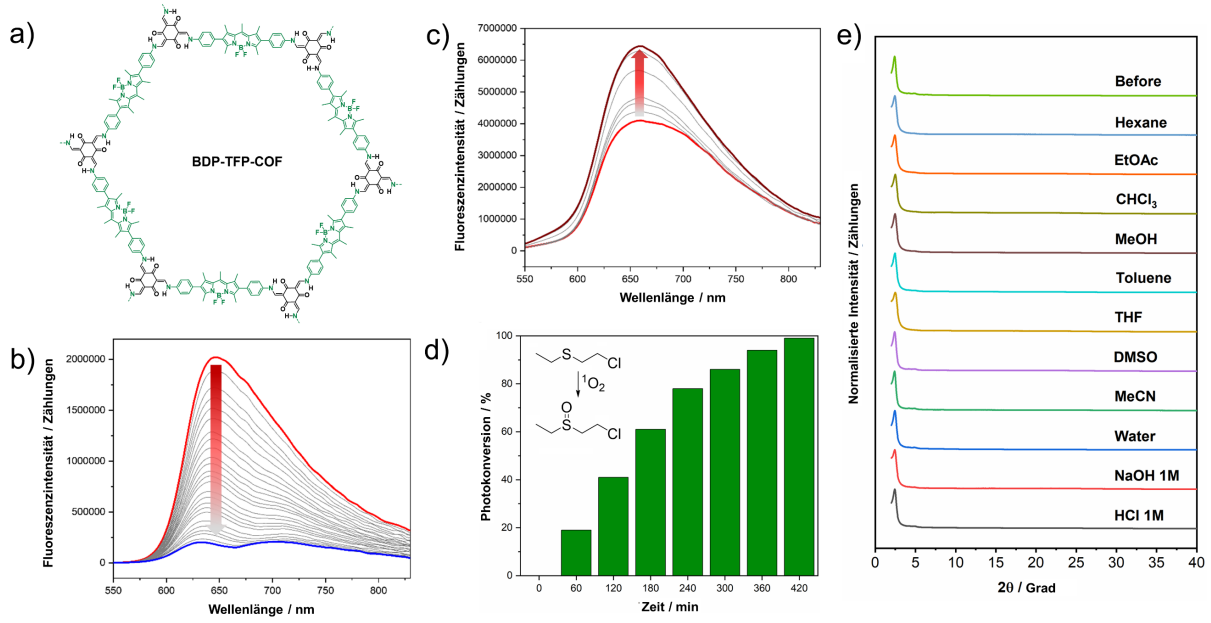

Abbildung 51. a) Chemische Struktur von **BDP-TFP-COF.** b) Spektrale Änderung der Fluoreszenz von **BDP-TFP-COF** (0.1 mg mL^{-1} in Wasser, λ_{exc} = 420 nm, rote Kurve) nach Zugabe von unterschiedlichen Mengen an MB (25 mg L^{-1} in Wasser, graue und blaue Kurven). c) Spektrale Änderung der Fluoreszenz von **BDP-TFP-COF** (0. 1 mg mL^{-1} in THF, λ_{exc} = 365 nm, rote Kurve) mit zunehmenden Mengen an TEA (graue und dunkelrote Kurven). d) Prozentale Photokonversion von CEES (0.1 M in MeOD) in Gegenwart von **BDP-TFP-COF** (1% mol) in Abhängigkeit von der Bestrahlungszeit mit weißem Licht (230 mW cm^{-2}). e) Pulverdiffraktogramm von **BDP-TFP-COF** vor und nach der Suspension für 24 Stunden in verschiedenen Lösungsmitteln.

Der Einbau der BODIPYs wurde durch NMR- und EDX-Spektroskopie eindeutig bestätigt. PXRD-Messungen zeigten die hohe Kristallinität des COFs und die chemische Robustheit des organischen Rückgrats. Die optischen Eigenschaften des Polymers wurden mittels DRS ermittelt und zeigten eine panchromatische Absorption mit einem Maximum bei 575 nm. Adsorptionsexperimente aus wässrigen Lösungen mit den Umweltgiften BPA und MB durchgeführt nutzten die Porösität und robuste Struktur des Polymers aus. **BDP-TFP-COF** zeigte eine sehr hohe Aufnahme von BPA (425.53 mg g^{-1}) und eine moderate Aufnahme von MB (96.06 mg g^{-1}) aus wässriger Lösung. Es ist davon auszugehen, dass die Adsorption durch die Fluor-Atome erzeugte hydrophobe Porenumgebung in Kombination mit intermolekularen CH–π- und π–π-Wechselwirkungen begünstigt wird. Die Exfoliation des laminierten **BDP-TFP-COFs** reduziert den in der Bulk-Phase vorherrschenden ACQ-Effekt und führt zu Dispersionen, die im roten Spektralbereich mit einem Emissionsmaximum von 646 nm emitieren. Nach Zugabe von MB-Aliquoten wird diese Emission gelöscht, was vermutlich mit einem Energietransfer von den BODIPY-Einheiten des COF-Wirts auf den Gast MB erklärt werden kann. Bemerkenswerterweise führte die Zugabe von TEA zu einer Dispersion von **BDP-TFP-COF** in THF zu einer Emissionsverstärkung. Die selektive Deprotonierung der NH-Gruppen an den β-Ketoenamin-Bindungen schwächt wahrscheinlich den PET ab. Dieses duale Fluoreszenzverhalten verdeutlicht das große Potenzial von **BDP-TFP-COF** als multifunktionaler Fluoreszenzsensor. Bei Bestrahlung mit sichtbarem Licht zeigte **BDP-TFP-COF** photosensibilisierende Eigenschaften und erzeugte Singulett-Sauerstoff. Dieses Phänomen wurde in UV-VIS-Experimenten durch die Photobleichung von DPBF in DMF oder ABDA in Wasser bestätigt. Diese Erzeugung von ROS wurde für die Photodetoxifikation eines Senfgas-Simulanten nach Bestrahlung mit sichtbarem Licht ausgenutzt. Die selektive Oxidation der toxischen CEES-Spezies zu unschädlichem CEESO unter Vermeidung einer Überoxidation zu schädlichem $CEESO_2$ wurde nachgewiesen. PXRD-Daten zeigten, das **BDP TFP-COF** während dieses Prozesses strukturell intakt bleibt, wodurch die Robustheit des Materials und das hohe Potenzial als recyclierbarer und metallfreier Photosensibilisator belegt wird.

Kapitel 5 beschreibt die Synthese und Charakterisierung des neuartigen DPP-haltigen **DPP-Py-COF**. Ein mäßig kristallines Material wurde durch solvothermische Synthese über eine Co-Kondensation von **DPP-1** und **$Py(NH_2)_4$**-Vorstufen erhalten. Die Struktur des farbstoffbasierten Netzwerks wurde durch FT-IR-, NMR- und EDX-Spektroskopie bestätigt. Die Struktur-Verfeinerung der PXRD-Daten mit der Materials Studio Software weist auf eine versetzte Stapelung der Schichten hin, wie sie bereits für andere pyrenbasierte COFs beobachtet

wurde. Die Pyreneinheiten nehmen dabei eine Sesselkonfiguration ein, um eine optimale Stapelung der aromatischen Einheiten zu ermöglichen. Diese Konformation führt zu einem Versatz zwischen benachbarten Schichten, der durch den Einbau von sperrigen Alkylsubstituenten an den komplementären DPP-Bausteinen noch verstärkt wird. Diese strukturellen Besonderheiten beeinträchtigten die Porösität des Materials, für das ein sehr geringer BET-Oberfläche von nur 41 m^2 g^{-1} und eine für nichtporöse Strukturen typische Stickstoff-Physisorptionsisotherme des Typs III bestimmt wurden. DRS für **DPP-Py-COF** zeigte eine panchromatische Absorption, die sich effizient in den NIR-Bereich bis zu 1000 nm ausdehnt und ein Maximum bei 706 nm aufweist. Diese Rotverschiebung kann mit der ausgedehnten Konjugation innerhalb der Schichten und die effiziente Stapelung der Farbstoffe zwischen den D-A-Schichten erklärt werdent. Aus dem Tauc-Diagramm wurde eine optische Bandlücke von 1.53 eV berechnet, womit das hohe Potenzial dieses COFs als Halbleiter- und Lichtsammelmaterial aufgezeigt ist. Weiterhin zeigte **DPP-Py-COF** photosensibilisierende Eigenschaften, wie durch UV-VIS-Messungen zur Erzeugung von Singulett-Sauerstoff bestätigt wurde.

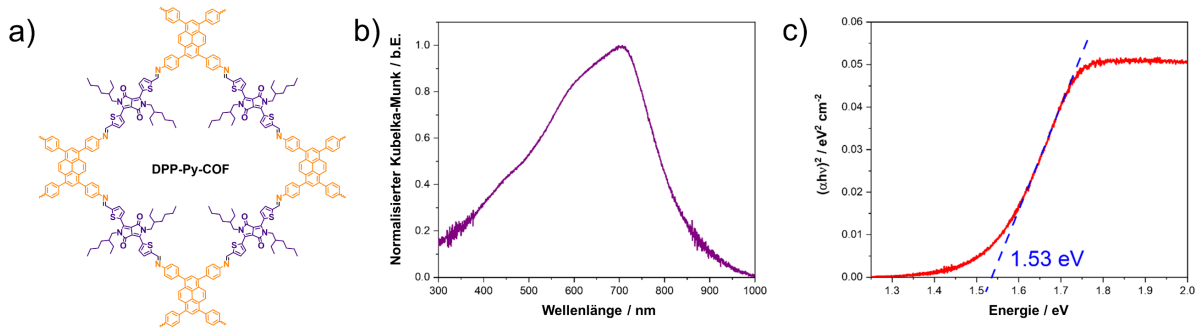

Abbildung 52. Chemische Struktur von **DPP-Py-COF**. b) UV-Vis-Absorptionsspektrum, das aus einer diffusen Reflexionsmessung mit der Kubelka-Munk-Funktion berechnet wurde und c) Tauc-Plot.

Zusammenfassend lässt sich sagen, dass sich durch den Einbau von organischen Farbstoffen in COFs chromophore Polymere mit verbesserten Lichtsammelgseigenschaften bei längeren Wellenlängen bis in den NIR-Bereich erhalten werden. Ein attraktives strukturelles Merkmal sind die hochgeordneten Strukturen, die Donor- und Akzeptordomänen in getrennten säulenförmigen Stapeln anordnen. Dadurch bietet sich eine zukünftige Verwendung dieser Materialien in optoelektronischen Geräten an. Ein weiterer wichtiger Einfluss auf die optischen und halbleitenden Eigenschaften ist die Art und Weise der Stapelung zwischen den einzelnen Chromophoren. Hier konnten wir zeigen, dass die Verteilung unterschiedlicher Mengen an FeO-Nanopartikeln zwischen den COF-Domänen eine Feinjustierung dieser Eigenschaften ermöglicht. Darüberhinaus werden Aggregation und Wechselwirkungen zwischen den Farbstoffen durch eine geeignete Wahl der komplementären monomeren Untereinheiten

optimiert, was zu einer verbesserten Lichtsammlung und geringeren optischen Bandlücken führt. Durch den Einbau funktioneller Farbstoffe mit unterschiedlichen physikochemischen Eigenschaften und Bindungsmotiven sind neuartige COFs für spezifische Anwendungen denkbar. Wir haben gezeigt, dass BODIPY-Farbstoffe attraktive Bausteine für die Konstruktion robuster und stark absorbierender COFs mit potenziellen Anwendungen in der Wasseraufbereitung, Sensorik oder Photokatalyse sind. Abschließend soll noch die chemische Vielseitigkeit dieser Farbstoffe für die Herstellung kristalliner Polymere mit abstimmbaren Strukturen hervorgehoben werden. Es ist davon auszugehen, dass maßgeschneiderte Variationen an den BODIPY-Untereinheiten, entweder an den Vorstufen oder in postsynthetischen Modifikationen, in zukünftigen Arbeiten die Entwicklung innovativer und hochleistungsfähiger funktioneller poröser Materialien ermöglichen werden.

Chapter 8: Appendix

8.1 Supporting information for Chapter 3: Modulation of Crystallinity and Optical Properties in Composite Materials Combining Iron Oxide Nanoparticles and Dye-Containing Covalent Organic Frameworks

8.1.1 Materials and Methods

All solvents were purchased from Sigma Aldrich, Germany. ^{n}BuOH came anhydrous and packed under argon and mesitylene was degassed before use. THF was dried with a solvent purification system "PureSolv MD 7" from Inert Technology. The tubes used in the solvothermal synthesis were purchased from ACE glass, with the following characteristics: Pressure vessel (15 mL, length 10.2 cm, outer diameter 25.4 mm) equipped with PTFE plugs. $BaSO_4$ as solid matrix for diffuse reflectance experiments was purchased from Alfa-Aesar, Germany. Iron(III) chloride hexahydrate ($FeCl_3 \cdot 6H_2O$, 97.0% purity) and iron(II) chloride tetrahydrate ($FeCl_2 \cdot 4H_2O$, 99.0% purity) were purchased from Honeywell. Aqueous ammonia solution (NH_3 25 wt% in H_2O) was purchased from Sigma-Aldrich. Citric acid monohydrate ($C_6H_8O_7 \cdot H_2O$, 99.5% purity) was provided from PanReac. 3-Aminopropyltriethoxysilane ($C_9H_{23}NO_3Si$, 98.0% purity) was received from abcr. Fourier transformation infrared spectroscopy was performed with a Jasco FT/IR-4600 Spectrometer equipped with ATR-module. Powder X-ray diffraction was conducted with a Bruker D8 Discover diffractometer in reflection mode with Ni-filtered K_α-radiation (λ = 1.54060 Å) and a position-sensitive detector (LynxEye). The PXRD measurements of resulting materials were carried out on a silicon wafer and by applying a scan speed of 0.25 s per step and a 2θ angle increment of 0.02°. Diffuse reflectance measurements were performed with a Perkin-Elmer Lambda 950 equipped with an integration sphere setup. Scanning electron microscopy images were recorded using a Zeiss Ultra Plus field emission scanning electron equipped with a GEMINI e-Beam column operated at 2 kV with an aperture size set to 30 µm to avoid excessive charging and radiation damage of the areas imaged. Energy dispersive X-ray spectroscopy was conducted with a X-Max 50 mm^2 detector from Oxford Instruments operated at 10 kV. Variable saturation magnetization measurements were performed at 300 K with a vibrating sample magnetometer (VSM,Quantum Design VersaLabTM 3T, Cryogen-free Vibrating Sample Magnetometer), cycling the applied

field from −30 to +30 kOe two times with a step rate of 50 Oe s^{-1}. Detailed analyses were carried out by cycling the applied field from −3 to +3 kOe at 5 Oe s^{-1}.

8.1.2 Synthesis and Characterization

The synthesis of the iron oxide nanoparticles is based on a published procedure.[215, 352] Compounds **DPP-1**,[198] **TAPP**,[353] and **DPP-TAPP-COF**[198] have been synthesized according to previously reported procedures.

Iron oxide nanoparticles (FeO)

For the precipitation of the iron oxide nanoparticles, $FeCl_3 \cdot 6\ H_2O$ (8.0 mmol) and $FeCl_2 \cdot 4H_2O$ (4.0 mmol) were dissolved in deionized H_2O (100 mL). Aqueous ammonia solution (8 mL) was quickly added with stirring. The black precipitate, which formed, was separated with a permanent handheld magnet after one minute and washed four times with H_2O (4×100 mL).

COOH functionalization of iron oxide nanoparticles (COOH-FeO)

The iron oxide nanoparticles were redispersed in citric acid (50 mL, 0.01 M) and stirred for 30 min. The dispersion was destabilized by adding sodium hydroxide (100 ml, 1.5 M), magnetically separated and washed four times with 4:1 EtOH/H_2O (200 mL). The precipitate was redispersed in water. The individual particles were inseparable, a stable ferrofluid was obtained. The COOH-functionalized **COOH-FeO** nanoparticles were separated by centrifugation and redispersed in ^{t}BuOH.

NH_2 functionalization of iron oxide nanoparticles (NH_2-FeO)

For the NH_2 functionalization, unmodified aqueous iron oxide nanoparticle dispersion (45 g, 2 wt%) was added to a three-necked flask. The dispersion was diluted with EtOH (22.5 g). 3-aminopropyltriethoxysilane (0.25 g) was diluted with EtOH (22.5 g) and added within 10 minutes while stirring. Subsequently, the reaction flask was refluxed at 78 °C for three hours whilst stirring. To remove all unreacted silane, the particles were magnetically separated and washed with EtOH for three times. Finally, the NH_2-FeO nanoparticles were separated by centrifugation and redispersed in ^{t}BuOH.

FeO@DPP-TAPP-COF composite materials

In a pyrex tube with screw cap, **DPP-1** (11.6 mg, 0.02 mmol) and **TAPP** (6.7 mg, 0.01 mmol) were dissolved in ^{n}BuOH and mesitylene. To this mixture, an aliquot of a presonicated dispersion of the corresponding functionalized nanoparticles **NH_2-FeO** or **COOH-FeO** (4 wt%

in ^{t}BuOH, see Table S1 and Table S2) was added. After the addition of acetic acid (100 µL, 6M), the tube was sealed, sonicated for five minutes and heated at 120 °C for five days. The reaction product was filtered, washed several times with anhydrous THF and further purified by solvent exchange with ethanol and acetone. To ensure the collection of composite materials, the magnetic fractions were attracted with a magnet prior to the solvent removal during this process. The obtained hybrid material was dried under high vacuum for four hours to obtain the composite materials as a black powder that shows magnetic properties.

Table S1. Synthetic conditions for amine functionalized nanoparticles **NH_2-FeO@DPP-TAPP-COF/POPs**.

NH_2-FeO @DPP-TAPP-COF/POP	V *n*-BuOH (mL)	V mesitylene (mL)	v **NH_2-FeO** dispersion (µL)	m product obtained (mg)
N1	3	1	5	11.0
N2	3	1	10	9.1
N3	2.95	1	50	11.9
N4	2.9	1	100	13.2
N5	2.75	1	250	16.6
N6	2.5	1	500	25.1

Table S2. Synthetic conditions for carboxylic acid functionalized nanoparticles **COOH-FeO@DPP-TAPP-COF/POPs.**

COOH-FeO @DPP-TAPP-COF/POP	V *n*-BuOH (mL)	V mesitylene (mL)	v **COOH-FeO** dispersion (µL)	m product obtained (mg)
C1	3	1	5	13
C2	3	1	10	11.6
C3	2.95	1	50	14.2
C4	2.9	1	100	15
C5	2.75	1	250	19.6
C6	2.5	1	500	22.0

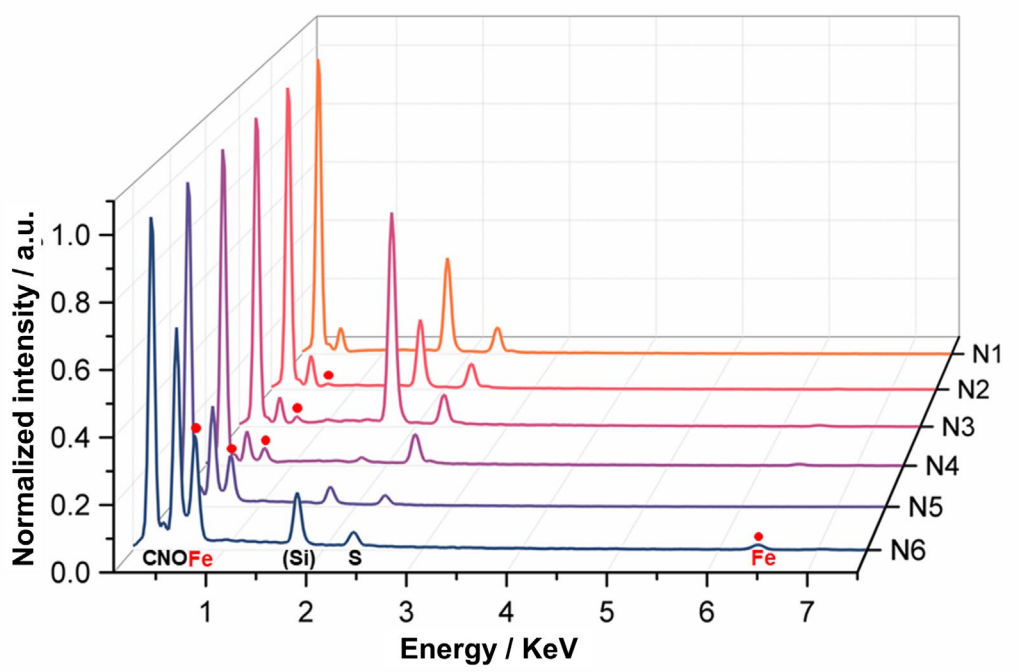

Figure S1. EDX spectra of **NH_2-FeO@DPP-TAPP-COF/POP** series**.** The pronounced Si peaks can be assigned to the SiO_x substrate.

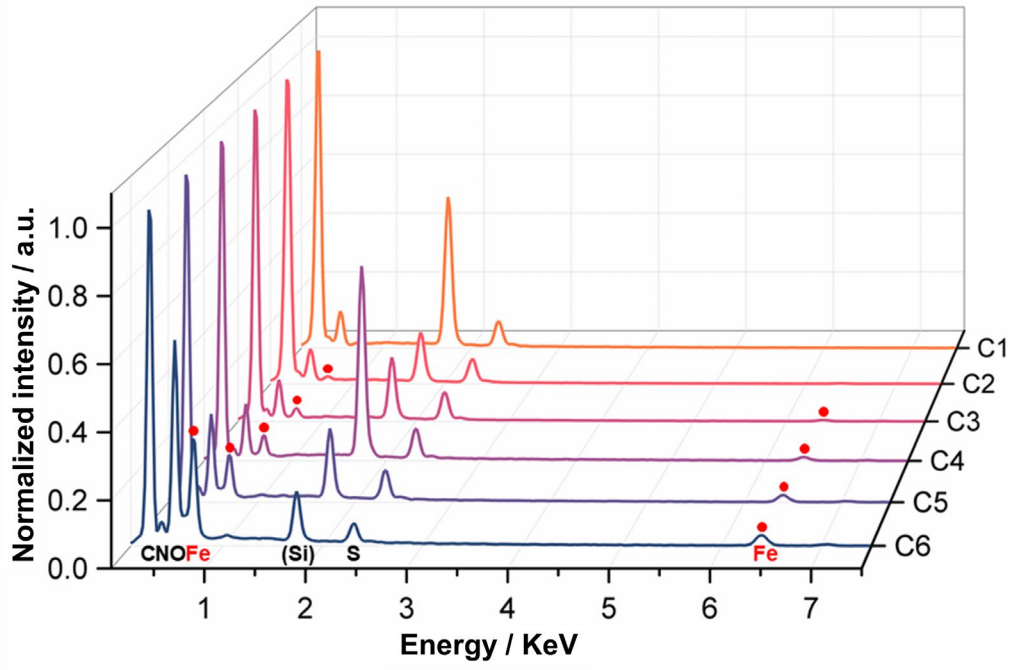

Figure S2. EDX spectra of **COOH-FeO@DPP-TAPP-COF/POP** series**.** The pronounced Si peaks can be assigned to the SiO_x substrate.

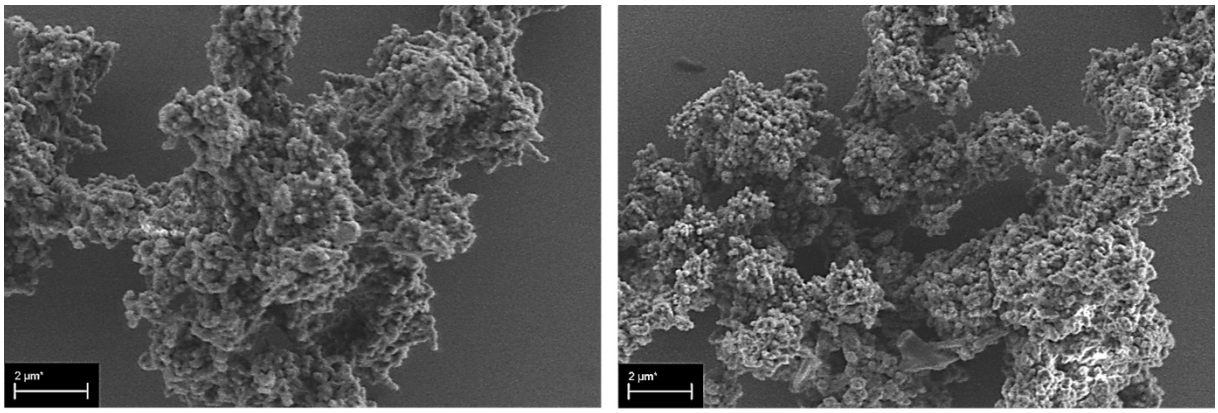

Figure S3. SEM images of **NH_2-FeO@DPP-TAPP-COF-1**.

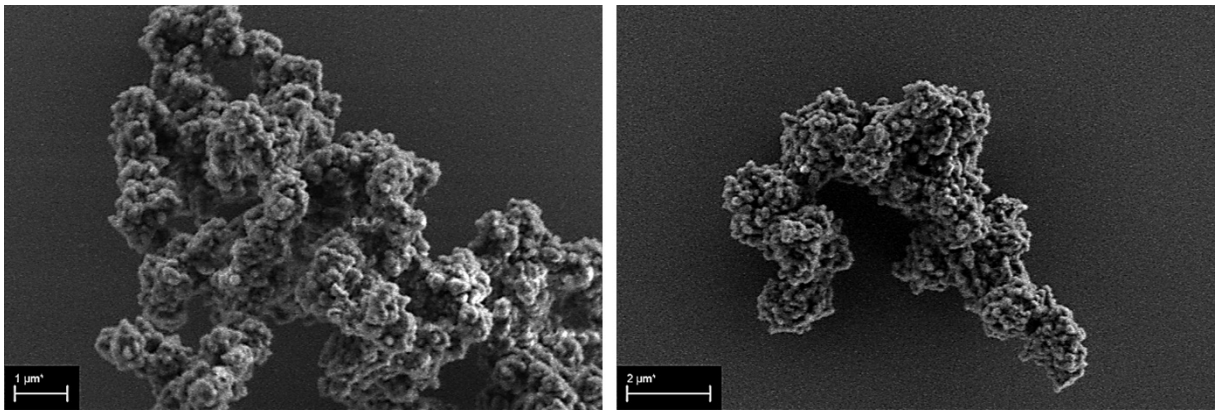

Figure S4. SEM images of **NH2-FeO@DPP-TAPP-COF-2**.

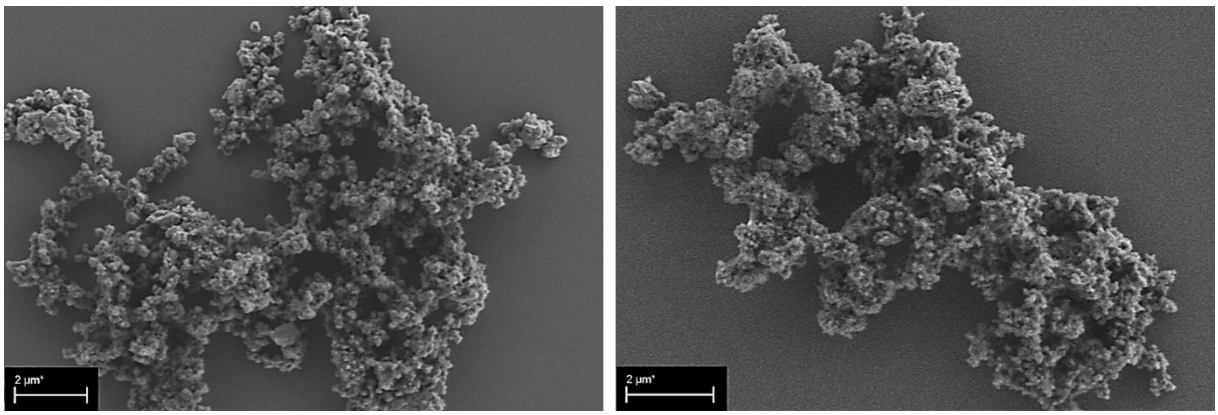

Figure S5. SEM images of **NH_2-FeO@DPP-TAPP-COF-3**.

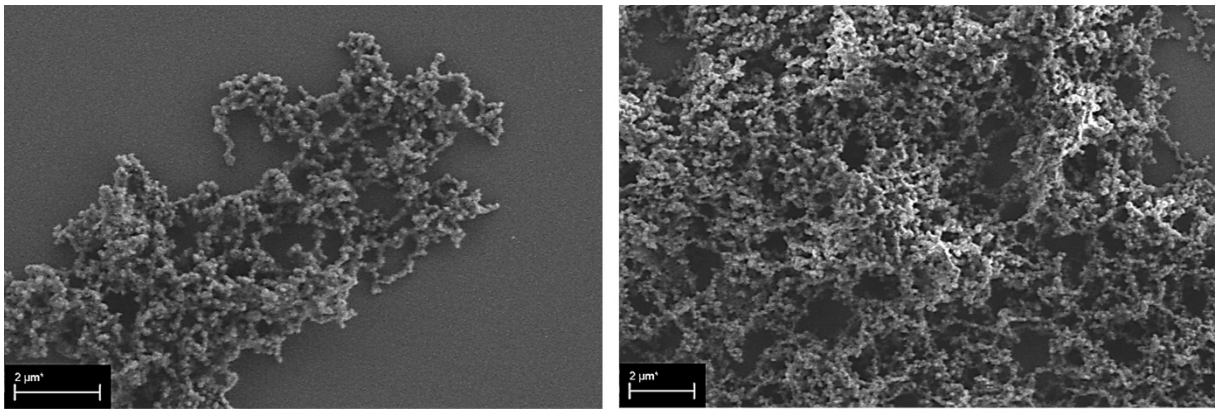

Figure S6. SEM images of **NH_2-FeO@DPP-TAPP-POP-4**.

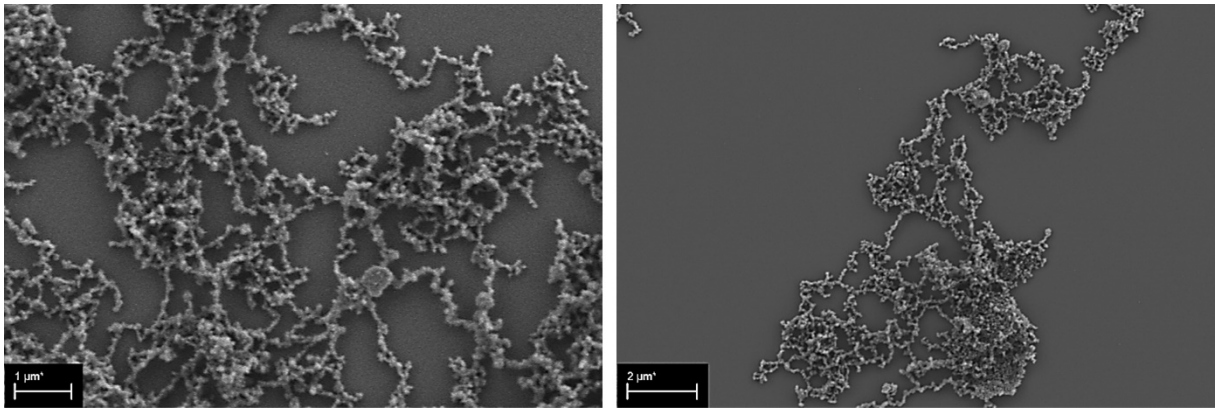

Figure S7. SEM images of **NH_2-FeO@DPP-TAPP-POP-5**.

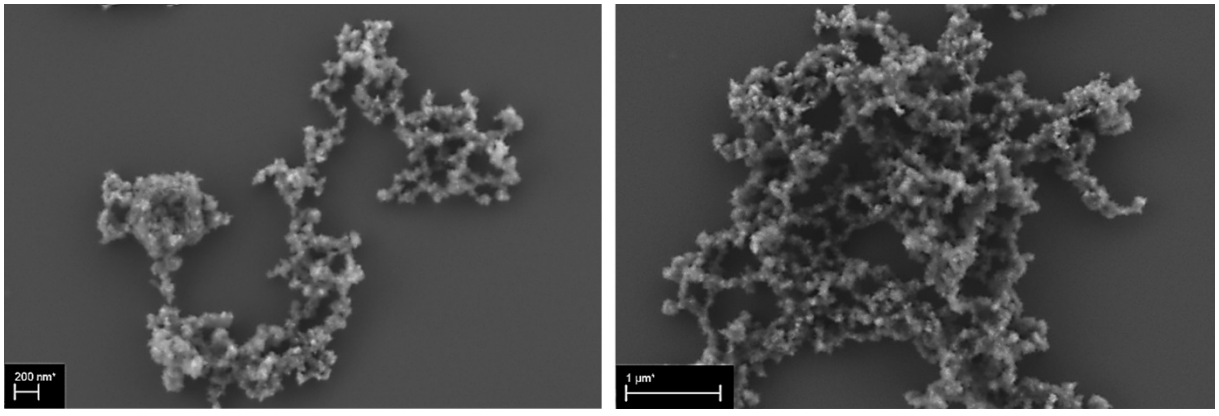

Figure S8. SEM images of **NH_2-FeO@DPP-TAPP-POP-6**.

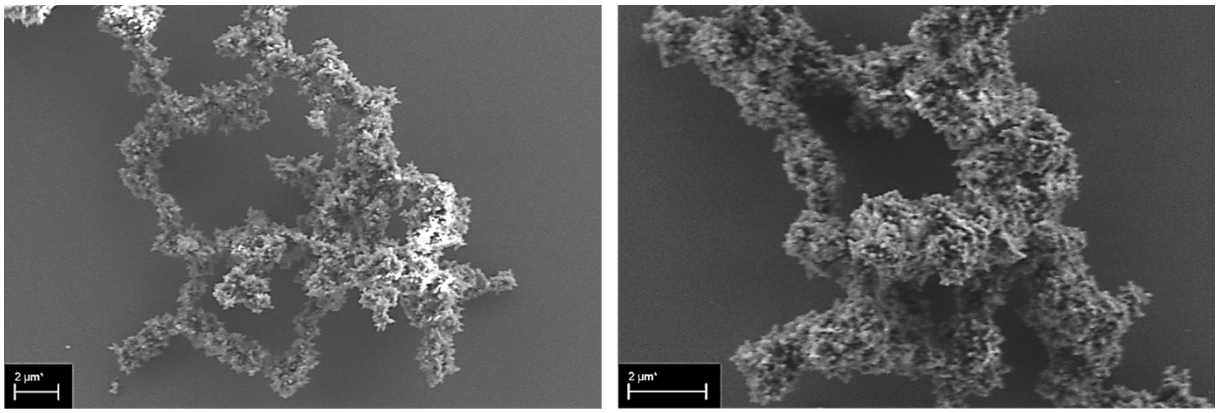

Figure S9. SEM images of **COOH-FeO@DPP-TAPP-COF-1**.

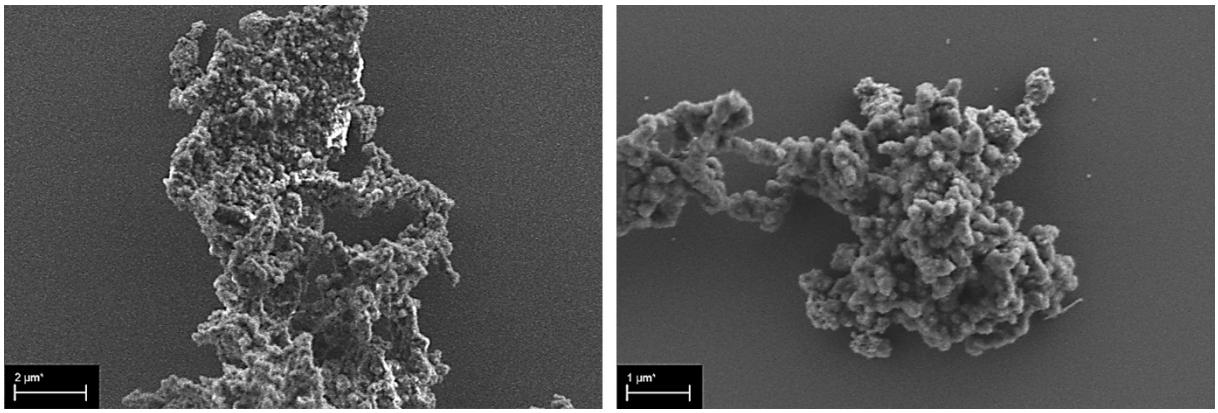

Figure S10. SEM images of **COOH -FeO@DPP-TAPP-COF-2**.

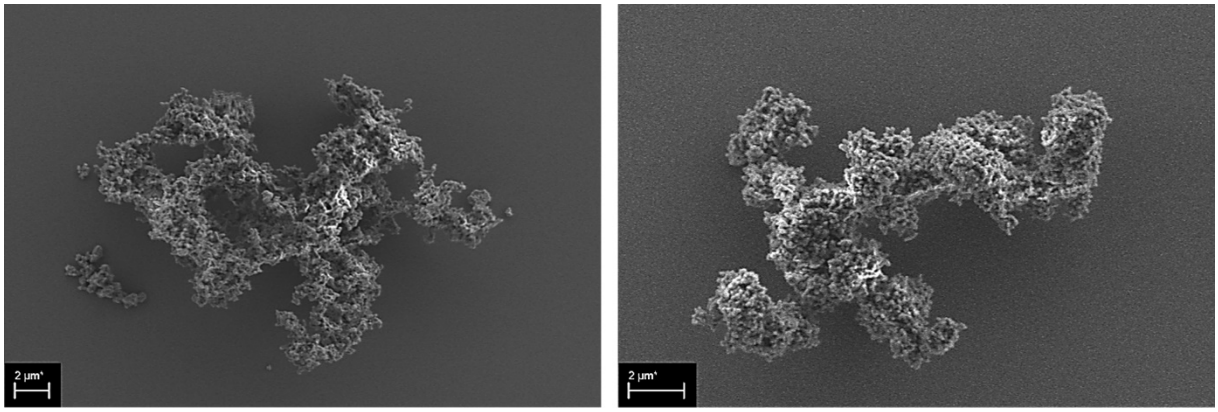

Figure S11. SEM images of **COOH -FeO@DPP-TAPP-COF-3**.

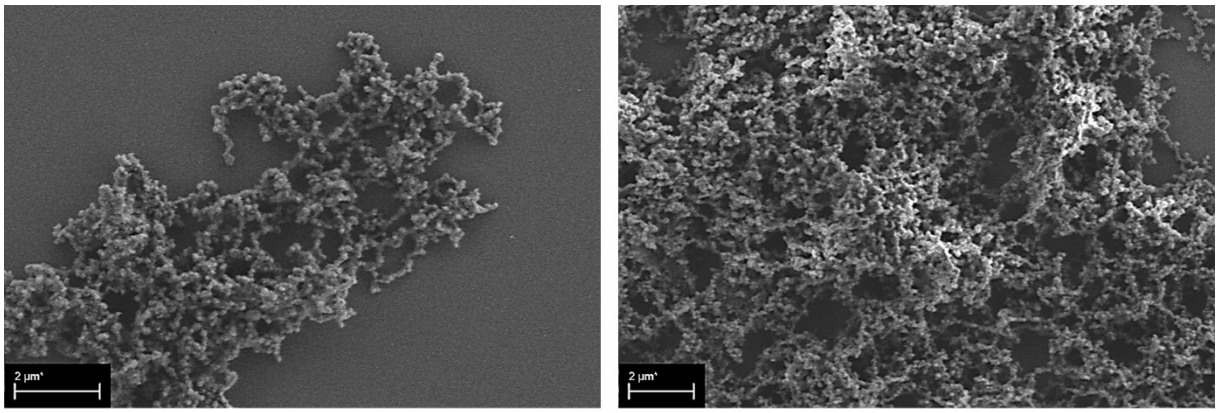

Figure S12. SEM images of **COOH -FeO@DPP-TAPP-COF-4**.

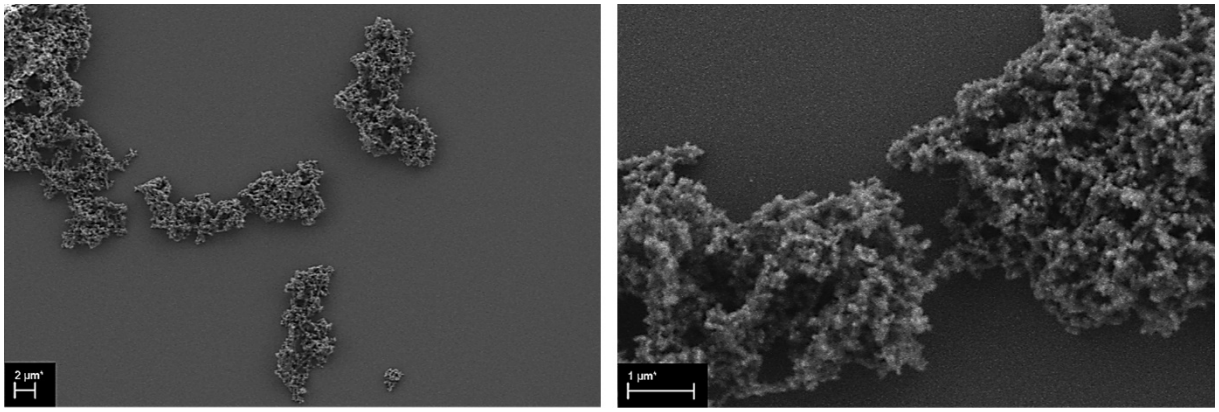

Figure S13. SEM images of **COOH -FeO@DPP-TAPP-POP-5**.

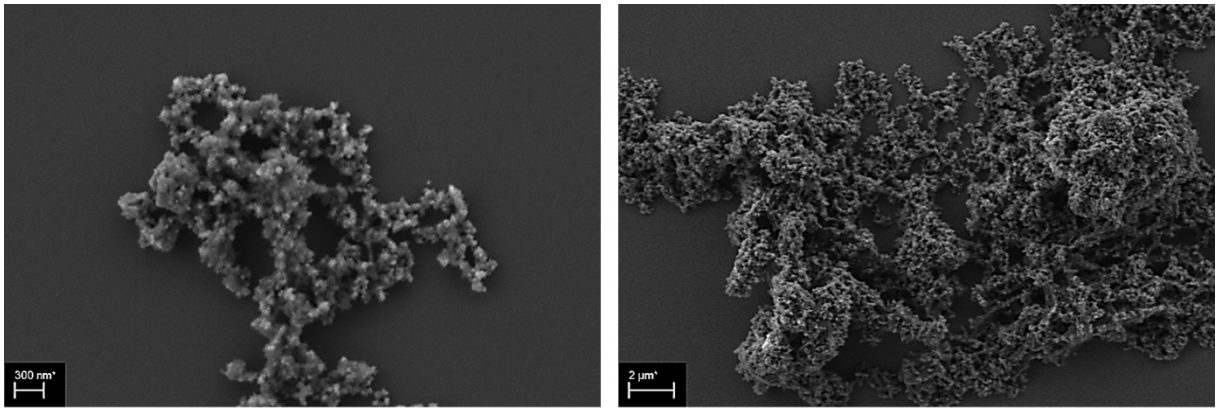

Figure S14. SEM images of **COOH -FeO@DPP-TAPP-POP-6**.

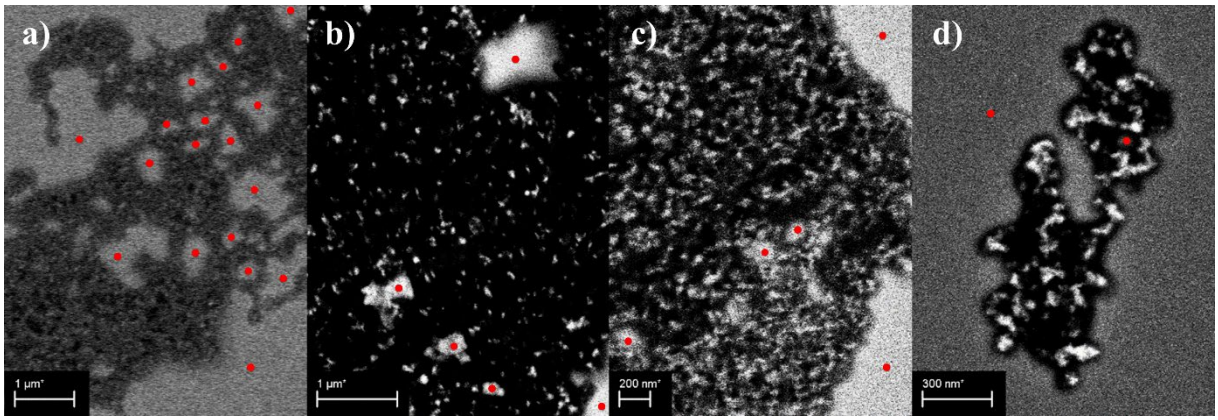

Figure S15. BSE images of a) **NH_2-FeO@DPP-TAPP-COF-3**, b) **NH_2-FeO@DPP-TAPP-POP-4**, c) **NH-FeO@DPP-TAPP-POP-5**, d) **NH_2-FeO@DPP-TAPP-POP-6**. The surface of the SiO_x substrate appears also bright in BSE image and is marked with the red circles.

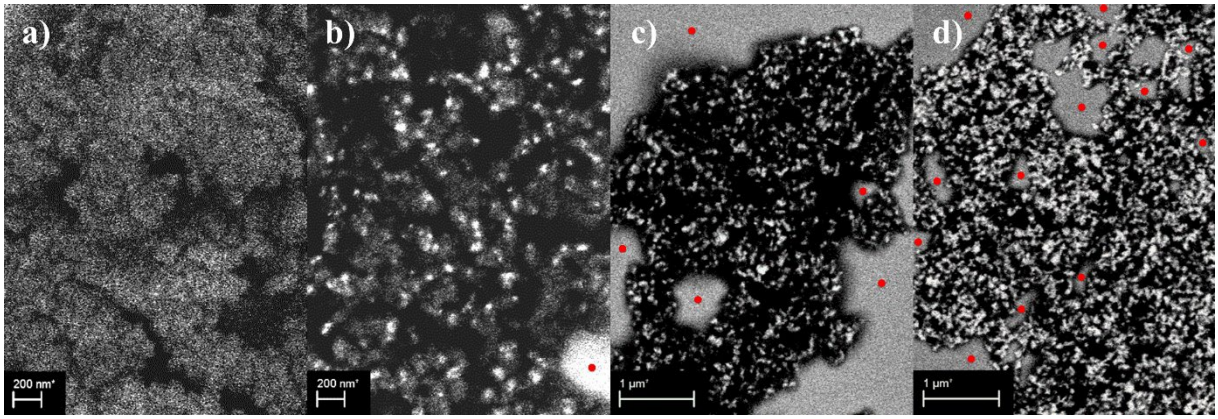

Figure S16. BSE images of a) **COOH-FeO@DPP-TAPP-COF-3**, b) **COOH-FeO@DPP-TAPP-COF-4**, c) **COOH-FeO@DPP-TAPP-POP-5**, d) **COOH-FeO@DPP-TAPP-POP-6**. The surface of the SiO_x substrate appears also bright in BSE image and is marked with the red circles.

Table S3. Magnetization values and real amount of nanoparticle percentage.

Sample	Saturation magnetization	Coercitivity	Remanence	Amount of NP (% w/w)
	Ms [emu/g]	Hc [Oe]	Mr [emu/g]	[%]
NH_2-FeO	**50**	-6.53	-0.45	
NH_2-FeO@DPP-TAPP-POP-6	**33**	-6.61	-0.50	**67%**
NH_2-FeO@DPP-TAPP-POP-5	**20**	-8.78	-0.41	**40%**
NH_2-FeO@DPP-TAPP-POP-4	**9**	-6.32	-0.13	**18%**
NH_2-FeO@DPP-TAPP-COF-3	**4**	-6.13	-0.05	**8%**
COOH- FeO	**56**	-7.01	-0.46	
COOH-FeO@DPP-TAPP-POP-6	**29**	-6.85	-0.20	**53%**
COOH-FeO@DPP-TAPP-POP-5	**18**	-6.65	-0.16	**33%**
COOH-FeO@DPP-TAPP-COF-4	**10**	-6.20	-0.09	**19%**
COOH-FeO@DPP-TAPP-COF-3	**6**	-5.40	-0.04	**10%**

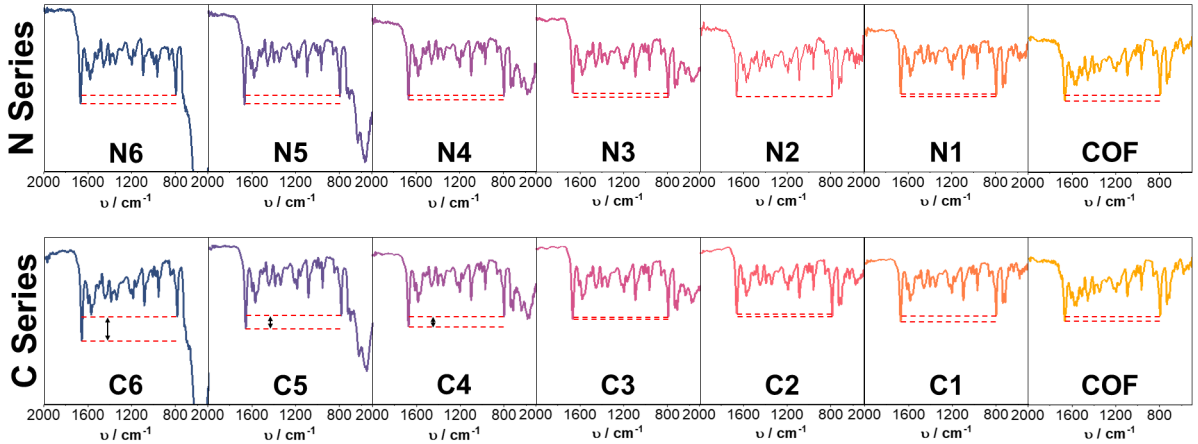

Figure S17. Compilation of FT-IR spectra of **NH_2-FeO@DPP-TAPP-COF/POPs N1–6**, **COOH-FeO@DPP-TAPP-COF/POPs C1–6** and **DPP-TAPP-COF** indicating the increasing intensity for amide signals in **C4–6** (black arrows) due to covalent attachment of **TAPP** molecules to the particle surface via amide bonds (note that amides from the **DPP** are detected in all materials).

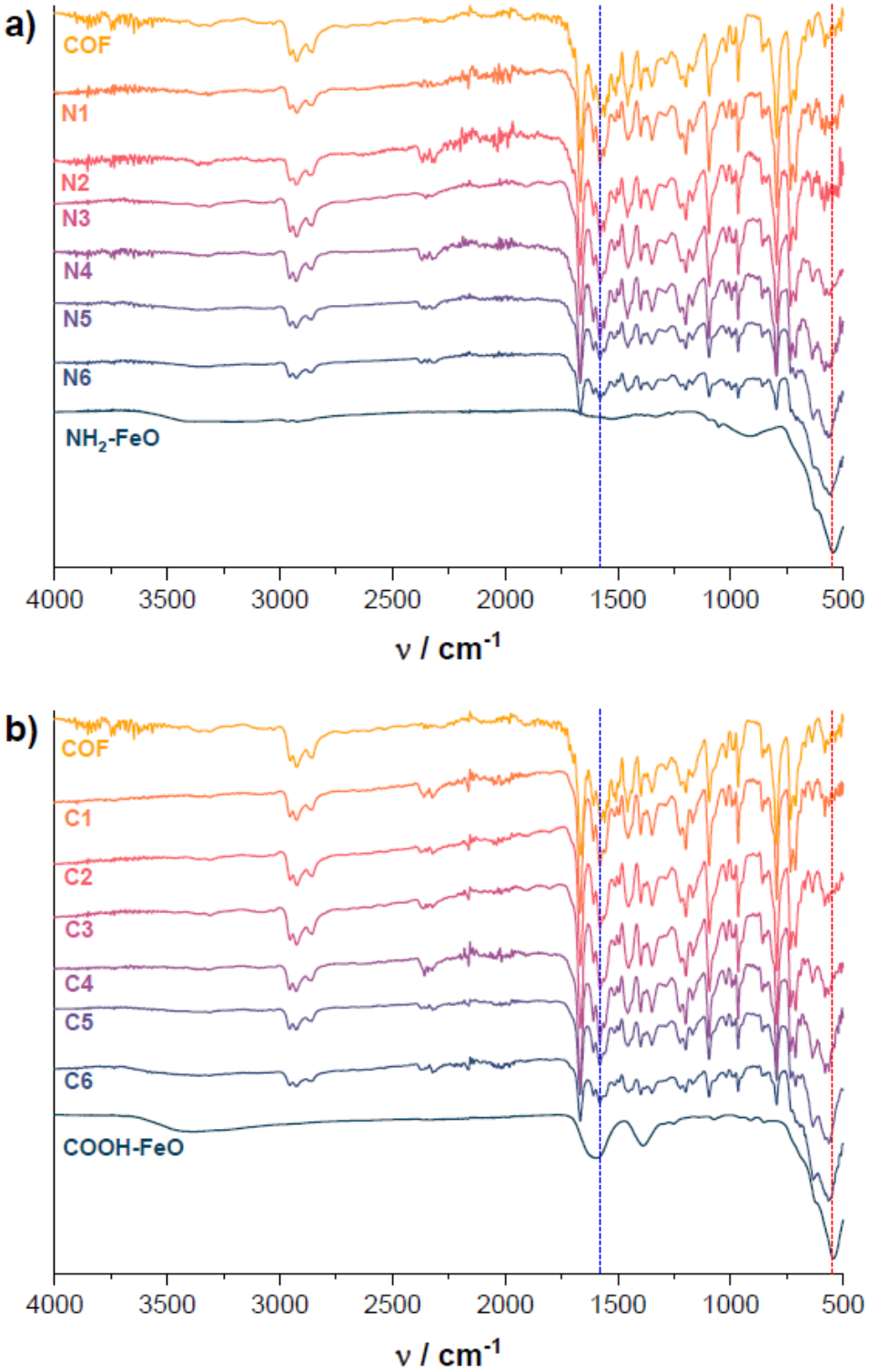

Figure S18. FT-IR spectra of a) **NH_2-FeO@DPP-TAPP-COF/POPs** and b) **COOH-FeO @DPP-TAPP-COF/POPs**. In blue, at 1578 cm^{-1} and in red, around 550 cm^{-1}, the frequencies corresponding to the C=N of the imine bond of the DPP-TAPP-COF and the Fe-O bond of the FeO nanoparticles, respectively.

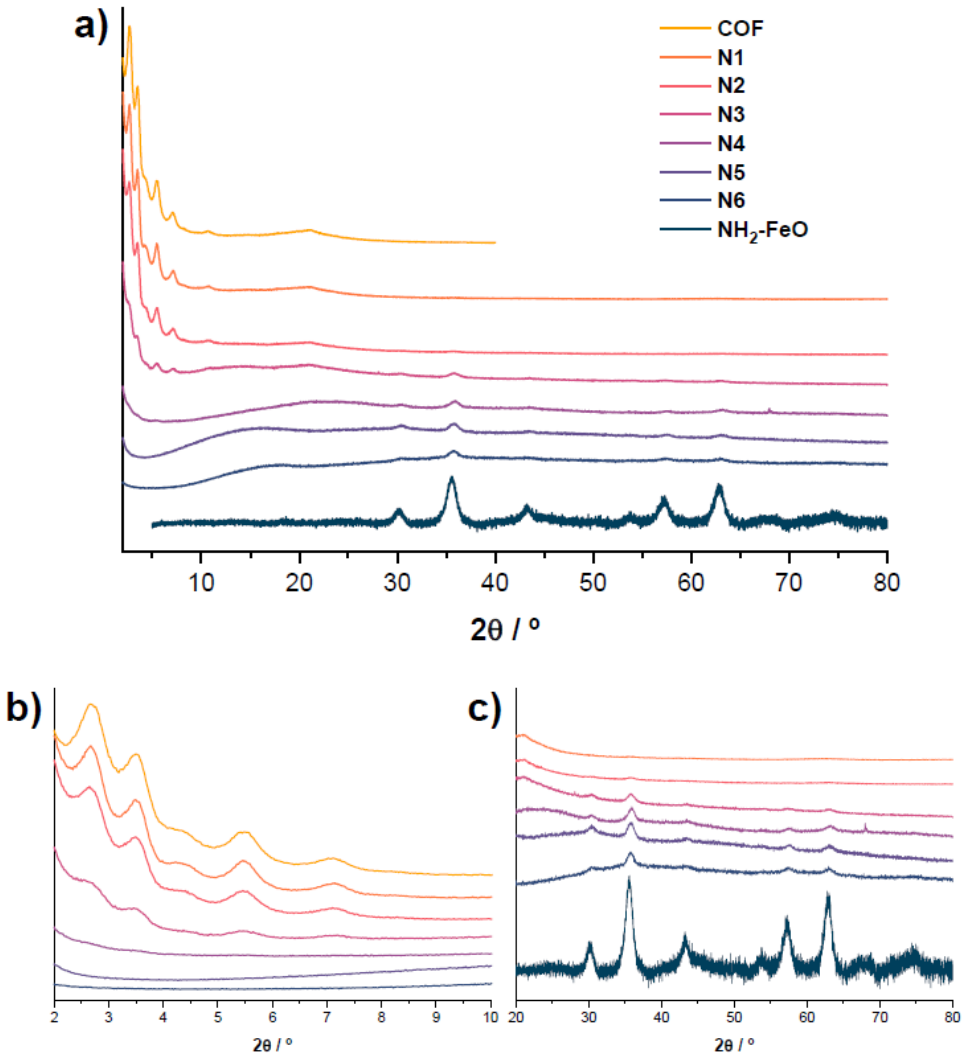

Figure S19. a) Powder X-ray diffractograms of **NH_2-FeO@DPP-TAPP-COF/POPs** and b), c) selected regions of the powder X-ray diffractograms.

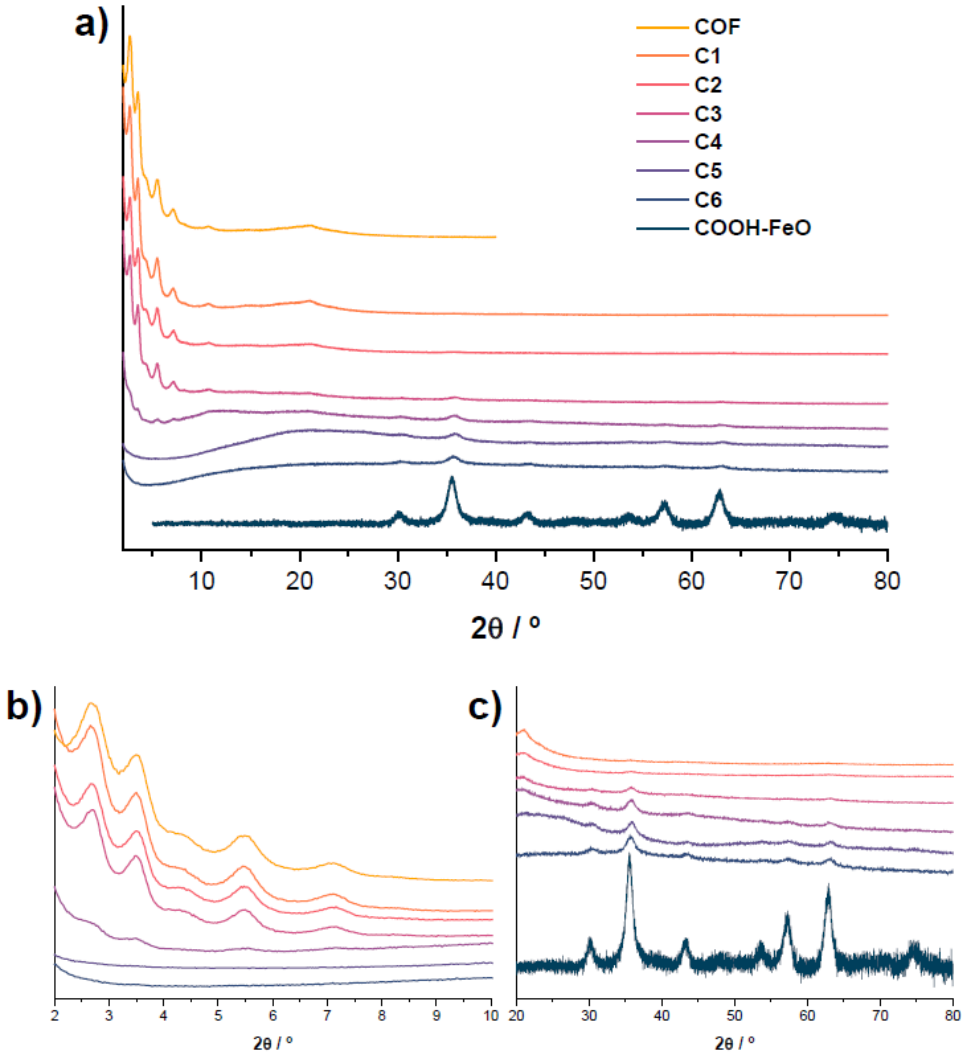

Figure S20. a) Powder X-ray diffractograms of **COOH-FeO@DPP-TAPP-COF/POPs** and b), c) selected regions of the powder X-ray diffractograms.

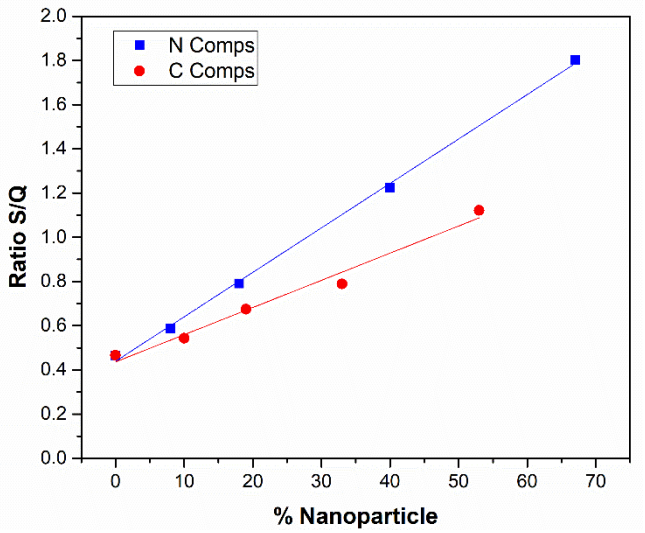

		Value
N composites	Intercept	0.44
	Slope	0.020
C composites	Intercept	0.44
	Slope	0.012

Figure S21. Graphic representation of the Soret/Q intensities ratio against the nanoparticle percentage obtained from the VSM measurements and linear fitting.

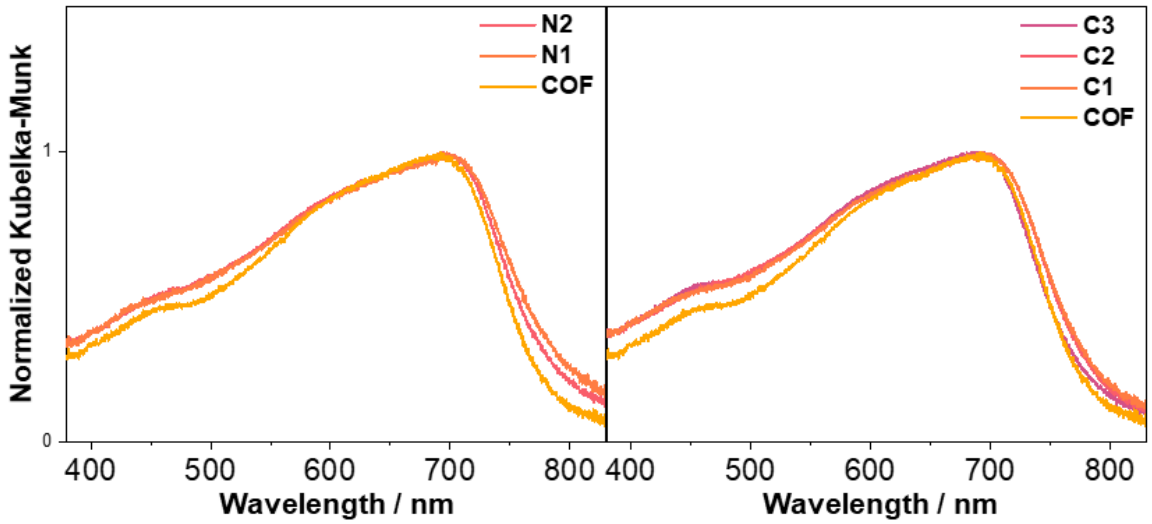

Figure S22. Normalized Kubelka-Munk functions of the **DPP-TAPP-COF** with the **N1-N2** and **C1-C3** composites. Normalized to the Q-Band intensity maximum = 1.

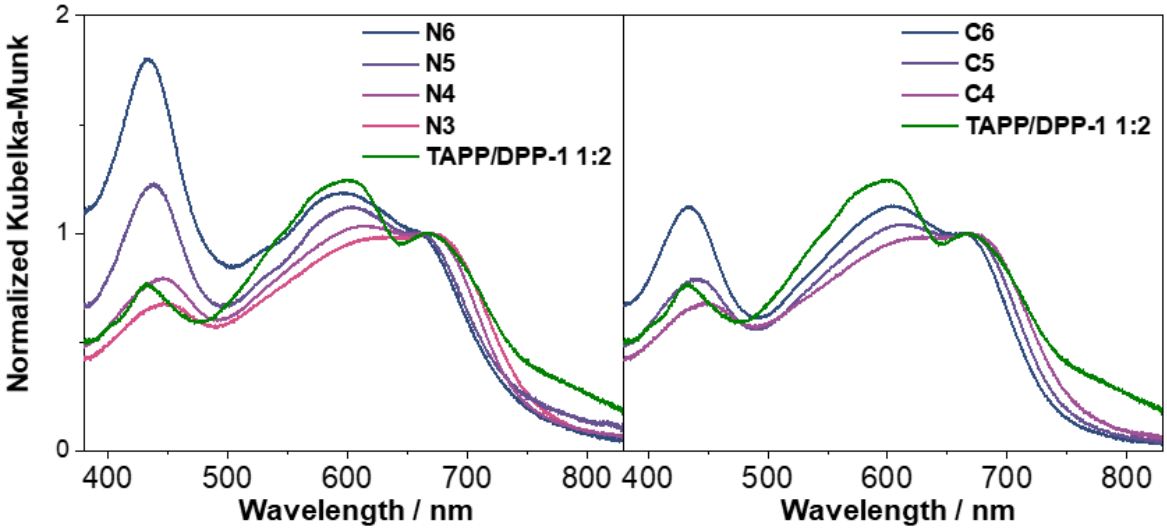

Figure S23. Normalized Kubelka-Munk functions of the reference mixture with the **N3-N6** and **C4-C6** composites. Normalized to the Q-Band intensity maximum = 1.

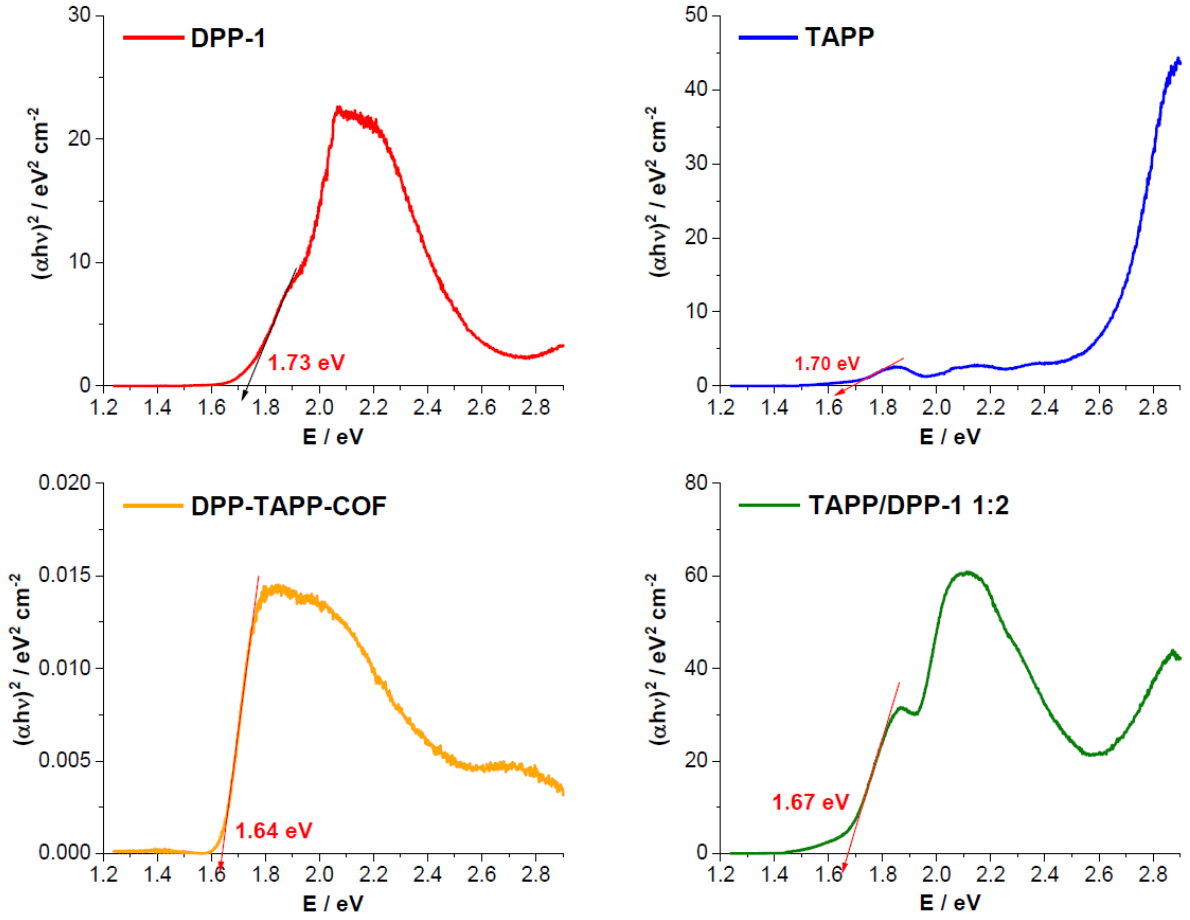

Figure S24. Tauc plots of the reference compounds **TAPP**, **DPP-1**, **DPP-TAPP-COF** and **TAPP/DPP-1 1:2** mixture.

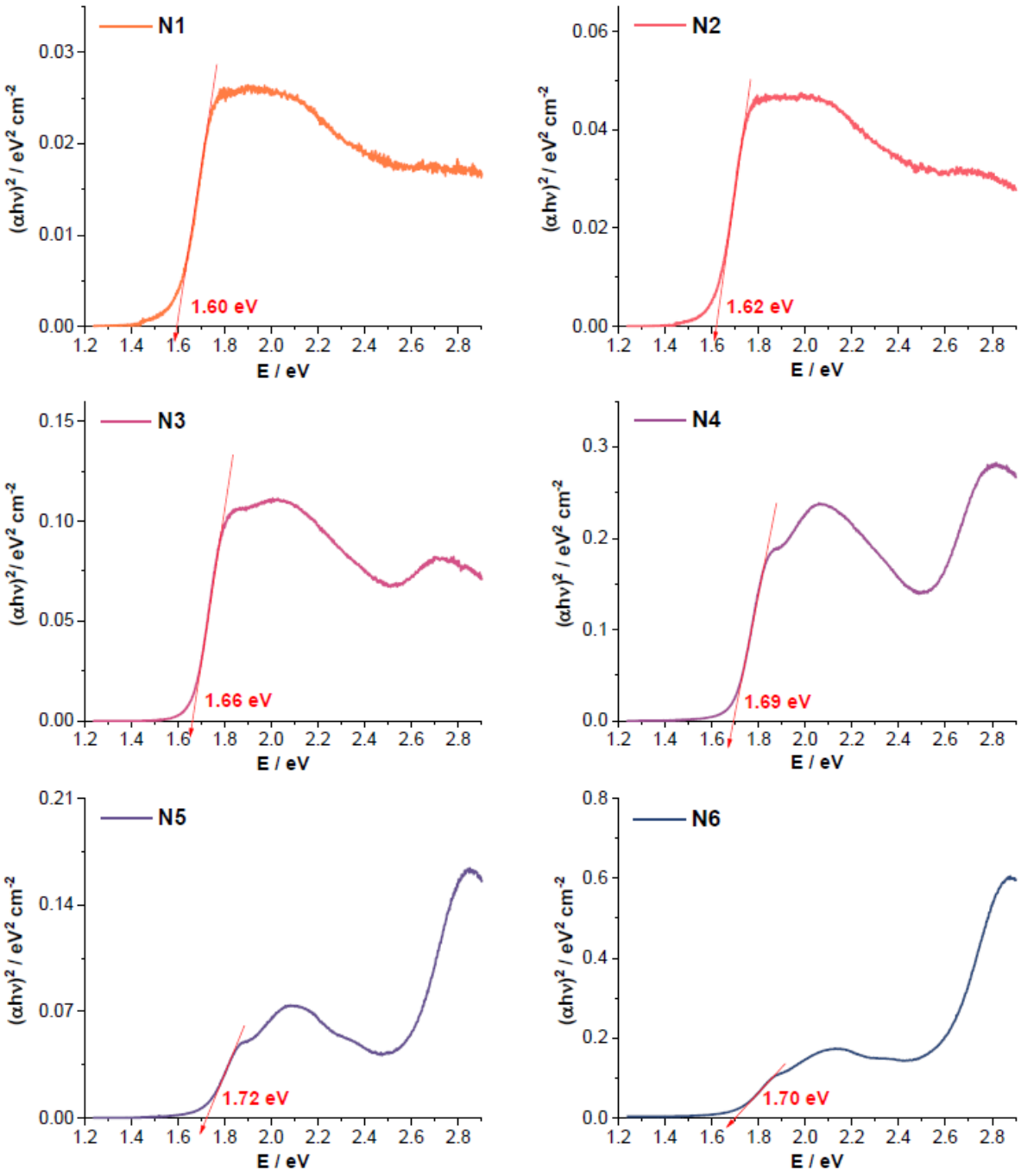

Figure S25. Tauc plots of **N composites**.

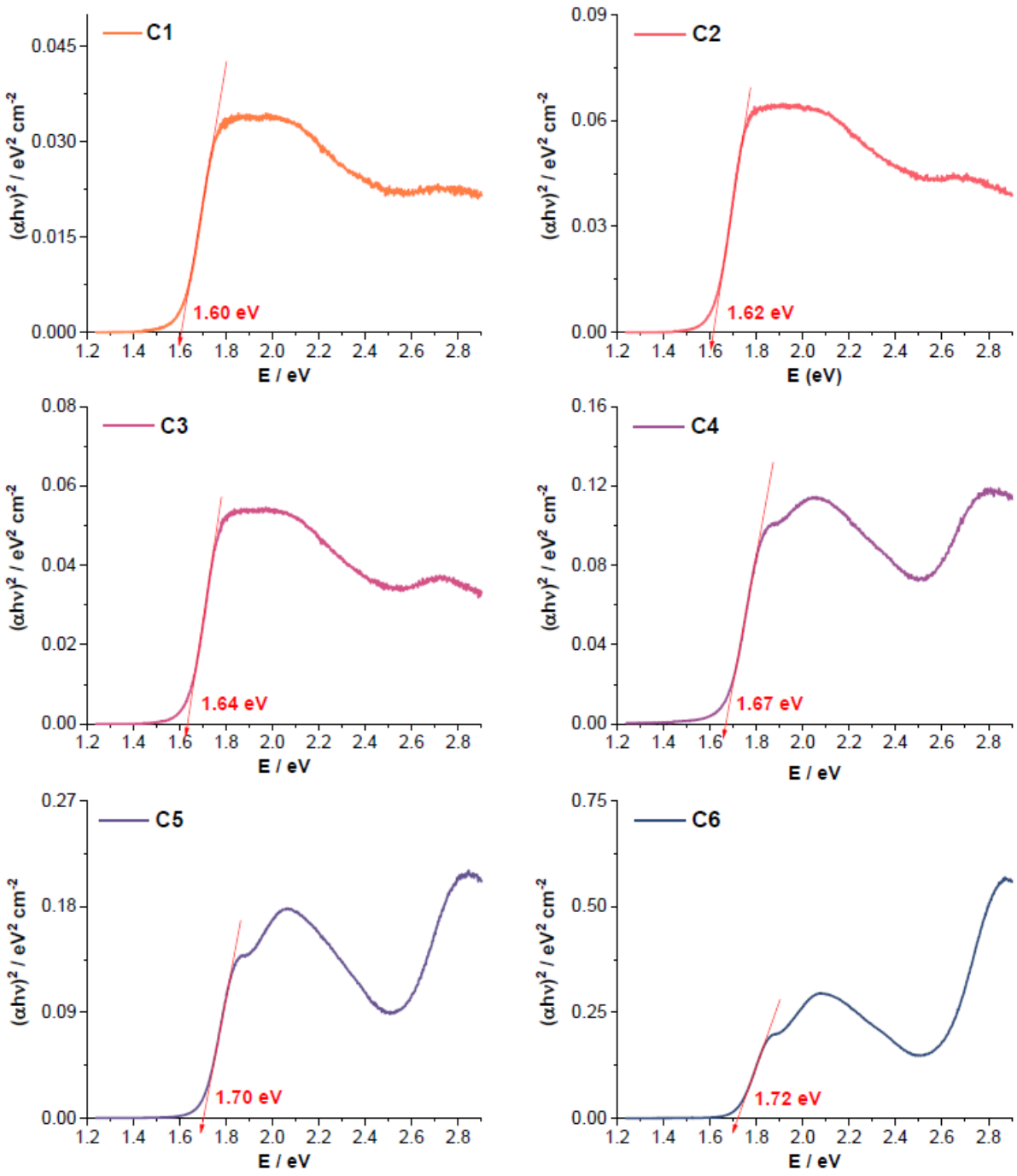

Figure S26. Tauc plots of **C composites**.

8.2 Supporting information for Chapter 4: A BODIPY-Containing Covalent Organic Framework as a Highly Porous Photosensitizer for Environmental Remediation.

8.2.1 Materials and Methods

Solvents and reagents, including pollutants, were bought from commercial suppliers (Sigma-Aldrich, Acros, VWR, ABCR, TCI chemicals) and, if not specified otherwise, used as received. Benzyl alcohol, anhydrous 99%, and 1,2-dichlorobenzene, anhydrous 99.8%, were bought from Sigma-Aldrich and THF was dried with a solvent purification system "PureSolv MD 7" from Inert Technology. The tubes used in the solvothermal synthesis were purchased from VWR, with the following characteristics: Culture tubes (DURAN®, 12x100 mm with GL 14 thread) equipped with screw caps (PBT with PTFE coated gaskets). $BaSO_4$ as solid matrix for diffuse reflectance experiments was purchased from Alfa Aesar. Deionized water was obtained from a Purelab Classic water purification system from ELGA LabWater. FT-IR spectroscopy was performed with a Jasco FT/IR-4600 spectrometer equipped with ATR-module. Powder X-Ray diffraction was conducted with a Bruker D8 Discover diffractometer in reflection mode with Ni-filtered Kα-radiation (λ = 1.54060 Å) and a position-sensitive detector (LynxEye). NMR spectra were recorded on a Bruker Avance 400 at 295 K. The spectra were calibrated to the residual solvent peak and the chemical shifts δ are given in ppm. Multiplicities are denoted as follows: s = singlet, d = doublet, t = triplet, q = quartet, quint = quintet, dd = doublet of doublets, dt = doublet of triplets, m = multiplet, br = broad. Solid state ^{13}C cross-polarization magic-angle spinning (CP-MAS) NMR spectra were measured on a Bruker Avance III HD 600 MHz NMR spectrometer with a spinning rate of 17000 Hz and a contact time of 2000 µs at a fixed temperature of 296.4 K. The theoretical model was simulated using the Reflex package of the BIOVIA Materials Studio software and cell unit parameters were refined using the experimental PXRD data from a .raw file data transformed into an .udf file using the Xpert HighScore software. SEM images were recorded using a Zeiss Ultra Plusfield emission scanning electron microscope equipped with a GEMINI e-Beam column operated at 2 kV with an aperture size set to 30 µm to avoid excessive charging and radiation damage of the areas imaged. EDX spectroscopy was conducted with an X-Max 50 mm^2 detector from Oxford Instruments operated at 10 kV. Diffuse reflectance measurements were performed with a Perkin-Elmer Lambda 950 equipped with an integration sphere setup. Thermogravimetric analysis measurements were performed on a Netzsch Jupiter ST 449 C instrument equipped with a Netzsch TASC 414/4 controller. The samples were heated from room temperature to 900 °C

under nitrogen atmosphere at a heating rate of 5 °C min^{-1}. Nitrogen sorption isotherm and BET surface were obtained after activation of the material under high vacuum for 16 h at 120 °C using a Micro 200 Surface area and Pore Size Analyzer from 3P instruments. Absorption spectra were recorded on a JASCO V-770 UV-Vis/NIR spectrophotometer, in quartz cell cuvettes (SUPRASIL, Hellma Analytics) with a path length of 1.0 cm. The spectral band width and the scan rate were 1 nm and 400 nm min^{-1}, respectively. Fluorescence spectra were recorded on a FLS980-D2D2-ST fluorescence spectrometer from Edinburgh instruments equipped with a Xe lamp and a Red PMT detector. The measures were carried out with the following conditions to avoid further precipitation of the solid over time and to achieve reproducible measurements: 1x Repetition, 0.5s of Dwell time, scan step of 2 nm, scan slit width of 4 nm and an offset slit width of 5 nm, without polariser. Photocatalytic experiments were performed with different ~7 W homemade led arrays using green (528 nm), amber (590 nm) and red (617 nm) light. The white light source setup consists of a 150 W xenon lamp from Newport equipped with a 400 nm cut-off filter. The intensity of the light was measured with a PM 200 optical power meter with a S121C sensor in combination with a CCS 200/M wide range spectrometer from Thorlabs. The measured value was 230 $mW \cdot cm^2$.

8.2.2 Synthesis and Characterization

TFP and **BDP(I)$_2$** were synthetized according to previously reported procedures.[249, 253, 354]

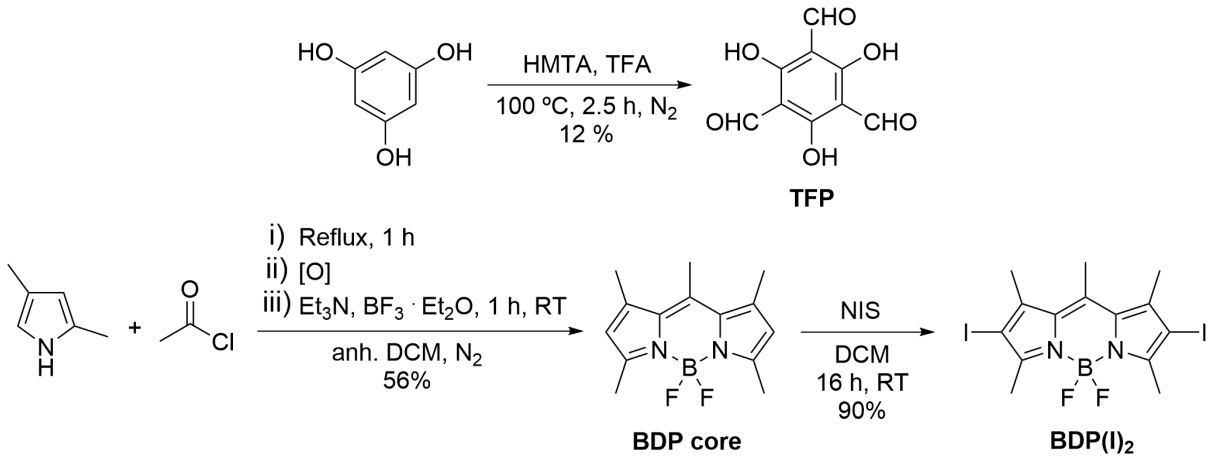

Scheme S1. Synthesis of **TFP** and **BDP(I)$_2$**.

BDP(NH$_2$)$_2$ was synthesized following a slightly modified literature procedure.[243]

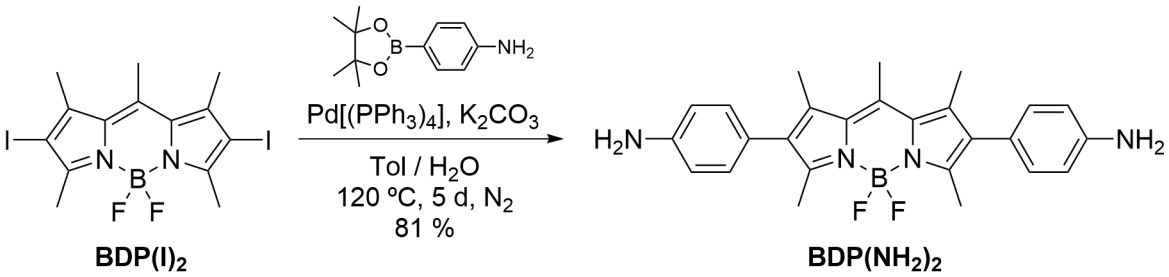

Scheme S2. Synthesis of **BDP(NH$_2$)$_2$**.

In a thick wall schlenk tube with a screw cap equipped with a magnetic stirrer, **BDP(I)$_2$** (500 mg, 0.973 mmol), 4-aminophenylboronic acid pinacol ester (850 mg, 3.67 mmol) and tetrakis(triphenylphosphine)palladium(0) (225 mg, 0.195 mmol) were dissolved in toluene (20 mL). The solution underwent three vacuum/nitrogen cycles and then an aqueous solution of potassium carbonate (1.34 g in 3 mL of H_2O) was introduced in one portion. After another three vacuum/nitrogen cycles, the solution was heated under stirring at 120 °C for five days. After the completion of the reaction, the crude mixture was cooled to room temperature and sodium sulphate was added. The crude product was passed through a first short silica column using DCM/EtOAc (1:1) as eluent mixture. After collecting the pink-red fractions and removing the solvent under vacuum, the crude product was further purified by a second silica column chromatography using DCM/*n*-hexane/EtOAc 8:1:1 as eluent mixture to yield **BDP(NH$_2$)$_2$** as a sparkly green solid (350 mg, 81%). If in any case, small impurities from the pinacol ester were found, the solid could be further washed with *n*-hexane, if required. **^{1}H NMR** (400 MHz, THF-d_8, RT): d = 6.91 (dt, ^3J = 8.5 Hz, 4H), 6.64 (dt, ^3J = 8.5 Hz, 4H), 4.60 (s_{br}, 4H), 2.71 (s, 3H), 2.41 (s, 6H), 2.34 (s, 6H) ppm. **^{13}C NMR** (101 MHz, THF-d_8, RT): 152.60, 148.44, 141.68, 136.75, 134.48, 132.71, 131.60, 122.18, 114.61, 17.21, 15.40, 13.24 ppm. **^{19}F NMR** (376 MHz, THF-d_8, RT): −147.13 (q, J_{BF} = 32.5 Hz, 2F) ppm.

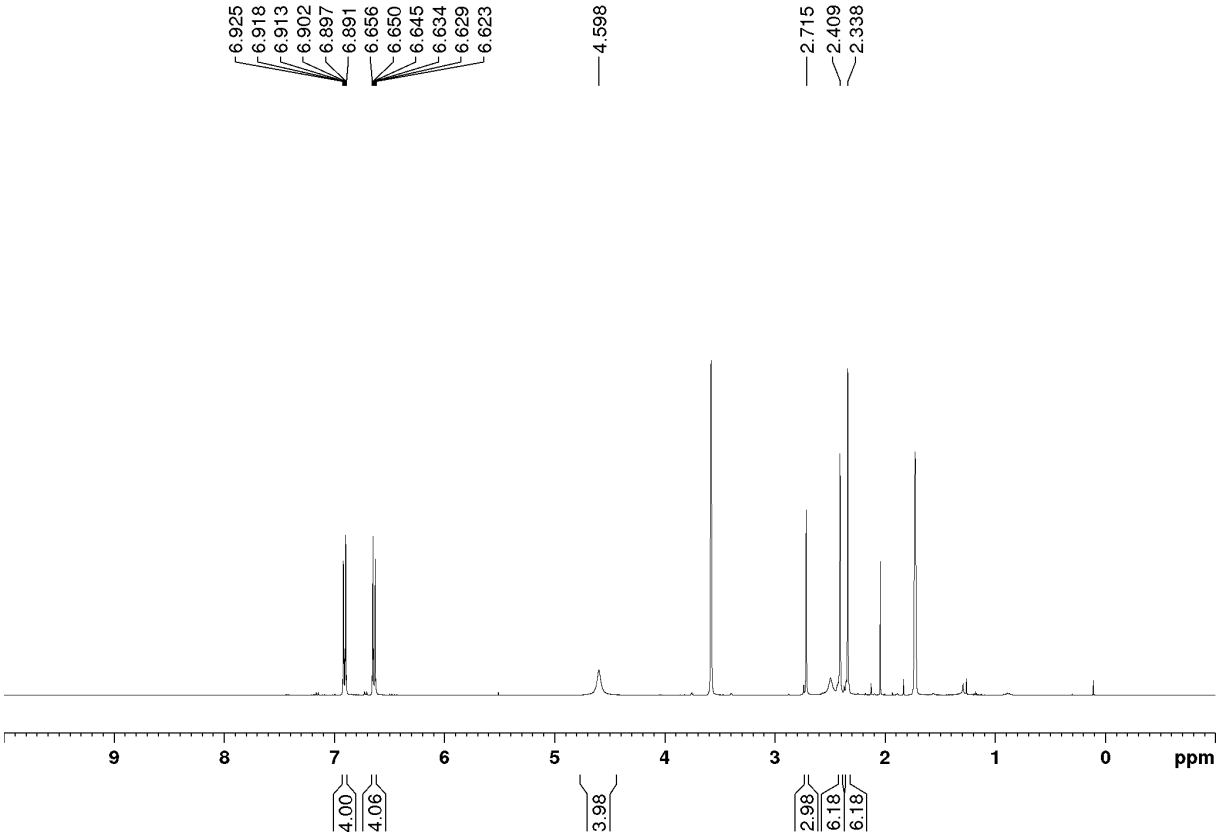

Figure S27. ^{1}H NMR (400 MHz, THF-d_8, RT) spectrum of **BDP(NH$_2$)$_2$**. The peak at 2.05 corresponds to acetone.

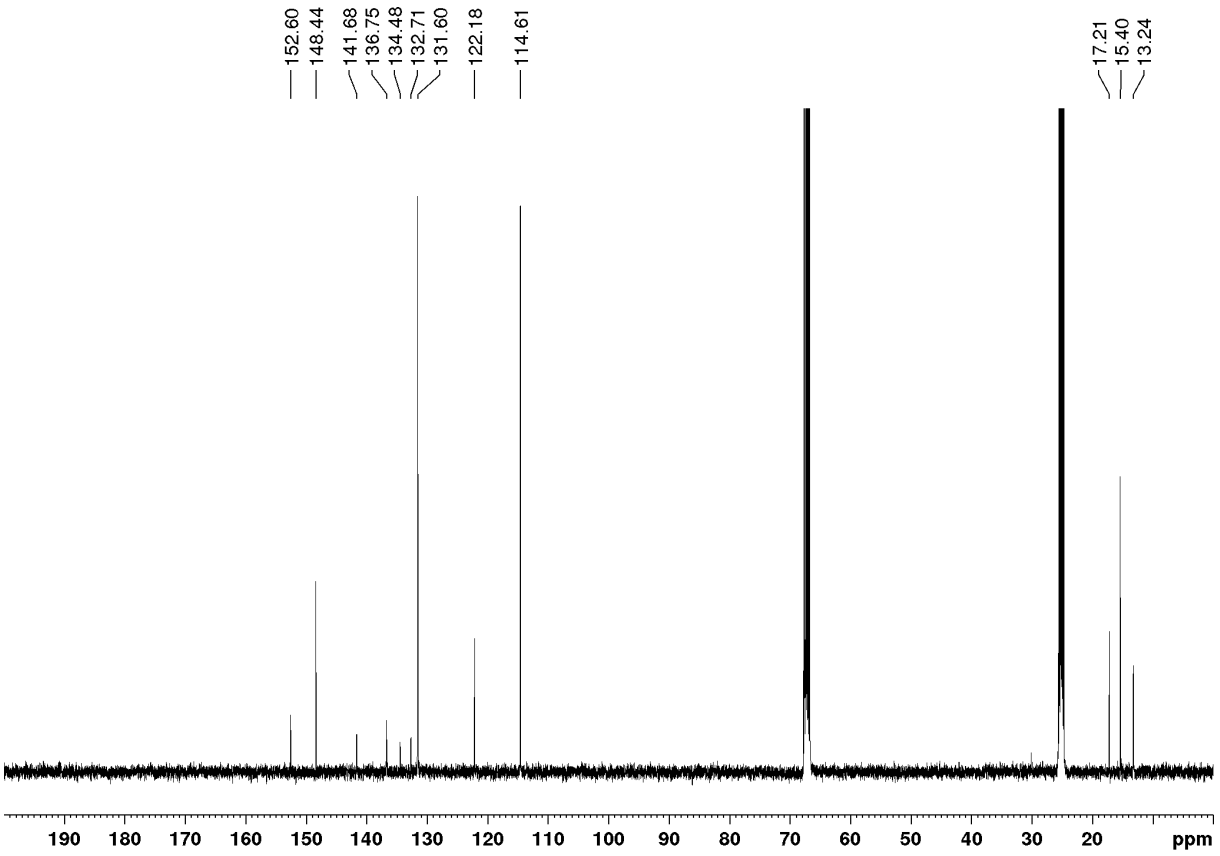

Figure S28. ^{13}C NMR (101 MHz, THF-d_8, RT) spectrum of **BDP(NH$_2$)$_2$**.

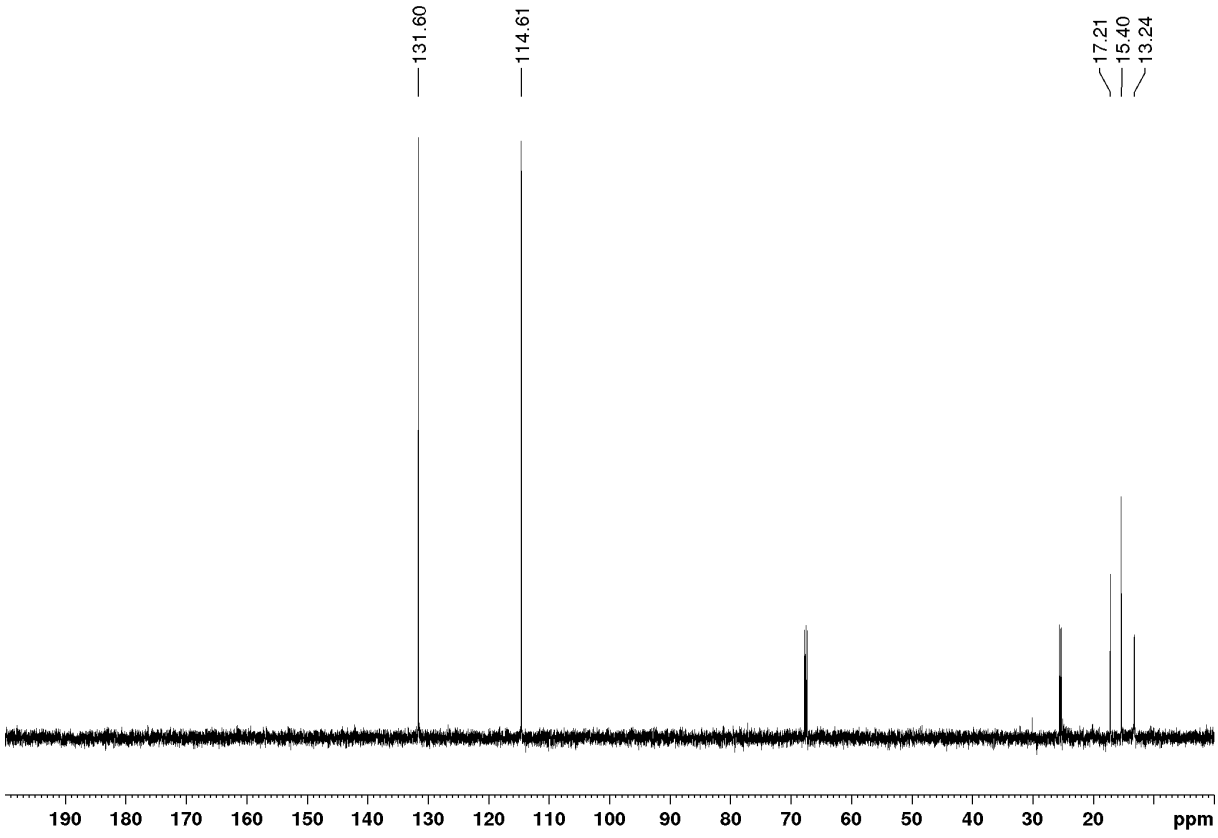

Figure S29. DEPT 135 of **BDP(NH$_2$)$_2$** (THF-d_8, RT).

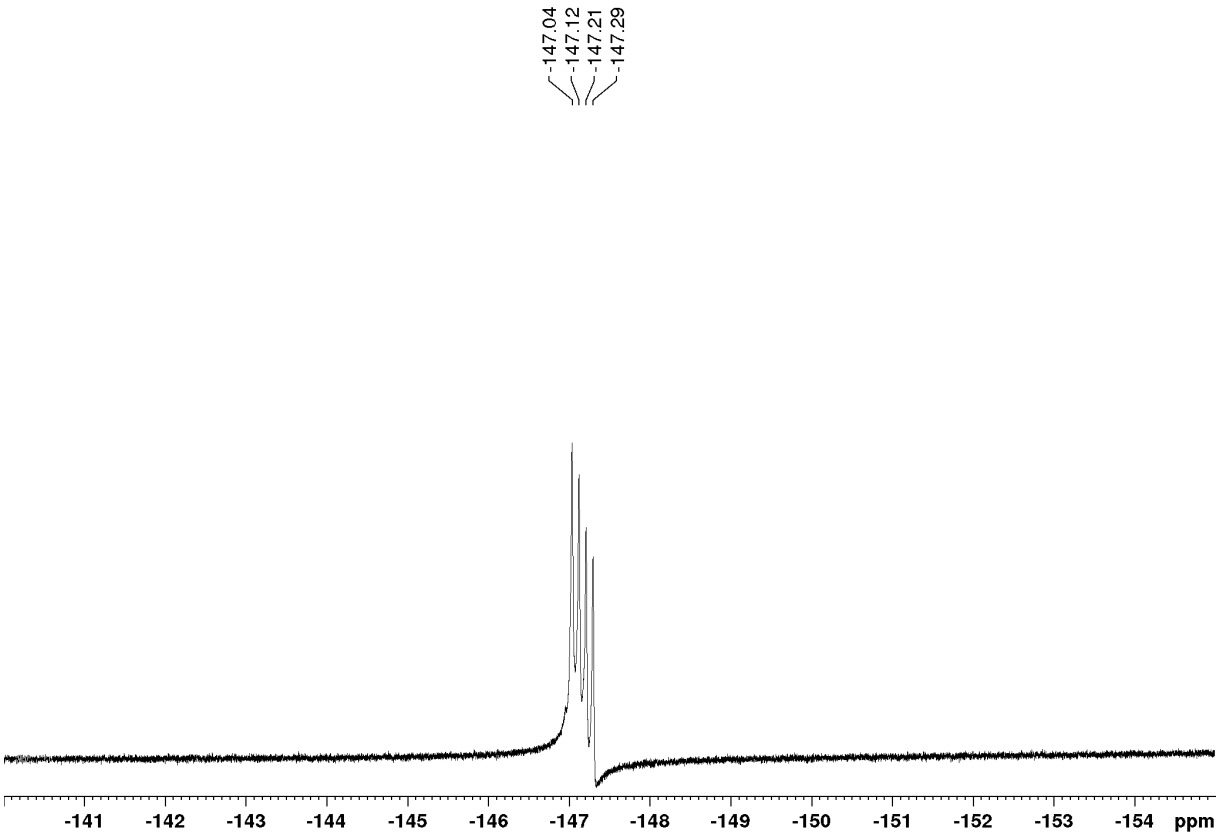

Figure S30. ^{19}F NMR (376 MHz, THF-d_8, RT) spectrum of **BDP(NH$_2$)$_2$**.

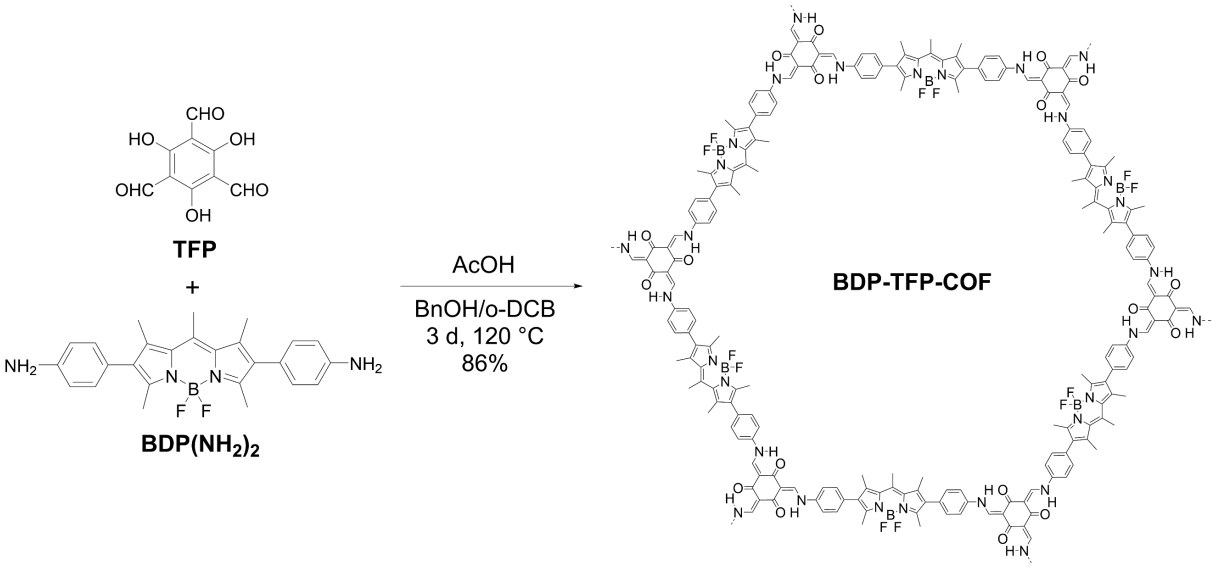

Scheme S3. Synthesis of **BDP-TFP-COF**.

In a culture tube with screw cap, **BDP(NH₂)₂** (13.3 mg, 0.03 mmol) and **TFP** (4.2 mg, 0.02 mmol) were immersed in BnOH (1 mL) and o-DCB (1 mL) and sonicated for ten minutes. To that mixture, aqueous acetic acid (100 µL of a 6 M solution) was added. The tube was sealed off under argon and the mixture was sonicated for another ten minutes to homogeneously disperse all the reactants. The tube was kept in a preheated oven at 120 °C for three days. The precipitate was filtered and washed by Soxhlet extraction with anhydrous THF overnight. Further washing via solvent exchange with acetone and pentane and drying under vacuum at room temperature for 4 h yielded **BDP-TFP-COF** as a red solid (14.1 mg, 86%). The reaction can be scaled up, and for larger batches, the precipitate was collected via centrifugation.

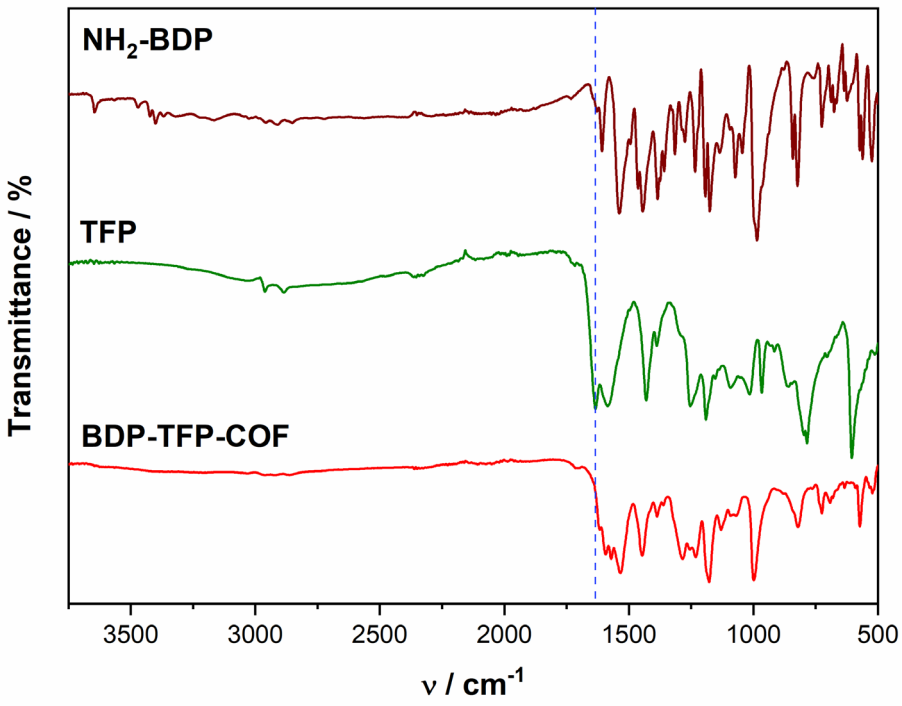

Figure S31. FT-IR spectra of the molecular building blocks and **BDP-TFP-COF**. In blue, C=O stretch band at 1646 cm^{-1} of the aldehyde moieties from the TFP block.

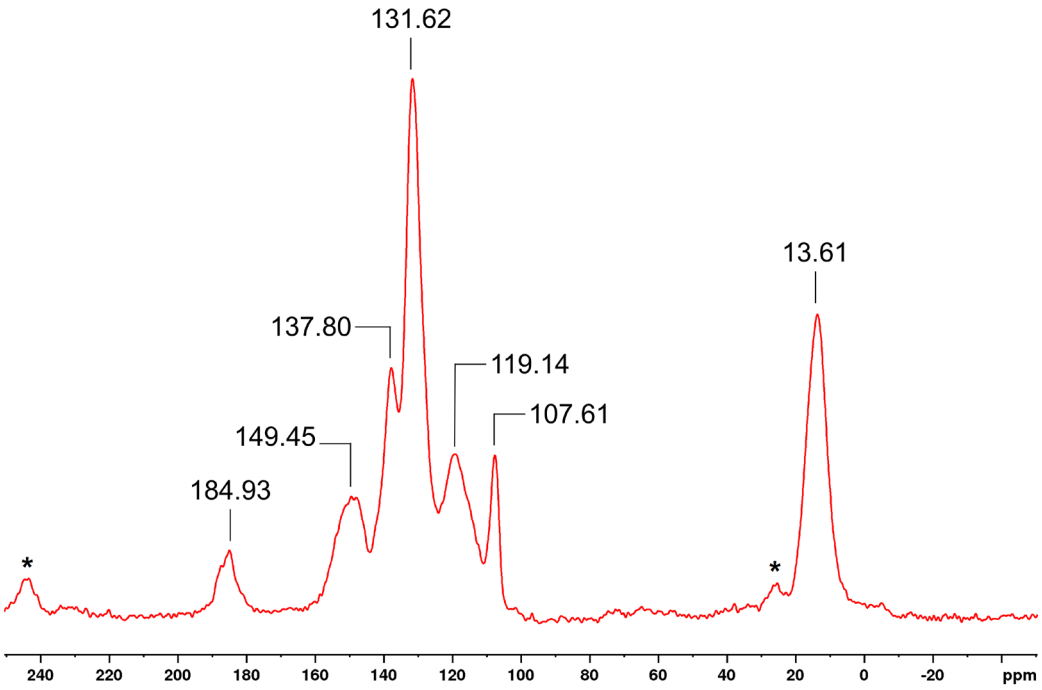

Figure S32. ^{13}C CP-MAS NMR (151 MHz) of **BDP-TFP-COF** at a spinning rate of 17000 KHz and a contact time of 2000 µs. The signals marked with asterisks correspond to the spinning sidebands of the measurement.

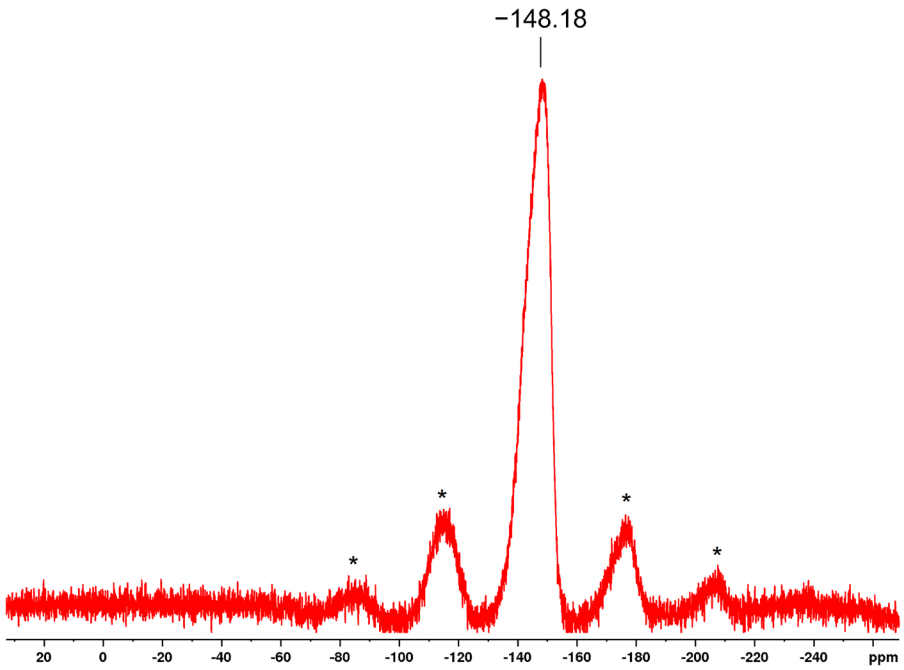

Figure S33. ^{19}F Solid State NMR (565 MHz) of **BDP-TFP-COF** at a spinning rate of 17000 KHz. The signals marked with asterisks correspond to the spinning sidebands of the measurement.

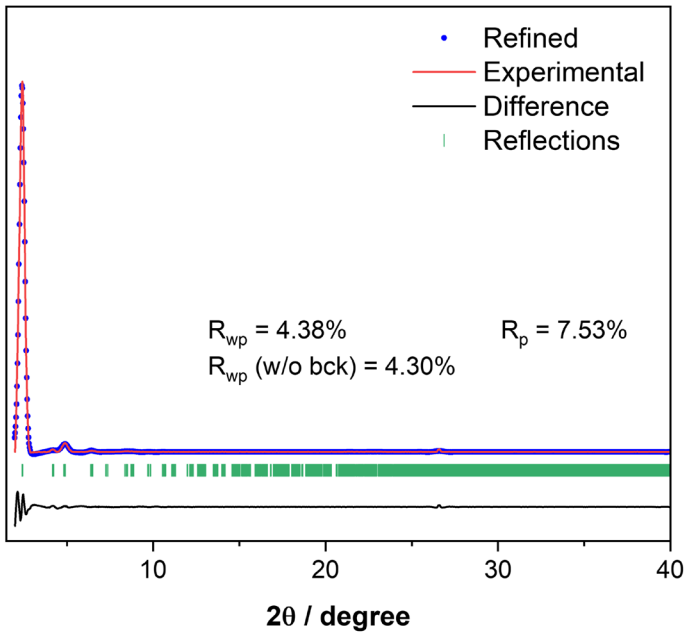

Figure S34. Pawley refinement of **BDP-TFP-COF**. Experimental data, Pawley refined simulation and their difference show good agreement of simulated PXRD and experimental patterns.

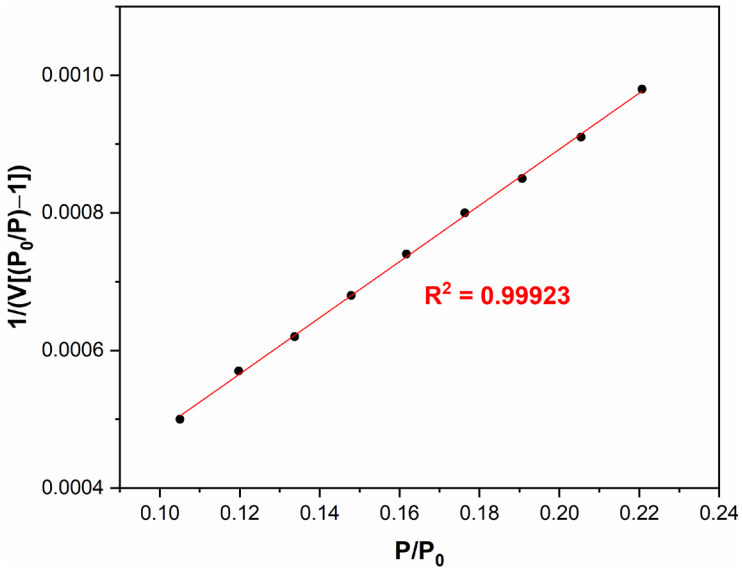

Figure S35. BET surface area plot.

8.2.3 Adsorption Experiments

8.2.3.1 Adsorption of Bisphenol A from water

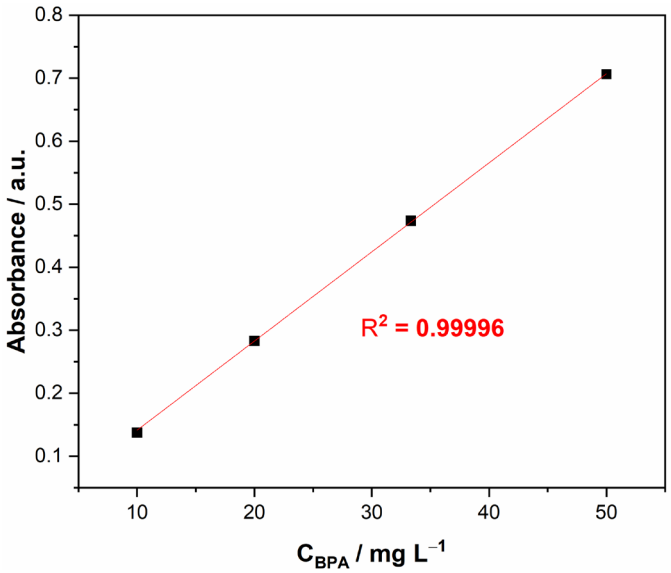

Figure S36. Calibration curve of BPA in water and linear fit.

Table S4. Concentrations of equilibrium and adsorption capacities for different dosages of **BDP-TFP-COF** in the adsorption of BPA from water at 298K.

Adsorbant dose $[g\ L^{-1}]$	C_e $[mg\ L^{-1}]$	q_e $[mg\ g^{-1}]$	**Adsorbant dose** $[g\ L^{-1}]$	C_e $[mg\ L^{-1}]$	q_e $[mg\ g^{-1}]$
0.05	81.56	368.76	0.5	13.10	173.81
	81.36	372.89		12.10	175.79
	82.04	359.22		9.38	181.23
0.1	65.75	342.45	0.75	7.46	123.38
	65.22	347.80		6.63	124.49
	64.91	350.86		5.10	126.53
0.25	32.92	268.32	1.0	2.18	97.82
	34.65	261.39		3.62	96.38
	29.13	283.48		2.99	97.00

8.2.3.2 Adsorption of Methylene Blue from water

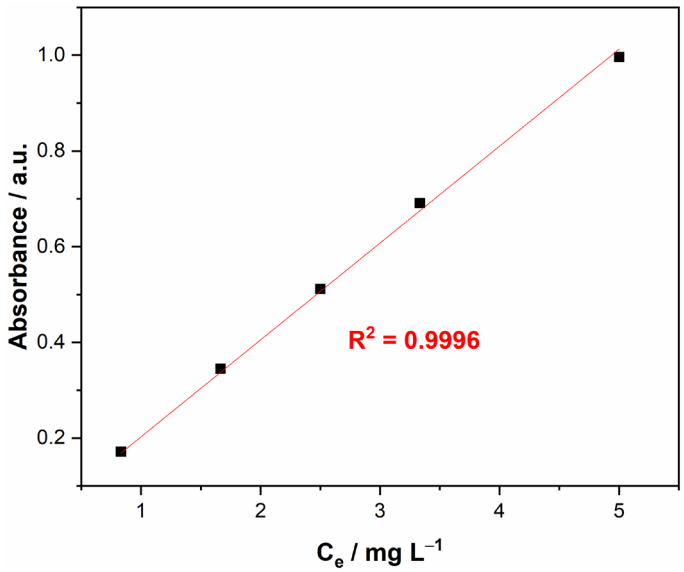

Figure S37. Calibration curve of MB in water and linear fit.

Table S5. Concentrations of equilibrium and adsorption capacities for different dosages of **BDP-TFP-COF** for the adsorption of MB from water at 298K.

Adsorbant dose $[g\ L^{-1}]$	C_e $[mg\ L^{-1}]$	q_e $[mg\ g^{-1}]$	**Adsorbant dose** $[g\ L^{-1}]$	C_e $[mg\ L^{-1}]$	q_e $[mg\ g^{-1}]$
0.1	45.02	49.82	0.75	17.32	43.57
	43.07	69.30		19.09	41.22
	42.70	72.98		20.23	39.69
0.25	36.15	55.39	1.0	8.89	41.11
	33.98	64.10		15.27	34.73
	36.12	55.52		14.54	35.46
0.5	22.93	54.14			
	27.00	45.99			
	25.83	48.34			

8.2.4 Sensing of Methylene Blue in water

For the measures, 2 mg of **BDP-TFP-COF** were sonicated in 20 mL of Millipore water for 10 minutes in order to achieve a homogeneous dispersion.

Figure S38. Photograph of the **BDP-TFP-COF** dispersion (0.1 mg mL^{-1} in water) in water manifesting Tyndall effect after irradiation with a laser.

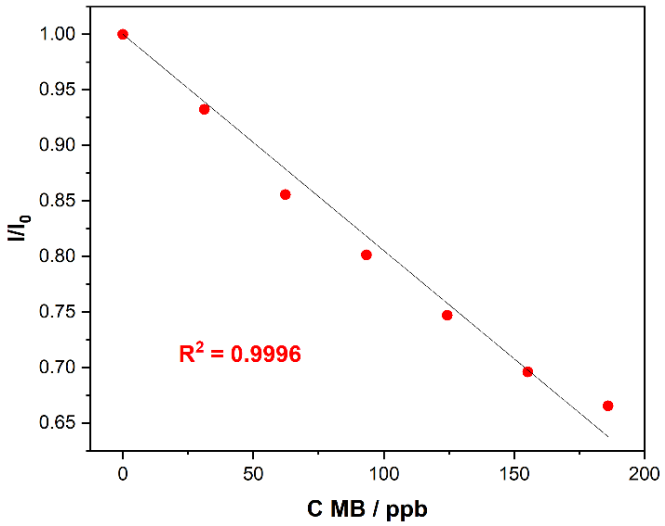

Figure S39. Linear fitting for the plot of the relative fluorescence intensity versus the concentration of MB in the range of 0 and 200 ppb.

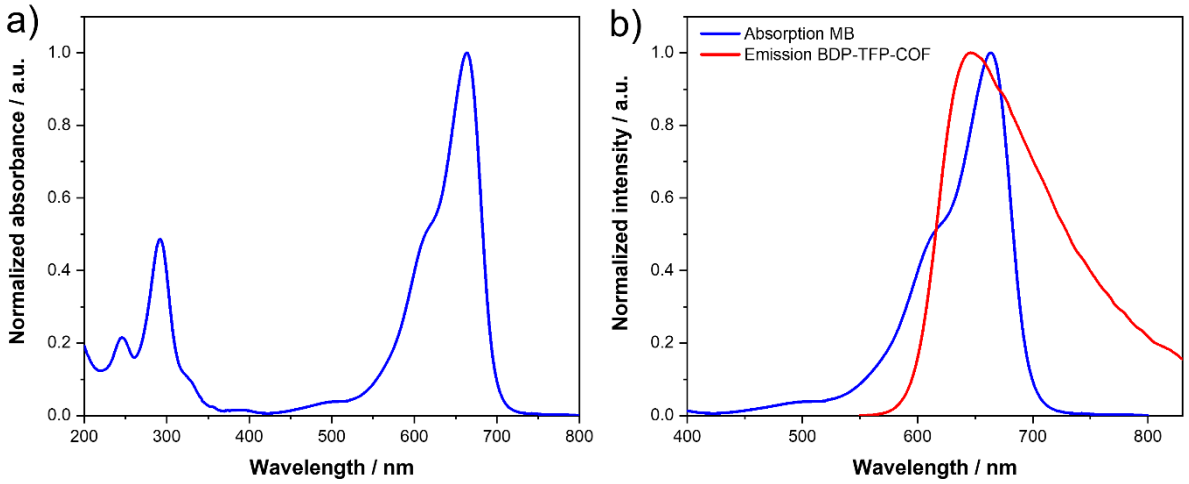

Figure S40. a) Normalized absorption spectrum of MB in water and b) spectral overlap of normalized absorption of MB and emission of **BDP-TFP-COF**.

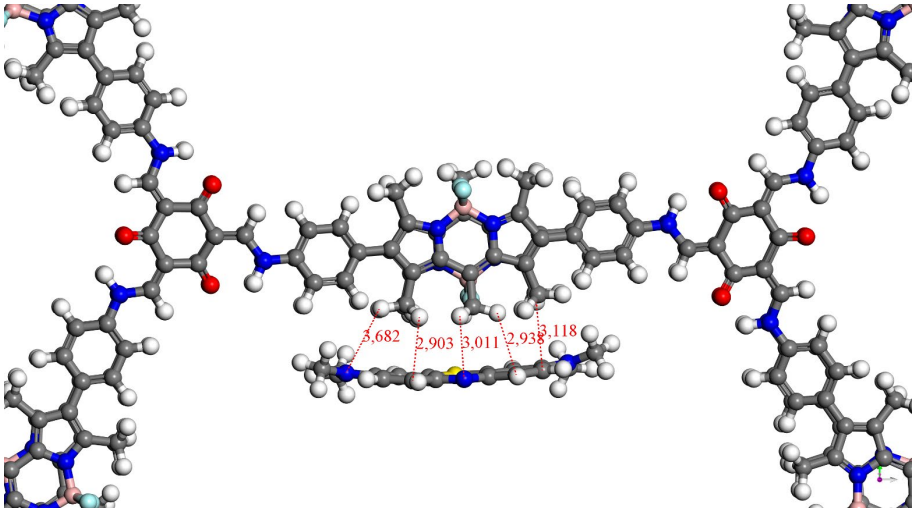

Figure S41. Proposed main intermolecular interactions and distances between MB molecules and the **BDP-TFP-COF** structure.

8.2.5 Singlet Oxygen Generation

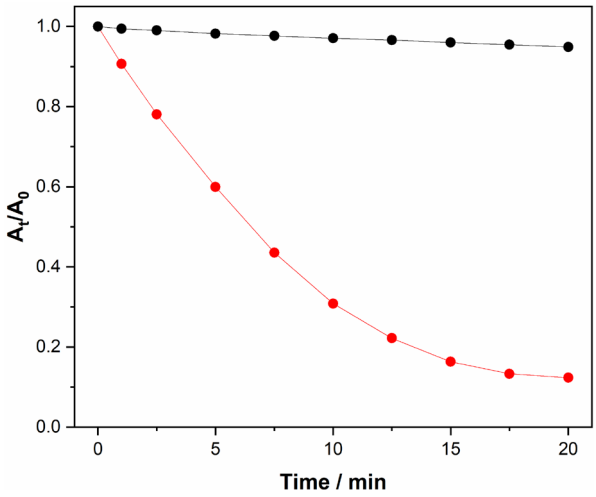

Figure S42. Plots of A_t/A_0 at 415 nm of DPBF ($1 \cdot 10^{-4}$ M in DMF) versus irradiation time (green light: λ = 528 nm, intensity ~7 W) in the absence (black) and in the presence (red) of **BDP-TFP-COF** (0.2 mg mL^{-1}).

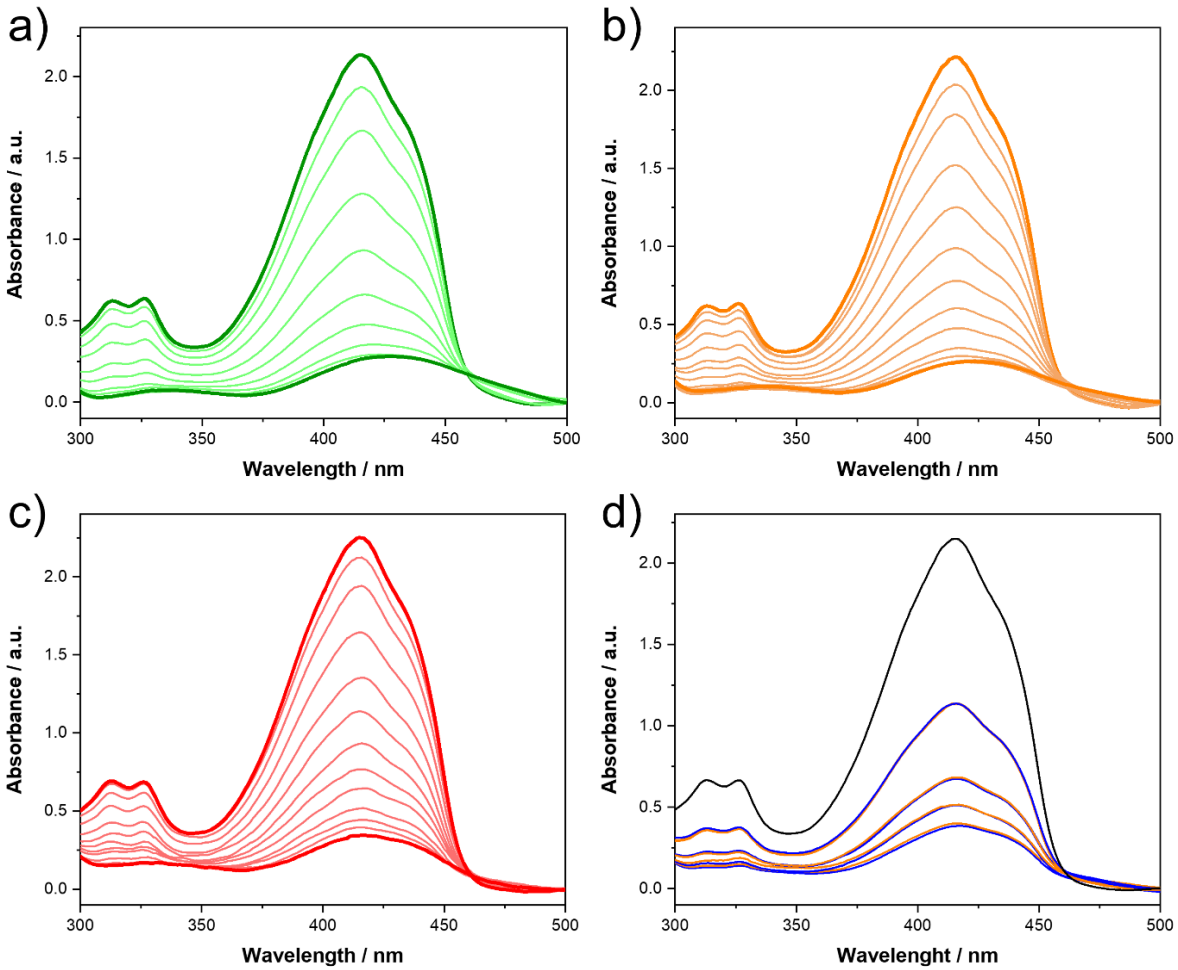

Figure S43. Absorption spectra of DPBF ($1 \cdot 10^{-4}$ M in DMF) over irradiation time in the presence of **BDP-TFP-COF** (0.2 mg mL^{-1}) with different wavelengths: a) green light: λ = 528 nm, intensity ~7 W, b) amber light: λ = 590 nm, intensity ~7 W, c) red light: λ = 617 nm, intensity ~7 W. d) Absorption spectra of DPBF ($1 \cdot 10^{-4}$ M in DMF) in the presence of **BDP-TFP-COF** (0.2 mg mL^{-1}) after light (orange) and dark (blue) cycles (green light: λ = 528 nm, intensity ~7 W).

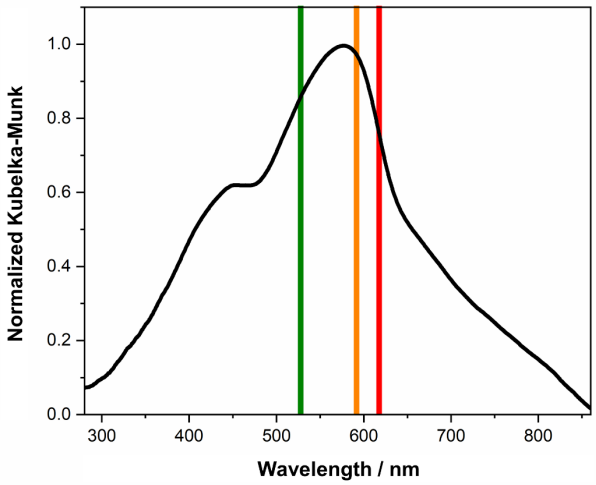

Figure S44. Wavelengths of employed LEDs superposed on the UV-Vis absorption spectra of **BDP-TFP-COF**.

8.2.6 Photoconversion of a Mustard Gas Simulant

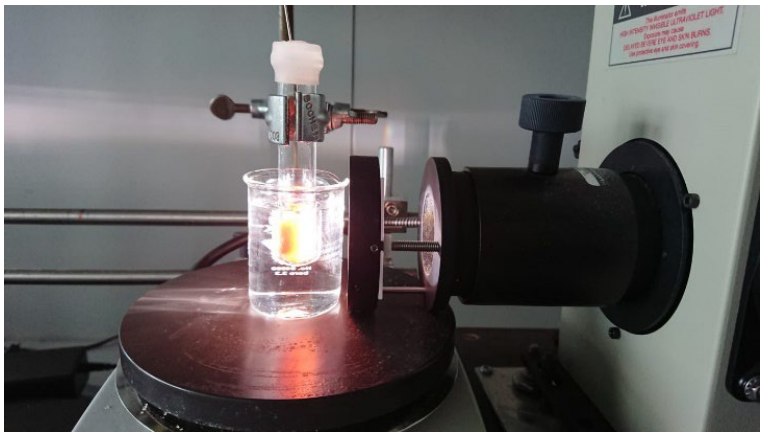

Figure S45. Photograph of the experimental setup for the photocatalytic transformation of CEES.

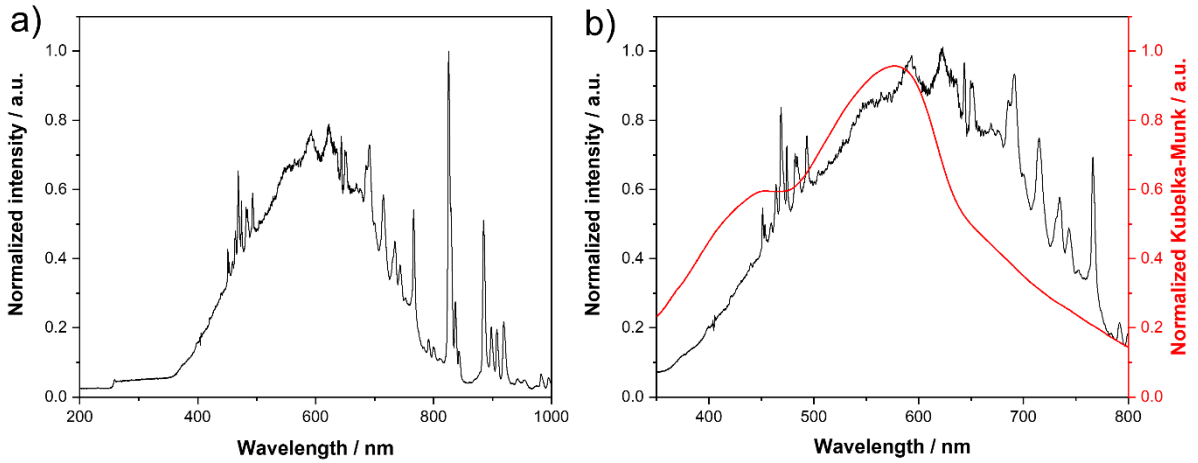

Figure S46. a) Irradiated light spectrum and b) overlapped lamp light spectrum and UV-Vis absorption spectrum derived from the diffuse reflectance of **BDP-TFP-COF**.

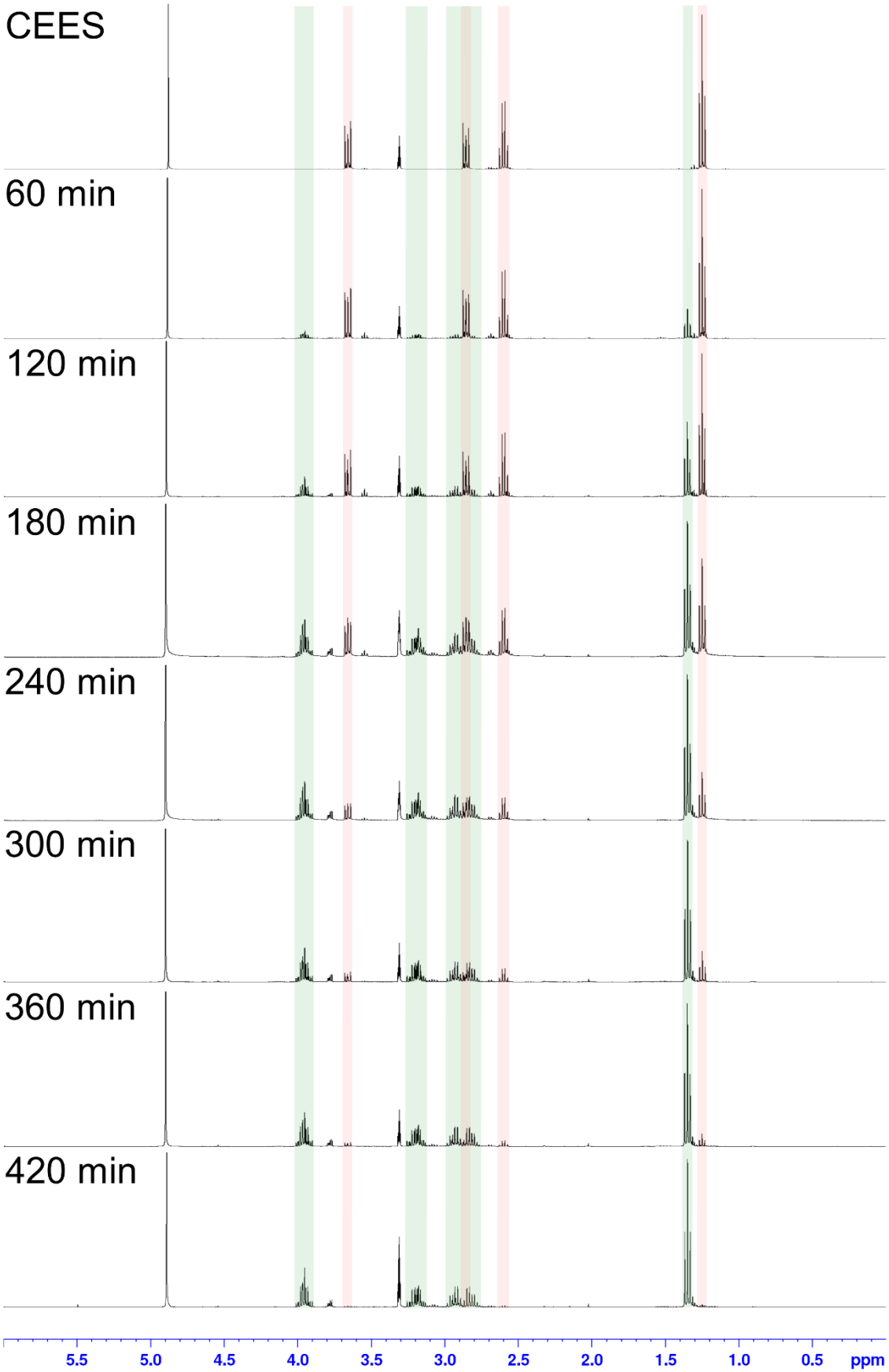

Figure S47. NMR spectra of CEES (400 MHz, 0.1 M in MeOD, RT) upon irradiation with white light (230 mW cm^{-2}) in presence of **BDP-TFP-COF** (1% mol) at different reaction times. The peaks found at 3.8 ppm are not attributed to the overoxidized $CEESO_2$ molecule but to a common slight CEES decomposition.[331]

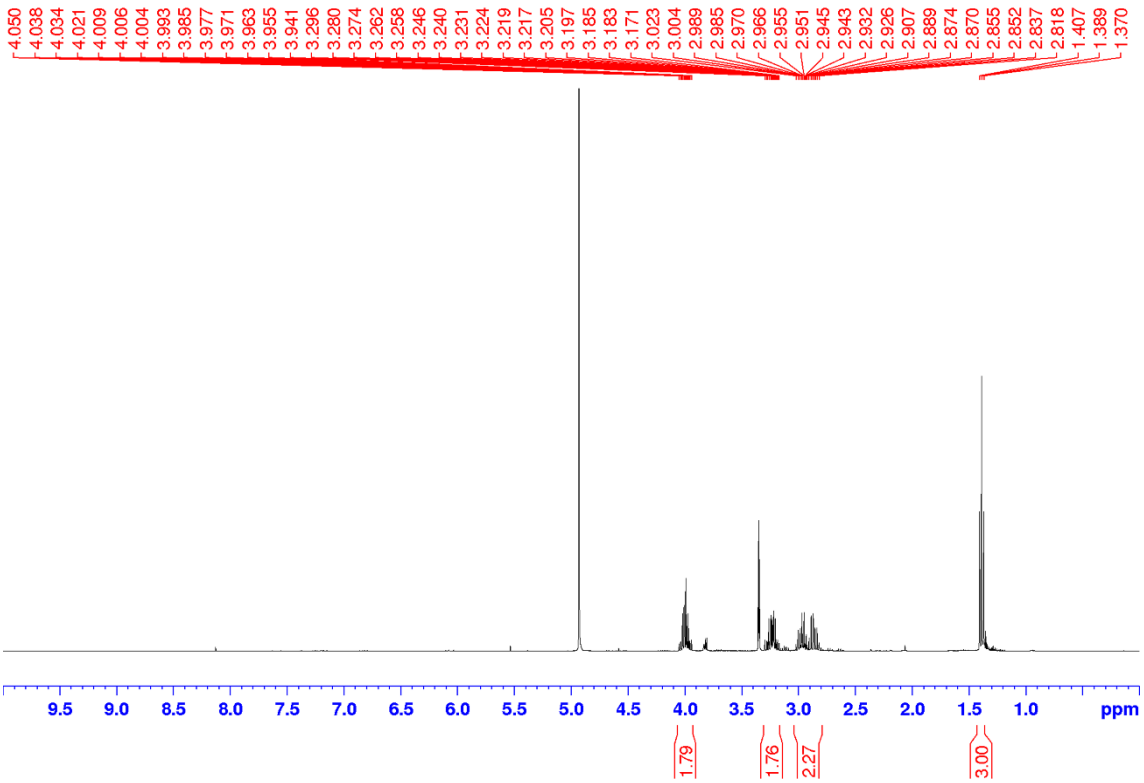

Figure S48. [1]H NMR (400 MHz, MeOD, RT) spectrum of CEESO obtained from the photooxidation of CEES.

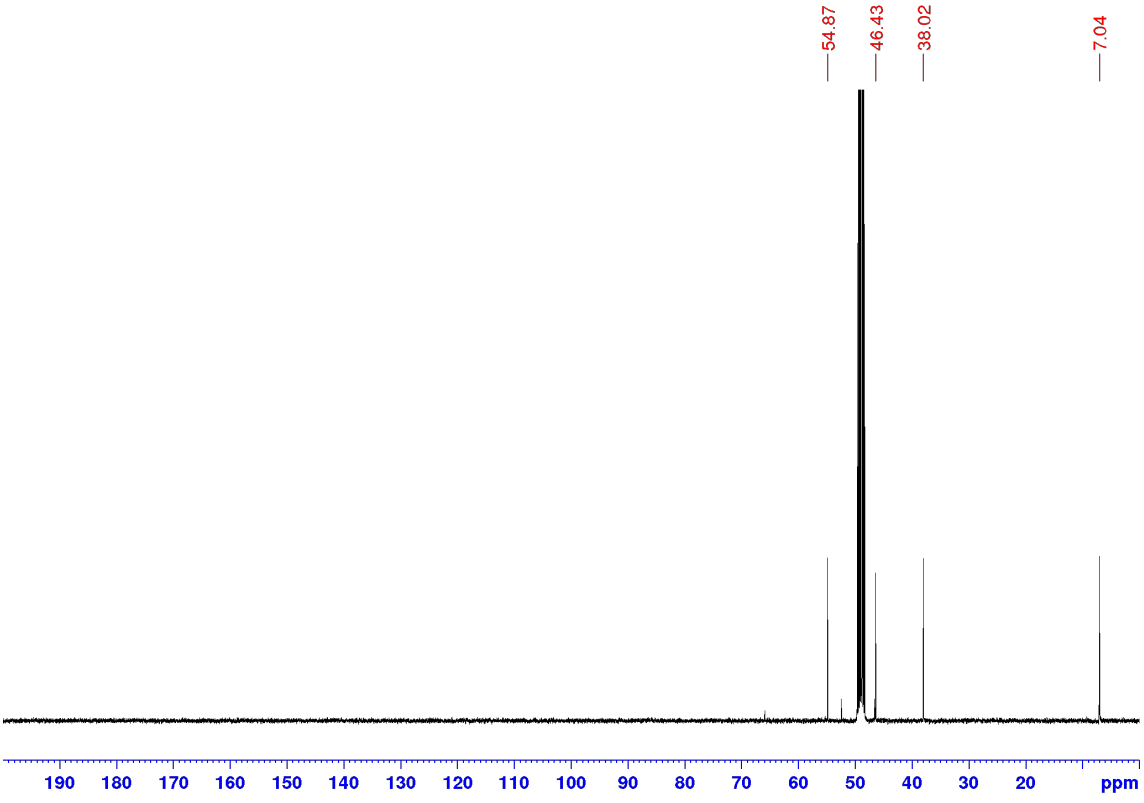

Figure S49. [13]C NMR (101 MHz, MeOD, RT) of CEESO obtained from the photooxidation of CEES.

8.3 Supporting information for Chapter 5: Synthesis and Characterization of a Low-Bandgap Diketopyrrolopyrrole-Pyrene Covalent Organic Framework.

8.3.1 Materials and Methods

Solvents and reagents were bought from commercial suppliers (Sigma-Aldrich, Acros, VWR, ABCR, TCI chemicals and, if not specified otherwise, used as received. Mesitylene, 99% "extra pure", and 1,4-dioxane, anhydrous 99.8%, were bought from Sigma-Aldrich and THF was dried with a solvent purification system "PureSolv MD 7" from Inert Technology. The tubes used in the solvothermal synthesis were purchased from VWR, with the following characteristics: Schlenk tube F58 with vacuum valve (5 or 10 mL from FengTecEx GmbH) equipped with stopcock plug (PTFE protected). $BaSO_4$ as solid matrix for diffuse reflectance experiments was purchased from Alfa Aesar. FT-IR spectroscopy was performed with a Jasco FT/IR-4600 spectrometer equipped with ATR-module. Powder X-Ray diffraction was conducted with a Bruker D8 Discover diffractometer in reflection mode with Ni-filtered Kα-radiation (λ = 1.54060 Å) and a position-sensitive detector (LynxEye). NMR spectra were recorded on a Bruker Avance 400 at 295 K. Solid state ^{13}C cross-polarization magic-angle spinning (CP-MAS) NMR spectra were measured on a Bruker Avance III HD 600 MHz NMR spectrometer with a spinning rate of 17000 Hz and a contact time of 2000 μs at a fixed temperature of 296.4 K. The theoretical model was initially built and optimized using the Forcite module of the BIOVIA Materials Studio software and the cell parameters were refined using the Reflex package in combination with the experimental PXRD data from a .raw file data transformed into an .udf file using the Xpert HighScore software. SEM images were recorded using a Zeiss Ultra Plusfield emission scanning electron microscope equipped with a GEMINI e-Beam column operated at 2 kV with an aperture size set to 30 μm to avoid excessive charging and radiation damage of the areas imaged. EDX spectroscopy was conducted with an X-Max 50 mm^2 detector from Oxford Instruments operated at 10 kV. Diffuse reflectance measurements were performed with a Perkin-Elmer Lambda 950 equipped with an integration sphere setup. Nitrogen sorption isotherm and BET surface were obtained after activation of the material under high vacuum for 16 h at 120 °C using a Micro 200 Surface area and Pore Size Analyzer from 3P instruments. Absorption spectra were recorded on a JASCO V-770 UV-Vis/NIR spectrophotometer, in quartz cell cuvettes (SUPRASIL, Hellma Analytics) with a path length of 1.0 cm. The spectral band width and the scan rate were 1 nm and 400 nm min^{-1}, respectively.

Photocatalytic experiments were performed with different ~7 W homemade led arrays using green (528 nm), amber (590 nm) and red (617 nm) light.

8.3.2 Synthesis and Characterization

DPP-1[198, 355] and **Py(NH4)2**[143, 155] were synthetized according to previously reported procedures.

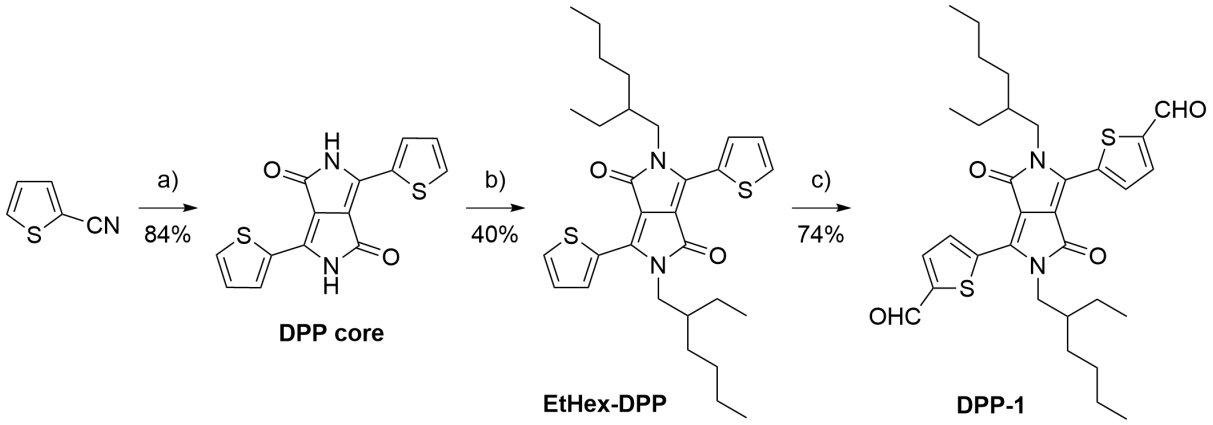

Scheme S4. Synthesis of **DPP-1**. a) Diethyl succinate, anh. ^{t}BuOK, *tert*-amyl alcohol, 110 °C, 48 h, N_2. b) 2-ethylhexyl bromide, K_2CO_3, anh. DMF, 140 °C, 48 h, N_2. c) i) LDA 1 M, anh. THF, −78 °C, 30 min, N_2; ii) *N*-formyl piperidine, anh. THF, 0 °C to RT, 3 h, N_2.

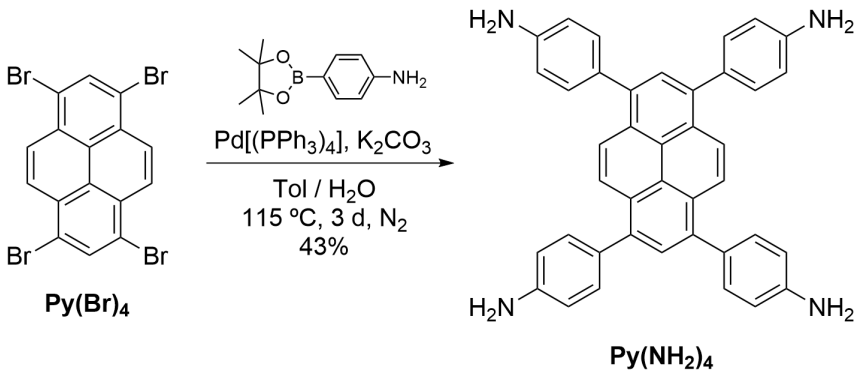

Scheme S5. Synthesis of **Py(NH4)2**.

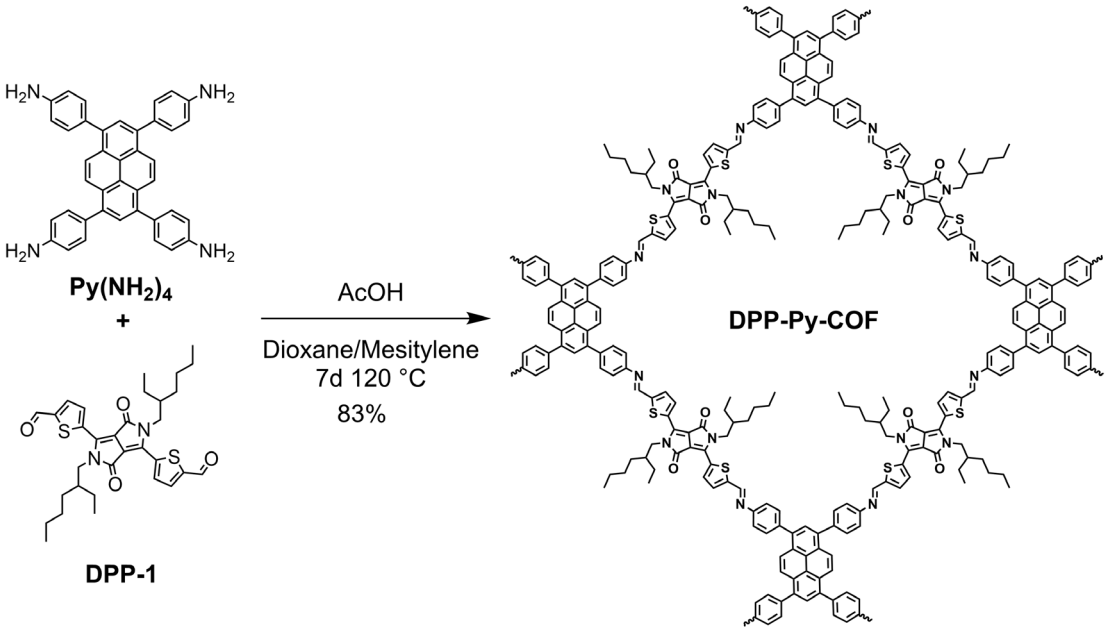

Scheme S6. Synthesis of **DPP-Py-COF**.

In a Schlenk pressure tube with a Teflon screw cap, **Py(NH$_2$)$_4$** (11.3 mg, 0.02 mmol) and **DPP-1** (23.2 mg, 0.02 mmol) were immersed in 1,4-dioxane (0.33 mL) and mesitylene (0.67 mL) and sonicated for ten minutes. To that mixture, aqueous acetic acid (100 µL of a 6 M solution) was added. The tube was sealed off under argon and the mixture was sonicated for another ten minutes to homogeneously disperse all reactants. The tube was kept in a preheated oven at 120 °C for seven days. After completion of the reaction, the precipitate was filtered and washed by Soxhlet extraction with anhydrous THF overnight. Further washing via solvent exchange with ethanol, acetone, pentane and drying under vacuum at room temperature for four hours yielded **DPP-Py-COF** as a dark purple/black solid (27.5 mg, 83%). Minor modifications of the reaction time, solvents or temperature led to less crystalline solids.

Table S6. Conditions screening for **DPP-Py-COF**.

C $Py(NH_2)_4$	C DPP-1	T	t	Dioxane:Mesitylene	V AcOH 6M	Crystallinity
mmol mL^{-1}		°C	d		µL	
0.0025	0.005	120	3	1:0	100	Amorphous*
0.0025	0.005	120	3	3:1	100	Amorphous*
0.0025	0.005	120	3	1:1	100	No reaction
0.0025	0.005	120	3	1:3	100	No reaction
0.0025	0.005	120	3	0:1	100	Insoluble blocks
0.01	0.02	120	3	1:0	100	Amorphous
0.01	0.02	120	3	3:1	100	Amorphous
0.01	0.02	120	3	2:1	100	Amorphous
0.01	0.02	120	3	1:1	100	Peaks found
0.01	0.02	120	3	1:2	100	Peaks found
0.01	0.02	120	3	1:3	100	Amorphous
0.01	0.02	120	3	1:4	100	Amorphous
0.01	0.02	120	3	0:1	100	Insoluble blocks
0.02	0.04	120	3	1:1	100	Low
0.02	0.04	120	3	1:2	100	Low
0.02	0.04	120	3	1:2	100	Low
0.02	0.04	120	4	1:2	100	Moderate
0.02	0.04	120	5	1:2	100	Moderate
0.02	**0.04**	**120**	**7**	**1:2**	**100**	**Good**
0.02	0.04	120	10	1:2	100	Minor
0.02	0.04	150	7	1:2	100	Amorphous

* Obtained in very low yield (15−20%)

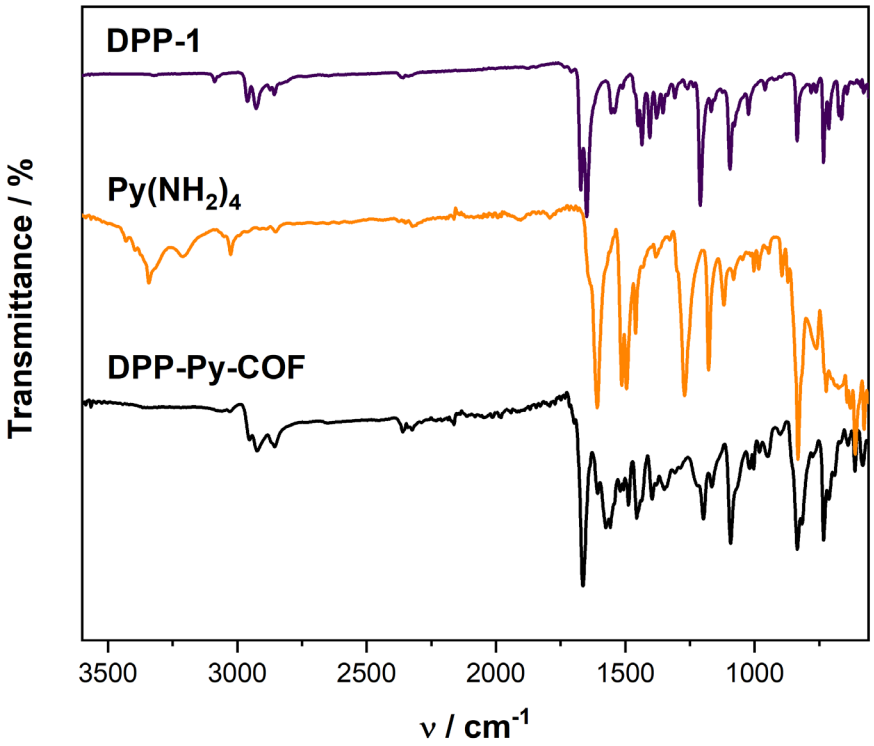

Figure S50. FT-IR spectra of the molecular building blocks and **DPP-Py-COF**.

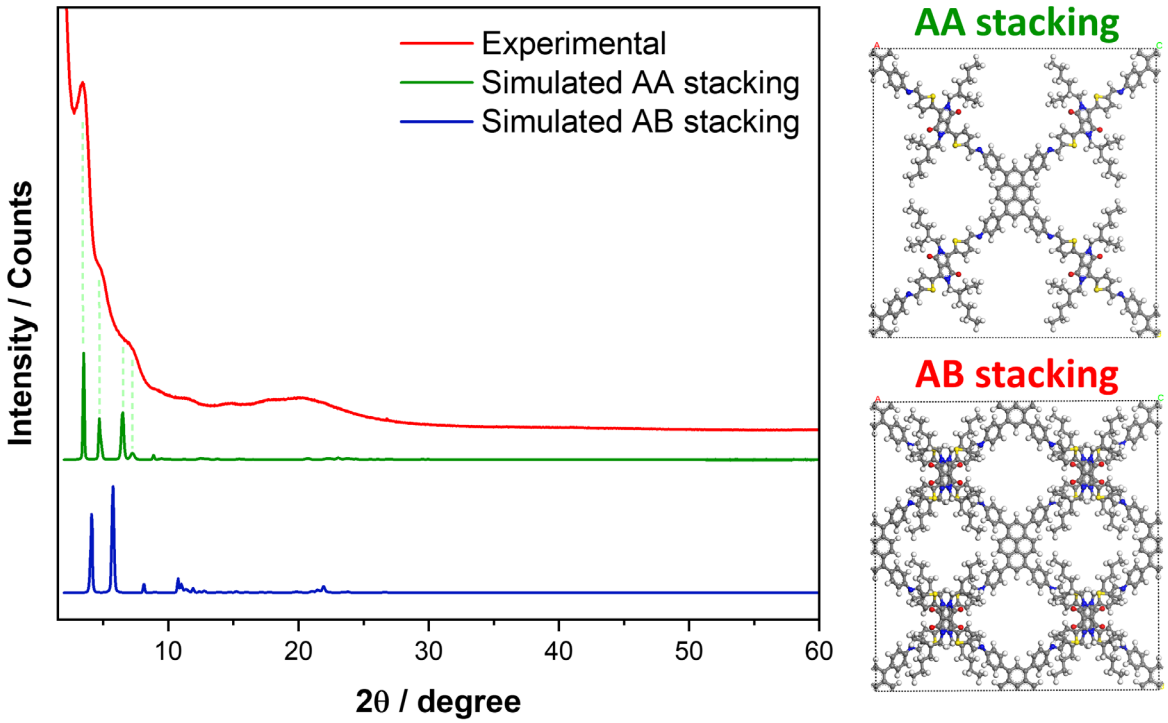

Figure S51. Experimental PXRD pattern **of DPP-Py-COF** and comparison with the simulated PXRD patterns for the AA and AB stacking modes.

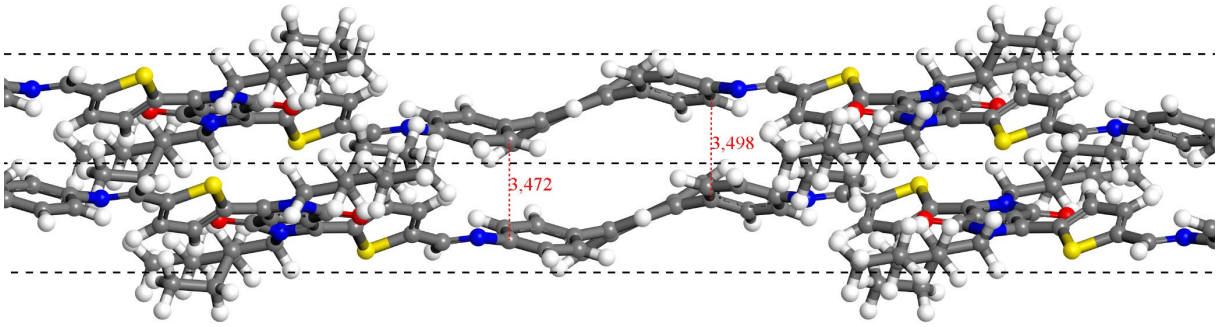

Figure S52. Zoomed region from the structural model of **DPP-Py-COF**. The distance of around 3.5 Å between phenyl moieties indicates the adequate π–π stacking of the aromatic substituents.

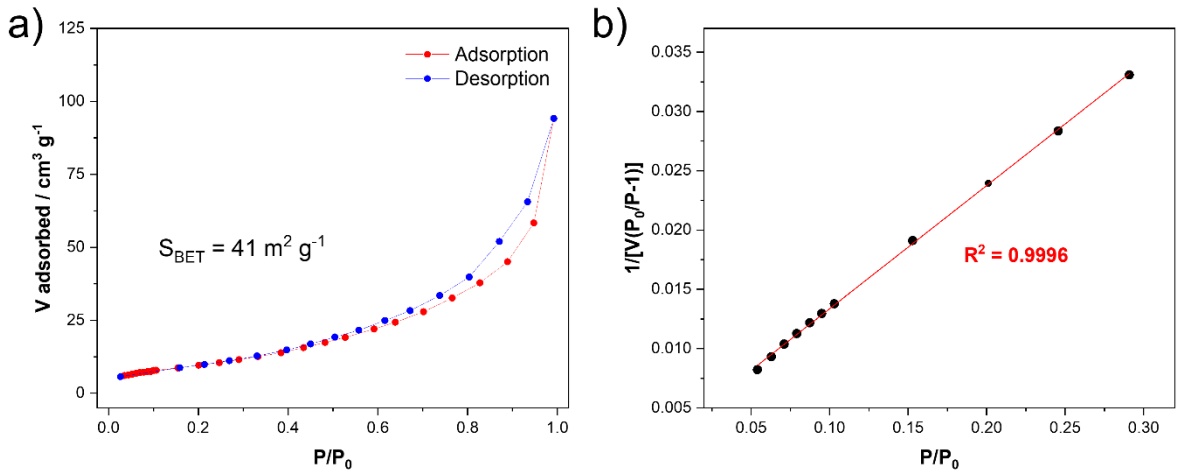

Figure S53. Nitrogen physisorption isotherm of **DPP-Py-COF** and b) BET surface area plot.

8.3.3 Singlet Oxygen Generation

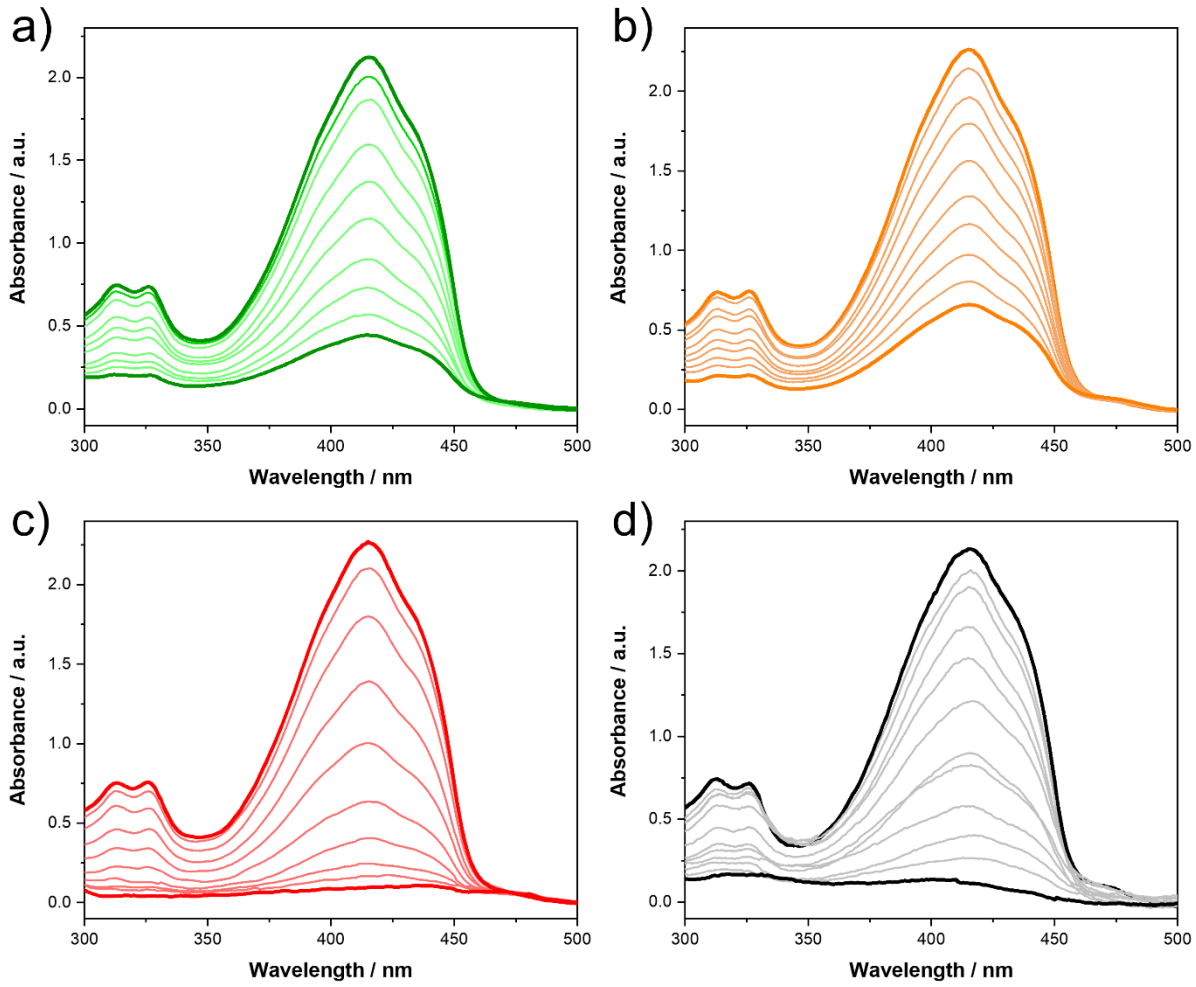

Figure S54. Absorption spectra of DPBF ($1 \cdot 10^{-4}$ M in DMF) over irradiation time in the presence of **DPP-Py-COF** (0.2 mg mL^{-1}) with different wavelengths: a) green light: λ = 528 nm, intensity ~7 W, b) amber light: λ = 590 nm, intensity ~7 W, c) red light: λ = 617 nm, intensity ~7 W. d) Absorption spectra of DPBF ($1 \cdot 10^{-4}$ M in DMF) over irradiation time in the presence of **DPP-Py-COF** (0.5 mg mL^{-1}) with green light: λ = 528 nm, intensity ~7 W.

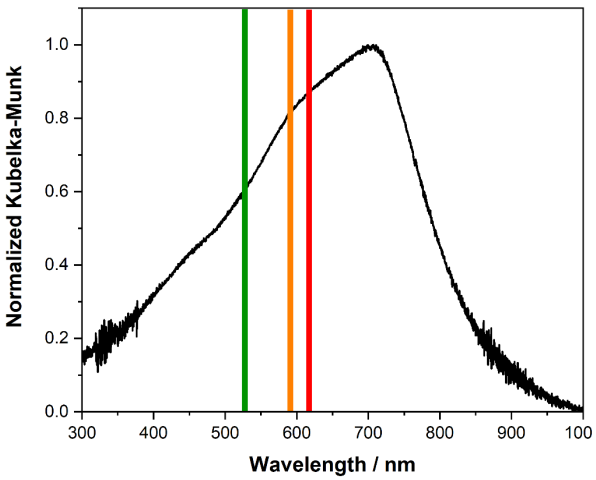

Figure S55. Wavelengths of employed LEDs superposed on the UV-Vis absorption spectra of **DPP-Py-COF**.

List of Publications

Modulation of Crystallinity and Optical Properties in Composite Materials Combining Iron Oxide Nanoparticles and Dye-Containing Covalent Organic Frameworks

Sánchez-Naya, R.; Stepanenko, V.; Mandel, K.; Beuerle, F. *Org. Mater.* **2021**, *3*, 17.

A BODIPY-Containing Covalent Organic Framework as a Highly Porous Photosensitizer for Environmental Remediation

Sánchez-Naya, R., Beuerle, F. *Manuscript in preparation.*

Synthesis and Characterization of a Low-Bandgap Diketopyrrolopyrrole-Pyrene Covalent Organic Framework

Sánchez-Naya, R., Beuerle, F. *Manuscript in preparation.*

Impact of Molecular Size and Shape on the Supramolecular Co-Assembly of Chiral Tricarboxamides: A Comparative Study.

Dorca, Y.; Sánchez-Naya, R.; Cerdá, J.; Calbo, J.; Aragó, J.; Gómez, R.; Ortí, E.; Sánchez, L. *Chem. Eur. J.* **2020**, *26*, 14700.

Solvent-directed helical stereomutation discloses pathway complexity on N-heterotriangulene based organogelators

Valera, J. S.; Sánchez-Naya, R.; Ramírez, F. J.; Zafra, J. L.; Gómez, R.; Casado, J.; Sánchez, L., *Chem. Eur. J.* **2017**, *23*, 11141.

Individual Contributions

The co-authors of the publications presented in this semicumulative Thesis are informed and agree with the reprint as well as with the individual contributions stated below.

Publication: Modulation of Crystallinity and Optical Properties in Composite Materials Combining Iron Oxide Nanoparticles and Dye-Containing Covalent Organic Frameworks, *Org. Mater.* **2021**, *3*, 17.

Authors: Roberto Sánchez Naya (Main author, RSN), Vladimir Stepanenko (co-author, VS), Karl Mandel (corresponding author, KM), Florian Beuerle (corresponding author, FB).
Detailed presentation of the contributions to the publication (in %).

Author	**RSN**	**VS**	**KM**	**FB**	**∑ in Percent**
Conceptualization	-	-	2%	3%	5%
Synthesis	30%	-	5%	-	35%
Characterization and studies	27%	3%	-	-	30%
Manuscript writing	7%	1%	2%	10%	20%
Manuscript correction	1%	1%	1%	7%	10%
Sum	65%	5%	10%	20%	100%

Individual contributions for *Chapter 4:* A BODIPY-Containing Covalent Organic Framework as a Highly Porous Photosensitizer for Environmental Remediation. *Manuscript in preparation*.

Author	**RSN**	**FB**	**∑ in Percent**
Conceptualization	3%	2%	5%
Synthesis	25%	-	25%
Characterization	15%	-	15%
Modelling	10%	-	10%
Applications	25%	-	25%
Manuscript writing	12%	3%	15%
Manuscript correction	-	5%	5%
Sum	90%	10%	100%

Individual contributions for *Chapter 5:* Synthesis and Characterization of a Low-Bandgap Diketopyrrolopyrrole-Pyrene Covalent Organic Framework. *Manuscript in preparation*.

Author	**RSN**	**FB**	**∑ in Percent**
Conceptualization	3%	2%	5%
Synthesis	25%	-	25%
Characterization	15%	-	15%
Modelling	15%	-	15%
Singlet oxygen generation experiments	10%	-	10%
Manuscript writing	17%	3%	20%
Manuscript correction	-	10%	10%
Sum	85%	15%	100%

Acknowledgements

Since I was little, I always wanted to be a scientist. I remember a 6-8 y.o. mini-me trying to mix stuff in the same pot to see if I could create the best potions. Now, 20 years later, this has become a reality (But somehow it was more complex that young me could imagine) and I have no words to sum up this. This Thesis has represented for me a rollercoaster of emotions, path of challenges and it developed my maturity as a chemist and as a person. It has been a long ride in which every person had an impact on my behaviour and way of thinking, so I will not hesitate to dedicate enough lines for all of you.

I cannot begin without expressing my deepest gratitude to **Dr. Florian Beuerle** for putting his confidence in me and offering me such a colourful project. I am greatly indebted to his good advice, unvaluable help and his remarkable friendly character during my stay here. I sincerely wish you all the success in your new stage.

I would like to pay special regards to **Prof. Dr. Frank Würthner** for providing excellent and modern facilities for the development of the projects and keeping the lab as a safe environment during the COVID pandemic.

I highly appreciate **Dr. Karl Mandel** (University of Erlangen) and his group for the synthesis of the iron oxide nanoparticles and the fruitful collaboration.

A special mention will go to **Dr. Suvendu Karak**, who, apart from being a good friend and coffee break partner, has shown me his excellent quality as a researcher. Thank you for sharing your vast knowledge with me and always having a moment for my questions. You have set an inflexion point in my PhD and all of this would not have been possible without your help.

I also express my sincere gratitude with **Dr. Vladimir Stepanenko** for all the numerous SEM and EDXS measures performed during my thesis. Furthermore, I thank to **Stephanie Bachmann**, **Dr. Marvin Grüne** and **Jun.-Prof. Dr. Ann-Christin Pöppler** for the solid-state NMR measurements, as well as providing some insights and information regarding the topic.

I would like to acknowledge **Dr. Matthias Stolte** and **Dr. David Schmidt** for some insightful discussions and the smooth running of the CNC building and the instrumentation during my stay. In addition, I want to thank **Julius Albert, Jennifer Begall, Olga Anhalt, Ana-Maria**

Krause, Astrid Kudzus, **Joachim Bialas** and **Ann-Kathrin Lenz** for keeping the lab running on a daily basis.

I am very grateful to **Eleonore Klaus** and **Lisa Weidmer** for all the assistance and invaluable help with all the application and many German documents.

It was a pleasure to work with my students: Thank you **Sophie**, **Aaron** and **Vasilios** for all the nice environment and conversations together inside and outside the lab.

I would also like to thank all the members of the **Würthner group** and the **Nowak-Król group** for all the cool "Stammtisch" together and the good atmosphere.

I obviously extend my gratitude to my small AK Beuerle for all the fun and enjoyable moments together. Thank you all, **Natalie**, **Svet**, **Philip**, **Tilman** and **Viki**. Dealing with my loud music in the morning was not an easy task but you survived. It was extremely relieving to share complains about crystallinity or synthetic problems while I was doing all this "nanosheet" stuff. I thank you for all the support and advice who helped me going a step forward.

I want to express my deepest gratitude to my dear friends **Pradeep**, **Santosh**, **Anurag**, **Suvendu**, **Niyas**, **Chia-An** and **Penzhong**, for the years of friendship and awesome moments together. I am really grateful for all the conversations and time inside and outside the lab that made some great memories and for sharing all your cultural aspects (and spicy food) with me. You really improved my stay here. I do not forget to mention you either **Evros**, our nice conversations made me briefly felt in the Mediterranean every time.

I am incredibly grateful for all the people I met outside the lab and I had the opportunity to share my time here with. **Esteban**, **Patty**, **Chris**, **Duru, Filip**, **Pau**, I am happy that I met you and I am extremely thankful for all the different plans that kept me disconnected a bit from the lab work. **Vicky**, all the plans with you, fun moments and your priceless help made my stay in Würzburg and in the WG amazing, I want to thank you for all these years being such a genuinely good friend. **Pascal**, I cannot imagine now how Würzburg would be without meeting you, thank you from the bottom of my heart for such a warm welcome in Germany while I was still lost here and for all the huge help that you provided me here, I really owe you a lot.

Chicas: **Cristina**, **Claga**, **Marta** y **Patricia**, estoy increíblemente agradecido de haberos conocido. Me habéis hecho sentir cómo en casa y animado cuando más lo necesitaba. Han sido unos años increíbles en los que ha pasado de todo y formáis una parte clave de mi estancia aquí.

Diego y **Paula**, gracias de corazón, ha sido maravilloso compartir este tiempo con vosotros. Han sido años geniales de muchas risas, viajes y planes juntos (Estudiar los exámenes de alemán ya algo menos). Sois unos amigos increíbles y habéis hecho de mi tiempo aquí algo memorable. Os debo muchísimo.

A mis compañeros de Máster: **Gorka**, **Nacho**, **Pedro**, **Álvaro y Alex**. Nunca me imaginaría que los Simpson me uniría tanto a unos extraños que me presentó la química orgánica. Gracias por estos años y momentos geniales a pesar de haber coincidido brevemente.

A mis amigos químicos y no tan químicos, que a pesar de la distancia todavía puedo contar con vosotros, no tengo palabras. **Manu G**., **Antonio**, **Mumu**, **Manu B**., **Sandra**, **Rubén**, **Sara**, **Andrea**: Muchas gracias por seguir ahí de verdad e intentar sacar un rato siempre que me paso fugazmente a Madrid.

Fer, **Raquel**, mis estimados compis de labo, gracias también a vosotros porque formáis parte de este proceso desde los comienzos.

Bea, mi compañera de penas en Alemania. Gracias por todos estos largos años que ya van desde el CSIM. Ha sido muy bonito poder contar contigo e ir más o menos a la par en nuestras tesis. Gracias además por tu inestimable ayuda con todo, los buenos momentos y los tips para sobrevivir aquí, especialmente a no decir servus en NRW para que no te miren raro.

Víctor y **Alberto**, me conocisteis hace más de 10 años como un pipiolo de 18. Me brindasteis vuestra amistad desde el primer día de universidad (Bueno, Víctor desde el segundo…) y vosotros sois ciertamente los primeros que han visto desarrollar mi pasión por esto. Habéis estado ahí desde el inicio y todavía seguís aquí. Sois los mejores.

Karina, it has been a crazy ride here. I deeply thank you for your companion and interest on my nerdy science talks. I felt your support constantly and you always have cheered me up and had the perfect choice of words to keep me motivated when I felt at the lowest point. I cannot repay you enough for this. I am extremely grateful to have you in my life, you deserve everything good that happened to you. Ich liebe dich.

Lorena. Tú sabes cómo nadie lo que es pasar por una situación así y tu apoyo y comprensión han sido vitales para mí. Literalmente he crecido contigo (sobre todo a lo ancho) y siempre has estado ahí para todo. No sabes la increíble suerte que tengo por contar contigo. Muchas gracias de corazón por tu amistad.

Ángela, si alguien me ha convencido de dar el salto y salir de mi zona de confort has sido tú. Yo no estaría aquí ni sería de la forma que soy si no fuese por ti, encontraste en mí un refugio que ni siquiera yo creía que era capaz de proveer. Te debo todo, seguiré con la autocrítica y pasión que has irradiado siempre y me has contagiado, intentando honrarte en mis acciones para que siempre estés aquí. Nos volveremos a ver.

En último lugar y más importante, le quiero agradecer **a mi familia** su apoyo y amor incondicional durante todos estos años. **Abuelo**, parece que por fin termino esto, sé que estarías orgulloso, así que esto va por ti. También quiero agradecer a toda mi familia, por siempre haber intentado sacar un rato para verme aun cuando pasaba brevemente por España. **Iria**, **Mamá**, **Papá**, desde el primer minuto que salí de España habéis creído en mí y habéis estado orgullosos cuando yo a veces no lo sentía. Han sido varios años sacrificados y aun así me habéis apoyado siempre y habéis estado ahí para mí. Esto es sin duda gracias a vosotros. Esta también es vuestra tesis. Os quiero de corazón.

References

(1) Li, B.; Wen, H.-M.; Zhou, W.; Chen, B. *J. Phys. Chem. Lett.* **2014**, *5*, 3468.

(2) Morris, R. E.; Wheatley, P. S. *Angew. Chem. Int. Ed.* **2008**, *47*, 4966.

(3) Furukawa, H.; Yaghi, O. M. *J. Am. Chem. Soc.* **2009**, *131*, 8875.

(4) Bai, L.; Phua, S. Z. F.; Lim, W. Q.; Jana, A.; Luo, Z.; Tham, H. P.; Zhao, L.; Gao, Q.; Zhao, Y. *Chem. Commun.* **2016**, *52*, 4128.

(5) Servatan, M.; Zarrintaj, P.; Mahmodi, G.; Kim, S.-J.; Ganjali, M. R.; Saeb, M. R.; Mozafari, M. *Drug Discovery Today* **2020**, *25*, 642.

(6) Lawson, H. D.; Walton, S. P.; Chan, C. *ACS Appl. Mater. Interfaces* **2021**, *13*, 7004.

(7) Misaelides, P. *Microporous Mesoporous Mater.* **2011**, *144*, 15.

(8) Liu, X.; Zhou, Y.; Zhang, J.; Tang, L.; Luo, L.; Zeng, G. *ACS Appl. Mater. Interfaces* **2017**, *9*, 20255.

(9) Zhang, N.; Ishag, A.; Li, Y.; Wang, H.; Guo, H.; Mei, P.; Meng, Q.; Sun, Y. *J. Cleaner Prod.* **2020**, *277*, 123360.

(10) Corma, A. *Chem. Rev.* **1997**, *97*, 2373.

(11) Dhakshinamoorthy, A.; Li, Z.; Garcia, H. *Chem. Soc. Rev.* **2018**, *47*, 8134.

(12) Guo, J.; Jiang, D. *ACS Cent. Sci.* **2020**, *6*, 869.

(13) Day, G. S.; Drake, H. F.; Zhou, H.-C.; Ryder, M. R. *Commun. Chem.* **2021**, *4*, 114.

(14) Tankersley, K. B.; Dunning, N. P.; Carr, C.; Lentz, D. L.; Scarborough, V. L. *Sci. Rep.* **2020**, *10*, 18021.

(15) Cortright, R. D.; Dumesic, J. A.; Madon, R. J. *Top. Catal.* **1997**, *4*, 15.

(16) Flanigen, E. M. Chapter 2 Zeolites and Molecular Sieves an Historical Perspective. In *Studies in Surface Science and Catalysis*, van Bekkum, H., Flanigen, E. M., Jansen, J. C. Eds.; Vol. 58; Elsevier, 1991; pp 13.

(17) Liu, J.; Yu, J. Chapter 1 - Toward Greener and Designed Synthesis of Zeolite Materials. In *Zeolites and Zeolite-Like Materials*, Sels, B. F., Kustov, L. M. Eds.; Elsevier, 2016; pp 1.

(18) Feldman, D. *Designed Monomers and Polymers* **2008**, *11*, 1.

(19) Lehn, J.-M. *Science* **1993**, *260*, 1762.

(20) Li, H.; Eddaoudi, M.; O'Keeffe, M.; Yaghi, O. M. *Nature* **1999**, *402*, 276.

(21) Côté, A. P.; Benin, A. I.; Ockwig, N. W.; O'Keeffe, M.; Matzger, A. J.; Yaghi, O. M. *Science* **2005**, *310*, 1166.

(22) Luo, S.; Wang, T.; Qi, L.; Tompsett, G. A.; Timko, M. T.; Auerbach, S. M.; Fan, W. *Chem. Mater.* **2022**, *34*, 1789.

(23) Wu, X.-P.; Choudhuri, I.; Truhlar, D. G. *Energy Environ. Mater.* **2019**, *2*, 251.

(24) Ma, T.; Wei, L.; Liang, L.; Yin, S.; Xu, L.; Niu, J.; Xue, H.; Wang, X.; Sun, J.; Zhang, Y.-B.; Wang, W. *Nat. Commun.* **2020**, *11*, 6128.

(25) Diercks, C. S.; Yaghi, O. M. *Science* **2017**, *355*, eaal1585.

(26) Lohse, M. S.; Bein, T. *Adv. Funct. Mater.* **2018**, *28*, 1705553.

(27) Song, Y.; Sun, Q.; Aguila, B.; Ma, S. *Adv. Sci.* **2019**, *6*, 1801410.

(28) Geng, K.; He, T.; Liu, R.; Dalapati, S.; Tan, K. T.; Li, Z.; Tao, S.; Gong, Y.; Jiang, Q.; Jiang, D. *Chem. Rev.* **2020**, *120*, 8814.

(29) Gui, B.; Lin, G.; Ding, H.; Gao, C.; Mal, A.; Wang, C. *Acc. Chem. Res.* **2020**, *53*, 2225.

(30) Zhang, L.; Yi, L.; Sun, Z.-J.; Deng, H. *Aggregate* **2021**, *2*, e24.

(31) Feng, X.; Ding, X.; Jiang, D. *Chem. Soc. Rev.* **2012**, *41*, 6010.

(32) Jin, Y.; Hu, Y.; Zhang, W. *Nat. Rev. Chem.* **2017**, *1*, 0056.

(33) El-Kaderi, H. M.; Hunt, J. R.; Mendoza-Cortés, J. L.; Côté, A. P.; Taylor, R. E.; O'Keeffe, M.; Yaghi, O. M. *Science* **2007**, *316*, 268.

(34) Evans, Austin M.; Ryder, M. R.; Ji, W.; Strauss, M. J.; Corcos, A. R.; Vitaku, E.; Flanders, N. C.; Bisbey, R. P.; Dichtel, W. R. *Faraday Discuss.* **2021**, *225*, 226.

(35) Li, X.; Cai, S.; Sun, B.; Yang, C.; Zhang, J.; Liu, Y. *Matter* **2020**, *3*, 1507.

(36) Rowan, S. J.; Cantrill, S. J.; Cousins, G. R. L.; Sanders, J. K. M.; Stoddart, J. F. *Angew. Chem. Int. Ed.* **2002**, *41*, 898.

(37) Haase, F.; Lotsch, B. V. *Chem. Soc. Rev.* **2020**, *49*, 8469.

(38) Jiang, J.; Zhao, Y.; Yaghi, O. M. *J. Am. Chem. Soc.* **2016**, *138*, 3255.

(39) Uribe-Romo, F. J.; Hunt, J. R.; Furukawa, H.; Klöck, C.; O'Keeffe, M.; Yaghi, O. M. *J. Am. Chem. Soc.* **2009**, *131*, 4570.

(40) Vitaku, E.; Dichtel, W. R. *J. Am. Chem. Soc.* **2017**, *139*, 12911.

(41) Zhan, G.; Cai, Z.-F.; Strutyński, K.; Yu, L.; Herrmann, N.; Martínez-Abadía, M.; Melle-Franco, M.; Mateo-Alonso, A.; Feyter, S. D. *Nature* **2022**, *603*, 835.

(42) Li, Y.; Chen, W.; Xing, G.; Jiang, D.; Chen, L. *Chem. Soc. Rev.* **2020**, *49*, 2852.

(43) Jin, F.; Nguyen, H. L.; Zhong, Z.; Han, X.; Zhu, C.; Pei, X.; Ma, Y.; Yaghi, O. M. *J. Am. Chem. Soc.* **2022**, *144*, 1539.

(44) Kuhn, P.; Antonietti, M.; Thomas, A. *Angew. Chem. Int. Ed.* **2008**, *47*, 3450.

(45) Maschita, J.; Banerjee, T.; Savasci, G.; Haase, F.; Ochsenfeld, C.; Lotsch, B. V. *Angew. Chem. Int. Ed.* **2020**, *59*, 15750.

(46) Díaz de Greñu, B.; Torres, J.; García-González, J.; Muñoz-Pina, S.; de los Reyes, R.; Costero, A. M.; Amorós, P.; Ros-Lis, J. V. *ChemSusChem* **2021**, *14*, 208.

(47) Campbell, N. L.; Clowes, R.; Ritchie, L. K.; Cooper, A. I. *Chem. Mater.* **2009**, *21*, 204.

(48) Biswal, B. P.; Chandra, S.; Kandambeth, S.; Lukose, B.; Heine, T.; Banerjee, R. *J. Am. Chem. Soc.* **2013**, *135*, 5328.

(49) Zwaneveld, N. A. A.; Pawlak, R.; Abel, M.; Catalin, D.; Gigmes, D.; Bertin, D.; Porte, L. *J. Am. Chem. Soc.* **2008**, *130*, 6678.

(50) Colson, J. W.; Woll, A. R.; Mukherjee, A.; Levendorf, M. P.; Spitler, E. L.; Shields, V. B.; Spencer, M. G.; Park, J.; Dichtel, W. R. *Science* **2011**, *332*, 228.

(51) Zhao, W.; Yan, P.; Yang, H.; Bahri, M.; James, A. M.; Chen, H.; Liu, L.; Li, B.; Pang, Z.; Clowes, R.; Browning, N. D.; Ward, J. W.; Wu, Y.; Cooper, A. I. *Nat. Synth.* **2022**, *1*, 87.

(52) Kim, S.; Choi, H. C. *Commun. Chem.* **2019**, *2*, 60.

(53) Du, Y.; Yang, H.; Whiteley, J. M.; Wan, S.; Jin, Y.; Lee, S.-H.; Zhang, W. *Angew. Chem. Int. Ed.* **2016**, *55*, 1737.

(54) Hunt, J. R.; Doonan, C. J.; LeVangie, J. D.; Côté, A. P.; Yaghi, O. M. *J. Am. Chem. Soc.* **2008**, *130*, 11872.

(55) Jackson, K. T.; Reich, T. E.; El-Kaderi, H. M. *Chem. Commun.* **2012**, *48*, 8823.

(56) Li, H.; Li, H.; Dai, Q.; Li, H.; Brédas, J.-L. *Adv. Theory Simul.* **2018**, *1*, 1700015.

(57) Segura, J. L.; Mancheño, M. J.; Zamora, F. *Chem. Soc. Rev.* **2016**, *45*, 5635.

(58) Ding, S.-Y.; Gao, J.; Wang, Q.; Zhang, Y.; Song, W.-G.; Su, C.-Y.; Wang, W. *J. Am. Chem. Soc.* **2011**, *133*, 19816.

(59) Lu, Z.; Yang, C.; He, L.; Hong, J.; Huang, C.; Wu, T.; Wang, X.; Wu, Z.; Liu, X.; Miao, Z.; Zeng, B.; Xu, Y.; Yuan, C.; Dai, L. *J. Am. Chem. Soc.* **2022**, *144*, 9624.

(60) Xiong, Y.; Liao, Q.; Huang, Z.; Huang, X.; Ke, C.; Zhu, H.; Dong, C.; Wang, H.; Xi, K.; Zhan, P.; Xu, F.; Lu, Y. *Adv. Mater.* **2020**, *32*, 1907242.

(61) Feldblyum, J. I.; McCreery, C. H.; Andrews, S. C.; Kurosawa, T.; Santos, E. J. G.; Duong, V.; Fang, L.; Ayzner, A. L.; Bao, Z. *Chem. Commun.* **2015**, *51*, 13894.

(62) Dalapati, S.; Jin, S.; Gao, J.; Xu, Y.; Nagai, A.; Jiang, D. *J. Am. Chem. Soc.* **2013**, *135*, 17310.

(63) Uribe-Romo, F. J.; Doonan, C. J.; Furukawa, H.; Oisaki, K.; Yaghi, O. M. *J. Am. Chem. Soc.* **2011**, *133*, 11478.

(64) Bunck, D. N.; Dichtel, W. R. *J. Am. Chem. Soc.* **2013**, *135*, 14952.

(65) Stegbauer, L.; Schwinghammer, K.; Lotsch, B. V. *Chem. Sci.* **2014**, *5*, 2789.

(66) Kandambeth, S.; Mallick, A.; Lukose, B.; Mane, M. V.; Heine, T.; Banerjee, R. *J. Am. Chem. Soc.* **2012**, *134*, 19524.

(67) Nagai, A.; Chen, X.; Feng, X.; Ding, X.; Guo, Z.; Jiang, D. *Angew. Chem. Int. Ed.* **2013**, *52*, 3770.

(68) Guo, J.; Xu, Y.; Jin, S.; Chen, L.; Kaji, T.; Honsho, Y.; Addicoat, M. A.; Kim, J.; Saeki, A.; Ihee, H.; Seki, S.; Irle, S.; Hiramoto, M.; Gao, J.; Jiang, D. *Nat. Commun.* **2013**, *4*, 2736.

(69) Stewart, D.; Antypov, D.; Dyer, M. S.; Pitcher, M. J.; Katsoulidis, A. P.; Chater, P. A.; Blanc, F.; Rosseinsky, M. J. *Nat. Commun.* **2017**, *8*, 1102.

(70) Rao, M. R.; Fang, Y.; De Feyter, S.; Perepichka, D. F. *J. Am. Chem. Soc.* **2017**, *139*, 2421.

(71) Beaudoin, D.; Maris, T.; Wuest, J. D. *Nat. Chem.* **2013**, *5*, 830.

(72) Das, G.; Skorjanc, T.; Sharma, S. K.; Gándara, F.; Lusi, M.; Shankar Rao, D. S.; Vimala, S.; Krishna Prasad, S.; Raya, J.; Han, D. S.; Jagannathan, R.; Olsen, J.-C.; Trabolsi, A. *J. Am. Chem. Soc.* **2017**, *139*, 9558.

(73) Jin, E.; Li, J.; Geng, K.; Jiang, Q.; Xu, H.; Xu, Q.; Jiang, D. *Nat. Commun.* **2018**, *9*, 4143.

(74) Zhuang, X.; Zhao, W.; Zhang, F.; Cao, Y.; Liu, F.; Bi, S.; Feng, X. *Polym. Chem.* **2016**, *7*, 4176.

(75) Jin, E.; Asada, M.; Xu, Q.; Dalapati, S.; Addicoat, M. A.; Brady Michael, A.; Xu, H.; Nakamura, T.; Heine, T.; Chen, Q.; Jiang, D. *Science* **2017**, *357*, 673.

(76) Bi, S.; Yang, C.; Zhang, W.; Xu, J.; Liu, L.; Wu, D.; Wang, X.; Han, Y.; Liang, Q.; Zhang, F. *Nat. Commun.* **2019**, *10*, 2467.

(77) Lyu, H.; Diercks, C. S.; Zhu, C.; Yaghi, O. M. *J. Am. Chem. Soc.* **2019**, *141*, 6848.

(78) Acharjya, A.; Pachfule, P.; Roeser, J.; Schmitt, F.-J.; Thomas, A. *Angew. Chem. Int. Ed.* **2019**, *58*, 14865.

(79) Pastoetter, D. L.; Xu, S.; Borrelli, M.; Addicoat, M.; Biswal, B. P.; Paasch, S.; Dianat, A.; Thomas, H.; Berger, R.; Reineke, S.; Brunner, E.; Cuniberti, G.; Richter, M.; Feng, X. *Angew. Chem. Int. Ed.* **2020**, *59*, 23620.

(80) Zhao, C.; Lyu, H.; Ji, Z.; Zhu, C.; Yaghi, O. M. *J. Am. Chem. Soc.* **2020**, *142*, 14450.

(81) Zhang, B.; Wei, M.; Mao, H.; Pei, X.; Alshmimri, S. A.; Reimer, J. A.; Yaghi, O. M. *J. Am. Chem. Soc.* **2018**, *140*, 12715.

(82) Haldar, S.; Wang, M.; Bhauriyal, P.; Hazra, A.; Khan, A. H.; Bon, V.; Isaacs, M. A.; De, A.; Shupletsov, L.; Boenke, T.; Grothe, J.; Heine, T.; Brunner, E.; Feng, X.; Dong, R.; Schneemann, A.; Kaskel, S. *J. Am. Chem. Soc.* **2022**, *144*, 9101.

(83) Roeser, J.; Prill, D.; Bojdys, M. J.; Fayon, P.; Trewin, A.; Fitch, A. N.; Schmidt, M. U.; Thomas, A. *Nat. Chem.* **2017**, *9*, 977.

(84) Zhang, S.; Zhao, X.; Li, B.; Bai, C.; Li, Y.; Wang, L.; Wen, R.; Zhang, M.; Ma, L.; Li, S. *J. Hazard. Mater.* **2016**, *314*, 95.

(85) Gropp, C.; Ma, T.; Hanikel, N.; Yaghi, O. M. *Science* **2020**, *370*, eabd6406.

(86) Grunenberg, L.; Savasci, G.; Terban, M. W.; Duppel, V.; Moudrakovski, I.; Etter, M.; Dinnebier, R. E.; Ochsenfeld, C.; Lotsch, B. V. *J. Am. Chem. Soc.* **2021**, *143*, 3430.

(87) Jiang, S.-Y.; Gan, S.-X.; Zhang, X.; Li, H.; Qi, Q.-Y.; Cui, F.-Z.; Lu, J.; Zhao, X. *J. Am. Chem. Soc.* **2019**, *141*, 14981.

(88) Seo, J.-M.; Noh, H.-J.; Jeong, H. Y.; Baek, J.-B. *J. Am. Chem. Soc.* **2019**, *141*, 11786.

(89) Ranjeesh, K. C.; Illathvalappil, R.; Veer, S. D.; Peter, J.; Wakchaure, V. C.; Goudappagouda; Raj, K. V.; Kurungot, S.; Babu, S. S. *J. Am. Chem. Soc.* **2019**, *141*, 14950.

(90) Su, Y.; Wan, Y.; Xu, H.; Otake, K.-i.; Tang, X.; Huang, L.; Kitagawa, S.; Gu, C. *J. Am. Chem. Soc.* **2020**, *142*, 13316.

(91) Li, C.; Ma, Y.; Liu, H.; Tao, L.; Ren, Y.; Chen, X.; Li, H.; Yang, Q. *Chin. J. Catal.* **2020**, *41*, 1288.

(92) Wang, P.-L.; Ding, S.-Y.; Zhang, Z.-C.; Wang, Z.-P.; Wang, W. *J. Am. Chem. Soc.* **2019**, *141*, 18004.

(93) Li, Z.; Zhang, Y.; Xia, H.; Mu, Y.; Liu, X. *Chem. Commun.* **2016**, *52*, 6613.

(94) Mu, Z.; Zhu, Y.; Li, B.; Dong, A.; Wang, B.; Feng, X. *J. Am. Chem. Soc.* **2022**, *144*, 5145.

(95) Corcos, A. R.; Levato, G. A.; Jiang, Z.; Evans, A. M.; Livingston, A. G.; Mariñas, B. J.; Dichtel, W. R. *ACS Materials Lett.* **2019**, *1*, 440.

(96) Zhang, L.; Xiao, Y.; Yang, Q.-C.; Yang, L.-L.; Wan, S.-C.; Wang, S.; Zhang, L.; Deng, H.; Sun, Z.-J. *Adv. Funct. Mater.* **2022**, 2201542.

(97) Wu, X.; Han, X.; Liu, Y.; Liu, Y.; Cui, Y. *J. Am. Chem. Soc.* **2018**, *140*, 16124.

(98) Albacete, P.; Martínez, J. I.; Li, X.; López-Moreno, A.; Mena-Hernando, S. a.; Platero-Prats, A. E.; Montoro, C.; Loh, K. P.; Pérez, E. M.; Zamora, F. *J. Am. Chem. Soc.* **2018**, *140*, 12922.

(99) Mähringer, A.; Medina, D. D. *Nat. Chem.* **2020**, *12*, 985.

(100) Cai, S.-L.; Zhang, K.; Tan, J.-B.; Wang, S.; Zheng, S.-R.; Fan, J.; Yu, Y.; Zhang, W.-G.; Liu, Y. *ACS Macro Lett.* **2016**, *5*, 1348.

(101) Ding, X.; Guo, J.; Feng, X.; Honsho, Y.; Guo, J.; Seki, S.; Maitarad, P.; Saeki, A.; Nagase, S.; Jiang, D. *Angew. Chem. Int. Ed.* **2011**, *50*, 1289.

(102) Zhou, T.-Y.; Xu, S.-Q.; Wen, Q.; Pang, Z.-F.; Zhao, X. *J. Am. Chem. Soc.* **2014**, *136*, 15885.

(103) Pang, Z.-F.; Zhou, T.-Y.; Liang, R.-R.; Qi, Q.-Y.; Zhao, X. *Chem. Sci.* **2017**, *8*, 3866.

(104) Cai, S.-L.; He, Z.-H.; Li, X.-L.; Zhang, K.; Zheng, S.-R.; Fan, J.; Liu, Y.; Zhang, W.-G. *Chem. Commun.* **2019**, *55*, 13454.

(105) Qian, C.; Qi, Q.-Y.; Jiang, G.-F.; Cui, F.-Z.; Tian, Y.; Zhao, X. *J. Am. Chem. Soc.* **2017**, *139*, 6736.

(106) Wang, X.; Han, X.; Cheng, C.; Kang, X.; Liu, Y.; Cui, Y. *J. Am. Chem. Soc.* **2022**, *144*, 7366.

(107) Dalapati, S.; Addicoat, M.; Jin, S.; Sakurai, T.; Gao, J.; Xu, H.; Irle, S.; Seki, S.; Jiang, D. *Nat. Commun.* **2015**, *6*, 7786.

(108) Bhambri, H.; Khullar, S.; Sakshi; Mandal, S. K. *Mater. Adv,* **2022**, *3*, 19.

(109) Zhang, B.; Mao, H.; Matheu, R.; Reimer, J. A.; Alshmimri, S. A.; Alshihri, S.; Yaghi, O. M. *J. Am. Chem. Soc.* **2019**, *141*, 11420.

(110) Nguyen, H. L.; Hanikel, N.; Lyle, S. J.; Zhu, C.; Proserpio, D. M.; Yaghi, O. M. *J. Am. Chem. Soc.* **2020**, *142*, 2218.

(111) Banerjee, T.; Haase, F.; Trenker, S.; Biswal, B. P.; Savasci, G.; Duppel, V.; Moudrakovski, I.; Ochsenfeld, C.; Lotsch, B. V. *Nat. Commun.* **2019**, *10*, 2689.

(112) Guan, X.; Chen, F.; Fang, Q.; Qiu, S. *Chem. Soc. Rev.* **2020**, *49*, 1357.

(113) Ma, T.; Kapustin, E. A.; Yin, S. X.; Liang, L.; Zhou, Z.; Niu, J.; Li, L.-H.; Wang, Y.; Su, J.; Li, J.; Wang, X.; Wang, W. D.; Wang, W.; Sun, J.; Yaghi, O. M. *Science* **2018**, *361*, 48.

(114) Martínez-Abadía, M.; Strutyński, K.; Lerma-Berlanga, B.; Stoppiello, C. T.; Khlobystov, A. N.; Martí-Gastaldo, C.; Saeki, A.; Melle-Franco, M.; Mateo-Alonso, A. *Angew. Chem. Int. Ed.* **2021**, *60*, 9941.

(115) Ma, T.; Li, J.; Niu, J.; Zhang, L.; Etman, A. S.; Lin, C.; Shi, D.; Chen, P.; Li, L.-H.; Du, X.; Sun, J.; Wang, W. *J. Am. Chem. Soc.* **2018**, *140*, 6763.

(116) Zhang, Y.-B.; Su, J.; Furukawa, H.; Yun, Y.; Gándara, F.; Duong, A.; Zou, X.; Yaghi, O. M. *J. Am. Chem. Soc.* **2013**, *135*, 16336.

(117) Fang, Q.; Wang, J.; Gu, S.; Kaspar, R. B.; Zhuang, Z.; Zheng, J.; Guo, H.; Qiu, S.; Yan, Y. *J. Am. Chem. Soc.* **2015**, *137*, 8352.

(118) Lin, G.; Ding, H.; Yuan, D.; Wang, B.; Wang, C. *J. Am. Chem. Soc.* **2016**, *138*, 3302.

(119) Lin, H.; Chen, C.; Zhou, T.; Zhang, J. *Solar RRL* **2021**, *5*, 2000458.

(120) Liu, R.; Tan, K. T.; Gong, Y.; Chen, Y.; Li, Z.; Xie, S.; He, T.; Lu, Z.; Yang, H.; Jiang, D. *Chem. Soc. Rev.* **2021**, *50*, 120.

(121) The physical and chemical basis of colour. In *Colour Chemistry*, 2 ed.; Christie, R. M. Ed.; The Royal Society of Chemistry, 2001; pp 12.

(122) Chen, X.; Addicoat, M.; Irle, S.; Nagai, A.; Jiang, D. *J. Am. Chem. Soc.* **2013**, *135*, 546.

(123) Keller, N.; Bein, T. *Chem. Soc. Rev.* **2021**, *50*, 1813.

(124) Hashemi, D.; Ma, X.; Ansari, R.; Kim, J.; Kieffer, J. *Phys. Chem. Chem. Phys.* **2019**, *21*, 789.

(125) Perepichka, D. F.; Bryce, M. R. *Angew. Chem. Int. Ed.* **2005**, *44*, 5370.

(126) Yue, Y.; Li, H.; Chen, H.; Huang, N. *J. Am. Chem. Soc.* **2022**, *144*, 2873.

(127) Calik, M.; Auras, F.; Salonen, L. M.; Bader, K.; Grill, I.; Handloser, M.; Medina, D. D.; Dogru, M.; Löbermann, F.; Trauner, D.; Hartschuh, A.; Bein, T. *J. Am. Chem. Soc.* **2014**, *136*, 17802.

(128) Sun, B.; Zhu, C.-H.; Liu, Y.; Wang, C.; Wan, L.-J.; Wang, D. *Chem. Mater.* **2017**, *29*, 4367.

(129) Ding, H.; Li, J.; Xie, G.; Lin, G.; Chen, R.; Peng, Z.; Yang, C.; Wang, B.; Sun, J.; Wang, C. *Nat. Commun.* **2018**, *9*, 5234.

(130) Haldar, S.; Chakraborty, D.; Roy, B.; Banappanavar, G.; Rinku, K.; Mullangi, D.; Hazra, P.; Kabra, D.; Vaidhyanathan, R. *J. Am. Chem. Soc.* **2018**, *140*, 13367.

(131) Meng, Y.; Luo, Y.; Shi, J.-L.; Ding, H.; Lang, X.; Chen, W.; Zheng, A.; Sun, J.; Wang, C. *Angew. Chem. Int. Ed.* **2020**, *59*, 3624.

(132) Wang, H.; Wang, H.; Wang, Z.; Tang, L.; Zeng, G.; Xu, P.; Chen, M.; Xiong, T.; Zhou, C.; Li, X.; Huang, D.; Zhu, Y.; Wang, Z.; Tang, J. *Chem. Soc. Rev.* **2020**, *49*, 4135.

(133) Guan, Q.; Zhou, L.-L.; Li, W.-Y.; Li, Y.-A.; Dong, Y.-B. *Chem. Eur. J.* **2020**, *26*, 5583.

(134) Wang, S.; Ma, L.; Wang, Q.; Shao, P.; Ma, D.; Yuan, S.; Lei, P.; Li, P.; Feng, X.; Wang, B. *J. Mater. Chem. C* **2018**, *6*, 5369.

(135) Xue, R.; Guo, H.; Wang, T.; Gong, L.; Wang, Y.; Ai, J.; Huang, D.; Chen, H.; Yang, W. *Anal. Methods* **2017**, *9*, 3737.

(136) Guo, L.; Yang, L.; Li, M.; Kuang, L.; Song, Y.; Wang, L. *Coord. Chem. Rev.* **2021**, *440*, 213957.

(137) Faheem, M.; Aziz, S.; Jing, X.; Ma, T.; Du, J.; Sun, F.; Tian, Y.; Zhu, G. *J. Mater. Chem. A* **2019**, *7*, 27148.

(138) Zhang, C.; Zhang, S.; Yan, Y.; Xia, F.; Huang, A.; Xian, Y. *ACS Appl. Mater. Interfaces* **2017**, *9*, 13415.

(139) Kowalczyk, T.; Lin, Z.; Voorhis, T. V. *J. Phys. Chem. A* **2010**, *114*, 10427.

(140) Li, Z.; Huang, N.; Lee, K. H.; Feng, Y.; Tao, S.; Jiang, Q.; Nagao, Y.; Irle, S.; Jiang, D. *J. Am. Chem. Soc.* **2018**, *140*, 12374.

(141) Wang, J.; Yan, B. *Anal. Chem.* **2019**, *91*, 13183.

(142) Feng, X.; Chen, L.; Dong, Y.; Jiang, D. *Chem. Commun.* **2011**, *47*, 1979.

(143) Auras, F.; Ascherl, L.; Hakimioun, A. H.; Margraf, J. T.; Hanusch, F. C.; Reuter, S.; Bessinger, D.; Döblinger, M.; Hettstedt, C.; Karaghiosoff, K.; Herbert, S.; Knochel, P.; Clark, T.; Bein, T. *J. Am. Chem. Soc.* **2016**, *138*, 16703.

(144) Ascherl, L.; Evans, E. W.; Hennemann, M.; Di Nuzzo, D.; Hufnagel, A. G.; Beetz, M.; Friend, R. H.; Clark, T.; Bein, T.; Auras, F. *Nat. Commun.* **2018**, *9*, 3802.

(145) Ding, X.; Feng, X.; Saeki, A.; Seki, S.; Nagai, A.; Jiang, D. *Chem. Commun.* **2012**, *48*, 8952.

(146) Liu, M.; Chen, Y.-J.; Huang, X.; Dong, L.-Z.; Lu, M.; Guo, C.; Yuan, D.; Chen, Y.; Xu, G.; Li, S.-L.; Lan, Y.-Q. *Angew. Chem. Int. Ed.* **2022**, *61*, e202115308.

(147) Gole, B.; Stepanenko, V.; Rager, S.; Grüne, M.; Medina, D. D.; Bein, T.; Würthner, F.; Beuerle, F. *Angew. Chem. Int. Ed.* **2018**, *57*, 846.

(148) Keller, N.; Calik, M.; Sharapa, D.; Soni, H. R.; Zehetmaier, P. M.; Rager, S.; Auras, F.; Jakowetz, A. C.; Görling, A.; Clark, T.; Bein, T. *J. Am. Chem. Soc.* **2018**, *140*, 16544.

(149) Xu, X.; Wang, S.; Yue, Y.; Huang, N. *ACS Appl. Mater. Interfaces* **2020**, *12*, 37427.

(150) Zhu, Y.; Zhu, D.; Chen, Y.; Yan, Q.; Liu, C.-Y.; Ling, K.; Liu, Y.; Lee, D.; Wu, X.; Senftle, T. P.; Verduzco, R. *Chem. Sci.* **2021**, *12*, 16092.

(151) Lin, G.; Ding, H.; Chen, R.; Peng, Z.; Wang, B.; Wang, C. *J. Am. Chem. Soc.* **2017**, *139*, 8705.

(152) Würthner, F. *Angew. Chem. Int. Ed.* **2020**, *59*, 14192.

(153) Dalapati, S.; Jin, E.; Addicoat, M.; Heine, T.; Jiang, D. *J. Am. Chem. Soc.* **2016**, *138*, 5797.

(154) Li, H.; Chang, J.; Li, S.; Guan, X.; Li, D.; Li, C.; Tang, L.; Xue, M.; Yan, Y.; Valtchev, V.; Qiu, S.; Fang, Q. *J. Am. Chem. Soc.* **2019**, *141*, 13324.

(155) Jin, S.; Sakurai, T.; Kowalczyk, T.; Dalapati, S.; Xu, F.; Wei, H.; Chen, X.; Gao, J.; Seki, S.; Irle, S.; Jiang, D. *Chem. Eur. J.* **2014**, *20*, 14608.

(156) Ascherl, L.; Evans, E. W.; Gorman, J.; Orsborne, S.; Bessinger, D.; Bein, T.; Friend, R. H.; Auras, F. *J. Am. Chem. Soc.* **2019**, *141*, 15693.

(157) Li, H.; Shao, P.; Chen, S.; Li, G.; Feng, X.; Chen, X.; Zhang, H.-J.; Lin, J.; Jiang, Y.-B. *J. Am. Chem. Soc.* **2020**, *142*, 3712.

(158) Wu, C.; Liu, Y.; Liu, H.; Duan, C.; Pan, Q.; Zhu, J.; Hu, F.; Ma, X.; Jiu, T.; Li, Z.; Zhao, Y. *J. Am. Chem. Soc.* **2018**, *140*, 10016.

(159) Rager, S.; Jakowetz, A. C.; Gole, B.; Beuerle, F.; Medina, D. D.; Bein, T. *Chem. Mater.* **2019**, *31*, 2707.

(160) Zhang, L.; Yang, G.-P.; Xiao, S.-J.; Tan, Q.-G.; Zheng, Q.-Q.; Liang, R.-P.; Qiu, J.-D. *Small* **2021**, *17*, 2102944.

(161) Wang, Y.; Geng, S.; Yan, G.; Liu, X.; Zhang, X.; Feng, Y.; Shi, J.; Qu, X. *ACS Appl. Energy Mater.* **2022**, *5*, 2495.

(162) Zhang, J.; Wang, L.; Li, N.; Liu, J.; Zhang, W.; Zhang, Z.; Zhou, N.; Zhu, X. *CrystEngComm* **2014**, *16*, 6547.

(163) Wang, L.; Dong, B.; Ge, R.; Jiang, F.; Xu, J. *ACS Appl. Mater. Interfaces* **2017**, *9*, 7108.

(164) Guo, C.; Liu, M.; Gao, G.-K.; Tian, X.; Zhou, J.; Dong, L.-Z.; Li, Q.; Chen, Y.; Li, S.-L.; Lan, Y.-Q. *Angew. Chem. Int. Ed.* **2022**, *61*, e202113315.

(165) Huang, N.; Ding, X.; Kim, J.; Ihee, H.; Jiang, D. *Angew. Chem. Int. Ed.* **2015**, *54*, 8704.

(166) Zhang, C.; Guo, J.; Zou, X.; Guo, S.; Guo, Y.; Shi, R.; Yan, F. *Adv. Healthcare Mater.* **2021**, *10*, 2100775.

(167) Bessinger, D.; Ascherl, L.; Auras, F.; Bein, T. *J. Am. Chem. Soc.* **2017**, *139*, 12035.

(168) Trenker, S.; Grunenberg, L.; Banerjee, T.; Savasci, G.; Poller, L. M.; Muggli, K. I. M.; Haase, F.; Ochsenfeld, C.; Lotsch, B. V. *Chem. Sci.* **2021**, *12*, 15143.

(169) Neti, V. S. P. K.; Wu, X.; Deng, S.; Echegoyen, L. *CrystEngComm* **2013**, *15*, 6892.

(170) Wan, S.; Guo, J.; Kim, J.; Ihee, H.; Jiang, D. *Angew. Chem. Int. Ed.* **2008**, *47*, 8826.

(171) Kim, T. W.; Jun, S.; Ha, Y.; Yadav, R. K.; Kumar, A.; Yoo, C.-Y.; Oh, I.; Lim, H.-K.; Shin, J. W.; Ryoo, R.; Kim, H.; Kim, J.; Baeg, J.-O.; Ihee, H. *Nat. Commun.* **2019**, *10*, 1873.

(172) Rager, S.; Dogru, M.; Werner, V.; Gavryushin, A.; Götz, M.; Engelke, H.; Medina, D. D.; Knochel, P.; Bein, T. *CrystEngComm* **2017**, *19*, 4886.

(173) Guan, Q.; Zhou, L.-L.; Lv, F.-H.; Li, W.-Y.; Li, Y.-A.; Dong, Y.-B. *Angew. Chem. Int. Ed.* **2020**, *59*, 18042.

(174) Sánchez-Naya, R.; Stepanenko, V.; Mandel, K.; Beuerle, F. *Org. Mater.* **2021**, *3*, 17.

(175) Sanchez, C.; Belleville, P.; Popall, M.; Nicole, L. *Chem. Soc. Rev.* **2011**, *40*, 696.

(176) Faustini, M.; Nicole, L.; Ruiz-Hitzky, E.; Sanchez, C. *Adv. Funct. Mater.* **2018**, *28*.

(177) Gower, L. B. *Chem. Rev.* **2008**, *108*, 4551.

(178) Mann, S. *Nature* **1993**, *365*, 499.

(179) Müller-Buschbaum, K.; Beuerle, F.; Feldmann, C. *Microporous Mesoporous Mater.* **2015**, *216*, 171.

(180) Mandel, K.; Granath, T.; Wehner, T.; Rey, M.; Stracke, W.; Vogel, N.; Sextl, G.; Muller-Buschbaum, K. *ACS Nano* **2017**, *11*, 779.

(181) Seuffert, M. T.; Wintzheimer, S.; Oppmann, M.; Granath, T.; Prieschl, J.; Alrefai, A.; Holdt, H.-J.; Müller-Buschbaum, K.; Mandel, K. *J. Mater. Chem. C* **2020**, *8*, 16010.

(182) Wintzheimer, S.; Reichstein, J.; Wenderoth, S.; Hasselmann, S.; Oppmann, M.; Seuffert, M. T.; Müller‐Buschbaum, K.; Mandel, K. *Adv. Funct. Mater.* **2019**, *29*, 1901193.

(183) Wehner, T.; Mandel, K.; Schneider, M.; Sextl, G.; Müller-Buschbaum, K. *ACS Appl. Mater. Interfaces* **2016**, *8*, 5445.

(184) Wehner, T.; Seuffert, M. T.; Sorg, J. R.; Schneider, M.; Mandel, K.; Sextl, G.; Müller-Buschbaum, K. *J. Mater. Chem. C* **2017**, *5*, 10133.

(185) Beuerle, F.; Gole, B. *Angew. Chem. Int. Ed.* **2018**, *57*, 4850.

(186) Chen, X.; Geng, K.; Liu, R.; Tan, K. T.; Gong, Y.; Li, Z.; Tao, S.; Jiang, Q.; Jiang, D. *Angew. Chem. Int. Ed.* **2020**, *59*, 5050.

(187) Bisbey, R. P.; Dichtel, W. R. *ACS Cent. Sci.* **2017**, *3*, 533.

(188) Ding, S.-Y.; Wang, W. *Chem. Soc. Rev.* **2013**, *42*, 548.

(189) Rogge, S. M. J.; Bavykina, A.; Hajek, J.; Garcia, H.; Olivos-Suarez, A. I.; Sepúlveda-Escribano, A.; Vimont, A.; Clet, G.; Bazin, P.; Kapteijn, F.; Daturi, M.; Ramos-Fernandez, E. V.; Llabrés I. Xamena, F. X.; Van Speybroeck, V.; Gascon, J. *Chem. Soc. Rev.* **2017**, *46*, 3134.

(190) Pachfule, P.; Acharjya, A.; Roeser, J.; Langenhahn, T.; Schwarze, M.; Schomacker, R.; Thomas, A.; Schmidt, J. *J. Am. Chem. Soc.* **2018**, *140*, 1423.

(191) Wang, X.; Chen, L.; Chong, S. Y.; Little, M. A.; Wu, Y.; Zhu, W. H.; Clowes, R.; Yan, Y.; Zwijnenburg, M. A.; Sprick, R. S.; Cooper, A. I. *Nat. Chem.* **2018**, *10*, 1180.

(192) Dogru, M.; Bein, T. *Chem. Commun.* **2014**, *50*, 5531.

(193) Mandal, A. K.; Mahmood, J.; Baek, J.-B. *ChemNanoMat* **2017**, *3*, 373.

(194) Liu, Q.; Bottle, S. E.; Sonar, P. *Adv. Mater.* **2020**, *32*, 1903882.

(195) Soberats, B.; Hecht, M.; Wurthner, F. *Angew. Chem. Int. Ed.* **2017**, *56*, 10771.

(196) Grzybowski, M.; Gryko, D. T. *Advanced Optical Materials* **2015**, *3*, 280.

(197) Stolte, M.; Suraru, S.-L.; Diemer, P.; He, T.; Burschka, C.; Zschieschang, U.; Klauk, H.; Würthner, F. *Adv. Funct. Mater.* **2016**, *26*, 7415.

(198) Gole, B.; Stepanenko, V.; Rager, S.; Grüne, M.; Medina, D. D.; Bein, T.; Würthner, F.; Beuerle, F. *Angew. Chem. Int. Ed.* **2018**, *57*, 846.

(199) Rager, S.; Jakowetz, A. C.; Gole, B.; Beuerle, F.; Medina, D. D.; Bein, T. *Chem. Mater.* **2019**, *31*, 2707.

(200) Banerjee, T.; Gottschling, K.; Savasci, G.; Ochsenfeld, C.; Lotsch, B. V. *ACS Energy Lett.* **2018**, *3*, 400.

(201) Bhadra, M.; Kandambeth, S.; Sahoo, M. K.; Addicoat, M.; Balaraman, E.; Banerjee, R. *J. Am. Chem. Soc.* **2019**, *141*, 6152.

(202) Pachfule, P.; Kandambeth, S.; Diaz Diaz, D.; Banerjee, R. *Chem. Commun.* **2014**, *50*, 3169.

(203) Mullangi, D.; Dhavale, V.; Shalini, S.; Nandi, S.; Collins, S.; Woo, T.; Kurungot, S.; Vaidhyanathan, R. *Adv. Energy Mater.* **2016**, *6*, 1600110.

(204) Stegbauer, L.; Schwinghammer, K.; Lotsch, B. V. *Chem. Sci.* **2014**, *5*, 2789.

(205) Romero, V.; Fernandes, S. P. S.; Rodriguez-Lorenzo, L.; Kolen'ko, Y. V.; Espiña, B.; Salonen, L. M. *Nanoscale* **2019**, *11*, 6072.

(206) Liao, Y.; Li, J.; Thomas, A. *ACS Macro Lett.* **2017**, *6*, 1444.

(207) He, S.; Zeng, T.; Wang, S.; Niu, H.; Cai, Y. *ACS Appl. Mater. Interfaces* **2017**, *9*, 2959.

(208) Li, Y.; Zhang, H.; Chen, Y.; Huang, L.; Lin, Z.; Cai, Z. *ACS Appl. Mater. Interfaces* **2019**, *11*, 22492.

(209) Wu, Y.; Sun, N.; Deng, C. *ACS Appl. Mater. Interfaces* **2020**, *12*, 9814.

(210) Lin, G.; Gao, C.; Zheng, Q.; Lei, Z.; Geng, H.; Lin, Z.; Yang, H.; Cai, Z. *Chem. Commun.* **2017**, *53*, 3649.

(211) Huang, L.; Mao, N.; Yan, Q.; Zhang, D.; Shuai, Q. *ACS Appl. Nano Mater.* **2020**, *3*, 319.

(212) Wang, M.; Gao, M.; Zhang, K.; Wang, L.; Wang, W.; Fu, Q.; Xia, Z.; Gao, D. *Microchim. Acta* **2019**, *186*, 827.

(213) Deng, Z. H.; Wang, X.; Wang, X. L.; Gao, C. L.; Dong, L.; Wang, M. L.; Zhao, R. S. *Microchim. Acta* **2019**, *186*, 108.

(214) Tan, J.; Namuangruk, S.; Kong, W.; Kungwan, N.; Guo, J.; Wang, C. *Angew. Chem. Int. Ed.* **2016**, *55*, 13979.

(215) Mandel, K.; Strasser, M.; Granath, T.; Dembski, S.; Sextl, G. *Chem. Commun.* **2015**, *51*, 2863.

(216) Mandel, K.; Hutter, F.; Gellermann, C.; Sextl, G. *ACS Appl. Mater. Interfaces* **2012**, *4*, 5633.

(217) Mandel, K.; Hutter, F.; Gellermann, C.; Sextl, G. *J. Magn. Magn. Mater.* **2013**, *331*, 269.

(218) Brede, F. A.; Mandel, K.; Schneider, M.; Sextl, G.; Müller-Buschbaum, K. *Chem. Commun.* **2015**, *51*, 8687.

(219) Müssig, S.; Fidler, F.; Haddad, D.; Hiller, K.-H.; Wintzheimer, S.; Mandel, K. *Adv. Mater. Technol.* **2019**, *4*, 1900300.

(220) Wei, Y.; Han, B.; Hu, X.; Lin, Y.; Wang, X.; Deng, X. *Procedia Eng.* **2012**, *27*, 632.

(221) Keller, N.; Calik, M.; Sharapa, D.; Soni, H. R.; Zehetmaier, P. M.; Rager, S.; Auras, F.; Jakowetz, A. C.; Görling, A.; Clark, T.; Bein, T. *J. Am. Chem. Soc.* **2018**, *140*, 16544.

(222) Bucher, L.; Tanguy, L.; Fortin, D.; Desbois, N.; Harvey, P. D.; Sharma, G. D.; Gros, C. P. *ChemPlusChem* **2017**, *82*, 625.

(223) Zanetti-Polzi, L.; Amadei, A.; Djemili, R.; Durot, S.; Schoepff, L.; Heitz, V.; Ventura, B.; Daidone, I. *J. Phys. Chem. C* **2019**.

(224) Long, B.; Bakr, O.; Stellacci, F. *J. Exp. Nanosci.* **2008**, *3*, 53.

(225) Loudet, A.; Burgess, K. *Chem. Rev.* **2007**, *107*, 4891.

(226) Boens, N.; Verbelen, B.; Dehaen, W. *Eur. J. Org. Chem.* **2015**, *2015*, 6577.

(227) Mu, H.; Miki, K.; Kubo, T.; Otsuka, K.; Ohe, K. *Chem. Commun.* **2021**, *57*, 1818.

(228) Qu, X.; Liu, Q.; Ji, X.; Chen, H.; Zhou, Z.; Shen, Z. *Chem. Commun.* **2012**, *48*, 4600.

(229) Nguyen, V.-N.; Yim, Y.; Kim, S.; Ryu, B.; Swamy, K. M. K.; Kim, G.; Kwon, N.; Kim, C.-Y.; Park, S.; Yoon, J. *Angew. Chem. Int. Ed.* **2020**, *59*, 8957.

(230) Wang, H.; Zhao, W.; Liu, X.; Wang, S.; Wang, Y. *ACS Appl. Bio Mater.* **2020**, *3*, 593.

(231) Tang, F.-K.; Zhu, J.; Kong, F. K.-W.; Ng, M.; Bian, Q.; Yam, V. W.-W.; Tse, A. K.-W.; Tse, Y.-C.; Leung, K. C.-F. *Chem. Commun.* **2020**, *56*, 2695.

(232) Ooyama, Y.; Hato, M.; Enoki, T.; Aoyama, S.; Furue, K.; Tsunoji, N.; Ohshita, J. *New J. Chem.* **2016**, *40*, 7278.

(233) Porubský, M.; Gurská, S.; Stanková, J.; Hajdúch, M.; Džubák, P.; Hlaváč, J. *RSC Adv.* **2019**, *9*, 25075.

(234) Ho, D.; Ozdemir, R.; Kim, H.; Earmme, T.; Usta, H.; Kim, C. *ChemPlusChem* **2019**, *84*, 18.

(235) Ozdemir, M.; Choi, D.; Kwon, G.; Zorlu, Y.; Cosut, B.; Kim, H.; Facchetti, A.; Kim, C.; Usta, H. *ACS Appl. Mater. Interfaces* **2016**, *8*, 14077.

(236) Huaulmé, Q.; Fall, S.; Lévêque, P.; Ulrich, G.; Leclerc, N. *Chem. Eur. J.* **2019**, *25*, 6613.

(237) Collado, L.; Naranjo, T.; Gomez-Mendoza, M.; López-Calixto, C. G.; Oropeza, F. E.; Liras, M.; Marugán, J.; de la Peña O'Shea, V. A. *Adv. Funct. Mater.* **2021**, *31*, 2105384.

(238) Mauger, A.; Farjon, J.; Nun, P.; Coeffard, V. *Chem. Eur. J.* **2018**, *24*, 4790.

(239) Huang, L.; Zhao, J. *RSC Adv.* **2013**, *3*, 23377.

(240) Luo, G.-G.; Fang, K.; Wu, J.-H.; Mo, J. *Chem. Commun.* **2015**, *51*, 12361.

(241) Wang, Z.; Huang, L.; Yan, Y.; El-Zohry, A. M.; Toffoletti, A.; Zhao, J.; Barbon, A.; Dick, B.; Mohammed, O. F.; Han, G. *Angew. Chem. Int. Ed.* **2020**, *59*, 16114.

(242) Qin, Y.; Liu, X.; Jia, P.-P.; Xu, L.; Yang, H.-B. *Chem. Soc. Rev.* **2020**, *49*, 5678.

(243) Musser, A. J.; Neelakandan, P. P.; Richter, J. M.; Mori, H.; Friend, R. H.; Nitschke, J. R. *J. Am. Chem. Soc.* **2017**, *139*, 12050.

(244) Lu, P.; Chung, K.-Y.; Stafford, A.; Kiker, M.; Kafle, K.; Page, Z. A. *Polym. Chem.* **2021**, *12*, 327.

(245) Yang, H.; Wang, J.; Ma, J.; Yang, H.; Zhang, J.; Lv, K.; Wen, L.; Peng, T. *J. Mater. Chem. A* **2019**, *7*, 10439.

(246) Guan, Q.; Fu, D.-D.; Li, Y.-A.; Kong, X.-M.; Wei, Z.-Y.; Li, W.-Y.; Zhang, S.-J.; Dong, Y.-B. *iScience* **2019**, *14*, 180.

(247) Dong, X.-J.; Li, W.-Y.; Guan, Q.; Li, Y.-A.; Dong, Y.-B. *Chem. Commun.* **2022**, *58*, 2387.

(248) Yang, G.-P.; Meng, X.-L.; Xiao, S.-J.; Zheng, Q.-Q.; Tan, Q.-G.; Liang, R.-P.; Zhang, L.; Zhang, P.; Qiu, J.-D. *ACS Appl. Mater. Interfaces* **2022**, *14*, 28289.

(249) Chong, J. H.; Sauer, M.; Patrick, B. O.; MacLachlan, M. J. *Org. Lett.* **2003**, *5*, 3823.

(250) Gallant, A. J.; Yun, M.; Sauer, M.; Yeung, C. S.; MacLachlan, M. J. *Org. Lett.* **2005**, *7*, 4827.

(251) DeBlase, C. R.; Silberstein, K. E.; Truong, T.-T.; Abruña, H. D.; Dichtel, W. R. *J. Am. Chem. Soc.* **2013**, *135*, 16821.

(252) Rocha, M.; Gil, D. M.; Echeverría, G. A.; Piro, O. E.; Jios, J. L.; Ulic, S. E. *J. Org. Chem.* **2019**, *84*, 11042.

(253) Nepomnyashchii, A. B.; Bröring, M.; Ahrens, J.; Bard, A. J. *J. Am. Chem. Soc.* **2011**, *133*, 8633.

(254) Matarranz, B.; Sampedro, A.; G. Daniliuc, C.; Fernández, G. *Crystals* **2018**, *8*, 436.

(255) Helmers, I.; Ghosh, G.; Albuquerque, R. Q.; Fernández, G. *Angew. Chem. Int. Ed.* **2021**, *60*, 4368.

(256) Thommes, M.; Kaneko, K.; Neimark, A. V.; Olivier, J. P.; Rodriguez-Reinoso, F.; Rouquerol, J.; Sing, K. S. W. *Pure Appl. Chem.* **2015**, *87*, 1051.

(257) Liguori, F.; Moreno-Marrodan, C.; Barbaro, P. *Chem. Soc. Rev.* **2020**, *49*, 6329.

(258) Wang, J.; Guo, X. *Chemosphere* **2020**, *258*, 127279.

(259) Cai, Y.; Zheng, L.; Fang, Z. *RSC Adv.* **2015**, *5*, 97435.

(260) Nassar, M. Y.; Khatab, M. *RSC Adv.* **2016**, *6*, 79688.

(261) Liu, L.; Luo, X.-B.; Ding, L.; Luo, S.-L. 4 - Application of Nanotechnology in the Removal of Heavy Metal From Water. In *Nanomaterials for the Removal of Pollutants and Resource Reutilization*, Luo, X., Deng, F. Eds.; Elsevier, 2019; pp 83.

(262) Park, J. M.; Jhung, S. H. *Chem. Eng. J.* **2020**, *396*, 125224.

(263) Liu, Y. *J. Chem. Eng. Data* **2009**, *54*, 1981.

(264) Li, Y.; Yang, C.-X.; Yan, X.-P. *Chem. Commun.* **2017**, *53*, 2511.

(265) Gao, Y.; Wang, C.; Hu, H.; Ge, R.; Lu, M.; Zhang, J.; Li, Z.; Shao, P.; Jiang, D. *Chem. Eur. J.* **2019**, *25*, 15488.

(266) Zhao, W.; Wang, T.-P.; Wu, J.-L.; Pan, R.-P.; Liu, X.-Y.; Liu, X.-K. *Chin. J. Polym. Sci.* **2019**, *37*, 1045.

(267) Hao, J.; Zhang, Q.; Liu, Y.; Chen, P.; Zheng, X.; Zhuang, X.; Fu, D.; Liu, H.; Liu, G.; Lv, W. *J. Taiwan Inst. Chem. Eng.* **2020**, *113*, 204.

(268) You, L.; Xu, K.; Ding, G.; Shi, X.; Li, J.; Wang, S.; Wang, J. *J. Mol. Liq.* **2020**, *320*, 114456.

(269) Zhong, X.; Lu, Z.; Liang, W.; Hu, B. *J. Hazard. Mater.* **2020**, *393*, 122353.

(270) Fu, D.; Zhang, Q.; Chen, P.; Zheng, X.; Hao, J.; Mo, P.; Liu, H.; Liu, G.; Lv, W. *RSC Adv.* **2021**, *11*, 18308.

(271) Liu, C.; You, J.; Hu, R.; Jiang, W.; Duan, Y.; Li, J.; Li, Z.; Zhu, R.; Li, Y.; Liu, Z.; Wang, K.; Chen, C. *Anal. Lett.* **2021**, *54*, 347.

(272) Wei, D.; Li, J.; Chen, Z.; Liang, L.; Ma, J.; Wei, M.; Ai, Y.; Wang, X. *J. Mol. Liq.* **2020**, *301*, 112431.

(273) Lu, F.; Lin, J.; Lin, C.; Qi, G.; Lin, X.; Xie, Z. *Talanta* **2021**, *231*, 122343.

(274) Zeng, T.; Jin, Z.; Li, S.; Bao, J.; Huang, Z.; Shen, Y.; Zhang, H.; Wang, D.; Song, S. *Chem. Commun.* **2021**, *57*, 4946.

(275) Dalvi, V. H.; Rossky, P. J. *Proc. Natl. Acad. Sci. U.S.A.* **2010**, *107*, 13603.

(276) Dorh, N.; Zhu, S.; Dhungana, K. B.; Pati, R.; Luo, F.-T.; Liu, H.; Tiwari, A. *Sci. Rep.* **2015**, *5*, 18337.

(277) Kand, D.; Liu, P.; Navarro, M. X.; Fischer, L. J.; Rousso-Noori, L.; Friedmann-Morvinski, D.; Winter, A. H.; Miller, E. W.; Weinstain, R. *J. Am. Chem. Soc.* **2020**, *142*, 4970.

(278) Singh, A. K. Chapter 8 - Nanoparticle Ecotoxicology. In *Engineered Nanoparticles*, Singh, A. K. Ed.; Academic Press, 2016; pp 343.

(279) Khan, I.; Saeed, K.; Zekker, I.; Zhang, B.; Hendi, A. H.; Ahmad, A.; Ahmad, S.; Zada, N.; Ahmad, H.; Shah, L. A.; Shah, T.; Khan, I. *Water* **2022**, *14*, 242.

(280) Cwalinski, T.; Polom, W.; Marano, L.; Roviello, G.; D'Angelo, A.; Cwalina, N.; Matuszewski, M.; Roviello, F.; Jaskiewicz, J.; Polom, K. *J. Clin. Med.* **2020**, *9*, 3538.

(281) Kannan, N.; Sundaram, M. M. *Dyes Pigm.* **2001**, *51*, 25.

(282) Santoso, E.; Ediati, R.; Kusumawati, Y.; Bahruji, H.; Sulistiono, D. O.; Prasetyoko, D. *Mater. Today Chem.* **2020**, *16*, 100233.

(283) Li, K.; Duan, X.; Jiang, Z.; Ding, D.; Chen, Y.; Zhang, G.-Q.; Liu, Z. *Nat. Commun.* **2021**, *12*, 2376.

(284) Skorjanc, T.; Shetty, D.; Valant, M. *ACS Sens.* **2021**, *6*, 1461.

(285) Zhao, J.; Wu, W.; Sun, J.; Guo, S. *Chem. Soc. Rev.* **2013**, *42*, 5323.

(286) Zhao, J.; Xu, K.; Yang, W.; Wang, Z.; Zhong, F. *Chem. Soc. Rev.* **2015**, *44*, 8904.

(287) Bassan, E.; Gualandi, A.; Cozzi, P. G.; Ceroni, P. *Chem. Sci.* **2021**, *12*, 6607.

(288) Bhadra, M.; Kandambeth, S.; Sahoo, M. K.; Addicoat, M.; Balaraman, E.; Banerjee, R. *J. Am. Chem. Soc.* **2019**, *141*, 6152.

(289) Wang, X.-F.; Yu, S.-S.; Wang, C.; Xue, D.; Xiao, J. *Org. Biomol. Chem.* **2016**, *14*, 7028.

(290) Xie, J.; Zhang, X.; Shi, C.; Pan, L.; Hou, F.; Nie, G.; Xie, J.; Liu, Q.; Zou, J.-J. *Sustainable Energy Fuels* **2020**, *4*, 911.

(291) Luo, G.-G.; Lu, H.; Zhang, X.-L.; Dai, J.-C.; Wu, J.-H.; Wu, J.-J. *Phys. Chem. Chem. Phys.* **2015**, *17*, 9716.

(292) Suryani, O.; Higashino, Y.; Sato, H.; Kubo, Y. *ACS Appl. Energy Mater.* **2019**, *2*, 448.

(293) Vyas, V. S.; Haase, F.; Stegbauer, L.; Savasci, G.; Podjaski, F.; Ochsenfeld, C.; Lotsch, B. V. *Nat. Commun.* **2015**, *6*, 8508.

(294) Chen, D.; Cheng, Y.; Zhou, N.; Chen, P.; Wang, Y.; Li, K.; Huo, S.; Cheng, P.; Peng, P.; Zhang, R.; Wang, L.; Liu, H.; Liu, Y.; Ruan, R. *J. Cleaner Prod.* **2020**, *268*, 121725.

(295) Koe, W. S.; Lee, J. W.; Chong, W. C.; Pang, Y. L.; Sim, L. C. *Environ. Sci. Pollut. Res.* **2020**, *27*, 2522.

(296) Xia, S.; Zhang, L.; Pan, G.; Qian, P.; Ni, Z. *Phys. Chem. Chem. Phys.* **2015**, *17*, 5345.

(297) Chen, D.; Yu, Q.; Huang, X.; Dai, H.; Luo, T.; Shao, J.; Chen, P.; Chen, J.; Huang, W.; Dong, X. *Small* **2020**, *16*, 2001059.

(298) Han, R.; Zhao, M.; Wang, Z.; Liu, H.; Zhu, S.; Huang, L.; Wang, Y.; Wang, L.; Hong, Y.; Sha, Y.; Jiang, Y. *ACS Nano* **2020**, *14*, 9532.

(299) Teng, K.-X.; Chen, W.-K.; Niu, L.-Y.; Fang, W.-H.; Cui, G.; Yang, Q.-Z. *Angew. Chem. Int. Ed.* **2021**, *60*, 19912.

(300) Zhuang, Z.; Dai, J.; Yu, M.; Li, J.; Shen, P.; Hu, R.; Lou, X.; Zhao, Z.; Tang, B. Z. *Chem. Sci.* **2020**, *11*, 3405.

(301) Baptista, M. S.; Cadet, J.; Di Mascio, P.; Ghogare, A. A.; Greer, A.; Hamblin, M. R.; Lorente, C.; Nunez, S. C.; Ribeiro, M. S.; Thomas, A. H.; Vignoni, M.; Yoshimura, T. M. *Photochem. Photobiol.* **2017**, *93*, 912.

(302) DeRosa, M. C.; Crutchley, R. J. *Coord. Chem. Rev.* **2002**, *233-234*, 351.

(303) Ogilby, P. R. *Chem. Soc. Rev.* **2010**, *39*, 3181.

(304) Pibiri, I.; Buscemi, S.; Palumbo Piccionello, A.; Pace, A. *ChemPhotoChem* **2018**, *2*, 535.

(305) Huang, L.; Zhao, J.; Guo, S.; Zhang, C.; Ma, J. *J. Org. Chem.* **2013**, *78*, 5627.

(306) Tobin, J. M.; Liu, J.; Hayes, H.; Demleitner, M.; Ellis, D.; Arrighi, V.; Xu, Z.; Vilela, F. *Polym. Chem.* **2016**, *7*, 6662.

(307) Yang, W.; Feng, S.; Zhang, X.; Wang, Y.; Li, C.; Zhang, L.; Zhao, J.; Gurzadyan, G. G.; Tao, S. *ACS Appl. Mater. Interfaces* **2021**, *13*, 38722.

(308) Atilgan, A.; Cetin, M. M.; Yu, J.; Beldjoudi, Y.; Liu, J.; Stern, C. L.; Cetin, F. M.; Islamoglu, T.; Farha, O. K.; Deria, P.; Stoddart, J. F.; Hupp, J. T. *J. Am. Chem. Soc.* **2020**, *142*, 18554.

(309) Díez-Mato, E.; Cortezón-Tamarit, F. C.; Bogialli, S.; García-Fresnadillo, D.; Marazuela, M. D. *Appl. Catal., B* **2014**, *160-161*, 445.

(310) Luo, L.; Xiao, Z.; Chen, B.; Cai, F.; Fang, L.; Lin, L.; Luan, T. *Environ. Sci. Technol.* **2018**, *52*, 3634.

(311) Chen, S.; Sun, T.; Zheng, M.; Xie, Z. *Adv. Funct. Mater.* **2020**, *30*, 2004680.

(312) Kamkaew, A.; Lim, S. H.; Lee, H. B.; Kiew, L. V.; Chung, L. Y.; Burgess, K. *Chem. Soc. Rev.* **2013**, *42*, 77.

(313) Wang, W.; Wang, L.; Li, Z.; Xie, Z. *Chem. Commun.* **2016**, *52*, 5402.

(314) Cullen, A. A.; Rajagopal, A.; Heintz, K.; Heise, A.; Murphy, R.; Sazanovich, I. V.; Greetham, G. M.; Towrie, M.; Long, C.; Fitzgerald-Hughes, D.; Pryce, M. T. *J. Phys. Chem. B* **2021**, *125*, 1550.

(315) García-Fresnadillo, D. *ChemPhotoChem* **2018**, *2*, 512.

(316) Liu, T.; Hu, X.; Wang, Y.; Meng, L.; Zhou, Y.; Zhang, J.; Chen, M.; Zhang, X. *J. Photochem. Photobiol. B: Biol.* **2017**, *175*, 156.

(317) Entradas, T.; Waldron, S.; Volk, M. *J. Photochem. Photobiol. B: Biol.* **2020**, *204*, 111787.

(318) Nosaka, Y.; Nosaka, A. Y. *Chem. Rev.* **2017**, *117*, 11302.

(319) Xue, F.; Shi, M.; Yan, Y.; Yang, H.; Zhou, Z.; Yang, S. *RSC Adv.* **2016**, *6*, 15509.

(320) Li, Z.; Liu, C.; Abroshan, H.; Kauffman, D. R.; Li, G. *ACS Catal.* **2017**, *7*, 3368.

(321) Chadwick, S. J.; Salah, D.; Livesey, P. M.; Brust, M.; Volk, M. *J. Phys. Chem. C* **2016**, *120*, 10647.

(322) Dong, Y.; Dick, B.; Zhao, J. *Org. Lett.* **2020**, *22*, 5535.

(323) Cao, M.; Pang, R.; Wang, Q.-Y.; Han, Z.; Wang, Z.-Y.; Dong, X.-Y.; Li, S.-F.; Zang, S.-Q.; Mak, T. C. W. *J. Am. Chem. Soc.* **2019**, *141*, 14505.

(324) BBC. *Syria war: IS 'used mustard gas' on Assad troops*. 2016. https://www.bbc.com/news/world-middle-east-35968604 (accessed April 5, 2016).

(325) Howarth, A. J.; Buru, C. T.; Liu, Y.; Ploskonka, A. M.; Hartlieb, K. J.; McEntee, M.; Mahle, J. J.; Buchanan, J. H.; Durke, E. M.; Al-Juaid, S. S.; Stoddart, J. F.; DeCoste, J. B.; Hupp, J. T.; Farha, O. K. *Chem. Eur. J.* **2017**, *23*, 214.

(326) Kilic, E.; Ortatatli, M.; Sezigen, S.; Eyison, R. K.; Kenar, L. *Cutan. Ocul. Toxicol.* **2018**, *37*, 332.

(327) Czub, M.; Nawała, J.; Popiel, S.; Dziedzic, D.; Brzeziński, T.; Maszczyk, P.; Sanderson, H.; Fabisiak, J.; Bełdowski, J.; Kotwicki, L. *Mar. Environ. Res.* **2020**, *161*, 105077.

(328) Bobbitt, N. S.; Mendonca, M. L.; Howarth, A. J.; Islamoglu, T.; Hupp, J. T.; Farha, O. K.; Snurr, R. Q. *Chem. Soc. Rev.* **2017**, *46*, 3357.

(329) Hao, Y.; Papazyan, E. K.; Ba, Y.; Liu, Y. *ACS Catal.* **2022**, *12*, 363.

(330) Zhi, Y.; Yao, Z.; Jiang, W.; Xia, H.; Shi, Z.; Mu, Y.; Liu, X. *ACS Appl. Mater. Interfaces* **2019**, *11*, 37578.

(331) Liu, Y.; Buru, C. T.; Howarth, A. J.; Mahle, J. J.; Buchanan, J. H.; DeCoste, J. B.; Hupp, J. T.; Farha, O. K. *J. Mater. Chem. A* **2016**, *4*, 13809.

(332) Wang, H.; Wagner, G. W.; Lu, A. X.; Nguyen, D. L.; Buchanan, J. H.; McNutt, P. M.; Karwacki, C. J. *ACS Appl. Mater. Interfaces* **2018**, *10*, 18771.

(333) Zou, J.; Yin, Z.; Ding, K.; Tang, Q.; Li, J.; Si, W.; Shao, J.; Zhang, Q.; Huang, W.; Dong, X. *ACS Appl. Mater. Interfaces* **2017**, *9*, 32475.

(334) Yan, Y.; Sukhanov, A. A.; Bousquet, M. H. E.; Guan, Q.; Zhao, J.; Voronkova, V. K.; Escudero, D.; Barbon, A.; Xing, Y.; Gurzadyan, G. G.; Jacquemin, D. *J. Phys. Chem. B* **2021**, *125*, 6280.

(335) Grzybowski, M.; Gryko, D. T. *Advanced Optical Materials* **2015**, *3*, 280.

(336) Liu, Q.; Bottle, S. E.; Sonar, P. *Adv. Mater.* **2020**, *32*, 1903882.

(337) Tang, A.; Zhan, C.; Yao, J.; Zhou, E. *Adv. Mater.* **2017**, *29*, 1600013.

(338) Huang, Z.; Luo, Y.-H.; Geng, W.-Y.; Wan, Y.; Li, S.; Lee, C.-S. *Small Methods* **2021**, *5*, 2100036.

(339) Xu, J.; Tang, W.; Yang, C.; Manke, I.; Chen, N.; Lai, F.; Xu, T.; An, S.; Liu, H.; Zhang, Z.; Cao, Y.; Wang, N.; Zhao, S.; Niu, D.; Chen, R. *ACS Energy Lett.* **2021**, *6*, 3053.

(340) Stegbauer, L.; Zech, S.; Savasci, G.; Banerjee, T.; Podjaski, F.; Schwinghammer, K.; Ochsenfeld, C.; Lotsch, B. V. *Adv. Energy Mater.* **2018**, *8*, 1703278.

(341) Wan, S.; Guo, J.; Kim, J.; Ihee, H.; Jiang, D. *Angew. Chem. Int. Ed.* **2009**, *48*, 5439.

(342) Ding, S.-Y.; Wang, W. *Chem. Soc. Rev.* **2013**, *42*, 548.

(343) Jin, S.; Supur, M.; Addicoat, M.; Furukawa, K.; Chen, L.; Nakamura, T.; Fukuzumi, S.; Irle, S.; Jiang, D. *J. Am. Chem. Soc.* **2015**, *137*, 7817.

(344) Zhang, J.; Xu, W.; Sheng, P.; Zhao, G.; Zhu, D. *Acc. Chem. Res.* **2017**, *50*, 1654.

(345) Zhang, Y.; Wu, G.; Liu, H.; Tian, R.; Li, Y.; Wang, D.; Chen, R.; Zhao, J.; Liu, S.; Li, Z.; Zhao, Y. *Mater. Chem. Front.* **2021**, *5*, 6575.

(346) Yang, J.; Zeng, Z.; Kang, J.; Betzler, S.; Czarnik, C.; Zhang, X.; Ophus, C.; Yu, C.; Bustillo, K.; Pan, M.; Qiu, J.; Wang, L.-W.; Zheng, H. *Nat. Mater.* **2019**, *18*, 970.

(347) Thommes, M.; Kaneko, K.; Neimark, A. V.; Olivier, J. P.; Rodriguez-Reinoso, F.; Rouquerol, J.; Sing, K. S. W. *Pure Appl. Chem.* **2015**, *87*, 1051.

(348) Lin, H.-W.; Lee, W.-Y.; Chen, W.-C. *J. Mater. Chem.* **2012**, *22*, 2120.

(349) Chen, H.; Guo, Y.; Yu, G.; Zhao, Y.; Zhang, J.; Gao, D.; Liu, H.; Liu, Y. *Adv. Mater.* **2012**, *24*, 4618.

(350) Scharber, M. C.; Sariciftci, N. S. *Adv. Mater. Technol.* **2021**, *6*, 2000857.

(351) Wang, H.; Zeng, Z.; Xu, P.; Li, L.; Zeng, G.; Xiao, R.; Tang, Z.; Huang, D.; Tang, L.; Lai, C.; Jiang, D.; Liu, Y.; Yi, H.; Qin, L.; Ye, S.; Ren, X.; Tang, W. *Chem. Soc. Rev.* **2019**, *48*, 488.

(352) Mandel, K.; Hutter, F.; Gellermann, C.; Sextl, G. *Colloids Surf., A* **2011**, *390*, 173.

(353) Meng, S.; Xu, Z.; Hong, G.; Zhao, L.; Zhao, Z.; Guo, J.; Ji, H.; Liu, T. *Eur. J. Med. Chem.* **2015**, *92*, 35.

(354) Bonnier, C.; Machin, D. D.; Abdi, O.; Koivisto, B. D. *Org. Biomol. Chem.* **2013**, *11*, 3756.

(355) Huo, L.; Hou, J.; Chen, H.-Y.; Zhang, S.; Jiang, Y.; Chen, T. L.; Yang, Y. *Macromolecules* **2009**, *42*, 6564.